Electrochemical Behaviour of Stainless Steel under Radiation and Exposed to Representative Chemistry in Pressurised Water Reactor Conditions

Mi Wang

PhD THESIS OF ÉCOLE POLYTECHNIQUE

Presented to obtain the degree of

DOCTOR OF ÉCOLE POLYTECHNIQUE

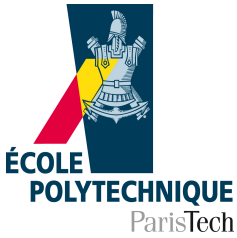

by

Mi WANG

Title:

Electrochemical Behaviour of Stainless Steel under Radiation and Exposed to Representative Chemistry in Pressurised Water Reactor Conditions

Defended in public on 24 September 2013 with the following thesis committee:

Digby MACDONALD	*Président*
Bernard NORMAND	*Rapporteur*
Nathalie MONCOFFRE	*Rapporteur*
Jean-Louis MARIGNIER	*Examinateur*
Frank CARRÉ	*Examinateur*
Stéphane PERRIN	*Encadrant*
Damien FÉRON	*Directeur de thèse*
Catherine CORBEL	*Directeur de thèse*

The author wishes to express her sincere acknowledgment to the "European Foundation for tomorrow's energies" ("Fondation Européenne pour les Energies de Demain") for the financial and continuous support through the École Polytechnique's lecturing program, "Chaire Energies Durables", for the research conducted in this thesis.

Acknowledgement

Foremost, I must express my most profound gratitude to my PhD advisors, Prof. Damien FÉRON and Dr. Stéphane PERRIN; this thesis would not be possible without them. Their enthusiasm, patience, encouragements, guidance, inspiration, motivation, and most importantly their great efforts to defend and protect me in all ways helped me to succeed during the past three years. They were, and will always be, there for me as my PhD advisors as well as "life" mentors; I cannot put into words how much that means to me.

I equally wish to thank my third advisor, Dr. Catherine CORBEL, for giving me the opportunity to run experiments using the Cyclotron at the CEMHTI Laboratory (Conditions Extrêmes et Matériaux: Haute Température et Irradiation) at the CNRS Orléans and also for her support. My thanks also go to Dr. Martine SOYER, Director of the Laboratory of Irradiated Solids (Laboratoire des Solides Irradiés, LSI) at the École Polytechnique (Palaiseau, France), who welcomed me in her laboratory and gave her continuous support over these past years.

I would also like to thank Dr. Benoist MUZEAU, who worked on this subject as a part of his postdoctoral project. His detailed introduction and extensive knowledge of the subject allowed me start working on the study immediately.

In the academic and financial world, I need to give my acknowledgement to the "Chaire Energies Durables" program for funding my thesis project, a project with I am very fortunate to have been a part of. I would like to express special thanks to Prof. Frank CARRÉ, who is not only the program director but has also been an important member of my thesis committee. Thanks to their financial support, I have had the opportunity to attend many international conferences which have helped me to accomplish my thesis goals and expose me to the scientific community.

I would like to thank my thesis committee members. Dr. Nathalie MONCOFFRE and Prof. Bernard NORMAND are my thesis reviewers, I really appreciate them for having read my manuscript in its entirety during their vacation time, especially considering its "thickness". I am also grateful to the rest of the members: Dr. Jean-Louis MARIGNIER, Prof. Frank CARRÉ and especially Prof. Digby MACDONALD who came from the United States for my defense and accepted to be the president of the committee. During my defense, they shared their thoughts and posed very interesting questions leading to a thought provoking discussion, thereby enlarging the perspectives of the study.

As a matter of fact, my experiments (high temperatures, high pressures and in presence of irradiation) were very difficult to be achieved; and have been made possible thanks to the collaboration between the Laboratory of Aqueous Corrosion Studies (Laboratoire d'Étude de la Corrosion Aqueuse, LECA) at the CEA Saclay (Saclay, France), the CEMHTI laboratory at the CNRS Orléans and the Laboratory of Irradiated Solids at the École Polytechnique. Therefore, my greatest thanks should be

sent to all the people I have had a chance to work with over the past three years.

I have spent most of my time in the Laboratory of Aqueous Corrosion Studies (LECA) and I am especially grateful to every single member of the laboratory.

Above all, my dearest sense of gratitude goes to my favorite technician, Mr Daniel BESNARD, for offering me his support and most importantly not abandoning me during the long and seemingly never ending experiments. From Orléans to the École Polytechnique, wherever I went he went with me. No words can express how much I enjoyed for his company during all these hard work and long hours. Furthermore, I have been very lucky to have been surrounded by my many intelligent and thoughtful colleagues who were always ready to listen to the many possible arguments and theories I proposed while progressing though the study, in particular Dr. Loïc MARCHETTI-SILLANS and Dr. Frédéric MISERQUE. I very much enjoyed all of our discussions, which were both extremely inspirational and helpful. I call them the "Master Minds" of our laboratory, and they really are. A massive thank you goes to my "roommate", Mr Marc ROY, for sharing an office with me and enduring my "bad temper" during the thesis redaction. I will never forget the time I spent with all my LECA colleagues during the coffee breaks; I really liked the typical and (not so) funny French jokes. Last but not least, I have to thank our service's secretary, Ms Myléne BELGOME, without whom my life as a foreigner in France would have been much more difficult.

I am grateful to all the co-workers who helped with the proton irradiation experiments in the CEMHTI laboratory at the CNRS Orléans, especially to Ms Rachelle OMNEE my local technician. I cannot imagine having done these complicated experiments without her assistance. I am also very thankful to all the members of the pilot crew in the control room. Their presence made my long and exhausting nighttime experiments much more enjoyable.

One very important person I could not forget to mention is Vincent METAYER, the one and only technician who worked on my electron irradiation experiments in the Laboratory of Irradiated Solids (LSI) at the École Polytechnique.

Next on the list, I would like to acknowledge all the people who have done analyses for this study. I will only mention the members from other laboratories, and skip the guys from my own who may or may not be named before, I am pretty sure they know who they are and just how grateful I am to them. I will begin with the researchers from the Laboratory LISL (Laboratoire d'Ingénierie des Surfaces et Lasers) at the CEA Saclay: Michel TABARANT, Hawa BADJI and Michel SCHLEGEL for the different techniques I employed in the study (ICP-AES, GD-OES, Interferometer, Raman Spectroscopy). Secondly, to the researchers from the SPCSI (Service de Physique et Chimie des Surfaces et Interfaces) at the CEA Saclay: Jacques COUSTY and Nick BARRETT for using "new" methods (CS-AFM and XPEEM) to characterise my samples. I would also like to thank Mr Sylvain VAUBAILLON from the JANNuS laboratory (Joint Accelerators for Nano-science and Nuclear Simulation) at the CEA Saclay, for his kind explanation and efficient NRA analyses. Lastly, a big thank you should be given to Dr. Mohamed SENNOUR from the Centre des Matériaux Pierre-Marie Fourt at the École Mines ParisTech, for his excellent TEM analyses which have brought plenty of useful information to this study.

I am very grateful to my two American colleagues, Travis WADE and Caitlin HURLEY, for helping to correct my English for this dissertation.

My greatest appreciation goes to my closest friends, Tatiana TAURINES, Carl Willem RISCHAU and Meng XIAO. Thanks to my buddies for not only supporting me on the good days but encouraging me to keep going on the dark days. I am forever grateful to my parents for supporting me through my studies and for encouraging me to follow my dreams ever since I was a child.

I do believe that a thesis study is a collective work. The success of my thesis is actually a success for every single person who has ever helped and/or worked with me. I also believe in the ancient Chinese proverb: Man proposes, God disposes. Without our first move, nothing can be done and therefore nothing can be achieved.

Contents

Introduction

Nuclear power is one of the world's major power sources providing almost 6% of the world's total energy and 13-15% of its electricity. Today, nuclear power is the primary energy source in France, providing nearly 80% of the country's electricity, thereby making France one of the world's largest consumers of nuclear power. In France, all the operational nuclear power plants are Pressurised Water Reactors (PWRs). Due to increasingly energy dependance and the necessity to emit few greenhouse gases, nuclear energy has many advantages and seems to be the most cost-effective energy source, if a price is placed on the heat-trapping carbon dioxide emissions from fossil-fuels.

Currently, there are two major concerns to be addressed with nuclear power plants (NPPs): (i) safety and security issues, especially after the accident at Fukushima in March of 2011, (ii) extension of the operational life of current NPPs. In general, today's nuclear reactors have an original design life of 40 years. In order to give these reactors a longer life expectancy, some evolutionary improvements have been made, including, but not limited to, improved fuel technology and superior thermal efficiency. The improvement of reactor life is based on the idea of replacing current components with new high-performance ones. In order to apply this method, it is extremely important to understand the many factors influencing material degradation in nuclear reactors, for instance the impact of radiation exposure in a hostile reactor environment (high temperature, high pressure...).

In Pressurised Water Reactors activated corrosion products in the primary circuit can cause material degradation in the reactor core eventually leading to the shutdown of nuclear reactors. The most common localised corrosion process is stress corrosion cracking (SCC), which can produce material failure by cracking. In the presence of an aggressive environment (radiation, radiolytic products, impurities like chloride), the general or localised corrosion process can be accelerated causing materials such as austenitic stainless steel, traditionally non-susceptible to SCC, to be affected by the corrosion process. This is the reason that understanding the effect of water radiolysis is important to minimise the corrosion issues in PWRs.

In the primary circuit of a PWR, water radiolysis occurs at high temperatures (HT), 280 - 320 °C, and high pressures (HP), 15.5 MPa. The products of water radiolysis can modify the corrosion issues of some materials, such as the internal components made of austenitic stainless steel (304L and 316L mainly). The presence of water radiolysis may change the PWR water environment into an oxidative environment and thus accelerate the corrosion process. It is proven that with the addition of hydrogen (25-50 cc/kg (STP)) radiolysis can be inhibited for bulk water; however there is very little experimental data at high temperatures and high pressures proving this theory valid for interfaces under PWR operational conditions.

This thesis is dedicated to an investigation of the effect of water radiolysis on the electrochemical

behaviour of austenitic stainless steel (316L grade) exposed to a representative PWR environment. The present approach uses either a proton or an electron beam to control the production of radiolytic species at a 316L/PWR water interface. Two types of corrosion cells are used: a specific and unique metallic type cell working at high temperature and high pressure (HTHP cell) and a Teflon® type cell working at room temperature and atmospheric pressure (Teflon® cell). *In-situ* monitoring of the evolution of the electrochemical potential under irradiation coupled with an *ex-situ* characterisation of the oxide film and the PWR water chemistry enable further understanding of the electrochemical behaviour in PWR environment at a 316L/PWR water interface.

This dissertation is divided into four main parts. Part I (Chapters $1-3$) provides the context of this study, including background information on PWRs, water radiolysis, and the relevant corrosion issues. A literature survey on the Light Water Reactors (LWRs) has been published recently with focus on radiolysis and corrosion [1]. A selection of this review will constitute the bibliography of this dissertation. Part II (Chapter 4) describes the experimental devices (the HTHP cell and the Teflon® cell), experimental procedures, and the *ex-situ* characterisations in detail. Part III (Chapters $5-7$) presents the results obtained by using the HTHP cell, followed by further developments based upon the interpretations and observations. It seems that some defects in the oxide film are induced by HTHP water radiolysis, which is also exhibited in irradiated PWR water. Part IV (Chapter 8) concerns the proton irradiation experiments at room temperature using the Teflon® cell and completes the study by investigating the evolution of irradiation induced solutes (cations, acidity, and H_2O_2) in the irradiated PWR water. The conclusion includes outlooks and industrial consequences, coming from the presented results, regarding the stainless steel behaviour in primary PWR conditions.

The goal of this study is to understand the electrochemical behaviour of irradiated stainless steel in simulated primary PWR conditions as well as the effect of water radiolysis on the corrosion behaviour of stainless steel using both electrochemical methods and the characterisation of the formed oxide films.

References

[1] Wang M. Irradiated Assisted Corrosion of Stainless Steel in Light Water Reactors - Focus on Radiolysis and Corrosion Damage. *Hal*-00841142 *v*1, 2013.

Part I

Bibliography

Chapter 1

Pressurised Water Reactors (PWRs)

Nuclear power is one of the major sources of energy and electricity production. Nuclear power plants provide about 6% of the world's energy and 13 - 15% of the world's electricty [1, 2]. Nuclear power plants are conventional thermal power stations in which the heat sources are nuclear reactors. They are devices to initiate and control sustained nuclear chain reactions and the heat from nuclear fission is passed to a thermal fluid (water or gas), which runs through turbines to generate power. Most of the nuclear reactors use energy form the the fission of the nucleus of the Uranium 235 isotope, ^{235}U. In France, the nuclear fuel is used in the form of uranium dioxide enriched to 3.5 - 4% in $^{235}UO_2$ [3].

The most common types of nuclear reactors are thermal reactors, among which the most popular are Light Water Reactors (LWRs). Because the LWRs are simple and less expensive to build compared to other nuclear reactors, they make up the vast majority of civil nuclear reactors and naval propulsion reactors in service. The LWRs can be subdivided into three categories: Boiling Water Reactors (BWRs), Pressurised Water Reactors (PWRs) and Supercritical Water Reactors (SWRs). BWRs and PWRs are currently in operation while SWRs are still at the design stage [4]. PWRs are the most common civil nuclear reactors in the world. In France, they are the only ones in operation today.

1.1 Pressurized Water Reactors (PWRs)

1.1.A The Primary and the Secondary Circuits of PWRs

PWRs are actually the most common type of commercial nuclear power plants which are widely used all over the world. Like BWRs, the first commercial PWR was designed and constructed in the USA during the late 1950*s*. Gradually, big companys like Westinghouse, General Electric, Areva, EDF, Toshiba and Mitsubishi have joined in the development of PWRs. Nowadays, most PWRs under construction are the Generation III and III+ type. For instance, the European Pressurised Reactors (EPRs) designed by Areva, EDF and Siemens AG, the AP600 and AP1000 of Westinghouse Electric Company and the Mitsubishi Advanced Pressurised Water Reactor (Mitsubishi APWR) developed by Mitsubishi Heavy Industries.

PWRs have two major systems which are normally called the primary and the secondary circuits. The primary (or primary coolant) circuit is responsible for transferring the heat produced from the nuclear fuels to the steam generator. The steam formed in the steam generator is transferred to the main turbine generator in the secondary circuit where steam is converted into electricity. In a PWR, the pressuriser provides a way of controlling the system pressure. The nuclear reactor coolant, usually water, is circulated by the coolant pump in order to transfer the heat form the reactor core to the steam generator at a constant flow rate. The heat being generated by the fission process inside the reactor core is then used to generate steam in the steam generator which contains many tubes inside. The reactor coolant fluid comes in the bottom of the steam generator and flows through the inside of the tubes. The secondary feedwater which is used to pick up the heat flows around the outside of the tubes. After absorbing sufficient heat, the secondary feedwater starts to boil and generate steam. Afterwards, the condensate/feedwater system takes over the steam and sends to the main turbine for generating electricity. As the fact that the primary and the secondary circuits are physically separated, all the fission products stay inside of the primary circuit. A schema of a Pressurised Water Reactor (PWR) has shown in Fig.1.1.

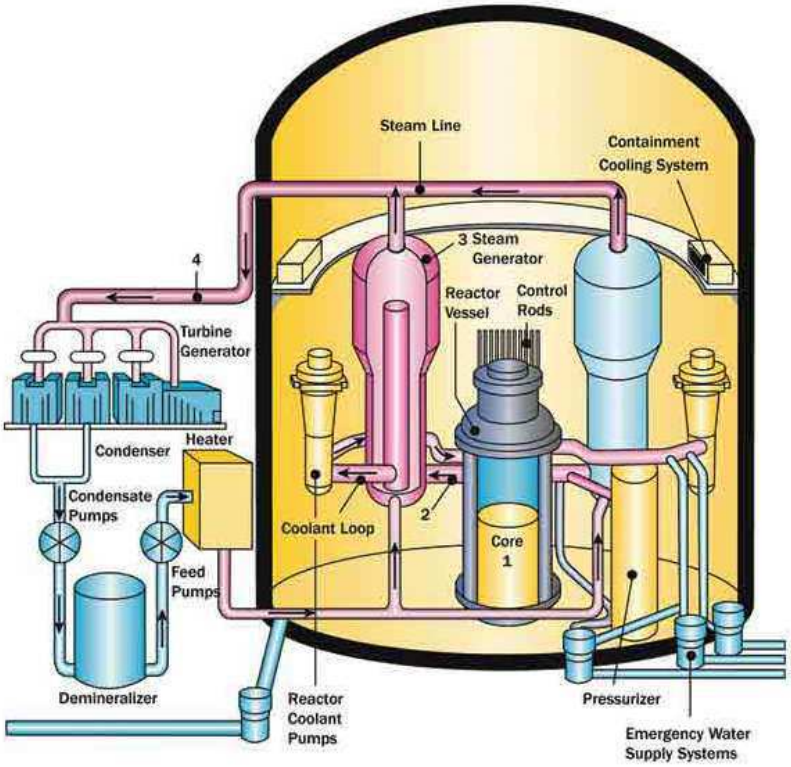

Figure 1.1: Schema of Pressurised Water Reactor.

The pressure in the primary coolant circuit is around 155 bars, which is the highest among all types of nuclear reactors. Thanks to this high pressure, the primary circuit coolant enters the bottom of the reactor core at about 275°C and is heated as it flows upwards through the reactor core to a temperature of about 320 $\sim$ 325°C [5]. The high temperature and high pressure in the primary coolant circuit are always regarded as a specific characteristic of PWRs.

PWRs normally use enriched uranium dioxide of ^{235}U, clad in a corrosion-resistant zirconium metal alloy Zircaloy, as the nuclear fuel. Light water is used as neutron moderator and coolant in PWRs. However, unlike BWRs, the coolant of PWRs is the demineralised water which contains Boron (B) and Lithium (Li). Boron, introduced in the form of boric acid (H_3BO_3 or $B(OH)_3$), a strong neutron absorber, is used as a neutron poison to slow down the fission reaction rate in PWRs. It can help to maintain the temperature of the primary coolant circuit at the desired point. A typical neutron absorption reaction in boron is written below Eq.1.1. This nuclear reaction leads to an increase of temperature. The energy is taken over by the primary circuit and transferred to the secondary circuit, reducing the power efficiency as the result.

$$^{10}_{5}B + ^{1}_{0}n \rightarrow ^{7}_{3}Li + ^{4}_{2}He + 2.35MeV \tag{1.1}$$

The ^{10}B has a high cross section for absorption of thermal neutrons. For PWRs, boric acid used contains 19.8% of ^{10}B. As the role of the control rod in PWRs, changes in boric acid concentration can effectively regulate the rate of fission taking place in the reactor. However, due to fuel corrosion concerns, the pH around 7 of the coolant at 300°C is strongly recommended. For this reason, lithium

hydroxide (LiOH) is also added in the primary coolant in order to achieve the desired pH. On the other hand, it can not be denied that the presence of boron and lithium in the primary coolant may cause complexness of water chemistry control in PWRs which will be explained in the following section Chap.1.1.B.

The secondary circuit of a PWR is composed of a main steam system and a condensate (or feedwater) system. The hot reactor coolant flows from the reactor to the steam generator, through many tubes inside. The secondary coolant, or feedwater, flows around the outside of the tubes, where it picks up heat from the primary coolant. When the feedwater absorbs sufficient heat, it starts to boil and form steam. Then the steam is transferred to the main turbine so that it can be converted into electricity [6].

1.1.B Water Chemistry Control in the Primary Circuit

In PWRs, water chemistry control is extremely important because it has a great influence on corrosion issues which occur inside the reactor, either the primary or the secondary circuits. Dissolved corrosion products from the out-of-core region, the primary side of the steam generator tubes, may be deposited on the fuel cladding surfaces. Then, these activated corrosion products in the primary circuit will cause materials degradation in the reactor core, high-radiation fields on out-of-core surfaces, compromise fuel performance etc...

In order to avoid water radiolysis and to treat these corrosion issues, dissolved hydrogen has been imposed on the primary coolant initially. Therefore, it can reduce the ECP and raise pH in the primary circuit. A certain concentration of hydrogen (about 30 $cm^3.kg^{-1}$) is also required to suppress *water radiolysis* in the reactor core. Actually, it shares more or less the same principal reason for the addition of dissolved hydrogen in both PWRs and BWRs. However, in the primary coolant circuit, a steadily decreasing concentration of boric acid is used as a chemical shim throughout the fuel cycle which results in the use of lithium hydroxide to maintain the pH_T around 7. Thus, the balance between B and Li in order to keep an optimal pH_T is becoming another key factor for water chemistry control in PWRs. Following successful experience of BWRs, zinc injection has been adopted in the primary circuit of PWRs in several countries. In BWRS, zinc injection has proved to mitigate IGSCC. In PWRs, it may limit the concentration of ^{60}Co and delay the initiation of Primary Water Stress Corrosion Cracking (PWSCC) [7].

1.1.B.1 Dissolved Hydrogen

The primary coolant composed of a demineralised water with boric acid and lithium hydroxide, is under a radiation mixed up with:

- γ**-rays** from the fission reactions;
- **fast neutrons** from the fission reactions;
- a radiation of $^{10}\mathbf{B(n,}\alpha\mathbf{)}^{7}\mathbf{Li}$ produced in water by the thermal neutron capture reactions;

The proportion of these different types of radiations depends on the configuration of the reactor core and the concentration of boric acid. Furthermore, these radiations are the causes of chemical

degradation of the water in the primary circuit. This is what is called **water radiolysis**. The products of water radiolysis can participate in corrosion process in the primary circuit of the reactor. In order to minimise the corrosion problem, the water has been deaerated to eliminate all trace of oxygen. Moreover, by adding molecular hydrogen dissolved into the water, the water decomposition is strongly inhibited by a radical mechanism, and the production of oxygen will be slowed down. This will be discussed in the next chapter.

Other than inhibition of water radiolysis, the dissolved hydrogen is also used to decrease the redox potential of the PWR primary water in order to avoid being under an oxidising conditions. In France, the dissolved hydrogen in the primary PWR water is recommended to be 25 to 35 $cm^3.kg^{-1}$ (STP[1]), with the maximum values from 25 to 50 $cm^3.kg^{-1}$ (STP). The recommended amount of hydrogen corresponds to a concentration about 0.001 $mol.L^{-1}$. For PWRs, the quantity of water in the primary circuit is between 200 and 290 tonnes, thus the volume of hydrogen is between 5 to 10 m^3 at 20°C and 1 bar.

1.1.B.2 Balance of Li/B/pH$_T$

Recent work [7–11] demonstrates that the effect of lithium, boron and pH on PWSCC is quite minimal on material susceptibility, comparing with stress state, temperature, pressure and other operational issues. Nevertheless, among the three parameters, at-temperature pH, pH$_T$ is the dominate which actually is adjusted by the concentration of both LiOH and boric acid.

A pH$_T$ between 6.9 and 7.4 was first recommended for the primary coolant in PWRs due to the fact that the temperature coefficients of solubility of magnetite and nickel ferrite are minimum at the range of these two pH values, and thus it can minimise the contamination of the circuit. The possibility of the deposit of corrosion products in the primary circuit is based on the solubilities of iron (magnetite) and nickel (nickel ferrite) which are strongly depend on pH, temperature, and redox potential. Thus, a maintained pH$_T$ in the range of [6.9, 7.4] is defined to reduce corrosion product release rates and continued to be used until now. Although, some details and specific precisions have been made to narrow the pH$_T$ range. Since the nickel ferrite is the prime constituent of CRUD, a preference of pH$_T \backsim$ 7.4 has been made little by little. General corrosion can be reduced on elevated pH$_T$ [12] and corrosion products release rates become less dependent on pH$_T$ as it approach to 7.4 [13]. Indeed, no significant adverse effect has been observed when the pH$_T$ increased to 7.3 in primary circuit of Comanche Peak PWR [14]. As a result, pH$_T$ in the ranges [7.1, 7.2], [7.3, 7.4] are becoming more and more popular. However, different voices on pH$_T$ has been brought up, a pH$_T$ even lower than 6.5 without any adverse effects has been observed in the most recent research [15]. After all, the discussion about pH$_T$ is still undergoing.

The effect of lithium is smaller than the pH$_T$ effect. Nonetheless, the concept of *coordinated of boron and lithium* has been developed form the very beginning. Originally, a limit of 2.2*ppm* of LiOH has been decided due to the Zircaloy corrosion concern. However, normally PWR fuel cycles start with a relatively high boric acid concentration, and reduce little by little until the end of the cycle. Thus, in order to maintain a constant pH$_T$, the concentration of LiOH needed to be gradually reduced in

[1]**STP: S**tandard conditions for **T**emperature and **P**ressure are standard sets of conditions for experimental measurements established to allow comparisons to be made between different sets of data. In PWRs, the STP is normally referred to the standard of NIST, which means a temperature at 20°Cand an absolute pressure of 101.325 kPa (1 atm).

line with the boric acid reduction. Fig.1.2 shows that concentration range between lithium hydroxide and boron in order to obtain a constant $pH_{300°C}$ at 7.2.

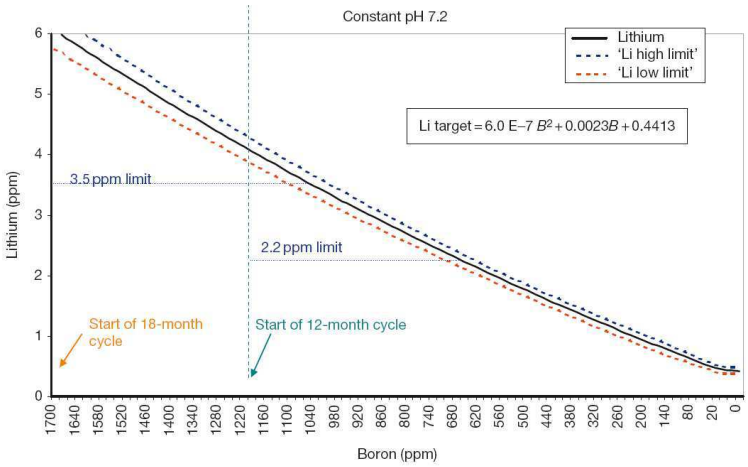

Figure 1.2: Concentration range of boric acid versus lithium hydroxide in order to maintain the $pH_{300°C}$ around 7.2 for different fuel cycle lengths [7].

The elevation of pH_T actually demands an increase in lithium concentration on the condition that the concentration of boric acid stays constant. However, new laboratory data indicate that increasing lithium may lead to an acceleration of stress corrosion cracking on irradiated stainless steel [15]. As a matter of fact, the cracking rate can decrease with the hydrogen concentration, either lower or higher. It depends on the reactors themselves. For a relatively new reactors, such as these ones in France, in Japan and the new ones have just been constructed in the developing countries, they prefer a lower hydrogen concentration. On the opposite, a higher concentration of Li, between $3ppm$ and $3.5ppm$, becomes popular in USA for their long-time served reactors.

As the last parameter in the balance of $Li/B/pH_T$, boron is usually considered as the minor influence. Enriched Boric Acid (EBA) enables to give a desired pH_T with less lithium hydroxide. Hence, EBA has been employed in several PWRs. Nevertheless, boric acid in water can result in an aggressive environment that uniformly attacks the surface of the metal in PWRs.

In general, the balance of $Li/B/pH_T$ is flexible for different plants and different countries. Actually, the pH adjustment for minimising PWSCC has not been ensured and totally proved yet [16]. Thus, different strategies are established: like the elevated pH/lithium, like the use of EBA... Overall, monitoring pH in the primary circuit is considered as the priority in water chemistry control in PWRs.

1.1.B.3 Zinc Injection

Zinc injection in PWRs is actually following the successful experiences of BWRs. Like avoiding IGSCC in BWRs, zinc injection may delay the initiation of PWSCC in PWRs [14]. A recent VTT report [17] has shown the benefits of zinc injection: a significant decrease of SCC, no adverse effects on core performance, negligible effect on cladding integrity and mitigating the CRUD deposition in the core. Thus, zinc injection is nowadays treated as one of the key factors of primary coolant chemistry optimisation for corrosion mitigation and source term reduction in PWRs. Zinc injection in PWRs is widely used in USA and Germany from the late $1990s$, however in France, zinc injection is not so

popular, it appears to be studied recently and might be adopted later.

1.2 Summary

The first chapter gives a short introduction about PWRs. However, the information about primary circuit of PWRs is referred as the most important concerning the thesis study, the followings are some important points about the primary circuit of PWRs should be mentioned again:

- **PWR solution:** Water used in a PWR, contains boric acid as a neutron poison to control the reactivity of nuclear fuel. The water also contains lithium hydroxide in order to adjust the pH to maintain around 7.2 at 300°C. Thus, this water will cause fewer corrosion problems.
- **Pressure:** Water in primary coolant circuit, a closed circuit, at a pressure of 155 **bar** in order to avoid boiling;
- **Temperature:** Water of a PWR is around $300 - 320$°C.
- **Hydrogen:** Water is deaerated and contains hydrogen, $25 - 50$ cm^3. kg^{-1} (STP), for inhibiting decomposition caused by radiolysis.
- **Radiation:** Water is under radiation of γ, fast neutron, and $^{10}B(n,\alpha)^7Li$ produced in water by the thermal neutron capture reactions.

References

[1] World Nuclear News. Another drop in nuclear generation, May 2010.

[2] Key World energy Statistics 2007, 2008.

[3] Wikipedia. Nuclear power in france, http://en.wikipedia.org/wiki/nuclear power in france.

[4] Zoran V. STOSIC. Gen -III/III+ Reactors: Solving the Future Energy Supply Shortfall - The SWR - 1000 Option. In *Proceeding of the International Conference Nuclear energy for New Europe*, 2006.

[5] Wikipedia. Pressurized water reactor, http://en.wikipedia.org/wiki/Pressurized water reactor.

[6] Reactor concepts manual - pressurized water reactor (pwr) systems,. Technical report, USNRC Technical Training Center.

[7] R. Konings, editor. *Comprehensive Nuclear Materials*. Elsevier Science, 1*st* Edition edition, 2012.

[8] Andresen, P.; Ahluwalia, A.; Hickling, J.; Wilson, J. Effects of PWR primary water chemistry on PWSCC of Ni alloys. In 13th International Conference onEnvironmental Degradation of Materials in Nuclear Power Systems, Whistler, Canada. 2007.

[9] Andresen, P.; Ahluwalia, A.; Wilson, J.; Hickling, J. Effects of dissolved H2 and Zn on PWSCC of Ni alloys. In *In VGB NPC 08 Water Chemistry Conference, Berlin*, 2008.

[10] Andresen P. L., Emigh P. W., Morra M. M., Hickling J. Effects of PWR Primary Water Chemistry and Deaerated Water on SCC. In Allen T. R., King P. J. and Nelson L., editor, *Proceedings of the 12th International Conference on Environmental Degradation of Materials in Nuclear Power System - Water Reactors*, pages 989–1008, 2005.

[11] Roman Celin, Franc Tehovnik. Degradation of a Ni-Cr-Fe alloy in a Pressurised-Water Nuclear Power Plant. *Materials and technology*, 45 (2):151–157, 2011.

[12] Fruzzetti, K.; Rochester, D.; Wilson, L.; Kreider, M.; Miller, A. Dispersant application for mitigation of steam generator fouling: Final results from the McGuire 2 long-term trial and an industry update and EPRI perspective for long-term use. In *In VGB NPC 08 Water Chemistry Conference, Berlin.*, 2008.

[13] Peter J. Millett, Christopher J. Wood. Recent Advances in Water Chemistry Control at US PWRs. In *Proceedings of 58th International Water Conference, Pittsburgh*, 2007.

[14] Stevens, J.; Bosma, J. Elevated RCS pH program at Comanche peak. In *In VGB NPC 08 Water Chemistry Conference, Berlin.*, 2008.

[15] Chemistry Update August 2012.

[16] K. Fruzzetti. Pressurized Water Reactor Primary Water Chemistry Guidlines, Volume 2, Revision 6. Technical report, EPRI, 2007.

[17] Iva Betova, Martin Bojinov, Petri Kinnunen, Timo Saario. Zn injectin in Pressurized Water Reactors - laboratory tests, field experience and modelling. Technical report, Technical Research Center of Finland (VTT), 2011.

Chapter 2

Water Radiolysis

Radiation chemistry deals with the chemical effects produced when materials are exposed to high-energy, ionising radiation. The most common types of radiation are those produced by the decay of radioactive nuclei (α, β and γ radiations), beams of accelerated charged particles (electrons, protons, helium nuclei, and heavier nuclei), and short-wavelength electromagnetic radiation (X-ray or bremβtrahlung radiation).

Radiation initiated chemical change, or **Radiolysis** is typically produced by a mixture of reactive intermediates that includes ions, excited molecules and free radicals at a critical stage in the process. The high energies (in the keV or MeV range) available in radiation-chemical initiation are sufficient to raise any one of the molecules present to one of its possible ionised or excited states which may cause the complex radiation-chemical reactions mechanisms.

In this chapter, we will focus on the radiolysis of pure water which is followed by the radiolysis of PWR solution. Before these two paragraphs, a brief introduction of radiation sources will be presented.

2.1 The Interaction of Radiation with Matter

All radiation is detected through its interaction with matter. When a particle travels through a piece of material, it may interact with the nuclei or with the electrons present in the material. This probability depends on the thickness, the number of potential target particles (scattering centres) per volume unit and the interactions. The **cross section** is a convenient concept to describe the interaction of particles with matter. Higher cross section brings more interactions, that's why most nuclear reactors use materials have high neutron absorption cross section as neutron poisons. These particles: electrons, photons, protons, neutrons and so on, charged or non charged, first interact with the matter and then transfer energy to this medium and eventually stop by dissipating all of their energy.

There are two types of radiation, direct ionising and indirect ionising radiation for charged and uncharged particles, respectively. When charged particles, like α particles, β particles, electrons and protons, penetrate matter, they interact with the electrons and nuclei present in the material through the Coulombic force. They cause ionizations[1] and excitations[2] of atoms through Coulombic interactions. Ionisation and excitation are the most important processes for the majority of radiation types and interaction situation. On the other hand, indirect ionising of uncharged particles, like photons and neutrons, they can transfer energy to charged particles, nuclei and electrons through electromagnetic or nuclear interactions.

2.1.A Energy Loss via Interactions

When a particle is moving through a material, it interacts with the matter in different ways and loses energy during the interactions. Different particles have different processes of energy loss. For photons, energy may be totally adsorbed via a single interaction. For energetic neutrons, it is mainly due to nuclear interactions. These will be detailed in the following sections 2.1.B.1 and 2.1.B.4. For charged particles, the process involves multiple reactions which can be roughly divide into two different ways:

[1] **Ionisation:** An outer shell electron is removed from an atom in the medium and an ion pair, the free electron and the charged positively atom, is formed.

[2] **Excitation:** An electron within one of the orbits of an atom absorbs energy and is moved into a higher energy.

- Energy loss by *ionisation*;
- Energy loss due to *radiation*;

Before discussing these two processes, I will briefly recall the **scattering** process, which is a basis for energy transferring in particle physics.

2.1.A.1 Scattering

In general, scattering theory is a natural phenomenon. It happens in a lot of domains: physics, optics, acoustics, etc. Scattering also occurs in particle physics, for both quantum mechanics and quantum chemistry, it involves a lot of partial differential equations and Schrödinger's equation and so on [1]. However, these equations and calculations are not our initial interests, only a general introduction about scattering will be included in the following discussion.

Scattering occurs when a projectile is fired at a target, the projectile can be scattered or remain unscattered. The scattering problem is actually about the characteristics of both the scatterer, which is the incident particles and the medium, meaning the target. There are many kinds of scattering, among which the most discussed are elastic, inelastic and multiple scatterings.

Elastic Scattering Elastic scattering is a specific form of scattering because there is no energy loss during the process. It is often referred to *billiard ball* collisions under the condition that the electrons and nuclei of medium are considered to be initially free and at rest. The kinetic energy of the incident particle is shared between itself and the medium after the collision, thus momentum is always conserved. The maximum energy that can be transferred in a single collision occurs if the collision is head-on. Actually, not only the energy can be transferred during the collision, but also the direction can be changed. For example, most energy loss of a proton interaction is due to the collision with the electrons in the matter and most of the change of direction is due to the collisions with the nuclei. Normally for charged particles, after penetrating matter, a trail of excited atoms and free electrons from acquired energy in the collision, will be left behind.

Inelastic Scattering Inelastic scattering, on the contrary, is the kinetic energy of the incident particle which is not conserved. It is lost inside the medium, given to some other internal process and only part of the energy is continuously moving in the medium. Generally, scattering due to inelastic collision is inelastic scattering. Different from elastic scattering, it may break up the medium into new forms [2].

Multiple Scattering Other than elastic and inelastic scatterings, there is also multiple scattering which is actually defined as the change in direction of charged particles after the collision with the nuclei. It is also named as *direction straggling*. Normally, charged particles will lose their original direction after scattering over a very large angle in one radiation length. Among all, the most affected by multiple scattering is the electron interactions. For heavy charged particles, they will stop before they have scattered over a large angle. Therefore, their path in the material will be a line in most cases. Oppositely, electrons can penetrate deeply in the material and their angles can be changed significantly, thus their trajectories are normally curve.

2.1.A.2 Energy loss by ionisation

The most classic way of describing energy loss by ionisation is the **Bethe Formula**[3]. It describes the mean rate of energy loss $-dE$ in a distance dx by moderately relativistic charged particles. There are different versions of this formula found in different textbooks [3–6], the most complete form is given in Eq.2.1.

$$-\langle\frac{dE}{dx}\rangle = 4\pi N_A r_e^2 m_e c^2 z^2 \frac{Z}{A}\frac{1}{\beta^2}[\frac{1}{2}ln\frac{2m_e c^2\gamma^2\beta^2}{I^2}T^{max} - \beta^2 - -\frac{\delta(\beta\gamma)}{2}] \tag{2.1}$$

where:

N_A is Avogadro's number;

r_e is the classical electron radius;

m_e is the electron mass;

c is the velocity of light in vacuum;

z it the particle charge;

Z is the atomic number of absorber;

A is the atomic mass of absorber;

$\beta = \frac{v}{c}$, which is speed of the particle relative to c;

$\gamma = \frac{1}{\sqrt{1-(\frac{v}{c})^2}}$, Lorentz factor;

I is the mean excitation energy (potential);

T^{max} is the maximum of kinetic energy; and

$\delta(\beta\gamma)$ is the density effect correction to ionisation energy loss.

It gives a precision on the mean rate of energy loss for a $\beta\gamma$ between 0.1 and 1000, and for an intermediate-Z ($7 \leqslant Z \leqslant 100$) material with an accuracy of a few %. Furthermore, it indicates that the energy loss is independent of the mass of the incident particle but depends on the square of its charge. It depends both on the mass and the charge of the medium. It can also be considered as proportional to $1/\beta^2$ while the slowly varying logarithmic term is treated as a constant. Last but not least, for the particle with very low energy, the **Bethe formula** is no longer applicable, because the state of the charge varies continuously along its course by losing or recapturing electrons.

Despite the complication of the **Bethe formula**, many approximations have been made to simplify the original equation by considering the different value of $\beta\gamma$ [3, 5]. To simplify the explanation, when the value of $\beta\gamma$ is between $3 \Rightarrow 4$, it can obtain the the **minimum ionisation loss**. When the value is less than 3, thus energy loss falls as as $\beta^{-\frac{5}{3}}$, thus it is the **low velocity regime**. Oppositely, if the value is more than 4, there is the **relativistic rise**, energy loss rises indefinitely due to the **density effect** which might cause a saturation at a large value of $\beta\gamma$. High energy particles lose energy slowly due to ionisation, and thus they will leave **tracks** in the medium.

By using the **Bethe formula**, energy loss in air versus the kinetic energy for several different types of charged particles is illustrated in Fig.2.1. Energy loss decreases with increasing kinetic energy and

[3]In previous literature, it is often named the **Bethe-Bloch formula**.

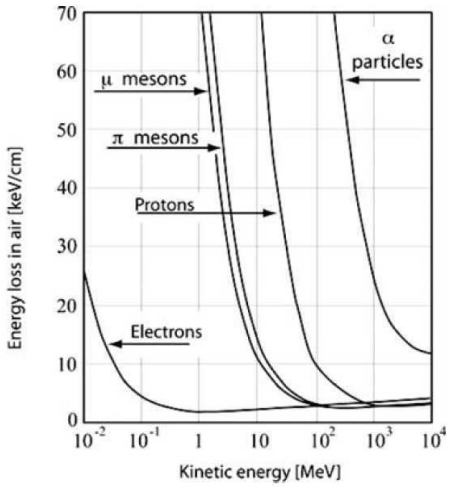

Figure 2.1: Energy loss in air versus kinetic energy for different charged particles. [3, 4].

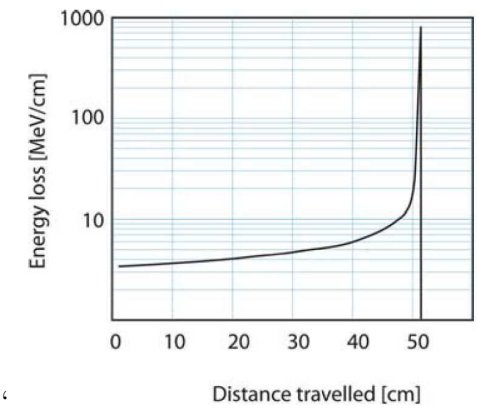

Figure 2.2: Energy loss of a 300MeV proton beam along its trajectory in water. [7].

gradually it arrives at a constant value which depends no more on energy. Except for α particles, the other particles share nearly the same value. For α particles, the energy loss is the greatest because of its low velocity compared with light.

Incident particles lose energy gradually on their way while traveling in the medium and eventually come to rest after losing their energy. The traveling distance is normally called the **range**. The range is defined as Eq.2.2, and it is not simply equal to the energy divided by the energy loss. Actually, if two different particles share the same velocity, the heavier one will travel further; and if they share the same initial kinetic energy, the lighter one travel further.

$$R = \int_{E_0}^{0} \frac{dE}{dE/dx} \tag{2.2}$$

The energy loss has a sudden increase towards the end of the range before it drops to zero, which is shown in the Fig.2.2 [7]. In literature, it is called as the **Bragg peak**. It clearly shows that most energy is deposited close to the end of its traveling path.

In addition, the energy loss can be considered as a statistical process: the particle starts with fixed energy E, and ends up with a spread of energies. This variability in energy values is referred as **energy loss straggling**[4]. Corollary to energy loss straggling, a spread of ranges can be observed in the end, so-called **range straggling**.

Finally, the concept of energy loss due to ionisation is not always true because many atoms may only be brought to an excited state and not ionised during the interaction. Fig.2.3 shows the process of energy loss step by step in a simplified distribution diagram. When the initial energy of the charged particle is strong enough, it can finally ionise the atoms and leave some of the electrons with sufficient energy themselves to excite or ionise atoms in the medium. These high-energy electrons are so-called δ electrons.

[4]In some literature, energy loss straggling is referred to energy straggling.

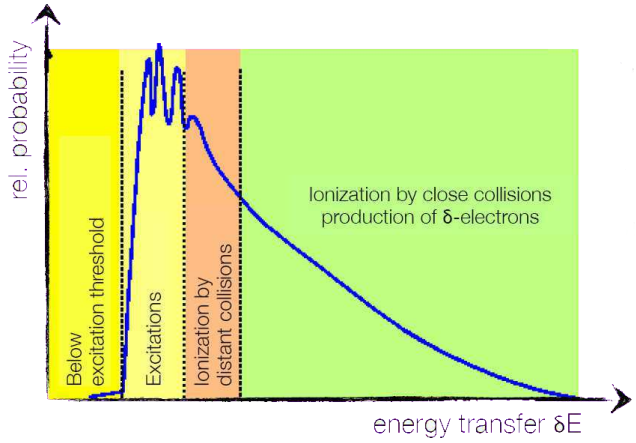

Figure 2.3: Simplified distribution diagram of energy loss in process during interactions.

2.1.A.3 Energy loss due to radiation

Energy loss of charged particles is also due to radiation, for example, the dominant mechanism of energy loss for high-energy electrons is electromagnetic radiation. Different interactions exist for energy loss due to radiation: **Bremβtrahlung**, **Cherenkov effect** and **transition radiation**. However, we will only focus on *Bremβtrahlung*, which is actually the most discussed.

Any charged particles undergoing acceleration will emit electromagnetic radiation. **Bremβtrahlung** is a unique form of it. For a charged particle penetrating a material, it emits radiation when it is accelerated or decelerated by the electric field of the material's atomic nuclei electrons, and therefore it will slow down and lose energy on its trajectory. This is so-called **Bremβtrahlung**. When a charged particle is lighter, the accelerations is greater.

In order to have a general idea on radiative energy loss, it is necessary to define the **radiation length**, X_0, it is parametrized by Y.S. Tsai [5, 6, 8, 9], Eq.2.3. In this equation, α is the fine structure constant; r_e, N_A, A and Z are the definition represented for the **Bethe formula** (Eq.2.1); the function f(Z) is an infinite sum, it could be represented as Eq.2.4 in general; and the values of L_{rad} and L'_{rad} are given in Tab.2.1.

$$\frac{1}{X_0} = 4\alpha r_e^2 \frac{N_A}{A}\{Z^2[L_{rad} - f(Z)] + ZL'_{rad}\} \tag{2.3}$$

$$F(Z) = \alpha^2 Z^2 [\frac{1}{1+\alpha^2 Z^2} + 0.20206 - 0.0369\alpha^2 Z^2 + 0.0083\alpha^4 Z^4 - 0.002\alpha^6 Z^6] \tag{2.4}$$

As the **Bethe formula** for energy loss by ionisation, the equation for energy loss due (dE) to bremsstrahlung per unit length (dx) can be written in Eq.2.5, in which the E means the reduced energy of the charged particle. It can be expressed by the initial energy E_0 and the thickness of the material x in Eq.2.6.

$$\left(\frac{dE}{dx}\right)_{brem\beta trahlung} = \frac{E}{X_0} \tag{2.5}$$

$$E = E_0 e^{-x/X_0} \tag{2.6}$$

Because of the **Bremβtrahlung** effect, track length of charged particle becomes quite variable. If the particle radiates a photon, it can lose a significant fraction of its energy suddenly, and thus shorten its track length. Furthermore, the **Bremβtrahlung** effect takes place over a wide distance along the track of charged particles, and leads a large variability of its range.

2.1.A.4 Total energy loss

The total energy loss of a charged particle can be simply defined as the sum of the loss via ionisation and radiation, 2.7.

$$\left(\frac{dE}{dx}\right)_{tot} = \left(\frac{dE}{dx}\right)_{Ion} + \left(\frac{dE}{dx}\right)_{Brem\beta} \tag{2.7}$$

Nevertheless, for different types of particles, the dominate energy loss is different, shown is Eqs.2.8 and 2.9. It indicates that for a charged particle heavier than electrons, the energy loss is dominated by ionisation.

$$\left(\frac{dE}{dx}\right)^{electrons}_{brem\beta trahlung} \gg \left(\frac{dE}{dx}\right)^{electrons}_{ionization} \tag{2.8}$$

$$\left(\frac{dE}{dx}\right)^{heavy\ particles}_{brem\beta trahlung} \ll \left(\frac{dE}{dx}\right)^{heavy\ particles}_{ionization} \tag{2.9}$$

2.1.B Different Types of Radiation

There are mainly two types of radiation sources used in the study of radiation-chemical radiation. One is the classical radiation sources and the second is generators and accelerators. There exist various types of accelerators, like for electrons, and also accelerators such as Van de Graaff accelerator or cyclotron used to generate beams of positive ions. Nuclear reactors have also been used as radiation sources of neutron beams.

Most particles interact primarily with electrons. The coulomb interaction is long-ranged so the slowing down of the charged particles is most effective and is a continuous process. The electromagnetic interactions requires a collision of a photon and electron and leads to a discrete stopping process. Neutrons are different, they interact only with nuclei.

Z	Element	L_{rad}	L'_{rad}
1	H	5.31	6.144
2	He	4.79	5.621
3	Li	4.74	5.805
4	Be	4.71	5.924
$\geqslant 5$	others	$\ln(184Z^{-1/3})$	$\ln(1194Z^{-2/3})$

Table 2.1: L_{rad} and L'_{rad} values for calculating the radiation length in any element by using Eq.2.3. [5, 6]

2.1.B.1 Interaction of Photon Radiation

X-ray and γ rays are both high energy photons, with energy range from 1 to 100keV referred as X-ray and energy above as γ ray [3]. However, in most literature, any photon energy above 1keV is regarded as γ ray, which is focused on the discussion below. γ rays are electromagnetic radiation of nuclear origin with wavelength in the region of 3.10^{-11} m to 3.10^{-13} m which indicates approximately 40 keV to 4 MeV in energy. Normally, the interactions between photons and matters have small perturbations, a slight change in trajectory and number of incident particles remains basically unchanged. The intensity of the photon beam decreases exponentially with the placement of additional layers of shielding material, it can be defined with Eq.2.10, where I and I_0 are the intensities of photon beam with and without shielding material present, t is the thickness of shielding material present and μ is the **linear attenuation coefficient** which is dependent on the material itself.

$$I(t) = I_0 e^{-\mu t} \tag{2.10}$$

The interaction of photons with matter involves some distinct processes. For instance, coherent elastic scattering, photo-excitation, the photoelectric effect, the Compton effect, pair production and so on. The relative importance of each process depends on the photon energy and the atomic number of the stopping material. Nevertheless, among these different processes, the three most important mechanisms are shown in the Fig.2.4.

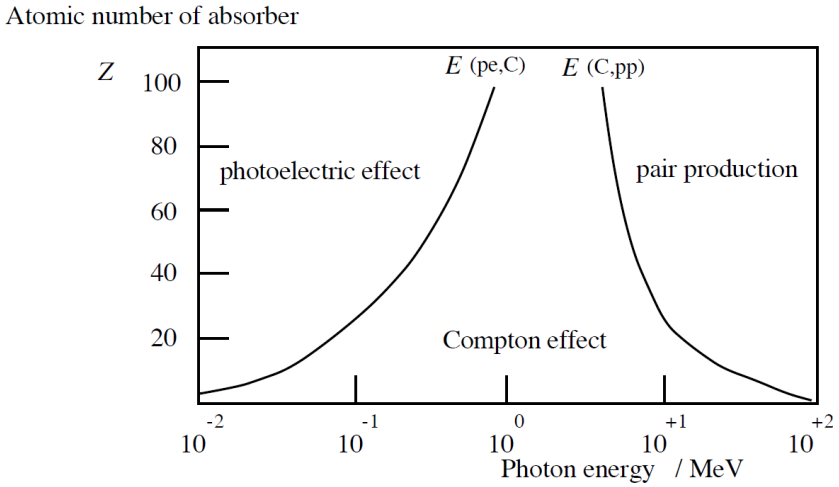

Figure 2.4: Effect of photon energy and atomic mass number of absorbing medium on dominant type of photon attenuation processes. [10].

Photoelectric effect: Photoelectric effects dominate at low energies, <100keV. When the energy of the incident photon is above the work function or binding energy of an electron in the host atom, it can eject an atomic electron and meanwhile the photon has been completely absorbed by the atom and disappears. The energy form the injected photon is carried off by the ejected electron, it can be raised to a higher lever within the atom or can become a free photoelectron, described in Eq.2.11. Afterwards, this photoelectron will ionise and excite other atoms until it loses all its energy. The upside of this may explain the reason why photon radiation is classified as an indirect ionising radiation. The

majority of the ionisation and excitation occurs during photon radiation and is not via the photon itself, but due to the photoelectron which are produced at the first ionisation caused by photon.

$$E_\gamma \rightsquigarrow e^- \tag{2.11}$$

Compton scattering: Compton scattering dominates at medium energies, ~ 1 MeV. It is an elastic collision between a photon and an electron. When the energy of a photon is well above electron binding energies, more likely, the photon will scatter off an electron and produce a photon degraded in energy and a recoil electron. The photon retains a portion of its original energy and continues moving in a new direction. Meanwhile, the electron ejected by the atom travels with the energy transferred to it from the photon minus the binding energy of its orbital shell. This process is illustrated in Eq.2.12, it contains both absorption and scattering components. However, if the atom takes up all the energy and the momentum transferred to the electron, this interaction will be called coherent Compton scattering or *Rayleigh scattering*. If the electron is ejected by the atom, the interaction is incoherent Compton scattering [3]. Generally, the probability of Compton scattering decreases with increasing photon energy and increasing atomic number (Z) of the medium. Moreover, concerning water radiolysis, which is a low atomic-number medium, Compton scattering is the predominant mode of photon interaction.

$$E_\gamma \rightsquigarrow E_\gamma^{'} + e^- \tag{2.12}$$

Pair production: Pair production dominates at high energies, > 1.024 MeV. When a photon has a mass at least 2 times larger than the mass of an electron[5] which means 1.024 MeV, it may create an electron and positron pair under the influence of the electromagnetic field of a nucleus. Eq.2.13 shows this process. Nevertheless, pair production only occurs under a strong electric field of nucleus, which means a much higher energy, like 5 or 10 MeV. Therefore, all the energy and momentum is taken up and conserved by the nucleus. In addition, the probability of pair production increases with atomic number (Z) of the medium and the photon energy. With *Bremsstrahlung* radiation, the electron and the positron produced will be projected in a forward direction relative to the incident photon. Afterwards, this electron-positron pair creates a large number of secondary γ-rays which will create continuously electron-positron pairs. This is called **electromagnetic showers**. The average energy of the photon has been decreased during each step of this process until it is totally absorbed or stopped.

$$E_\gamma \rightsquigarrow e^+ + e^- \tag{2.13}$$

For most cases of photon radiation, reactions can be shifted from high energies to low energies, thus it might involve some, maybe all of these processes. And unlike the other radiation types, the ranges of photon irradiations are normally indeterminate.

[5]The mass of an electron: 9.108^{-31}kg, also equals to 0.511 MeV in energy units.

2.1.B.2 Interaction with energetic of electrons

Electrons lose energy by exciting and ionising atoms along their trajectories. The interactions of electron radiation normally can be identified by two classes, elastic and inelastic scattering. The relative importance of these processes varies strongly with the energy of the incident electrons and sometimes also with the nature of the absorbing material.

If the electron passes through the medium without any scattering, they are a direct beam with no energy loss. During the elastic scattering, the electron is deflected form its path towards the core by Coulomb interaction with the positive potential inside the electron cloud which loses very little energy. Furthermore, if the electron is too close to the nucleus, it might be scattered back, which is called *backscattering*. Nevertheless, this is a rare case. There is also inelastic scattering where energy is transferred during the collision. It might generate several processes: inner-shell ionisation, *Bremβtrahlung* radiation, secondary electrons, etc [11]. At low energies, energy loss is mainly through elastic collision; at high energies, energy is lost predominantly by radiation emission. For electrons, it is negligible below 100 keV but increases rapidly with increasing energy, becoming the predominant mode of energy loss at an electron energy between 10 and 100 MeV. For example, *Bremsstrahlung* becomes a significant fraction of energy loss at high energy.

Electrons are more penetrable than proton and heavy charged particle radiation. However, due to the fact that the masses for both projectile and target are identical, they can scatter in any direction and lose large fractions of energy. Moreover, multiple scattering occurs subsequently thus the path of an electron is normally very erratic.

It is worth mentioning that when the energy is above a threshold, **Cherenkov** radiation is also possible for electron interactions. The *Cherenkov* effect is a light emission effect that occurs whenever a charged particle travels in a medium faster than the speed of light in that medium. For one thing, this effect will not cost a lot of energy loss compared with ionisation. However it only depends on the velocity of the particle. If the energy exceeds 264keV, electrons can show *Cherenkov* radiation in water.

2.1.B.3 Interaction with charged-particle

Charged particles, normally refer the particles like protons, α particle ($^4He^{2+}$), β particles. They interact with matter in the same way as electrons, but much strongly. It means a higher probability of interaction with the medium, producing large numbers of ions per unit length of their paths. Thus, they have a larger linear rate of energy loss and are less penetrating. For example, the ion density along the track of an α particle is several hundred times greater than that along the track of an electron of the same energy. On the other hand, the range through matter, which means a characteristic average traveling distance, normally depends on its initial kinetic energy. Furthermore, for both α particles and protons, the trajectories are approximately straight.

Among all the different particles, the way of interaction is more or less the same. However, α particles are often regarded as the most damaging radiation of internal deposition due to the fact that large amounts of energy are deposited within a very small distance of medium. Thus, only α particle will be explained in the following paragraph.

α particles can interact either with nuclei or orbital electrons in any absorbing medium. In fact,

the scattering with nuclei may be deflect with no or very small exchange in energy or absorbing by nucleus, so-called **Rutherford scattering**[6]. However, it is negligible for α particles. On the contrary, ionisation, atomic or collective excitation are the process more important during the absorption of α particles. When an α particle comes close enough to an orbital electron of the medium, it can pull it out from orbit. This is the ionisation which costs the kinetic energy of the α particle. Thus, the α particle is slowed down. At the same time, when the α particle is not sufficient to trigger an ionisation with interaction, it can also lose its kinetic energy by exciting orbital electrons. The α particles have tendency to cause ionizations at an increasing rate when it is slowed, thus most energy is deposited at the end of its track, in the **Bragg** peak. In the end, the α particle collects two electrons and becomes a helium atom when it stops.

2.1.B.4 Interaction with energetic neutrons

Neutron radiation is most commonly found in nuclear reactors which create significant neutron fluxes. Materials surrounding will be activated by capturing neutrons, it is normally an undesirable outcome. Concerning their interactions with matter, due to the fact that they have no charge, the ionisation via electromagnetic interaction with atomic electrons is negligible. Hence, it leaves only nuclear collision as an important source of dissipating energy. Neutrons have comparable masses to protons so that *billiard-ball* type collisions are possible during the interaction. This will give a large amount of scattering angles, thus the range is difficult to estimate. Nevertheless, neutrons can penetrate much greater thickness of material, and the consequences of neutron irradiation are not confined to the surface region of the absorber.

Like photon radiation, the intensity of the neutron beam decreases exponentially with the thickness of the material, it can be defined as Eq.2.14, where I and I_0 are intensities of neutron beam before and after passing through matter of thickness, t is the thickness and N is the atom density of the material, σ is nuclear cross-section which describes the attenuation of neutrons. It is pointed out that more interactions with neutrons will be possible if the material has a higher cross-section.

$$I(t) = I_0 e^{-N\sigma t} \tag{2.14}$$

Neutrons are generally categorised by their energy: high-energy neutrons, energy $>$ 1 GeV; fast neutrons, energy between 100 keV and 10 MeV; slow neutrons, energy $<$ 0.5 eV. The neutrons produced in a nuclear reactor are generally fast neutrons. The process of elimination of neutrons was introduced briefly in the previous chapter (Chapter Light Water Reactor). Nevertheless, it will be detailed as below.

At first, the neutrons undergo **thermalisation** via elastic and inelastic scattering form the absorber nuclei. The maximum energy loss for the neutrons is when it scatters a proton which share the same mass. Hence the energy loss is mainly due to the elastic scattering and until their energy is equal to the thermal energy of the surrounding environment. On the other hand, during the inelastic scattering the nucleus is left in an excited state which later decays by γ emission or some other type of radiation.

[6]**Rutherford scattering:** Rutherford scattering is based on the elastic deflection of charged particles in Coulomb field of an atomic nucleus.

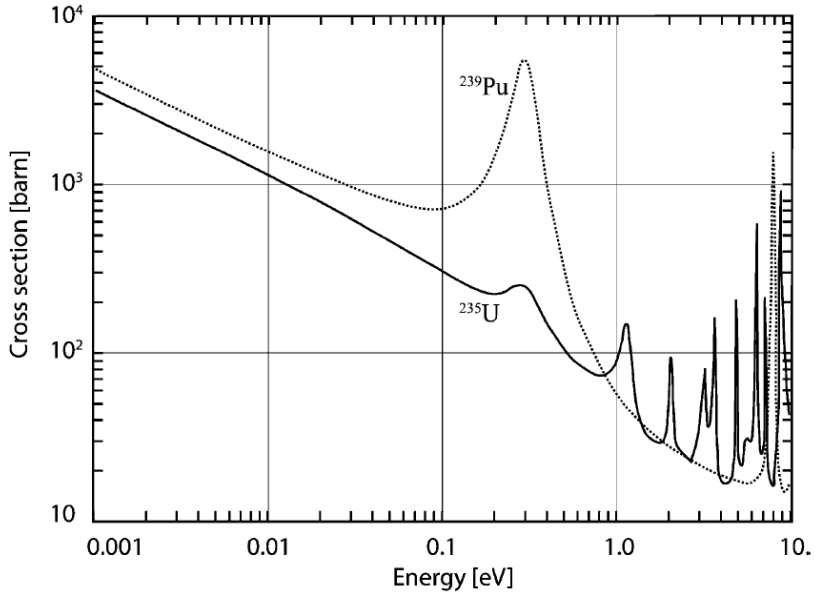

Figure 2.5: Fission cross section of ^{235}U and ^{239}Pu as a function of energy. [12]

Afterwards, the thermalised neutrons will be captured and absorbed by the nuclei and then eventually disappear. The cross section dependence of the neutron capture cross section in uranium and plutonium has been illustrated in Fig.2.5. It shows that at the lowest energies the cross sections increase monotonically with decreasing energy and become very large at thermal energies. Besides, sharp structure is observed at higher energies, which means the cross section shows a peak at a particular energy because of the capture of neutrons into specific nuclear energy levels populated in the reactions. There are several disintegration reactions types for neutron capturing [3], for example:

- **(n,** γ**)** with the emission of a photon;
- **(n,** α**)** with an α particle;
- **(n,** p**)** with a proton.

As mentioned before, thermalised neutrons are important for a nuclear reactor to stay at operational efficiency, and hence the absorption of thermalised neutrons need to be treated carefully. On one hand, they need to be eliminated for the safety concerns. On the other hand, they have to be preserved for efficient nuclear operation. The best choice for the materials are those who have high neutron capture cross sections, such as boron shown in Eq.1.1. The cross section of boron is quite high, σ=3838 barn. On the contrary, in order to avoid too much neutron loss, the neutron preservation is done by using materials with very small cross sections for neutron capture reactions, such as hydrogen atoms, shown in Eqs.2.15 and 2.16, or oxygen atoms, the σ=1.8×10^{-4} barn. These indicate that water contains hydrogen, light water is an effective materials for thermalising neutrons with minimum loss due to reactions. This might also explain the reason that light water is chosen as a moderator for LWRs.

$$1^n + 1^H \rightarrow 2^H \qquad \sigma = 0.322\ barn \tag{2.15}$$

$$1^n + 2^H \rightarrow 3^H \qquad \sigma = 5.7 \times 10^{-4}\ barn \tag{2.16}$$

2.1.C Stopping Power and Linear Energy Transfer (LET)

2.1.C.1 Definition

When a charged particle penetrates a medium, it transfers its energy to the medium and thus slows down, eventually it dissipates all its energy and stops. From the angle of the charged particle, we emphasis the average linear rate of energy loss in a medium during the interactions. This has been discussed in the previous section. Oppositely, if we focus on the medium, thus a concept of **Stopping Power** of the material should been introduced. It is often referred as the **Linear Energy Transfer (LET)**, which is a measure of the rate of energy deposition or transferring in the medium. It is defined as the linear-rate of energy loss by an ionising particle crossing a material medium, and a rough average value calculated by dividing the total energy(E) of a particle by its path length(x), shown in the Eq. 2.17.

$$LET = -\frac{dE}{dx} \tag{2.17}$$

The official unit is J.m^{-1}, but more often keV.μm^{-1} is used. In general, at the same velocity, the particle with larger charge loses more energy per length unit, therefore, it will have a higher LET.

While this formula serves to indicate the order of magnitude of the **LET**, it ignores several important factors that must be reconsidered to obtain a more precise value. Like the fact that the rate of energy loss of an electron changes as it slows down so that the LET will vary at different positions along the track and so on. Thus, for high-energy charged particles, the **LET** is often calculated by the **Bethe** formula, Eq.2.1, discussed previously. Some average **LET** values in water for various radiation are given in Table 2.2, they are calculated by the program TRIM [13, 14]. The *primary* interaction of radiation with matter depends on the nature of the radiation. **LET** is a parameter to describe the radiation, but not sufficient to compare the effects of different radiations in water radiolysis. Track structure of energy deposition is probably a better parameter to describe the initial effects of a radiation with matter.

Particles (energy)	LET (keV.μm^{-1})
^{60}Co γ rays (Compton electron, 1.17 MeV)	0.23
Electrons (2 MeV)	0.2
Protons (100 MeV)	0.65
α particles (5.3 MeV)	92
He^{2+} (1.5 MeV)	192
Li^{+} (0.85 MeV)	223.5
Carbon ions (25 MeV)	520

Table 2.2: Average values of LET for several different types of radiation in water [15–18]

2.1.C.2 Track structure

The energy lost when a moving charged particle is slowed down in matter gives rise to a trail of excited and ionized atoms and molecules in the path of the particle. The result of the absorption of any type of ionizing radiation by matter is thus the formation of tracks of excited and ionised species. Therefore, tracks are formed by a set of heterogeneous zones containing highly reactive species localised around the path of energy deposition. These species normally will be the same in a particular material regardless of the type or energy of the radiation responsible. However, radiation of different types and energy will lose energy in matter at different rates, and consequently will form tracks that may be densely or sparsely populated with the active species. Track structure varies greatly depending on the characteristics of radiation, it can mainly be distinguished by two types: the photons and the electrons, **low LET**, and heavy charged particle **high LET**.

- **Track structure produced by low LET**

When the LET value is low, the energy deposition is distant from each other in general. Depending on the amount of energy deposited by radiation, those heterogeneous zones can be divided into three groups:

Spur: low energy deposition: E $<$ 100 eV;

Blob: middle energy deposition: 100 eV $<$ E $<$ 500 eV;

Short tracks or branch tracks: high energy deposition: E $>$ 5 keV;

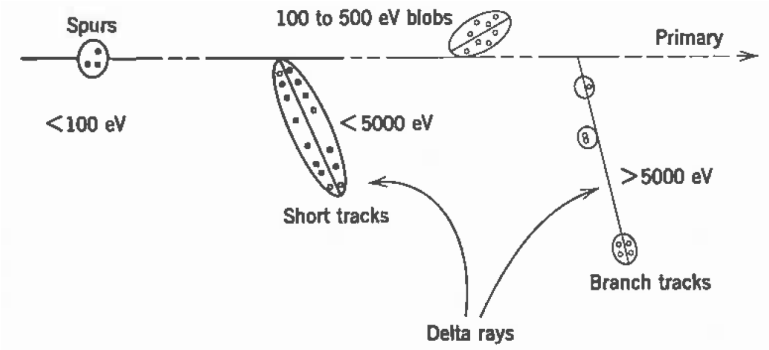

(a)

Figure 2.6: Distribution of ions and excited molecules in the track of a fast electron. [15]

Electrons ejected as a consequence of the ionisation produced by radiation may themselves be sufficiently energetic to produce further ionisation and excitation. If the energy of these secondary electrons is relatively low, less than 100eV, their range in liquid or solid materials will be short and any secondary ionizations that they produce will be situated close to the origin of the ionisation, giving a small cluster or **spur** of excited and ionised species. The average spur contains 2 to 3 ions pairs and excited species. Some of the secondary electrons will have sufficient energy to travel further from the site of the original ionisation and will form tracks of their own, branching from the primary track,

such electrons are known as δ ray. For δ electrons in a middle energy range which is between 100 - 500 eV, they will generate a large spur described as a *blob*. For higher energy δ electrons from 500 eV to 5 keV, they are defined as **short tracks** or **branch tracks**. Fig.2.6 shows the distribution of ions and excited molecules in the track of a fast electron. The quantity of energy deposited determines whether an individual event will give rise to a *spur* or a larger group of ions and excited molecules: *blobs*, *short tracks* or *branch tracks*. Open circles represent positive ions, each of which will be associated with an electron and one or more excited molecules. The fraction of the energy deposited by electrons with energies in the MeV range that appears in short tracks and in spurs of different sizes.

- **Track structure produced by high LET**

Densely ionising radiation, like α particles, have a high LET. The number of interactions per unit length traveled is large because the velocity of the incident particle is small. Moreover, the energy depositions occur in a track more or less straight due to the angular deviations in an interaction which are inversely proportional to the mass of the particle. The spurs overlap and form a single cylindrical track. The track can be divided into two: the **core** and the **penumbra**. More than 50% of the initial energy is deposited in the *core* which is a small area so that the density of the species created is high. The rest of the energy is deposited in the *penumbra* by the secondary electrons also called δ rays. The dimensions of the core and the penumbra vary depending on the velocity of the particle.

The concept of the **LET** is fundamental for understanding the interaction of radiation with matter. However, two particles with the same LET but different velocities do not produce tracks with the same dimensions, that influence the manner of species interacting with each other. Therefore, the effects of two radiation with the same LET may be different.

2.2 Pure Water Radiolysis

Water radiolysis [15–17, 19–25] is the decomposition of water molecules when they are irradiated by ionising radiation. Water molecules are decomposed to form radiolysis products: ions, excited molecules and free radicals[7] are the first reactive species formed. While both ions and excited molecules can give stable chemical products directly, the free radicals are unstable with high reactivity. Therefore, most of them only exist during the intermediated formation, and eventually disappear in the water.

In general, the reaction of water radiolysis can be written as Eq.2.18. Due to ionizing radiation, the radiolysis of water produces: hydrated electrons, $H^\bullet$ atoms, $HO^\bullet$ and $HO_2^\bullet$ radicals, H_3O^+ and OH^- ions, H_2 (dihydrogen) and H_2O_2 (hydrogen peroxide) molecules. The global equation of water radiolysis is now well understood experimentally as well as theoretically [15–17, 19–22].

$$H_2O \xrightarrow{Ionizing\ Radiation} e_{aq}^-, H^\bullet, HO^\bullet, HO_2^\bullet, H_3O^+, OH^-, H_2O_2, H_2 \tag{2.18}$$

[7] In chemistry, a **free radical** also called a *radical*, which is an atom, molecule or ion with at least one unpaired electron.

2.2.A Mechanism of Water Radiolysis

Ionising radiation produces ionisation and excitation by transferring energy to electrons present in water molecules. The energy is first absorbed, and then deposited into water molecules. During the initial interaction, inner-shell electrons may be excited and the absorbed energy is rapidly redistributed. Thus, chemically important ions and excited states are produced by loss or excitation of less-firmly bound electrons, such as the outer-shell electrons [15].

One of the recent models about the mechanism of water radiolysis was proposed by Sxiatla-Wojcik and Buxton [20], shown in Fig.2.7. It divides the water radiolysis mainly into three steps:

- the **physical stage**;
- the **physico-chemical stage**;
- the **chemical stage**.

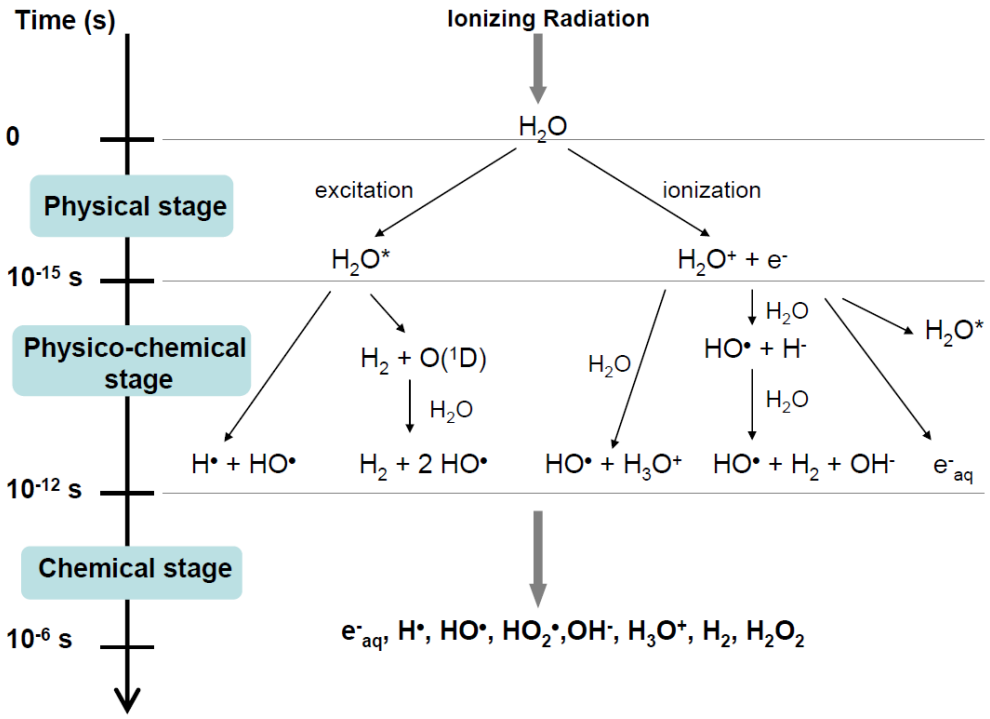

Figure 2.7: Schematic diagrams of water radiolysis [19].

As shown in the Fig.2.7, it illustrates the water decomposition as a function of time after the irradiation. Precisely, it shows the chemical reactions have been taken place during the first 1 μs after the radiation energy deposited into the water molecules.

2.2.A.1 The physical stage

The **physical stage** is the absorption of ionising radiation by water, which leads the ionisation and excitation of water molecules. Therefore, the incident particles and the electrons in water molecules are generated and both slowed down. It is the period that consists of energy deposition followed by

fast relaxation processes. The physical stage is the first step of water radiolysis, which only lasts about 10^{-15} s[8], 1 fs, after the initial interaction.

The water molecule H_2O can either be ionised, by removing an electron, Eq.2.19:

$$H_2O \xrightarrow{Radiation} e^- + H_2O^+ \tag{2.19}$$

$$H_2O + e^- \rightarrow 2e^- + H_2O^+ \tag{2.20}$$

or be excited, by transferring an electron from a fundamental state to an excited state, Eq.2.21:

$$H_2O \xrightarrow{Radiation} H_2O^* \tag{2.21}$$

$$H_2O + e^- \rightarrow H_2O^* + e^- \tag{2.22}$$

Nevertheless, Eqs.2.20 & 2.22 are considered as the continuous reactions of water molecule and the ejected electron by Eq.2.19. At the end of this stage, the reactions have formed: excited water molecules $\mathbf{H_2O^*}$, ionised water molecules $\mathbf{H_2O^+}$ and sub-excitations electrons $\mathbf{e^-}$.

2.2.A.2 The physico-chemical stage

The **physico-chemical stage** is the second step of water radiolysis, from 10^{-15} to 10^{-12} s, in which a thermal equilibrium is established. During this period, the ionised and excited water molecules undergo transformations and thus they dissipate energy by transferring it to their neighbouring molecules and breaking bonds. In the mean time, the sub-excitations electrons become thermalised and then subsequently hydrated. There are many different processes in this stage and not all of them have been well characterised experimentally. However, some important processes are well detailed which will be represented in the following sections.

- **Excited water molecules $\mathbf{H_2O^*}$:**

Dissociative relaxation The dissociation of the excited water molecule H_2O^* produces the radicals $HO^\bullet$ and $H^\bullet$ by bond breaking, Eq.2.23. Two models have been described in the literature. One leads to dihydrogen molecule H_2 and $O(^1D)$ which can react quickly with water molecule and give the $OH^\bullet$ radical. In the second model, the $H^\bullet$ radical and $O(^3P)$ can be formed by the reaction below, but due to the weak quantity in the liquid water, this reaction is often negligible [26], That is the reason for its absence in the scheme of main reactions (Fig. 2.7). It is worth mentioning that $O(^1D)$ and $O(^3P)$ are the singlet and triplet state of the atomic oxygen respectively. It needs to be pointed out that the excited water molecule can return to its fundamental state without any dissociation, but only by losing heat. In the case of liquid water, the role of excited molecules is normally less important compared to the ionised ones [27].

$$H_2O^* \rightarrow HO^\bullet + H^\bullet \tag{2.23}$$

[8]In some literature, they define the duration as 10^{-16} s, one tenth of a femtosecond.

$$H_2O^* \rightarrow H_2 + O(^1D) \xrightarrow{H_2O} H_2 + 2OH^\bullet \ (or H_2O_2) \tag{2.24}$$

$$H_2O^* \rightarrow 2H^\bullet + O(^3P) \tag{2.25}$$

- **Ionized water molecules H_2O^+:**

Ion-molecule reaction The ion-molecule reaction can also be thought as transferring a proton to a neighbouring molecule. The ion H_2O^+ is not stable and it reacts very quickly with water molecules, Eq.2.26. This reaction is important because it leads to the production of $HO^\bullet$ radical and proton H_3O^+, which may have other role in further reactions [28].

$$H_2O^+ + H_2O \rightarrow HO^\bullet + H_3O^+ \tag{2.26}$$

- **Sub-excitation electrons e^-:**

Thermalisation and solavatation of sub-excitation electrons Most ejected electrons have low energy. However, some of them may have considerable energy during ionisation, in keV or even in MeV range. They can lose their energy through collisions with other molecules before the electron neutralises a positive ion. In other words, the electrons is reduced to thermal or near thermal energy before recombination occurs, Eq.2.27. Then it can interact with the surrounding water molecules and eventually becomes an **hydrated electron**, $\mathbf{e}^-_{aq}$, Eq.2.28. The energy of thermalization is about 0.0025 eV at 25 °C.

$$e^- \rightarrow e^-_{th} \tag{2.27}$$

$$e^-_{th} + n\ H_20 \rightarrow e^-_{aq} \tag{2.28}$$

Germinate recombination The germinate recombination process is an ion recombination. The energy is lost during molecular collisions and the molecule rapidly drops to its lowest excited state, Eq.2.29. During the ionisation of the water molecules, the potential is about 8 eV. The incident particle or the electromagnetic radiation can have a sufficient energy to eject an electron which can recombine with a neighbouring water molecule, a positive water ion, in order to give an excited water molecule.

$$e^- \rightarrow e^-_{th} + H_2O^+ \rightarrow H_2O^* \tag{2.29}$$

Dissociative electron attachment (DEA) Before the thermalization, apart from the recombination process, the sub-excitation electrons can also react with a water molecule by giving the H_2, $HO^\bullet$ and OH^-, Eqs.2.30 & 2.31. This process is thus called *dissociative electron attachment*. It involves the resonant capture of e^- to a water molecule followed by the dissociation of the transient anion and by reaction of the hydride anion with another water molecule through a prompt proton transfer process [21]. The electron capture by this process may lead to a disproportionately high rate of decomposition [15].

$$e^- + H_2O \rightarrow HO^\bullet + H^- \tag{2.30}$$

$$H^- + H_2O \rightarrow H_2 + OH^- \tag{2.31}$$

After 1 ps of the energy deposition into water molecules, which is also the end of the physicochemical stage, the spatial distribution around the axis of the ionisation track includes e^-_{aq}, H_3O^+ and $HO^\bullet$ which are the species involving in the reactions for the next stage. The species H_2 and H_2O_2 are also created in this stage. All these species are referred as the **initial yields** of water radiolysis.

2.2.A.3 The chemical stage

The **chemical stage** is often considered as highly non-homogeneous, and hence in some literature, it is named as the non-homogeneous chemical stage. However, one thing can be sure that the chemical stage starts with a non-homogeneous state and ends homogeneously. It takes place between 10^{-12} and 10^{-6} s. The radical species react in the tracks and then diffuse in solution. They can thus react with each other and also with surrounding molecules in the solution, Eqs.2.32, 2.33 & 2.34.

$$HO^\bullet + HO^\bullet \rightarrow H_2O_2 \tag{2.32}$$

$$H^\bullet + H^\bullet \rightarrow H_2 \tag{2.33}$$

$$e^-_{aq} + e^-_{aq} \rightarrow H_2 + 2OH^- \tag{2.34}$$

In general, this stage can be divided into two: the heterogeneous and the homogeneous ones. At the heterogeneous chemical stage, normally extends from 10^{-11} to 10^{-8} s, the recombination reactions are favoured which lead to the formation of molecular products in a relative high concentration in small zones along the radiation track. Afterwards, the track of the particles expands because of the diffusion of radicals and their subsequent chemical reactions. Therefore, it brings the homogeneous state of the radicals and molecules to the solution at the end of the chemical stage.

1 μs after the particles pass through, the distribution of radiolyic species in water is considered homogeneous. The reactions occur after these three stage can generally be well described homogeneously while all the species have diffused evenly into the water. All the species have been produced after these three stages are call **primary products** of water radiolysis, already shown in the global

equation, Eq.2.18.

Several remarks need to be pointed out:

- The oxygen is not a primary product of water radiolysis, it is formed in the stage of homogeneous chemistry which means after 10^{-6} s of energy deposition in the water [29].
- The radical superoxide, $OH_2^\bullet$, is presented like a primary product in the global equation, but actually it is formed in the heterogeneous stage and the mechanism of its formation is not clear yet. The most cited hypothesis is that it is formed by the reaction between $HO^\bullet$ radical and an oxygen atom at triplet state.
- The formation of molecular hydrogen H_2 is involved in two stages after the initial energy disposition: it can be produced by the Eqs. 2.33 & 2.34, in the chemical stage. In the earlier physicochemical stage, the formation of H_2 can be presented by the dissociation of excited water molecules, Eq.2.24 and the dissociative electron attachment, Eqs.2.30 & 2.31. Indeed, the dominant way of H_2 formation is the dissociative recombination process of the water cation and the non-hydrated electron during the physicochemical stage [30], not in the last stage.
- The production of H_2 has two different types of tracks along the radiation path, either are spherical spurs formed at more than 100 nm separations with low LET radiation, or are cylindrical track of connecting spurs with high LET radiation [22].

2.2.B Radiolytic Yields

2.2.B.1 Definition

The radiolytic yield, noted as **g(X)**, is defined as the number of species created or destroyed for 100 eV deposited energy. SI unit for the radiolytic yield is $mol.J^{-1}$ which equals to 9.649×10^6 molecules/100 eV. It can measure the radicals and molecular products that escape from the **spurs** and **tracks**. Actually, there is a competition between the diffusion and the reaction of these species as the non-homogeneous concentration gradients relax. However, these yields are usually referred to as homogeneous or steady-state yields, and they are representative of the state of an electron track as found at about 10^{-7} s[9], after the passage of an ionising particle which has deposited energy in the system. It means that any reactions occurring within spurs and tracks have been completed [31].

The primary yields of both radical (e_{aq}^-, $H^\bullet$, $OH^\bullet$, $OH_2^\bullet$) and molecular (H_2, H_2O_2) products can be simply subdivided into two groups: the reducing radicals e^- and $H^\bullet$, and the oxidising products $OH^\bullet$, $HO_2^\bullet$ and H_2O_2. The molecular hydrogen is relatively inert and normally plays little part in the subsequent reactions [15].

To maintain a material balance, the relationship between the radical and molecular yields are written as the equations (Eqs.2.35, 2.36 and 2.37) below, in which g(-H_2O) is defined as the corresponding yield of decomposition of water at this stage.

Oxygen part:

$$g(-H_2O) = g(e_{aq}^-) + g(OH) + 2g(H_2O_2) + 2g(HO_2) + g(OH^-) \tag{2.35}$$

[9] In the literature, the duration is defined as 10^{-6} s [15, 19].

Hydrogen part:

$$g(-H_2O) = g(H_2) + g(e^-_{aq}) + g(H_2O_2) + \frac{1}{2}[g(H) + g(OH) + g(H^+) + g(OH^-) + g(HO_2)] \quad (2.36)$$

Charges conservation:

$$g(H^+) = g(e^-_{aq}) + g(OH^-) \quad (2.37)$$

With the three precise equations, we can establish the relation of all the primary products:

$$g(-H_2O) = g(OH) + 2g(H_2O_2) + 3g(HO_2) = g(H) + g(e^-_{aq}) + 2g(H_2) \quad (2.38)$$

The equation expressed in Eq.2.38 is often used in the determination of radiolytic yields. The first thing to point out is that all the radiolytic yields evolute with time, illustrated in Fig.2.8. It indicates that the radicals yields decrease while the molecular yields increase as a function of time. In other words, it means that the radicals recombine and form molecular products with time. Therefore, the radicals are difficult to detect after a short time of the radiation.

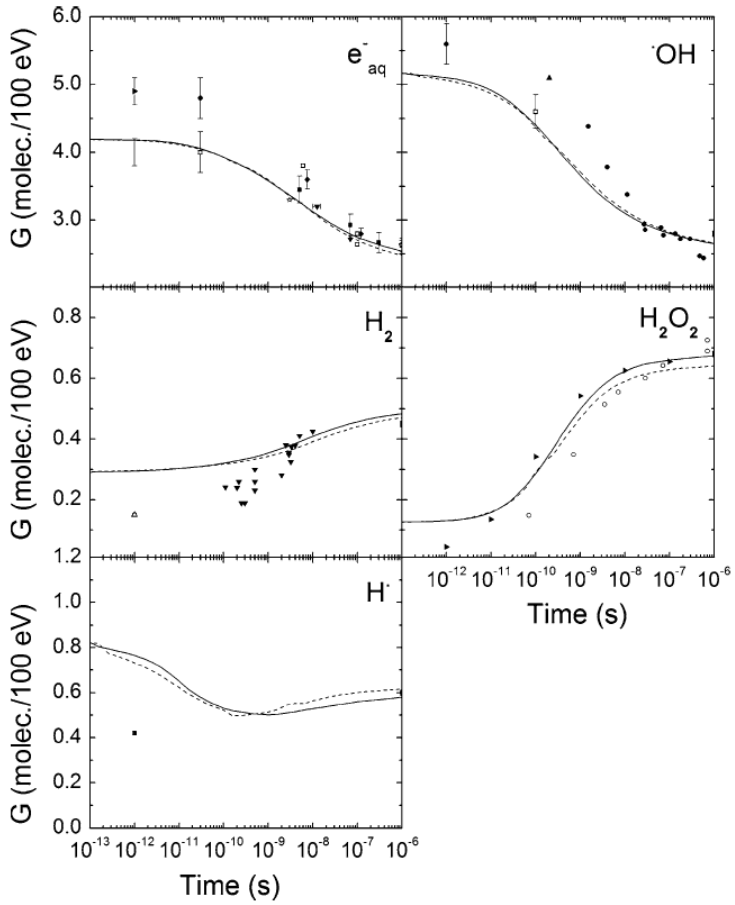

Figure 2.8: Time-dependent of primary yields; $H^\bullet$, $HO^\bullet$, H_2, H_2O_2 and e^-_{aq} produced by low LET radiation tracks of proton (300 MeV, LET $\sim$ 0.3 keV/μm) at neutral pH and 25°C. Broken line: IONLYS-IRT calculation; solid line: SBS calculation; spline: Monte-Carlo simulation results [32].

In general, the radiation types do not have a huge influence on the radiolytic yields, especially

for low LET radiations. Nevertheless, for LET $>$ 10 keV/μm, g($H^\bullet$) increases as the incident ion velocity increases [33]. The radiolytic yields still depend on a lot of parameters: the characteristics of irradiation, such as LET and dose rate; the characteristics of water itself, like temperature, pressure and pH.

2.2.B.2 Influence of LET

The Linear Energy Transfer **LET** of incident radiation can significantly change the values of primary radiolytic yields. The radiation tracks can be very differently due to the LET, low LET gives isolated spurs and high LET gives cylindrical tracks. Therefore, different tracks cause different diffusion models for the primary yields [34–36]. The radicals $H^\bullet$ and $HO^\bullet$ in cylindrical tracks are easier to combine with each other because they are closer in distance and more concentrated than in spurs, then result in form more molecular products. On the contrary, spurs are favoured to form more radical products. In short, with the increase of LET, the yields of radical products (e^-_{aq}, $H^\bullet$, $HO^\bullet$) decrease while the molecular yields (H_2O_2 and H_2) increase, as shown in Fig.2.9. However, for $H^\bullet$ yields, it reaches a maximum value around 6-10 keV/μm and then decreases with LET [32, 33, 37] at neutral pH and 25°C. The yields of O_2, not shown in the figure, actually, increase significantly with LET at the similar conditions, [38].

Source	LET (keV/μm)	g(-H_2O)	g(e^-_{aq})	g(OH)	g(H)	g(H_2)	g(H_2O_2)	g(HO_2)
^{60}Co γ-ray [39]	0.23	4.08	2.63	2.72	0.55	0.45	0.68	0.008
H^+ [39]	12.3	3.46	1.48	1.78	0.62	0.68	0.84	-
Fast neutron [40]	40	3.19	0.93	1.09	0.50	0.88	0.99	0.04
He^{2+} [39]	108	2.84	0.54	0.54	0.27	1.11	1.08	0.07
^{10}B(N, α)^{7}Li [41–43]	220	3.9	0.33	0.30	0.10	1.8	1.67	0.13

Table 2.3: Primary yields (molecules/100 eV) of water radiolysis for different types of radiations at room temperature: evolution of primary yields versus LET.

Tab.2.3 shows the values of primary yields of different LET radiations. It is worth noting that at low LET, the value of $HO_2^\bullet$ is actually too little to be taken into account, thus it can be neglected for the determination of the radiolytic yields. Overall, the G-values for neutral water at room temperature under low LET radiation conditions have been well established [15, 39]. They are the basis for further studies.

2.2.B.3 Influence of dose rate

Dose rate is defined as the dose received per unit time, it is often expressed in Gy/s. It can be thought as the intensity of radiation. The influence of dose rate is similar to the LET effect. High dose rate results in high concentration of radicals produced by the irradiation, and thus the radical-radical reactions are favoured [44]. In short, with the increase of dose rate, the radicals yields decreases while the molecular yields increase [17]. In consequence, the water decomposition is promoted, as illustrated in Fig.2.10 [45].

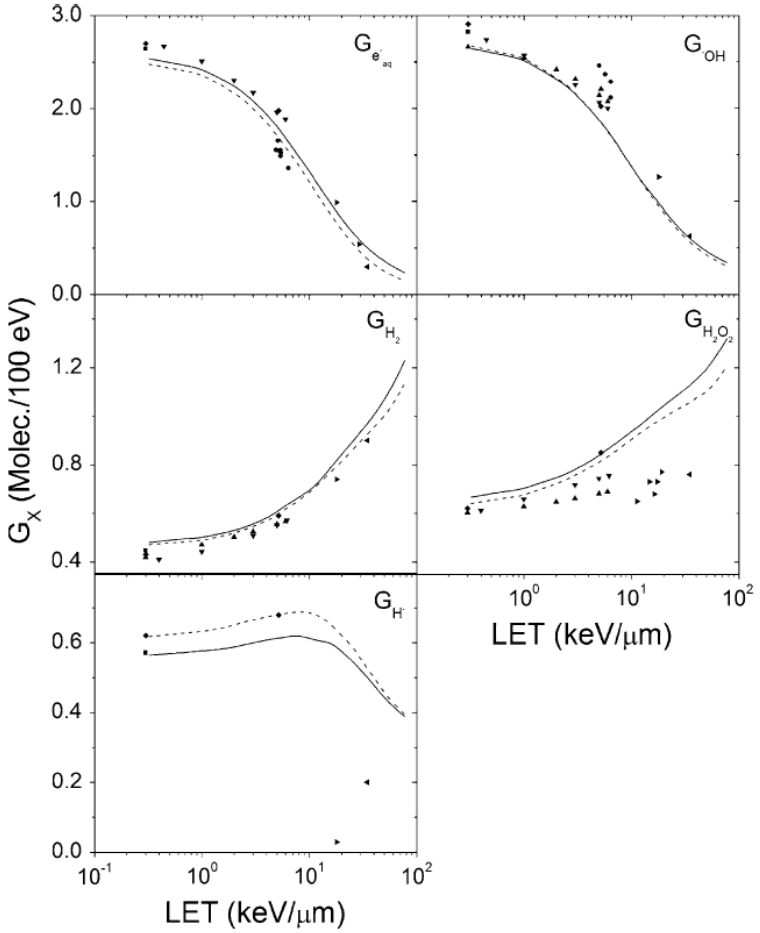

Figure 2.9: Primary yields of $H^\bullet$, $HO^\bullet$, H_2, H_2O_2 and e^-_{aq} in neutral liquid water irradiated by proton (300-0.1 MeV, LET $\sim$ 0.3-85 keV/μm) at 25°C. Broken line: IONLYS-IRT calculation; solid line: SBS calculation; spline: Monte-Carlo simulation results [32].

2.2.B.4 Influence of pH

The pH influence has been studied for a long time, as Draganić and Draganić conclude, which I quote: "*There is no strong dependence of the primary yields on pH, although the situation at extreme pH's is not yet quite clear.*" [47]. Therefore, we consider that the radiolytic yields are not affected by the pH between 4 and 9 [16, 17, 48, 49]. Furthermore, even for the time less than 10^{-6} s after energy deposition, pH can also be regarded as no large influence on the radiolytic yields ranging form 1 to 13 [50].

More precisely, Fig.2.11 illustrates the radiolytic yields as a function of pH up to 7. To get a better understanding, the polynomials indicated in Tab.2.4 shows the constant reaction rate of some important reaction concerning about pH. At pH equals to 4, the rate constant of Eq.2.39 is 2.1×10^{10} $M^{-1}s^{-1}$ and $[H^+]=10^{-4}$, which implies the time scales of this reaction is about 5×10^{-7} s. It is quite close to 10^{-6} s, which is the end of spur expansion. Therefore, for a higher pH which means a lower $[H^+]$, the primary yields are not affected. Oppositely, for a higher $[H^+] \geqslant 10^{-4}$ M, it brings more $H^\bullet$ due to Eq.2.39. In the competition between e^-_{aq} and $H^\bullet$, they both react with $HO^\bullet$, Eqs.2.40 & 2.41, and the reaction Eq.2.40 is more efficient than Eq.2.41. This can explain that at pH $\leqslant$ 4, the value of

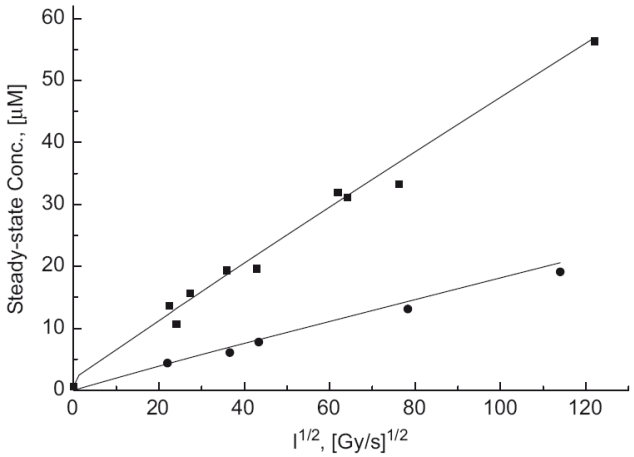

Figure 2.10: Steady-state concentration of oxide species as function of the square root of dose rate. ■: $[H_2O_2]+2[O_2]$; •: $[H_2O_2]$. [45, 46].

yields e^-_{aq} and $H^\bullet$ increase while g($HO^\bullet$) decrease as the pH decreases. Another reason for the decrease of $HO^\bullet$ is due to Eq.2.42, they recombine with each other and to form H_2O_2. It brings the increase of the yields H_2O_2 with the decrease of pH. The gradually decrease of H_2 yields with pH form 4 to 0 is due to the reaction rate of Eq.2.44 is much smaller than Eq.2.43 [32, 51].

Reaction (Eq n°)		Constant reaction rate k L.mol^{-1}.s^{-1}	Estimated at 25°C L.mol^{-1}.s^{-1}
$e^-_{aq} + H^+ \rightleftharpoons H^\bullet$	(2.39)	$10^{(39.127-3.888\times10^4/T+2.054\times10^7/T^2-4.899\times10^9/T^3+4.376\times10^{11}/T^4)}$	2.1×10^{10}
$HO^\bullet + e^-_{aq} \rightarrow OH^-$	(2.40)	$10^{(13.123-1.023\times10^3/T+7.634\times10^4/T^2)}$	3.5×10^{10}
$HO^\bullet + H^\bullet \rightarrow H_2O$	(2.41)	$4.26 \times 10^{11}e^{-1091/T}$	1.1×10^{10}
$OH^\bullet + OH^\bullet \rightarrow H_2O_2$	(2.42)	$10^{(8.054+2.193\times10^3/T-7.395\times10^5/T^2+6.870\times10^7/T^3)}$	4.8×10^9
$e^-_{aq}+H^\bullet(+H_2O) \rightarrow H_2+OH^-$	(2.43)	$1.14 \times 10^{13}e^{-1795.7/T}$	2.76×10^{10}
$H^\bullet + H^\bullet \rightarrow H_2$	(2.44)	$2.70 \times 10^{12}e^{-1867.5/T}$	5.1×10^9

Table 2.4: Table of reaction rate constant over the temperature range $20 - 350$°C, and the g-Value estimated at 25°C, based on information available in 2008. [52].

On the other hand, when pH is higher than 9, the primary yields are also affected. However, for alkaline solutions, the evolution of the primary yields is still not very clear yet. However, under basic condition, they are most influenced by the radical $O^{\bullet-}$. The most cited explanation is that the yields of H_2O_2 and e^-_{aq} + $H^\bullet$ decrease while g($HO^\bullet$) increase as the pH increase from 12 to 14 [48, 53, 54]. However, there is an inverse explanation of the primary yields due to the selection of the constant reaction rate of the radical $O^{\bullet-}$. The table below, Tab.2.5, shows the primary yields of water radiolysis at different pH value at room temperature in general.

2.2.B.5 Influence of temperature

The temperature of the water is one of the most important parameters on primary radiolytic yields. Many parameters are affected by temperature, for example, reaction constant rate, diffusion coefficient,

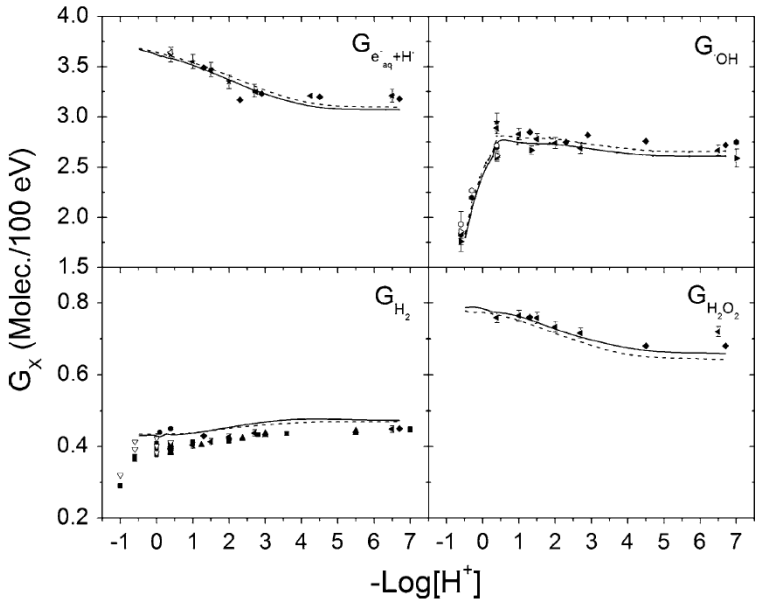

Figure 2.11: Primary yields of $HO^{\bullet}$, H_2O_2, H_2 and reducing species (e^-_{aq}+$H^{\bullet}$) versus -Log[H^+] for the radiolysis of air-free aqueous slufuric solution at 25°C with 300 MeV protons. Broken line: IONLYS-IRT calculation; solid line: SBS calculation; spline: Monte-Carlo simulation results [32].

pH	g(H^+)	g(OH^-)	g(e^-_{aq})	g($H^{\bullet}$)	g(H_2)	g($HO^{\bullet}$)	g(H_2O_2)
0-2	3.45	0.4	3.05	0.6	0.45	2.95	0.8
4-9	3.4	0.7	2.7	0.6	0.45	2.8	0.7
12-13	3.6	0.55	3.05	0.55	0.4	2.9	0.75

Table 2.5: Primary yields (molecules/100 eV) of water radiolysis for at different pH value at room temperature [46].

and Onsager radius[10] [55]. The primary yields are significantly influenced by these parameters. Many studies have been done [20, 33, 56–59], including the most cited literature by Elliot *et al.* [52, 60]. Many experiments have been performed to measure the primary radiolytic yields at various temperatures, and they also collected data from all over the world. Therefore, their values are normally regarded as the most complete [52]. The reaction constant rate has been calculated as a function of temperature (Tab.2.4). Figs.2.12 (a) & (b) illustrate a simulation of g-values for the primary species formed by water radiolysis as a function of temperature: (a) uses the data for γ or electron radiation, both can be regarded as low LET radiation, and (b) shows the data collected from fast neutron radiation which implies for high LET radiation.

For low LET radiation, most primary yields increase with the increase of temperature in different ways, except for H_2O_2 which actually decreases. The diffusion coefficients and the constant reaction rates both strongly depend on the temperature, and thus the diffusion rate and reaction rate increase sharply with temperature. At high temperatures, the diffusion rates for all the radicals are higher than the recombination rates, and results in the augmentation of the radical yields. Normally, the increase of radicals yields leads to the decrease of the molecular yields, H_2 and H_2O_2. However, in the

[10]**Onsager Radius:** the distance at which the energy of the Coulomb interaction in dielectric continuum becomes equal to thermal energy k_BT.

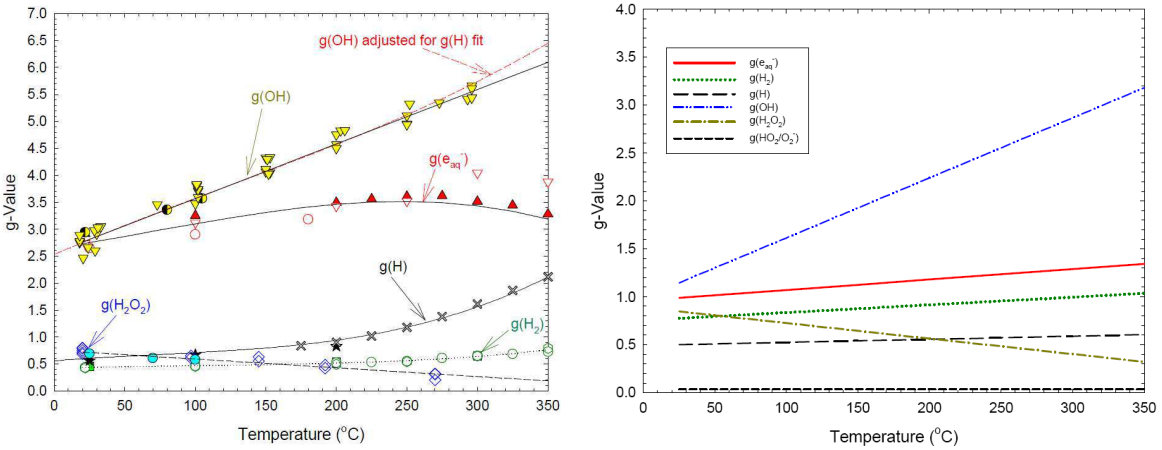

(a) (b)

Figure 2.12: The g-values for the primary species formed in reaction 2.18 as a function of temperature: (a) low LET radiation; (b) high LET radiation (fast neutron radiation for natural uranium fuel). [52].

.

case of H_2, it also increases with temperature. One explanation is considered as the formation of H_2 during the physicochemical stage, Eqs.2.24 & 2.31. There exists other explanations and arguments which are ongoing. The diminution of H_2O_2 yields is the consequence that the radicals are escaped from recombination.

For high LET radiation, as a function of temperature, the yields of $g(e^-_{aq})$, $g(HO^\bullet)$ and $g(H_2)$ increase, $g(H^\bullet)$ and $g(HO^\bullet_2/O_2)$ stay nearly constant, while $g(H_2O_2)$ decreases. Tab.2.6 lists polynomial function of LET for every primary yield in order to give a relationship between temperature dependence and LET. It clearly shows that with the increase of LET, the temperature dependences of $g(e^-_{aq})$, $g(H^\bullet)$ and $g(HO^\bullet)$ decrease while the one of $g(H_2)$ increases. Therefore, it results in slight difference of temperature dependence between low and high LET. In the same time, $g(H_2O_2)$ is actually not sensitive with LET, it actually decreases in almost the same tendency with the temperature in both high and low LET [52, 61].

In general, by comparing the two figures, it seems that the g-values of primary yields vary more significantly in low LET. The temperature dependences of these g-values decrease with increasing LET [62]. It might also link to the different tracks produced by low and high LETs. The isolated spurs of low LET are favoured for diffusion while the cylindrical tracks of high LET promote recombination.

Parameter	Function
$d(g(e^-_{aq}))/d(\text{temperature})$	$1.92 \times 10^3 - 2.56 \times 10^{-5}$LET
$d(g(H_2))/d(\text{temperature})$	$7.59 \times 10^{-4} + 1.32 \times 10^{-6}$LET
$d(g(H^\bullet))/d(\text{temperature})$	$6.70 \times 10^{-4} - 1.08 \times 10^{-5}$LET
$d(g(HO^\bullet))/d(\text{temperature})$	$7.34 \times 10^{-3} + 3.37 \times 10^{-5}$LET
$d(g(H_2O_2))/d(\text{temperature})$	-1.62×10^{-3}
$d(g(HO_2/O_2))/d(\text{temperature})$	No temperature dependence

Table 2.6: The temperature dependency of each primary yields as a function of track-averaged LET [52].

Last but not least, the influence of temperature may be more pronounced on the physicochemical stage rather than on the later radical diffusion stage [63].

2.2.B.6 Influence of pressure

In the $1960's$, a lot of research about pressure influence was done. Hentz *et al.* [64–69] figured out that the primary yields in water radiolysis are independent of pressure until 6.34 kbar. It is worth mentioning that pressure may play an important role in other solutions or in another phase (gas phase [70, 71]).

The primary yields vary with many parameters, among them the most important is the LET linked to the irradiation. Afterwards, they are influenced by the temperature, which is linked to the nature of water itself. Under some extreme conditions, like very high pressure, very acid or basic pH, may also influence the primary yields.

Summary Irradiation of pure water leads to buildup of a steady-state concentration of hydrogen peroxide in solution, and the continual formation of hydrogen and oxygen. In a simply way, we may just consider that the radiation decomposes the water into hydrogen and oxygen.

Water radiolysis occurs in many situations, especially in nuclear reactors. It is also a key factor to nuclear corrosion phenomena. However, only pure water radiolysis is not enough to understand the radiolysis which occurs inside of nuclear reactors. The water used in nuclear reactors, either light water or heavy water, they both have a specific chemical conditioning. Therefore, the radiolysis process is more complex than in pure water. The following section will show the PWR water radiolysis, which is the main interest this thesis study.

2.3 PWR Water Radiolysis

The light water used in PWR is deaerated pure water with addition of dissolved hydrogen, boric acid and lithium hydroxide. The process of radiolysis is modified by these components. Meanwhile, the radiolytic yields are also affected.

2.3.A Radiolysis in the Presence of H_2, H_2O_2 and O_2

2.3.A.1 Reducing - a chain reaction: H_2

The study of the influence of the three stable products H_2, H_2O_2 and O_2 of radiolyisis reactions on the water decomposition can be traced back to the $1950's$. Allen *et al.* [72] and Hochanadel [73] have established a basic mechanism for the forward and backward reactions between H_2 and H_2O_2, moreover the production of O_2. Both O_2 and H_2O_2 accelerate the water decomposition while H_2 is always regarded as an inhibitor of radiolysis. That is the reason why H_2 is added into the PWR water. Its role is to decompose the H_2O_2 and thus to suppress the production of O_2. There is a chain reaction involved in radiolysis process: dissolved hydrogen captures an oxidising species $HO^\bullet$ and transfers into a reducing species $H^\bullet$, then the $H^\bullet$ reacts with rapidly with H_2O_2 and re-form $HO^\bullet$, listed in Tab.2.7, Eqs.2.48 & 2.49. Finally a global reaction is given in Eq.2.57, [16, 74].

Reactions (Eq. n°)		k [46] L.mol^{-1}.s^{-1}	k estimated at 25°C [52] L.mol^{-1}.s^{-1}	E_a [46] kJ.mol^{-1}	E_a [52] kJ.mol^{-1}
$HO^\bullet + H^\bullet \rightarrow H_2O$	(2.45)	7.0×10^9 [75]	1.1×10^{10}		9.1
$HO^\bullet + HO^\bullet \rightarrow H_2O_2$	(2.46)	5.3×10^9	4.8×10^9	8.0	
$H^\bullet + H^\bullet \rightarrow H_2$	(2.47)	7.9×10^9	5.1×10^9	12.6	15.5
$HO^\bullet + H_2 \rightarrow H_2O + H^\bullet$	(2.48)	3.74×10^7		18.0	
$H^\bullet + H_2O_2 \rightarrow HO^\bullet + H_2O$	(2.49)	3.44×10^7 [75]	3.6×10^7	13.6	21.2
$HO^\bullet + H_2O_2 \rightarrow HO_2^\bullet + H_2O$	(2.50)	3.8×10^7	2.9×10^7	14.0	13.8
$HO_2^\bullet \rightleftharpoons H^+ + O_2^-$	(2.51)	7×10^5	pK=4.8	12.6	
$HO_2^\bullet + HO_2^\bullet \rightarrow H_2O_2 + O_2$	(2.52)	8.1×10^5	8.4×10^5	24.7	6.6
$HO_2^\bullet + O_2^- \rightarrow HO_2^- + O_2$	(2.53)	9.5×10^7	$\sim$ 1×10^8	8.8	8.1
$O_2 + H^\bullet \rightarrow HO_2^\bullet$	(2.54)	2.0×10^{10}	1.13×10^{10}	12.6	15.2
$O_2 + e_{aq}^- \rightarrow O_2^-$	(2.55)	1.94×10^{10}	2.3×10^{10}	13.0	11.6
$H_2O_2 + e_{aq}^- \rightarrow HO^\bullet + HO^-$	(2.56)	1.14×10^{10}	1.4×10^{10}	15.1	15.7

Table 2.7: Table of reactions, constant reaction rates k (L.mol^{-1}.s^{-1}) and activation energies E_a (kJ.mol^{-1}) [46, 52, 75].

$$H_2 + H_2O_2 \rightarrow 2H_2O \tag{2.57}$$

The chain reaction can retain effective as long as enough HO$^\bullet$ and H$^\bullet$ presented. In other words, all the species reacting/recombining with H$^\bullet$ and HO$^\bullet$ make the process less efficient, for instance reaction Eq.2.54 in Tab.2.7. Furthermore, it also reveals that the process can be stabilised due to the effective recombination, such as Eqs.2.45, 2.46 and 2.47, listed in the same table.

2.3.A.2 Oxidising - inhibitors of chain reaction: H_2O_2 and O_2

The hydrogen peroxide H_2O_2 on one hand can react with H$^\bullet$ in the chain reaction, Eq.2.49, on the other hand it can also react with the radical HO$^\bullet$ to inhibit the chain reaction and produce the radical $HO_2^\bullet$, Eq.2.50 in Tab.2.7. The recombination of $HO_2^\bullet$ can either form H_2O_2 and O_2, or oxidise the O_2^- to O_2. (Eqs.2.51, 2.52 and 2.53 Tab.2.7. Then, the global reaction of H_2O_2 and HO$^\bullet$ can be written as Eq.2.58. That is the reason H_2O_2 are often regarded as the precursor of O_2.

$$2HO^\bullet + H_2O_2 \rightarrow 2H_2O + O_2 \tag{2.58}$$

The oxygen molecule O_2 can also directly participe in the radiolysis process. O_2 react with H$^\bullet$ or e_{aq}^- and reduced to be $HO_2^\bullet$ and O_2^- respectively (Eqs.2.54 & 2.55 in Tab.2.7) and then eventually form H_2O_2 or re-form O_2 in result (Eqs.2.52 & 2.53, same table).

Normally, once there is O_2 present in the water, they will be reduced by e_{aq}^- and H$^\bullet$ immediately. Considering about the constant reaction rate of Eq.2.54 and 2.55 for O_2, which are much larger than those of Eq.2.48 and 2.49 for H_2. O_2 can be referred as the chain reaction *killer*, it will certainly

accelerate water decomposition. So long as the concentration of O_2 stay very low, the H_2O_2 produced during the radiolysis can be consumed by Eq.2.49 (Tab.2.7). Therefore, the decomposition of water can be avoided. Oppositely, when the concentration of O_2 is too high, they will join in the competition with H_2 for $HO^{\bullet}$. As explained, the reactions of O_2 are much more efficient than H_2 thus even a little bit of O_2 can totally block the role of dissolve hydrogen. In consequence, the chain reaction of H_2O_2 and O_2 is stopped and water decomposition takes place.

Latest, Ershov *et al.* have established a model of radiolysis of water and aqueous solution of H_2, H_2O_2 and O_2 [46]. It includes almost all the relevant experimental results. As illustrated in Fig.2.13, (a) indicates that with higher $[H_2O_2]$ in the solution, more O_2 is going to be formed. Moreover, the rate of H_2O_2 decomposition also depends on Eq.2.55 and 2.56 (Tab.2.7); (b) on the other hand, shows the efficiency of H_2O_2 decomposition decreases with its initial concentration in the water.

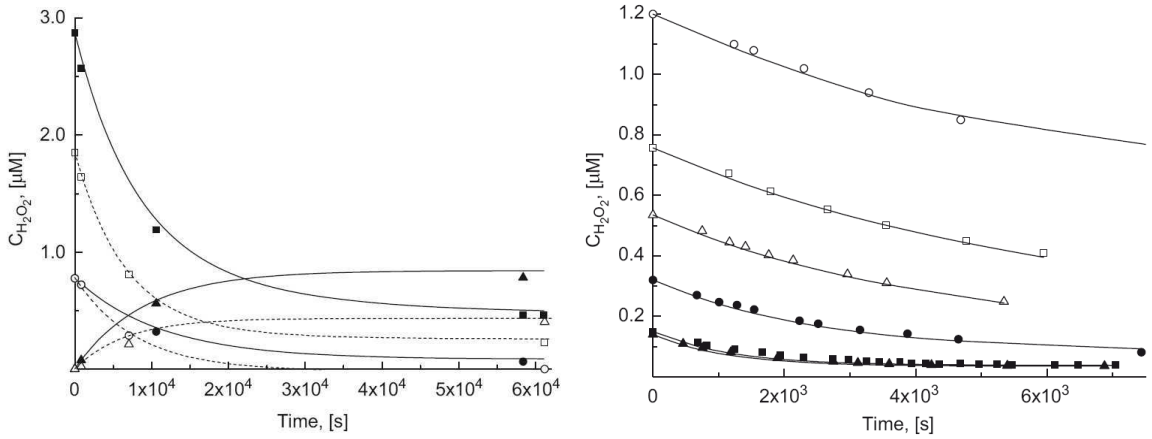

(a) (b)

Figure 2.13: (a) γ ray effect on solutions containing H_2 and excess H_2O_2, constant dose rate = 0.77 Gy.s^{-1}, constant $[H_2] = 7.8 \times 10^{-4}$ M: ■ for high $[H_2O_2]$ & □ for low $[H_2O_2]$; ○ high $[H_2]$ & ● low $[H_2]$; ▲ for high $[O_2]$ & △ for low $[O_2]$; calculation curve of $[H_2O_2]$ in decreasing order: straight line, dot line [46, 73]; (b) Decomposition of neutral deareated aqueous solution, constant dose rate = 0.2 Gy.s^{-1} $[H_2O_2]$ in a decrease order: ○, □, △ ●, ■, ▲, [46, 76].

.

2.3.B Critical Hydrogen Concentration (CHC)

In PWRs, the water is deareated to eliminate O_2 and a certain quantity of H_2 is added, as introduced in Chapter 1. However, dissolved hydrogen has its inconvenience: bringing stress corrosion problem, increasing the maintenance fee etc,. Therefore, a concept of critical hydrogen concentration (**CHC**) need to be brought into conversation, which has become a hot topic. Early studies [77] has already shown that 1 cc/kg of H_2 is more than enough to reduce hydrogen peroxide generated by radiolysis.

Recently, Bartels *et al.* [78–81] have done a lot of research on finding the value of CHC, it is first relevant with the types of reactors, the core design, the parameters of PWR water and etc. In general, the normal-industry level of dissolved hydrogen for operating PWR varies from 25 to 40 cm^3 (STP).kg^{-1}, depending on different countries. Still these values are largely above the CHC, the most recent modelling in the AECL reactor [81] says that the CHC is approximately 0.5 cm^3 (STP).kg^{-1} for

a typical PWR conditions. This value seemed quite low, whereas the modelling value should be lower if there are no ammonia impurities problems. Actually, under PWR conditions, rather than factors mentioned before, the only major factor for CHC is the sensitivity of the constant rate of reaction Eq.2.48 (Tab.2.7) at high temperature. The steady state H_2 concentration in pure water is almost completely determined by the equilibrium of this reaction [78]. Despite the fact that these research are under the PWR condition, some of these conclusions are obtained without the presence of boric acid which can lead to $^{10}B(n,\alpha)^7Li$ reactions. In this case, the value of CHC may be increased due to the fact that no radicals produced in α radiation [81].

Nevertheless, Takiguchi *et al.* [82, 83] also found the optimal dissolved hydrogen value was below 0.5 $cm^3(STP).kg^{-1}$ in the out-of-core region in the INCA loop. However, the approximate dissolved hydrogen threshold for in-core region was at least twice higher than the out-of-core value.

The study of CHC starts from the mid-1990$'s$ and still goes on today, it is not only important in the point view of suppress radiolysis with minimum amount of H_2 which can bring an economic benefits, but also in the aspect of avoiding the corrosion problems trigged or accelerated by the excess H_2.

2.3.C Radiolysis in the Presence of Boron and Lithium

Before talking about the effect of ^{10}B, the influence of LET needs to be discussed. As explained in the previous section, low LET like γ-ray gives more radicals products than molecular ones and favours the recombination of the chain reaction. In short, there will be no water decomposition with low LET. Reversely, high LET leads to a higher concentration of H_2O_2 and thus limits the chain reaction and produces O_2 [84–86]. Therefore, the water decomposition is more likely occurring with high LET. $^{10}B(n,\alpha)^7Li$ happens to be one of high LET radiation.

In PWRs, the global LET actually depends on the ratio between high ($^{10}B(n,\alpha)^7Li$) and low (γ-ray) LET radiation. In different parts of PWRs, like the in-core and out-of-core, the LET is different. Without any doubt, the concentration of ^{10}B directly affects on the local ratio of $^{10}B(n,\alpha)^7Li/\gamma$. The ratio increases with the concentration of ^{10}B, thus the global LET also increase and tends to high LET radiation. In consequence, the augmentation of $[^{10}B]$ results in higher probability of water decomposition. Fig.2.14 illustrates this influence of $[^{10}B]$ on the radiolytic yields of H_2O_2 and O_2 [87, 88], which seem to be linked with the temperature:

- At room temperature, (30°C), it appears to have a threshold about 0.13 $mol.L^{-1}$. Above this threshold, both H_2O_2 and O_2 increase sharply with the concentration of ^{10}B.
- In the middle temperature, (100°C), this threshold is shifted towards a higher concentration, approximately 0.19 $mol.L^{-1}$.
- At high temperature, (200°C), there is no visible threshold shown in the Fig.2.14. It implies that more ^{10}B can be added into PWR water without bringing the water decomposition as temperature increases. The reason might be explained in three aspects:
    1. The radical yields increases with temperature as mentioned before, and hence the recombination reactions are favoured.

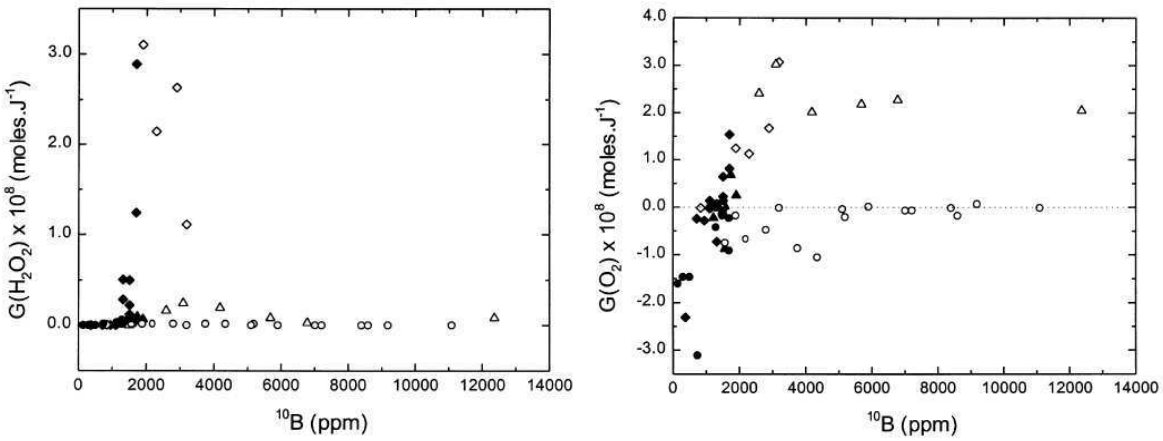

(a) (b)

Figure 2.14: The effect of ^{10}B concentration on water radiolysis: (a) $g(H_2O_2)$ vs. [^{10}B]; (b) $g(O_2)$ vs. [^{10}B]. 30°CNBA (◊), 30°C EBA (♦) ; 100°C NBA (▲), 100°C EBA △; 200°C NBA (●), 200°C EBA (○). NBA (open symbols): Natural Boric Acid, contains 19.8% of ^{10}B; EBA (solid symbols): Enriched Boric Acid, contains 99.5% of ^{10}B [87].

2. The kinetics of the chain reaction are favoured over those of forming oxidising species H_2O_2 and O_2. The reason will be explained in the section of temperature influence.
3. The hydrogen solubility increases with temperature, thus more H_2 at high temperature, more chain reaction taking place and less water decomposition.

No specific effect of enriched boric acid (EBA) on water radiolysis has been observed. At the same concentration, EBA and NBA show the same behaviours. Therefore, EBA can be safely used for replacing NBA in PWRs as far as the concern of radiolysis.

Actually, the presence of ^{7}LiOH causes more water decomposition, as shown in Fig.2.15. The explanation of this phenomenon is not very clear yet. The main role of ^{7}LiOH is to adjust and maintain the pH at 7 for PWR water. But, as shown previously, this variation of pH will not affect on the water decomposition, and hence the pH effect should not be the cause of the increase brought by ^{7}LiOH. Li^+ does not seem to react with the radicals normally. Briefly, a negative influence on PWR water radiolysis is brought by the presence of ^{7}LiOH, although further studies need to be done.

2.3.D Influence of Other Parameters on Radiolytic Yields

Under PWR conditions, other than the influence of H_2, ^{10}B and ^{7}LiOH, the radiolytic yields can also be affected by a lot of parameters before or after steady-state. However, like the influence of LET has already been detailed in the previous section 2.3.C, and the influence of dose rate does not seem different between pure and PWR waters, then they will not be discussed in the following sections.

2.3.D.1 Influence of temperature

According the temperature effect on pure water, the radicals yields increase while the molecular yields decrease as a function of temperature. Consequently, the recombination reactions are promoted. In the

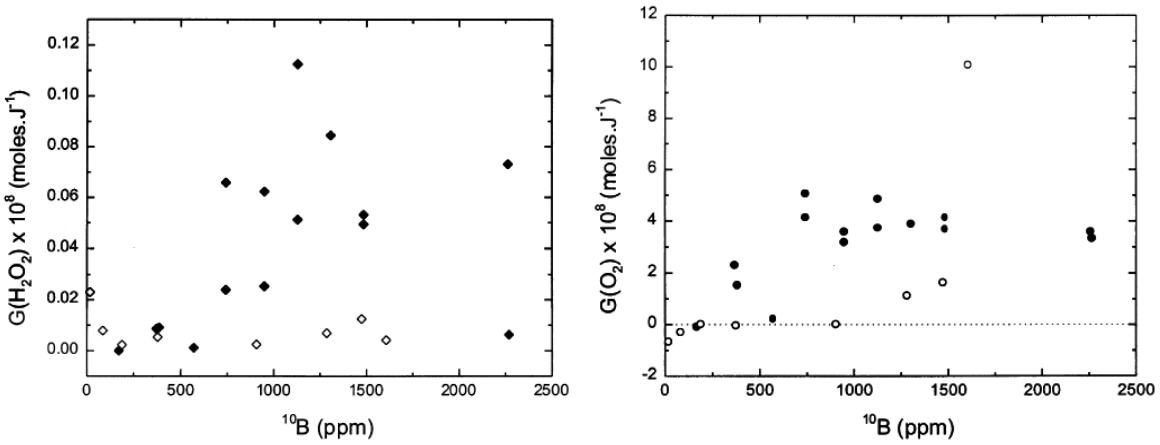

(a) (b)

Figure 2.15: The effect of ^{7}LiOH on water radiolysis at 200°C: (a) g(H_2O_2) vs. [^{10}B]; (b) g(O_2) vs. [^{10}B]. Solid symbols: solution contains ^{7}LiOH, calculated by MULTEQ® to achieve a pH = 7 at 200°C; Open symbols: blank solution without ^{7}LiOH [87].

case of PWR water, with the increase of temperature, the chain reaction of H_2 is preferred to others. One explanation is linked to the activation energy $\mathbf{E}_a$[11]. It can be expressed by the **Arrhenius Equation** as written in Eq.2.59, in which, k is the constant reaction rate, E_a means the activation energy, R is the ideal gas constant and A is the frequency factor (or attempt frequency) of the reaction.

$$ln(k) = -\frac{E_a}{RT} + ln(A) \tag{2.59}$$

As indicated in Tab.2.7, the values of E_a for the chain reaction, Eqs.2.48 & 2.49, are higher than Eqs.2.45, 2.46 and 2.47, which are the chain *stoppers*. Nevertheless, the increase of E_a is less significant than the augmentation of the radicals with the raise of temperature. On the other hand, as mentioned in Ch.2.3.C, the solubility of H_2 increases with temperature and results in favour of the chain reaction. Therefore, it seems that the effect of temperature may slow down the PWR water decomposition.

2.3.D.2 Influence of pH

Fig.2.16 illustrates the pH of PWR water with temperature. At 300°C the pH is about 7, and the pH behaviour of PWR water is actually following the one of boric acid. Below this temperature, the pH seems to reach a minimum of the curve at 150°C [89, 90].

Fig.2.17 has portrayed the variation of steady-state concentration of H_2O_2 and O_2 as a function of pH [46, 91]. Briefly, it describes:

- The concentration of H_2O_2 increases sharply with the decrease of pH from 4 to 0. For a higher pH, it seems to have no effects on the H_2O_2;
- The concentration of O_2 is not affected by the pH from 4 to 8. Then in the two extreme zones, it increases with the pH. As a result, in the alkaline environment, the concentration of O_2 is much higher than it of acid zone.

[11] $\mathbf{E}_a$: the energy needs to be overcome in order to achieve a chemical reaction.

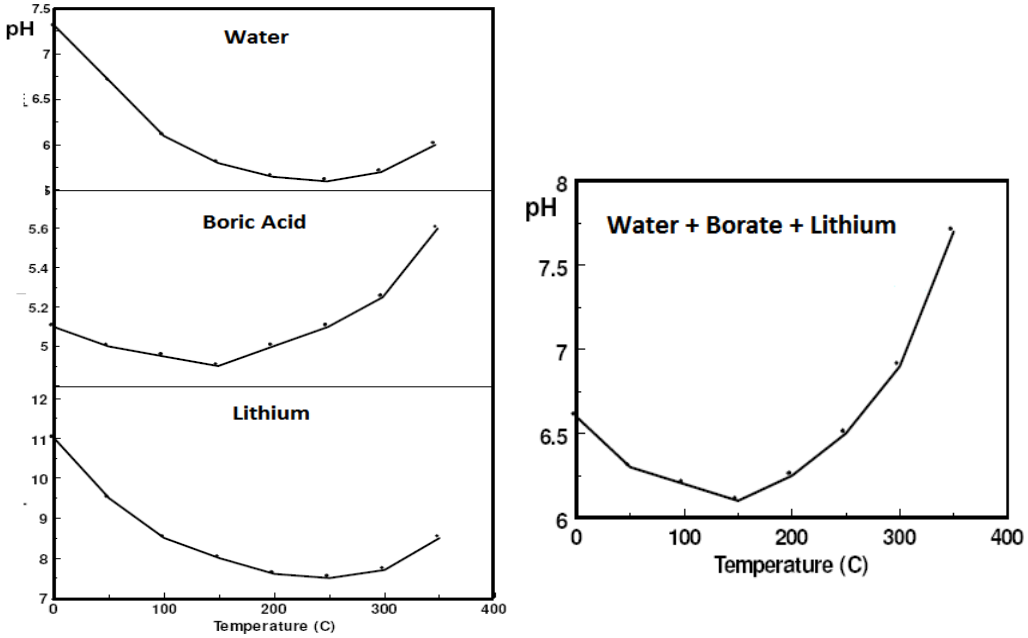

(a) (b)

Figure 2.16: The effect of boric acid and lithium on pH as a function of temperature: (a) water, boric acid and lithium respectively; (b) PWR water by including the three elements [89].

Generally, regardless the temperature, the pH of PWR water stays in the range form 6 to 8 approximately. Thus, the pH ($4 \leqslant pH \leqslant 10$) appears to have no specific effect on PWR water decomposition. However, either in acidic or in basic environment, the pH can still affect the water decomposition, especially for the molecular products, H_2O_2, O_2 and H_2.

The variation of steady-state concentration of H_2O_2 and O_2 from pH is strongly depend on the reaction between e^-_{aq} and a proton, H_3O^+, as shown in Eq.2.60, $k = 2.3 \times 10^{10}$ L.mol^{-1}.s^{-1}. Both e^-_{aq} and $H^\bullet$ reduce H_2O_2 and O_2, written in Eqs.2.61, and thus inhibit the water decomposition. The constant reaction rate decreases while the pH increases [92], Eq.2.60 is thus less efficient. Higher pH, the less $H^\bullet$ is produced.

$$e^-_{aq} + H_3O^+ \rightarrow H^\bullet + H_2O \tag{2.60}$$

As the constant reaction rates indicated for Eqs.2.61, H_2O_2 prefers to react with e^-_{aq} over $H^\bullet$. For the O_2, there is no difference since the k values are practically the same. With the increase of pH, H_2O_2 appears to be more competitive for e^-_{aq} and $H^\bullet$, and thus to be reduced [46].

$$\begin{aligned} e^-_{aq} + H_2O_2 &\rightarrow O_2^- \qquad k = 1.14 \times 10^{10} L.mol^{-1}.s^{-1} \\ e^-_{aq} + O_2 &\rightarrow OH^- + HO^\bullet \qquad k = 1.94 \times 10^{10} L.mol^{-1}.s^{-1} \\ H^\bullet + H_2O_2 &\rightarrow H_2O + HO^\bullet \qquad k = 3.44 \times 10^{7} L.mol^{-1}.s^{-1} \\ H^\bullet + O_2 &\rightarrow OH_2^- \qquad k = 2.0 \times 10^{10} L.mol^{-1}.s^{-1} \end{aligned} \tag{2.61}$$

In a highly alkaline medium, Matheson *et al.* [93] found the evidence of the reaction Eq.2.62. Thereby, the decrease of $H^\bullet$ while the increase of e^-_{aq} leads to the same conclusion as before.

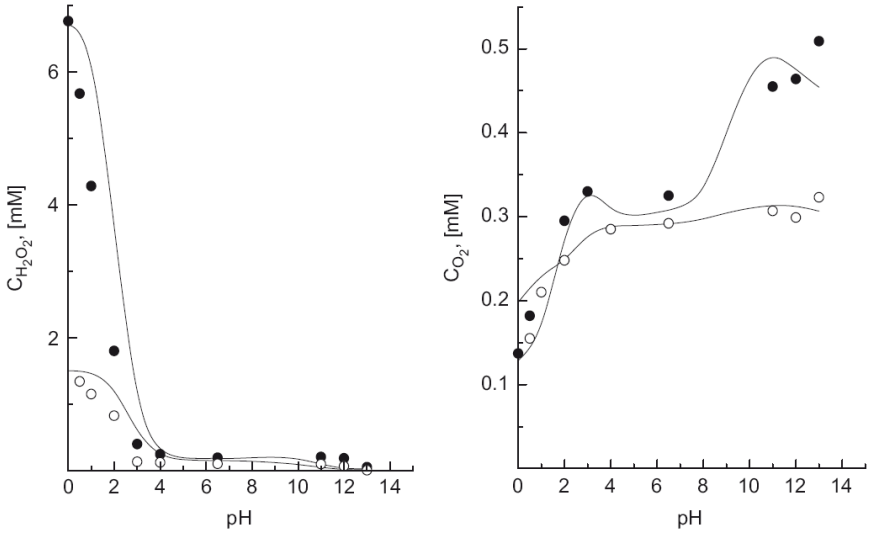

Figure 2.17: The concentration of H_2O_2 and O_2 versus pH at room temperature under different dose rates: • = 4.72 Gy.s^{-1}; ∘ = 0.42 Gy.s^{-1} [46, 91].

$$OH^-_{aq} + H^\bullet \rightarrow e^-_{aq} + H_2O \tag{2.62}$$

The acid-base equilibria reactions are listed in Tab.2.8 [52]. They play an important role in homogeneous chemistry.

Equilibrium Reaction (Eq n°)		pK$_a$ at 20°C	pK$_a$ at 150°C	pK$_a$ at 300°C
$HO_2^\bullet \rightleftharpoons H^+ + O_2^-$	(2.63)	4.83	4.91	6.57
$H_2O \rightleftharpoons H^+ + OH^-$	(2.64)	15.92	13.43	13.24
$H_2O_2 \rightleftharpoons H^+ + HO_2^-$	(2.65)	11.84	10.29	10.35
$HO^\bullet \rightleftharpoons H^+ + O^-$	(2.66)	11.84	10.29	10.35
$H^\bullet \rightleftharpoons H^+ + OH^-$	(2.67)	9.74	6.92	6.64
$H^\bullet + H_2O \rightleftharpoons H_2 + HO^\bullet$	(2.68)	12.17	7.95	5.57

Table 2.8: Table of acid-base equilibria reactions and their acid dissociation constant in minus logarithmic form, pK_a values, at different temperature [52].

The radical $HO_2^\bullet$ in Eqs.2.52 & 2.53 (in Tab.2.7) can both form oxidising species H_2O_2 and O_2. The constant reaction rate $k_{Eq.2.52}$ is at least 200 times smaller than $k_{Eq.2.53}$. At pH = 4.8, the acid-base equation Eq.2.52 comes to equilibrium, thus the reaction rate of Eq.2.53 comes to the maximum. With the increase of pH, not only the constant reaction rate reduces, but also the equilibrium of Eq.2.52 towards right side. As a result, more O_2^- accumulates in the solution, which can react with $HO^\bullet$, Eq.2.69, then decreasing the probability of the chain reaction. In this point of view, the increase of pH brings a negative effect on PWR water radiolysis.

$$(Eq.2.52) \qquad HO_2^\bullet + HO_2^\bullet \rightarrow H_2O_2 + O_2$$

$$(Eq.2.53) \qquad HO_2^\bullet + O_2^- \rightarrow HO_2^- + O_2$$

$$HO^\bullet + O_2^- \rightarrow O_2 + OH^- \tag{2.69}$$

Besides, under basic environment, the radical $HO^\bullet$ and transient species like O_2^- and O_3^-, play a major role in the radiation chemical transformations and in the determination of the steady-state concentration of molecular products H_2, O_2 and H_2O_2, as listed in Eqs.2.70 [46, 89].

$$\begin{aligned} HO^\bullet + OH^- &\rightarrow O^- + H_2O \qquad k = 1.3 \times 10^{10} L.mol^{-1}.s^{-1} \\ O^- + H_2O_2 &\rightarrow O_2^- + H_2O \qquad k = 5.0 \times 10^{8} L.mol^{-1}.s^{-1} \\ O^- + H_2 &\rightarrow H^\bullet OH^- \qquad k = 8.0 \times 10^{7} L.mol^{-1}.s^{-1} \\ O^- + O_2 &\rightarrow O_3^- \qquad k = 3.6 \times 10^{9} L.mol^{-1}.s^{-1} \\ O_3^- + HO^\bullet &\rightarrow O_2 + HO_2^- \qquad k = 8.5 \times 10^{9} L.mol^{-1}.s^{-1} \end{aligned} \tag{2.70}$$

Otherwise, in an acid environment, with the decrease of pH, the recombination of $H^\bullet$ is promoted over e_{aq}^- [35], thus the concentration of O_2 decreases while the one of H_2O_2 increases.

In brief, higher pH brings higher concentration of O_2, lower pH results in more H_2O_2. However, in the range of pH from 4 to 10, the steady-state concentration of H_2O_2 and O_2 are not affected.

2.3.D.3 Influence of pressure

As told, pressure has no effect on the primary yields until 6.34 kbar on pure water radiolysis [64–69]. It is still true under PWR conditions. However the constant reaction rate may be affected by the pressure if there is a change in activation volume during the *transition state*. **Transition State Theory** (**TST**) completes the Arrhenius rate law and explains the reaction rates of elementary chemical reactions [94].

$$ln(k) = ln(k_0) - \left(\frac{\Delta V^\ddagger}{RT}\right) P \tag{2.71}$$

In Eq.2.71, k and k_0 are the constant reaction rate at the pressure P and the atmospheric pressure P_0 respectively, R and T are the ideal gas constant and the absolute temperature in Kelvin, $V^\ddagger$ is actually the activation volume, normally in $cm^3.mol^{-1}$. The volume of activation is defined as the difference between the partial molar volumes of the transition state and the sums of the partial volumes of the reactants at the same temperature and pressure according **TST**. In practice, the $V^\ddagger$ may also be a function of pressure, thus the situation becomes more complicated. Briefly, the variation of k depends on $\Delta V^\ddagger$ and the pressure itself if it is high enough. In most water radiolysis reactions, $\Delta V^\ddagger$ dose not vary much. Therefore, the variation of constant reaction rate can be neglected unless the pressure is too high [16].

2.3.D.4 Influence of impurities

Under PWR conditions, impurities in the water provokes serious problems like the deposition of CRUD on the tubing and so on. For PWR waters, the most studied impurity without any doubt is iron [95].

Iron impurities: Fe^{2+}, Fe^{3+} Generally, only ferrous ions can be released from the metal surface. However, they can be oxidised into ferric ions by water itself or oxidising radiolysis products, such as $HO^{\bullet}$, $HO_2^{\bullet}$, O_2^- and H_2O_2, written in Eqs.2.72 [87, 95].

$$\begin{aligned} 2Fe^{2+} + 2H^+ + \tfrac{1}{2}O_2 &\rightarrow 2Fe^{3+}_{aq} + H_2O \\ Fe^{2+} + HO^{\bullet} &\rightarrow Fe^{3+} + OH^- \\ Fe^{2+} + HO_2^{\bullet} &\rightarrow Fe^{3+} + OH_2^- \\ Fe^{2+} + O_2^- &\rightarrow Fe^{3+} + H_2O_2 + 2OH^- \\ 2Fe^{2+} + H_2O_2 &\rightarrow 2Fe^{3+} + OH_2^- \end{aligned} \tag{2.72}$$

Oppositely, ferric ions can also be reduced by $H^{\bullet}$, e^-_{aq} and so on, shown in Eqs.2.73 [87, 95].

$$\begin{aligned} Fe^{3+} + H^{\bullet} &\rightarrow Fe^{2+} + H^+ \\ Fe^{3+} + e^-_{aq} &\rightarrow Fe^{2+} \end{aligned} \tag{2.73}$$

Fig.2.18 shows the influence of $Fe(NO_3)_3$ on H_2O_2 and O_2 yields at room temperature. An increase of H_2O_2 can be observed due to the presence of ferric ions. Actually, Fe^{3+} and (Fe^{2+}) acts as scavengers of the radicals and result in less water recombination reactions. In a word, the presence of iron impurities leads to more radiolysis products at high boron concentration, and thus it is not a desirable phenomenon for PWR waters. Indeed, this conclusion is dragged out without considering the temperature influence on the solubility, though the solubility of ferric oxide appears not to depend on temperature between $250 - 350°C$ [96].

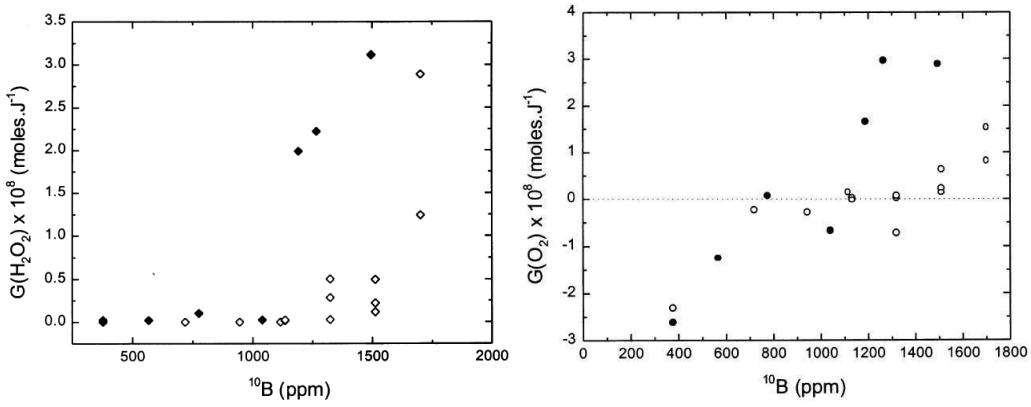

(a) (b)

Figure 2.18: The effect of $Fe(NO_3)_3$ at 30°C on water radiolysis: (a) $G(H_2O_2)$ vs. [^{10}B]; (b) $G(O_2)$ vs. [^{10}B]. Solid points: • and ♦ for 2ppm $Fe(NO_3)_3$; open points: ∘ and ◇ for blank solution [87].

Zinc impurities : Zn^{2+}, Zn^+ Zinc is added in PWR water to suppress the radioactivity build-up on metallic surfaces due to cobalt-60 accumulation. Zn is not an impurity, it is actually an added element, though the concentration is quite low, few ppb.

Many studies [16, 87, 97, 98] have demonstrated in different ways that no negative effect of Zn on the radiolysis of the PWR water. Zn^{2+} can react with e^-_{aq} and be reduced to Zn^+. Also, it is hardly oxidised by other substances, thus Zn^{3+} is seemed not possible in the radiolysis water. On the

other hand, Zn^+ can react with the molecular products H_2O_2 and the radical $HO^\bullet$, which is somehow a diffusion controlled reaction. In consequence, Zn^+ may be oxidised back to Zn^{2+} or form other products. Briefly, in the point of view of water radiolysis, the presence of Zn have no major influence.

$$\begin{gathered} Zn^{2+} + e^-_{aq} \rightarrow Zn^+ \\ Zn^+ + H_2O_2 \rightarrow Zn^{2+} + HO^\bullet + OH^- \\ Zn^+ + OH^\bullet \rightarrow Zn^{2+} + OH^- \end{gathered} \tag{2.74}$$

Nitrate and nitrite impurities: NO_3^-, NO_2^- The influence of both nitrate and nitrite are still debatable, though it tends to be desirable for water radiolysis [99–101]. Even with a low concentration, they can react with the radicals formed during water radiolysis, such as e^-_{aq}, $HO^\bullet$ and $^\bullet O^-$, as Eqs.2.75 listed below. The competition between nitrate and nitrite for the radicals result in increasing the concentration of H_2 and H_2O_2.

$$\begin{gathered} e^-_{aq} + NO_3^- \rightarrow^\bullet NO_3^{2-} + H_2O \rightarrow^\bullet NO_2 + 2OH^- \\ {}^\bullet O^- + NO_3^- \rightarrow^\bullet NO_3^{2-} + H_2O \rightarrow^\bullet NO_2 + 2OH^- + O_2 \\ e^-_{aq} + NO_2^- \rightarrow^\bullet NO_2^{2-} + H_2O \rightarrow^\bullet NO + 2OH^- \\ HO^\bullet + NO_2^- \rightarrow^\bullet NO_2^{2-} + OH^- \\ 2^\bullet NO_2 + H_2O \rightarrow NO_3^- + NO_2^- + 2H^+ \end{gathered} \tag{2.75}$$

NO_3^- reacts more efficient with e^-_{aq} than NO_2^-. Nevertheless, the consequence is that the concentration of H_2O_2 is increased. Besides, NO_2^- can act as a good scavenger for $HO^\bullet$ which is important for the chain reaction of H_2 to suppress the radiolysis [102]. Furthermore, as long as the intermediate product $2^\bullet NO_2$ exists in the solution, which may also be directly excited by radiation, the net conversion between NO_3^- and NO_2^- will be continuous. Therefore, even with little NO_3^- and NO_2^- presence, the influence can be significant.

When the steady-state is achieved, the presence of nitrogen species depends on pH value, either as NO_3^- or in form of NO_3^-. Nitrate is the dominant species as pH $\lessapprox$ 10 while nitrite takes the leading at higher pH value.

Other impurities: Other than the impurities mentioned before, the existence of copper, Cl^-, SO_4^{2-} and so on should be brought into conversation too. Indeed, no one kind of impurity has been proved to have beneficial effect. Regardless the aspect of corrosion problem, even in the point view of water radiolysis, impurities accelerate PWR water decomposition, except for Zn which appears to have no effect.

Indeed, the presence of impurities copper [16, 103, 104] leads to more serious problem for water decomposition. As expressed in Eqs.2.76, Cu^{2+} and Cu^+ react with oxidising species and form O_2 and H_2O_2 in one hand, on the other hand they are also good scavenger for $HO^\bullet$ and $H^\bullet$, thus inhibit the chain reaction.

$$\begin{gathered} Cu^{2+} + O_2^- \rightarrow Cu^+ + O_2 \\ Cu^+ + O_2^- + (2H_2O) \rightarrow Cu^{2+} + H_2O_2 + 2OH^- \\ Cu^+ + HO^\bullet \rightarrow Cu^{2+} + OH^- \\ Cu^{2+} + H^\bullet \rightarrow Cu^+ \end{gathered} \tag{2.76}$$

Moreover, the copper ions may act as catalysis and accelerate the decomposition of H_2O_2 into O_2. In brief, the presence of copper is not favoured in PWR water, no matter what concentration.

Other impurities, like Cl^-, SO_4^{2-} will not be detailed here. However, their effects seems to be more serious for corrosion than for radiolysis [16].

2.4 Summary

In this chapter, three aspects of radiation chemistry have been detailed, the interaction of radiation with matter, radiolysis in pure water and radiolysis in PWR water.

During the interaction of radiation with matter, the energy loss leads to ionisation and radiation. The concept of LET is the most common method to describe a source of radiation. The ways of interaction with matter, the LETs and the tracks left in the medium are different, depending on the different types of interactions.

Water radiolysis happens within 1μs after the energy deposition of a particle in the water and afterwards the water is regarded as a homogenous state. Therefore, the primary yields, both radical and molecular products, refer to homogenous and steady-state yields. They can be influenced by many parameters, the most dominant factors are the LET of radiation and the water temperature.

Concerning PWR water decomposition, which can be simply thought as the pure water radiolysis with presence of H_2, $B(OH)_3$ and LiOH. However, the radiolysis process becomes more complex. In one hand, dissolved hydrogen can join in the reaction from the beginning to the end. On the other hand, the presence of ^{10}B can directly affect on LET and cause more water decomposition. And ^{7}LiOH also accelerates PWR water decomposition, but the reason is still not clear yet. Nevertheless, the high temperature of PWR water may slow down the water decomposition.

Generally, the radiation damages the materials and through the production of oxidising species, the radiolysis causes corrosion problem, which are two serious factors to limit the PWR life extension.

References

[1] Erik Koelink. Scattering Theory wi4211 Advanced Topics in Analysis. Technical report, TUDelft, 2006.

[2] Scattering, course of University of Oxford, Physics Department, WEB, http://www.physics.ox.ac.uk/documents/PUS/dis/scattering.htm.

[3] S. Tavernier. *Experimental Techniques in Nuclear and Particle Physics*. Springer; 2010 edition, 2010.

[4] C. Leroy, P. Rancoita. *Principals of Radiation Interaction in Matter and Detection*. World Scientific Publishing Company, 2 edtion edition, February, 2009 February 2009.

[5] Wiliam Frass. Passage of Particles Through Matter. Technical report, Oxford Physics, 2009.

[6] J. Beringer et al. (Particle Data Grourp). Review of particle physics. *Phys. Rev. D*, 86, 2012.

[7] National Institute of Standards and Technology, Physical reference data, httm://physics.nist.gov/PhysRefData/content.html.

[8] Y. Tsai. Pair production and bremsstrahlung of charged leptons. *Rev. Mod. Phys.*, Vol.46, 815 (1974), Vol.49, 421 (1977).

[9] C. Amsler et al . Review of Particle Physics. *Physics Letters B*, 667:1 – 6, 2008. Review of Particle Physics.

[10] Yoneho Tabata, Yasuo Ito. *CRC Handbook of radiation chemistry.* CRC Pr, 1991.

[11] Frank Krumeich. Properties of Electrons, their Interactions with matter and Applicaitons in Electron Microscopy. Technical report, Laboratory of Inorganic Chemistry.

[12] Nuclear Data Center tables, Brookhaven national laboratory, available from the WEB at http://www.nndc.bnl.gov/.

[13] U. Littmark J.F. Ziegler, J. Biersack. *The Stopping and Range of Ions in Matter*. Pergamon Press, 1985.

[14] James F. Ziegler, M.D. Ziegler, and J.P. Biersack. Srim the stopping and range of ions in matter (2010). *Nuclear Instruments and Methods in Physics Research Section B: Beam Interactions with Materials and Atoms*, 268:1818–1823, 2010. 19th International Conference on Ion Beam Analysis.

[15] J.W.T. Spinks and R.J. Woods. *An introduction to radiation chemistry*. Wiley, 1990.

[16] PASTINA Barbara. *Etude sur la radiolyse de l'eau en relation avec le circuit primaire de refroidissement des réacteurs nucléaires á eau sous pression.* PhD thesis, Universite de Paris-SUD U.F.R. Scientifique d'Orsay, 1997.

[17] TRUPIN-WASSELIN Virginie. *Processus primaries en chimie sous rayonnement. Influence du Transfert d'Energie Linéique sur la radiolyse de l'eau*. PhD thesis, Universite de Paris-SUD U.F.R. Scientifique d'Orsay, 2000.

[18] Ferradini, Christiane and Jay-Gerin, Jean-Paul. *Canadian Journal of Chemistry*, 77(9):1542–1575, 1999.

[19] Le Caër S. Water Radiolysis: Influence of Oxide Surfaces on H_2 Production under Ionizing Radiation. *Water*, 3(1):235–253, 2011.

[20] Swiatla-Wojcik, Dorota and Buxton, George V. Modeling of radiation spur processes in water at temperatures up to 300 °C. *The Journal of Physical Chemistry*, 99(29):11464–11471, 1995.

[21] V. Cobut and J.-P. Jay-Gerin and Y. Frongillo and J.P. Patau. On the dissociative electron attachment as a potential source of molecular hydrogen in irradiated liquid water. *Radiation Physics and Chemistry*, 47(2):247 – 250, 1996.

[22] Xing L. Yan and Ryutaro Hino, editor. *Nuclear Hydrogen Production Handbook (Green Chemistry and Chemical Engineering)*. CRC Press, 1 edition edition, March 2011.

[23] Nikola and Getoff. Radiation chemistry and the environment. *Radiation Physics and Chemistry*, 54(4):377 – 384, 1999.

[24] Craw M. T. Han Ping Trifunac A. D. Bartels, D. M. Hydrogen/deuterium isotope effects in water radiolysis. 1. the mechanism of chemically induced dynamic electron polarization generation in spurs. *The Journal of Physical Chemistry*, 93(6):2412–2421, 1989.

[25] Frongillo Y, Fraser M J, Cobut V, Goulet T, Jay-Gerin J P and Patau J P. Evolution of the species produced by slowing down of fast protons in liquid water: simulation based on the independent reaction times approximation. *J. Chim. Phys.*, 96:93–102, 1996.

[26] Weldon G. Brown and Edwin J. Hart. Effect of ph on oxygen(3p) atom formation in .gamma.-ray irradiated aqueous solutions. *The Journal of Physical Chemistry*, 82(24):2539–2542, 1978.

[27] V. Cobut, Y. Frongillo, J.-P. Patau, T. Goulet, M.-J. Fraser and J.-P. Jay-Gerin. Monte carlo simulation of fast electron and proton tracks in liquid water - I. physical and physicochemical aspects. *Radiation Physics and Chemistry*, 51(3):229 – 243, 1998.

[28] Ping Han and D.M. Bartels. H/D isotope Effects in Water Radiolysis. 4. The mechanism of $(H)_{aq} \rightleftharpoons (e^-)_{aq}$ Interconverison. *J. Phys. Chem.*, 96:4899–4906, 1992.

[29] G H Olivera, C Caraby, P Jardin, A cassimi, L Adoui and B Gervais. Multiple ionization in the earlier stage of water radiolysis. *Phys. Med. Biol.*, 43:2347–2360, 1998.

[30] LaVerne, Jay A. and Pimblott, S. M. New Mechanism for H_2 Formation in Water. *The Journal of Physical Chemistry A*, 104(44):9820–9822, 2000.

[31] LaVerne, Jay A. and Pimblott, Simon M. Scavenger and time dependences of radicals and molecular products in the electron radiolysis of water: examination of experiments and models. *The Journal of Physical Chemistry*, 95(8):3196–3206, 1991.

[32] Ianik Plante. A Monte-Carlo step-by-step simulation code of the non-homogeneous chemistry of the radiolysis of water and aqueous solutions - Part II: calculation of radiolytic yields under different conditions of LET, pH, and temperature. *Radiat Environ Biophys*, 50:405–415, 2011.

[33] Jintana Meesungnoen, Jean-Paul Jay-Gerin, Abdelali Filali-Mouhim, samlee Mankhetkorn. Monte-Carlo calculation of the primary $H^\bullet$ atom yield in liquid water radiolysis: effet of radiaiton type and temperature. *Chemical Physics Letters*, 335:458–464, 2001.

[34] Aryeh H. Samuel, John L. Magee. Theory of Radiation Chemistry. II. Track Effects in Radiolysis of Water. *The Journal of Chemical Physics*, 21(6):1080–1087, 1953.

[35] Schwarz H. A. Application of the Spur Diffusion Model to the Radiation Chemistry of Aqueous Solutions. *The Journal of Chemical Physics*, 73(6):1928–1937, 1969.

[36] Appleby A., Schwarz H. A. Radical and Molecular Yields in Water Irradiated by γ Rays and Heavy Ions. *The Journal of Chemical Physics*, 73(6):1937–1941, 1969.

[37] LaVerne, Jay A. Track Effects of Heavy Ions in Liquid Water. *Radiation Research*, 153:487–496, 2000.

[38] B. Gervais, M. Beuve, G.H. Olivera, M.E. Galassi. Numerical simulation of multiple ionization and high LET effects in liquid water radiolysis. *Radiation Physics and Chemistry*, 75(4):493 – 513, 2006.

[39] Michael A.J. Rodgers Farhataziz. *Radiation chemistry: principles and applications.* VCH Publishers, 1987.

[40] Burns W. G. and Moore P. B. Water radiolysis and its effect upon in-reactor zircaloy corrosion. *Radiat. Eff.*, 30:233–242, 1976.

[41] Yokohata A. and Tsuda S. A slovated electron formed the water by the irradiation of the recoil particles of $^{10}B(n,\alpha)^{7}Li$ and $Li(n,\alpha)T$. *Bull. chem. Soc. Jap.*, 47:2869–2870, 1974.

[42] J. A. La Verne. The production of OH radiacals in the radiolysis of water with He ions. *Radiat. Res.*, 118:201–210, 1989.

[43] Miller N. Radical yield measurement in irradiated aqueous solutions II. Radical yields with 10.9-MeV Deuterons, 21.3-MeV and 3.4-MeV alpha particles, and $^{10}B(n, \alpha)^{7}Li$ recoil radiations. *Rad. Res.*, 9:633–646, 1958.

[44] Ned E. Bibler. Dose Rate Effects in the Steady and pulse Radiolysis of Liquid Chloroform. *The Journal of Chemical Physics*, 75(16):2436– 2442, 1971.

[45] Schwarz H. A. A Determination of Some Rate Constants for the Radical Process in the Radiation Chemistry of Water. *J. Phys. Chem.*, 66:255–262, 1962.

[46] B.G. Ershov, A.V. Gordeev. A model for radiolysis of water and aqueous solutions of H_2, H_2O_2 and O_2. *Radiation Physics and Chemistry*, 77(8):928 – 935, 2008.

[47] Zorica D. Draganić Ivan G. Draganić. *The Radiation Chemistry of Water*. 1971.

[48] Christiane Ferradini and Jean-Paul Jay-Gerin. The Effect of pH on Water Radiolysis: A Still Open Question - A Minireview. *Res. Chem. Intermed.*, 26 (No.6):549–565, 2000.

[49] Swiatla-Wojcik, Dorota. Computation of the effect of pH on spur chemistry in water radiolysis at elevated temperatures. *NUKLEONIKA*, 53(Supplement 1):31–37, 2008.

[50] Vincent Cobut and Catherine Corbel and Jean Paul Patau. Influence of the pH on molecular hydrogen primary yields in He_2^+ ion tracks in liquid water. A Monte Carlo study. *Radiation Physics and Chemistry*, 72:207 – 215, 2005. <ce:title>Christiane Ferradini Memorial Issue</ce:title>.

[51] Narongchai Autsavapromporn, Jintana Meesungnoen, Ianik Plante, and Jean-Paul Jay-Gerin. Monte Carlo simulation sutdy of the effects of acidity and LET on the primary free-radical and molecular yields of water radiolysis - Application to the Fricke dosimeter. *Canadian Journal of Chemistry*, 85:214–229, 2007.

[52] A.J. Elliot, D.M. Bartels. The Reaction set, rate sonstants and g-Values for the Simulation of the Radiolysis of Light Water over the Range 20°C to 350°C Based on Information Available in 2008. Technical report, Atomic energy of Canada Limited, 2009.

[53] Roth, Olivia and LaVerne, Jay A. Effect of pH on H_2O_2Production in the Radiolysis of Water. *The Journal of Physical Chemistry A*, 115(5):700–708, 2011.

[54] Trupin V., Frongillo Y., Baldacchino G., Le Parc D. et Hikel B. Détermination de constantes de vitesse de réactions de recombinaison de radicaux. *J. Chem. Phys.*, 96:30–34, 1999.

[55] Plante I. A Monte-Carlo step-by-step simulation code of the non-homogeneous chemistry of the radiolysis of water and aqueous solution. Part I: theoreticla framework and implementation. *Radiat Environ Biophys*, 2011.

[56] Herve du Penhoat M. A. and Meesungnoen J. and Goulet T. and Filali-Mouhim A., mankhetkorn S. and Jay-Gerin J. P. Linear-energy-transfer effects on the radiolysis of liquid water at temperatures up to 300°C- a Monte-Carlo study. *Chemical Physics Letters*, 341:135 – 143, 2001.

[57] Herve du Penhoat M. A., Goulet T., Frongillo Y., Fraser M. J., Bernat P., and Jay-Gerin J. P. Radiolysis of Liquid Water at Temperatures up to 300°C: A Monte Carlo Simulation Study. *The Journal of Physical Chemistry A*, 104(50):11757–11770, 2000.

[58] Stefanic, Igor and LaVerne, Jay A. Temperature Dependence of the Hydrogen Peroxide Production in the γ-Radiolysis of Water. *The Journal of Physical Chemistry A*, 106(2):447–452, 2002.

[59] David M. Bartels. Comment on the possible role of the reaction $H^{\bullet} + H_2O \rightarrow H_2{+}OH$ in the radiolysis of water at high temperatures. *Radiation Physics and Chemistry*, 78(3):191 – 194, 2009.

[60] A . J. Elliot, M. P. Chenier, D . C Ouellette. Temperature dependence of g values of H20 and D20 irradiated with low linear energy transfer radiation. *J . Chem. Soc. Faraday Trans.*, Vol. 89:1193–1197, 1993.

[61] Eillot A. J., Chenier M. P., Ouellette D. C. and Koslowsky V. T. Temperature Dependence of g-Values for Aqueous Solutions Irradiated with 23 MeV $^2H^+$ and 157 MeV $^7Li^{3+}$ Ions Beams. *J. Phys. Chem.*, 100:9014–9020, 1996.

[62] Dorota Swiatla-Wojcik and George V. Buxton. Modelling of linear energy transfer effects on track core processes in the radiolysis of water up to 300 °C. *J. Chem. Soc., Faraday Trans.*, 94(15):2135–2141, 1998.

[63] Hochanadel C. J. and Ghormley J. A. Effect of temperature on the decomposition of water by gamma rays. *Radiation Research*, 16:653–660, 1962.

[64] Robert R. Hentz, Farhataziz, David J. Milner and Milton Burton. γ Radiolysis of Liquids at High Pressures. I. Aqueous Solutions of Ferrous Sulfate. *J. Phys. Chem.*, 46(8):2995–3000, 1967.

[65] Robert R. Hentz, Farhataziz, David J. Milner and Milton Burton. γ Radiolysis of Liquids at High Pressures. III. Aqueous Solutions of Sodium Bicarbonate. *J. Chim. Phys.*, 47(2):374–377, 1967.

[66] Robert R. Hentz, Farhataziz, and David J. Milner. γ Radiolysis of Liquids at High Pressures. IV. Primary Yields in Neutral Aqueous Solutions. *J. Phys. Chem.*, 47:4856–4867, 1967.

[67] Robert R. Hentz, Farhataziz, and David J. Milner. γ Radiolysis of liquids at High Pressures. V. Reaction of the Hydrated Electron with Water. *J. Phys. Chem.*, 47(12):5381–5384, 1967.

[68] Robert R. Hentz and Glarence G. Johnson Jr. γ Radiolysis of liquids at High Pressures. VII. Oxidation of Iodide Ion by Hydrogen Atoms in Aqueous Solutions. *J. Phys. Chem.*, 51(3):1236–1241, 1969.

[69] Robert R. Hentz and Ronald J. Knight. γ Radiolysis of liquids at High Pressures. VIII. Primary Yields at 8.7 kbar and Reactions of the Hydrated Electron with H_2O and H_3O^+. *J. Phys. Chem.*, 52(5):2456–2459, 1970.

[70] P. Ausloos, R. Gorden, Jr., and S.G. Lias. Effect of Pressure in the Radiolysis and Photolysis of Methane. *J. Phys. Chem.*, 40(7):1854–1860, 1964.

[71] Sava Lukac. *Radiolysis of N-Pentane in the Gas Phase*. PhD thesis, Ecole Polytechnique Federale de lausanne, 1978.

[72] Allen, A. O. and Hochanadel, C. J. and Ghormley, J. A. and Davis, T. W. Decomposition of Water and Aqueous Solutions under Mixed Fast Neutron and γ-Radiation. *The Journal of Physical Chemistry*, 56(5):575–586, 1952.

[73] Hochanadel C. J. Effects of Cobalt γ-Radiation on Water and Aqueous Solutions. *J. Phys. Chem.*, 56:587–594, 1952.

[74] Chien C. Lin. *Radiochemistry in Nuclear Power Reactors*. The National Academies Press, 1996.

[75] Alam M. S., Kelm M., Rao B. S. M., Janata E. Reaction of $H^{\bullet}$ with H_2O_2 as observed by optical absorption of perhydroxyl radicals or aliphatic alcohol radicals and of $^{\bullet}OH$ with H_2O_2. A pulse radiolysis study. *Radiation Physics and Chemistry*, 71:1087–1093, 2004.

[76] Hayon E. Radiolysis of Air-Free Aqueous solutions of Hydrogen Peroxide. *Trans. Faraday Soc. I*, 60:1059–1067, 1967.

[77] Garbett K., Henshaw J., Sims H. E. Hydrogen and oxygen behaviour in PWR primary coolant. 85. In *Water Chemistry in Nuclear Reactor System 8, British Nuclear Energy Society.*, 2000.

[78] Kotchaphan Kanjana and Kyle S. Haygarth and Weiqiang Wu and David M. Bartels. Laboratory studies in search of the critical hydrogen concentration. *Radiation Physics and Chemistry*, 82:25 – 34, 2013.

[79] Janik, Dorota and Janik, Ireneusz and Bartels, David M. Neutron and $\beta\gamma$ Radiolysis of Water up to Supercritical Conditions. 1. $\beta\gamma$ Yields for H2, $H^{\bullet}$ Atom, and Hydrated Electron. *The Journal of Physical Chemistry A*, 111(32):7777–7786, 2007. PMID: 17645317.

[80] Haygarth, Kyle and Bartels, David M. Neutron and β/γ Radiolysis of Water up to Supercritical Conditions. 2. SF6 as a Scavenger for Hydrated Electron. *The Journal of Physical Chemistry A*, 114(28):7479–7484, 2010.

[81] David M. Bartels, Jim Henshaw, Howard E. Sims. Modeling the critical hydrogen concentration in the AECL test reactor. *Radiation Physics and Chemistry*, 82:16–24, 2013.

[82] Takiguchi Hideki, Ullberg Mats and Uchida shunsuke. Optimization of Dissolved Hydrogen Concentraion for Control of Primary Coolant Radiolysis in Pressurized Water Reactors. *Journal of NUCLEAR SCIENCE and TECHNOLOGY*, 41(5):601–609, 2004.

[83] TAKIGUCHI Hideki, TAKAMATSU Hiroshi, UCHIDA Shunsuke , ISHIGURE Kenkichi, NAKAGAMI Motonori and MATSUI Makoto . Water Chemistry Data Acquisition, Processing, Evaluation and Diagnostic Systems in Light Water Reactors. *Journal of NUCLEAR SCIENCE and TECHNOLOGY*, 41 (2):214 – 225, 2004.

[84] Allen, A. O. *The radiation chemistry of water and aqueous soluitons.* Princeton, N. J., Van Nostrand, 1961.

[85] Pastina, Barbara and LaVerne, Jay A. Hydrogen Peroxide Production in the Radiolysis of Water with Heavy Ions. *The Journal of Physical Chemistry A*, 103(11):1592–1597, 1999.

[86] Pastina, Barbara and LaVerne, Jay A. Effect of Molecular Hydrogen on Hydrogen Peroxide in Water Radiolysis. *The Journal of Physical Chemistry A*, 105(40):9316–9322, 2001.

[87] B. Pastina, J. Isabey, B. Hickel. The influence of water chemistry on the radiolysis of the primary coolant water in pressurized water reactors. *Journal of Nuclear Materials*, 264:309–318, 1998.

[88] B. Pastina, J. Isabey and B. Hickel. Water radiolysis: the influence of some relevant parameters in PWR nuclear reactors. *Water Chemistry of Nuclear Reactor Systems 7.*, pages 153–155, 1996.

[89] Mahmoud N. S., El-Fawal M. M. and Gadalla A. A. Assessment of Cooling Water Chemistry on the Safety of Water Cooled Power Reactors. *Nature and Science*, 9(9):27–34, 2011.

[90] AREVA. Primary coolant chemistry: Fundamental aspects & improvements/ optimizations. In *Fundamentals & Developments*, Nov. 2008.

[91] Kabakchi S. A., Shubin V. N., Dolin P.I. Effect of pH on the stationary concentration of radiolysis products of aqueous solution of oxygen. *High Energ. Chem.*, 1(2):148–153, 1967.

[92] Bielski B. H. J., Cabelli E., Arudi A.L. Reactivity of HO_2/O_2^- Radicals in Aqueous Solution. *J. Phys. Chem. Ref. Data*, 14(4):1041–1100, 1985.

[93] Matheson M. S. and Rabani J. Pulse Radiolysis of Aqueous Hydrogen Solutions. I. Rate Constants for Reaction of e_{aq}^- with Itself and Other Trasients. II. The Interconvertibility of e_{aq}^- and H. *The Journal of Chemical Physics*, 69(4):1324–1335, 1965.

[94] Pinede J.R.E.T. and Schwartz S. D. Prottein dynamics and catalysis: the problems of transition state theory and the subtlety of dynamic control. *Phil. Trans. R. Soc. B*, 361:1433–1438, 2006.

[95] Allen A. O., Rothschild W. G. Studies in the Radiolysis of Ferrous Sulfate Solutions. Effect of Oxygen Concentration in 0.8 N Sulfuric Acid. *Radiation Research*, 7:591–602, 1957.

[96] You D. Bilan des mesures de solubilité des ferrites mixtes, private communication. Technical report, CEA, 1998.

[97] Domae M., Chitose N., Zuo Z., Katasumura Y. Pulse radiolysis study on redox reactions of zinc (II). *Radiation Physics and Chemistry*, 56:315–322, 1999.

[98] Buxton G.V., Sellers R. M. and McCracken D. R. Pulse Radiolysis Study of Monovalent Cadmium, Cobalt, Nickel and Zinc in Aqueous Soltuion. *J. Chem. Soc., Faraday Trans. 1*, 76:1464–1476, 1972.

[99] Hyder M. L. The Radiolysis of Aqueous Nitrate Solutions. *The Journal of Physical Chemistry*, 69(6):1858–1865, 1965.

[100] Yakabuskie P. A., Joseph J. M., Stuart C. R. and Wren C. Long-Term γ-Radiolysis Kinetics of NO_3^- and NO_2^- Solutions. *The Journal of Physical Chemistry A*, 115:4270–4278, 2011.

[101] Cunningham J. Radiation Chemistry of Ionic Solids. IV. Modifying Nitrate Radiolysis in Crystals by Compression. *The Journal of Physical Chemistry*, 70(1):30–39, 1966.

[102] Hiroki, Akihiro and Pimblott, Simon M. and LaVerne, Jay A. Hydrogen Peroxide Production in the Radiolysis of Water with High Radical Scavenger Concentrations. *The Journal of Physical Chemistry A*, 106:9352–9358, 2002.

[103] Schwarz H. A. The Effect of Solutes on the Molecular Yields in the Radiolysis of Aqueous Solutions. *J. Am. Chem. Soc.*, 77(19):4960–4964, 1955.

[104] Bernhardt P. V. and Lawrance G. A. Pulse radiolysis of mono-and binuclear copper (II) marcrocyclic complexes. *Polyhedron*, 10(12):1373–1377, 1991.

Chapter 3

Corrosion issues of Stainless Steel under Primary PWR Conditions

Stainless steels are one of the most widely used alloys in the industry. In the case of PWRs, stainless steels, such as 304 and 316L, are largely employed, for the internal core, for the pressure boundary pipings etc. Their good mechanical properties and corrosion resistance serve very well for the extreme conditions of PWRs.

However, corrosion-related materials failures, particularly stress corrosion cracking, is one of the major issues concerning the ageing of PWRs. Irradiation can create point defects like vacancies, interstitials, dislocations, and results in significant changes in microstructure and mechanical properties. In addition, irradiation may also decrease the resistance to stress corrosion cracking. The specific corrosion cracking, IASCC (Irradiation-Assisted Stress Cracking Corrosion) alone with other types may occur in the PWRs, IGSCC (Inter-granular Stress Corrosion Cracking) and PWSCC (Primary Water Stress Corrosion Cracking), can totally affect and damage the nuclear materials, including the stainless steels.

This chapter is focused on the corrosion behaviour of stainless steel 316L in primary PWR water, which is the main concern of this study. On one hand, the characterisation of the protective and passive film formed on 316L under primary PWR conditions will be described in detail. On the other hand, one of the main corrosion issue of 316L in the PWR conditions, IASCC (*Irradiation-Assisted Stress Corrosion Cracking*), will also be presented. Furthermore, in some cases, not only high temperature, but also room temperature have been studied in order to get a complete understanding of the corrosion issue.

3.1 The Oxide on 316L Formed under Primary PWR Water

Stainless steel 316, is an iron-based alloy containing at least 16% chromium and 10% nickel. The chemical compositions are indicated in Tab.3.1. The added molybdenum element to 316 gives a higher resistance to pitting and crevice corrosion and also to stress corrosion cracking in chloride environments compared to 304 which does not contain molybdenum. 316L refers to a low carbon content ($< 0.03\%$) and is a material suitable for welding which is not the case for the 316 with higher carbon content. On the other hand, 316L offers an excellent toughness, higher creep, stress to rupture and tensile strength at elevated temperatures, Tab.3.2 lists some mechanical and physical properties.

	Cr	Ni	Mo	Mn	Si	N	P	C	S	Fe
Min.	16.0	10.0	2.0	-	-	-	-	-	-	balance
Max.	18.0	14.0	3.0	2.0	0.75	0.10	0.045	0.03	0.03	balance

Table 3.1: Composition ranges for 316L stainless steels, (%mass.).

Density (kg/m^3)	Elastic Modulus (GPa)	Thermal Conductivity (W/m.K)	Elec Resistivity (nΩ.m)	Tensile Stress (MPa) min	Yield Stress 0.2% Proof (MPa) min
8×10^3	193	16.3 (at 100°C) 21.5 (at 500°C)	740	485	170

Table 3.2: Some mechanical and physical properties for 316L stainless steel.

Without any doubt, the excellent corrosion resistance of 316L is due to the oxide layer formed on

its surface, which will be detailed in the following section.

3.1.A Double-Layer Structure Oxide

During the last thirty years, many works have been done in order to understand the mechanism of oxide formed on austenitic stainless steel under high temperature in aqueous solution [1–6]. Gradually, the influence of different chemical conditions have also been studied, such as lithium, dissolve hydrogen and so on [7, 8].

The latest studies [7–10] show that the oxide formed on 316L under PWR conditions is identified as a **double-layer structure**, called inner and outer layers. They are two spinel oxide layers, an iron-based outer layer on top of a chromite-based inner layer. The inner layer is often regarded as the protective layer while the outer layer is not so protective [2].

3.1.A.1 Composition

According to the studies, the compositions of the oxide film formed on stainless steel 316L may be changed, as demonstrated by different papers [6–10]. This is due to the fact that the mechanism of the corrosion process is sensitive to the environment. A small change in the corrosion environment may cause a change in the oxide layer.

Nevertheless, a proposition for both inner and outer layer has been made, spinel oxide $\mathbf{AB_2O_4}$. **A** refers to a divalent cation and **B** represent a trivalent cation, where A = Ni(II) and Fe(II), B = Fe(III) and Cr(III). For both layers, Ni and Cr maintain the same valence, Ni(II) and Cr(III), whereas Fe may have both valence, (II) and (III) [4–7, 11].

Indeed, the dominant component for either inner or outer layer is different.

- Outer layer is mainly magnetite, Fe_3O_4 and AB_2O_4 in which Fe(III) is the main constituent for **B** and Fe(II) also takes the majority parts over Ni(II) for **A**. In result, the AB_2O_4 can be written as $(Ni_{1-x}Fe_x)(Fe_yCr_{1-y})_2O_4$, where x and y are certainly much larger than 0.5, especially for y, which may very well equals 1.

- Inner layer is mostly chromite, Cr_2O_3 [7, 12, 13] and AB_2O_4 in which Cr(III) is the main constituent for **B**. Concerning **A**, Fe(II) still holds the dominant position against Ni(II). Thereby, it can also be written as $(Ni_{1-x}Fe_x)(Fe_yCr_{1-y})_2O_4$, where $x > 0.5$ while $y < 0.25$.

Briefly, it has been considered for a long time that the outer layer is more or less like $NiFe_2O_4$ and $FeCr_2O_4$ for the inner layer. Da Cunha Belo *et al.* [7] divided the oxide film formed on 316L under primary PWR conditions into three regions, the outermost is $Ni_{0.75}Fe_{2.25}O_4$ spinel oxide, the intermediated is both $Ni_{0.75}Fe_{2.25}O_4$ and Fe_3O_4 spinel oxide, and the innermost is the chromium-rich oxide.

Last but not least, Terachi *et al.* have identified a nickel enrichment at the metal/oxide interface of 316 under simulated PWR primary conditions, as shown in Fig.3.1 (a), (b) and (c). The nickel enrichment at the metal/oxide interface is somehow more than twice that of its bulk concentration in the matrix [14]. This phenomenon is also observed before in nickel-based alloys [15], there the mechanism or the explanation is based on the diffusion of chromium to form a chromium-rich oxide

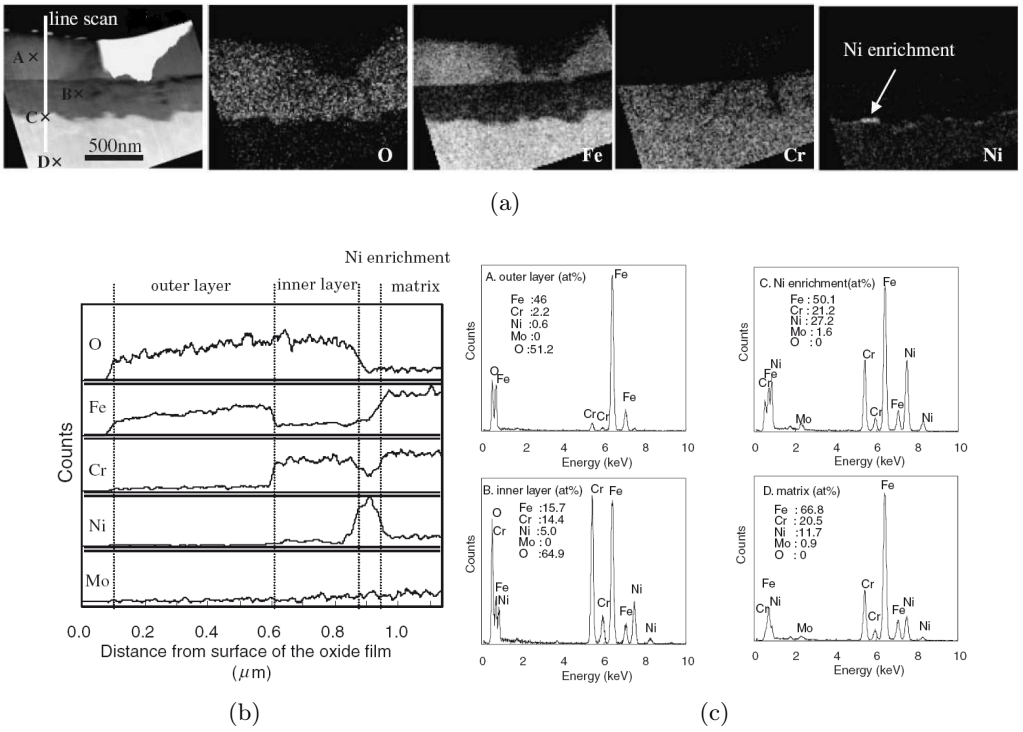

Figure 3.1: TEM/EDS analysis of an oxide film formed on 316L under simulated PWR primary water at 320°C for approximately 500 hours : (a) TEM elemental maps of oxygen, iron, chromium, and nickel; (b) EDS line scan (shown in (a) leftmost figure) profiles penetrates the oxide film; (c) EDS analysis for chemical composition of the oxide and the matrix (A, B, C and D shown in (a) leftmost figure) [14].

.

and thus the chromium depleted area is below this layer. Consequently, nickel enriches at oxide/ metal interface.

3.1.A.2 Structures

The structure of the oxide formed on the 316L stainless steel under primary PWR conditions is a spinel structure, which can be proved by a XRD analysis shown in Fig.3.2. No peak of hydroxide or corundum was observed, and hence the oxide film consisted only of the spinel structures.

3.1.A.3 Morphology

The morphologies of the oxide film formed on 316L austenitic stainless steel under primary PWR conditions have also been investigated for a long time [4, 8]. The iron-rich outer oxide, formed on top of the original alloy and grows outwards in the solution; while the Cr-rich inner oxide is growing into the original alloy surface.

The outer layer is considered porous and loosely adherent, it is mainly in the form of crystals or crystallites depending on the size. Generally, they show a well-defined polyhedral shapes. However the sizes and the densities are related to plenty of parameters: content of Cr, corrosion process, etc. In general, the crystal size varies from hundreds of nanometers to several micrometers. The inner

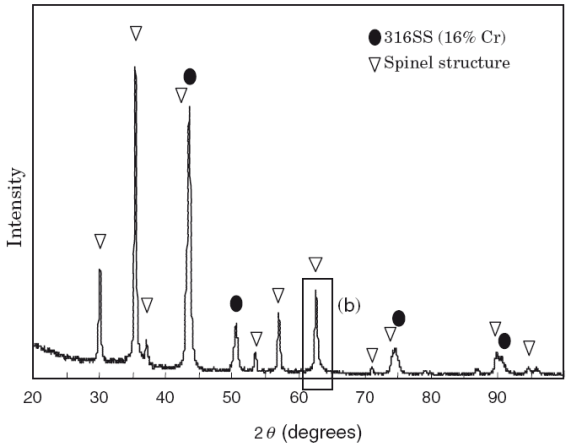

Figure 3.2: XRD analysis of 316L formed under PWR simulated conditions, 320°C, 380 hours [10].

oxide is a non-porous, tightly adherent layer, considered as a compact structure [5]. This thin inner chromium-rich layer plays an important role on the passivity of stainless steel. It is often regarded as the *protective layer*.

The equivalent thickness of the oxide film of 316L formed under primary PWR conditions is normally from 200 to 500 nm, whereas the passive film formed on it at ambient temperature is only a few nanometers [11]. It depends on the temperature of the environment and also the duration spent at this temperature.

As represented by Terachi *et al.* [10], a TEM/EDS analysis, Fig.5.21, on the cross-section of the oxide film on 316L under simulated PWR primary conditions. It illustrates the double layer structure oxide film:

- Fig.3.3 (a) clearly shows the difference in crystal size between outer and inner layer: the outer layer has big polyhedral shape particles while the inner layer is actually formed by extreme fine particles.

- Fig.3.3 (b) indicates that the oxide film formed is a spinel oxide: the spot pattern for outer layer (upper figure) and the ring pattern for inner layer (lower figure). They both match spinel pattern, however the different sizes of particles cause the divergence in the pattern.

- Fig.3.3 (d) gives the EDS analysis on a selected zone (indicated in (a), a zoom image in (c)) for estimating the chemical compositions: more chromium-rich oxide formed in the inner layer and the outer layer is mainly iron-rich.

In summary, we consider that the outer oxide layer is iron-rich and discontinuous; the inner layer is continuous and rich in chromium oxide, as depicted in Fig.3.4, which shows a simplified schematic view of the oxide film formed on 316L under simulated PWR primary conditions.

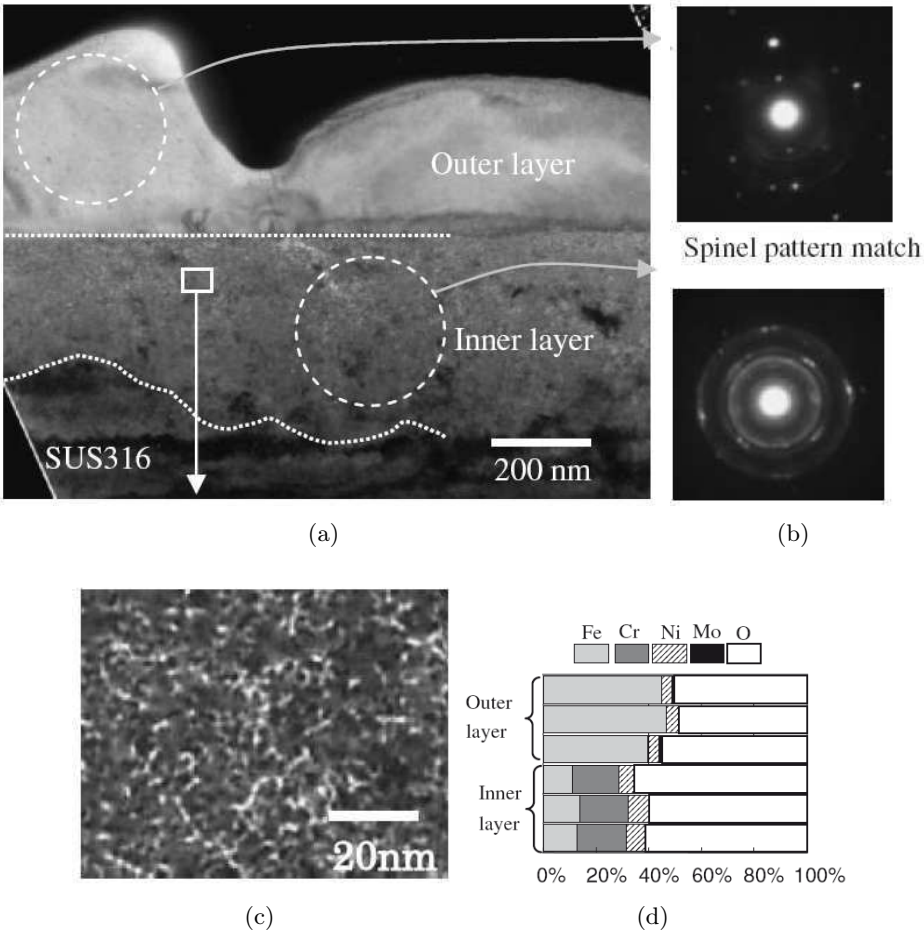

Figure 3.3: TEM and EDS analysis of 316L formed under PWR simulated condition, 320°C, 380 hours : (a) TEM image of both layers; (b) Electron diffraction pattern; (c) A zoom TEM image in inner layer; (d) Estimated chemical composition [10].

.

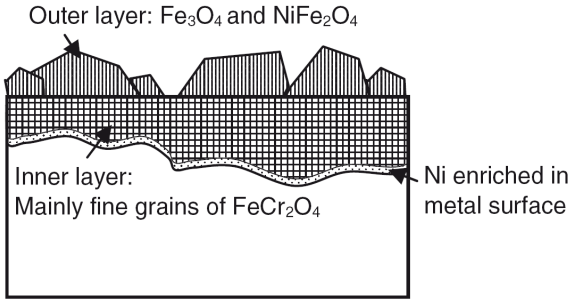

Figure 3.4: Simplified diagrammatic sketch of cross section of the oxide film on 316L austenitic stainless steel under simulated PWR primary water [10].

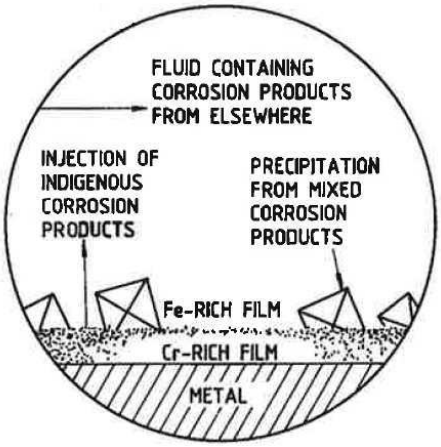

Figure 3.5: Schematic diagram of the mechanism model from Lister *et al.* [2].

3.1.B The Mechanism of Oxide Formation

3.1.B.1 Formation of the Outer Layer

Lister *et al.* [2] have proposed and established a mechanism model of the oxide formation on austenitic stainless steel, as illustrated in Fig.3.5. More precisely, it focused on the outer layer formation. It relates the formation of the oxide layer to the corrosion products release. Among Fe, Ni and Cr, Fe is the easiest cation which can diffuse through the oxide and be released into solution [16]. Therefore, the model proposed by Lister has ruled out the Ni and Cr release under consideration. The release of iron can be divided into three directions:

- release to the water;
- take part in the precipitation/re-deposition process of the iron-rich outer layer;
- diffuse through and be fixed in the chromium-rich oxide at the metal-oxide interface;

According to Lister, the outer layer can not be formed in corrosion product free water. Moreover, once the inner layer of chromium rich layer has been well established, the outer layer may be suppressed [2]. On the contrary, if the water is saturated with corrosion products, the scale of iron and nickel oxide in the outer layer will become important. Evidence has been found for the Nickel alloy 690, the dissolution or iron and nickel from the alloy prevails even at the very beginning stage of corrosion [17]. Similar results for 316L stainless steel are pronounced [18], the presence of the outer layer can be found in a extremely short duration after exposed to the environment.

The re-deposition process of the outer layer has been explained by Berge [19]. It is considered that the growth of magnetite crystallite on the surface is actually from the decomposition of ferrous hydroxide in aqueous solution at high temperature, through the **Schikorr Reaction** Eq.3.1.

$$3Fe(OH)_2 \rightleftarrows Fe_3O_4 + H_2 + 2H_2O \tag{3.1}$$

It formally describes the conversion of the Fe(II) hydroxide into Fe(II, III) oxide, whereas $Fe(OH)_2$ appears to be unstable above 85°C [20]. Though under PWR primary water, the existence of nickel hydroxide have both been found [21–23]. Therefore, through the same type reaction of Schikorr reaction, the spinel oxide nickel ferrite can be formed with magnetite as precipitates on the outer layer during the re-deposition process [24].

3.1.B.2 Formation of the Inner Layer

Recently, with the observation of nickel enrichment in the oxide/metal interface [14, 25], Lozano-Perez *et al.* [25] have explained the oxidation process for the inner layer into three steps:

1. chromium oxide starts to be formed when oxygen diffuses in and iron diffuses out while nickel stays static, the growth of inner and outer oxide layer inward and outward, respectively;
2. chromium oxide grows and pushes away nickel when the atomic concentration of oxygen reaches above 20%, and result in accumulation of nickel at the oxide/metal interface;

3. when the atomic concentration of oxygen is about 30%, nearly no nickel remains in the oxide while chromium oxide keeps growing.

It implies the oxidation of the inner layer is initially incomplete until it pushes aways all the nickel from the inner oxide and then forms a *real* chromium oxide.

In addition, Perrin *et al.* [26] have explained the growth of the inner oxide layer is due to oxygen diffusion along the grain boundary of the oxide.

In conclusion, the formation of the oxide layers can be divided into two parts: the re-deposition process of the iron oxide for the outer layer; and oxidation process of the chromium for the inner layer. The diffusion of oxygen along the grain boundaries of the oxides may play a significant role in the kinetics of the process. It may be emphasised that this mechanism is mainly observed in high temperature oxidation. It is completely different from the formation of the oxide layer on stainless steel at room temperature which is well described by the Point Defect Model.

3.1.B.3 Point Defect Model

The **Point Defect Model** (PDM) was proposed and has been well developed by Macdonald [27, 28]. It recognizes both the growth of the barrier oxide layer into the metal via the generation of oxygen vacancies at the metal/film interface and the dissolution of the barrier layer at the film/solution interface.

As verbalised in Fig.3.6(a), the PDM model bases on bilayer passive film formed on the metal surfaces, which is highly disordered. The outer porous precipitated film may incorporate with anions and/or cations in the solution. Between the inner passive film and substrate alloy, the transmission of ions is also possible, and may even pass through the barrier layer. Simple cation vacancies are produced at the film/solution interface, then are consumed at the metal/film interface. Anion vacancies are formed at the metal/film interface and consumed at the film/solution interface.

Further explanation of PDM has been delineated in Fig.3.6(b), it separates the process into three cases:

- The cation vacancy can be produced via Mott-Schottky pair reaction and may also be autocatalytic generated. If the annihilation reaction is not capable of consuming all the cation vacancies arriving at the metal/film interface, they will condense and eventually lead to the local detachment of the film.

- The regeneration of isolated oxygen vacancies may be caused by the submergence of cation vacancies into film. Besides, the anion-catalysed generation of cation vacancies at the film/solution interface can also penetrate into the film. As a result, vacancy condensation occurs at the metal/film interface.

- The oxygen and cation vacancies may remain on the surface and finally coalesce to destroy the lattice at the film/solution interface.

Combining these processes, a layout of different stages of pit nucleation is represented in Fig.3.6(c). At steady-state, a balance is established between the film formation at the metal/film interface and

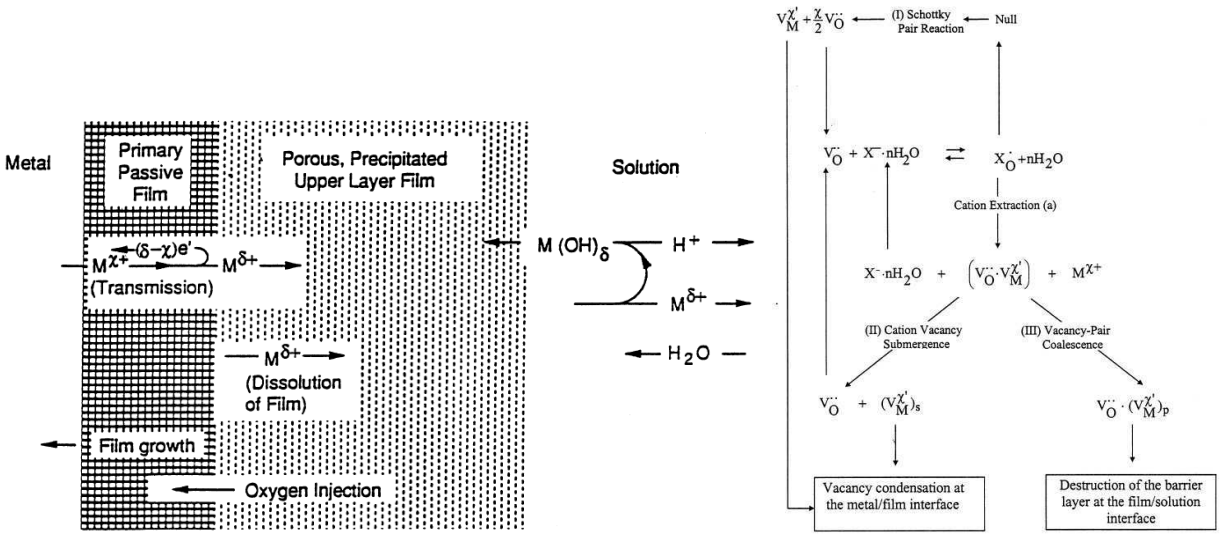

(a) (b)

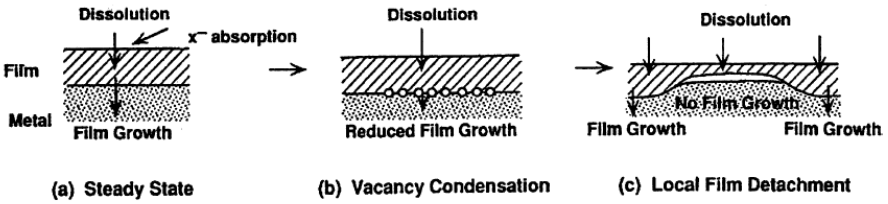

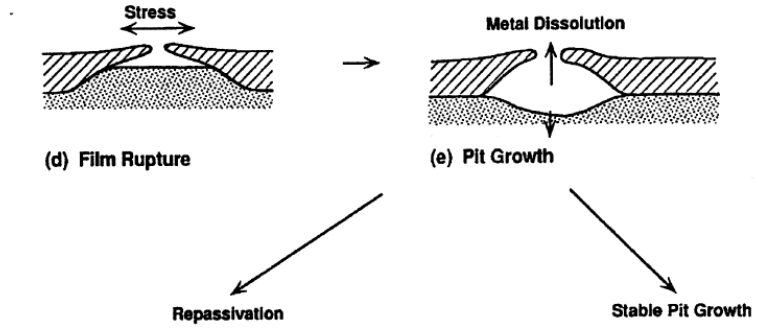

(c)

Figure 3.6: Schematic sketch of **Point Defect Model**: (a) process of bilayer passive film formation on the metal surfaces; (b) proposed reactions leading to cation vacancy condensation at the metal/film, film/solution interfaces and eventually the passivity breakdown; (c) cartoon outlining various stages of pit nucleation according the PDM [27].

the dissolution at the film/solution interface. With the condensation of vacancies, the film will gradually detached locally from the metal. When the film ruptures, more metal dissolves into solution. Afterwards, the competition occurs between the re-passivation and stable pit growth.

A recent study of Macdonald [29] has demonstrated that the potential drop across the metal/film interface decreases linearly with increasing film thickness. And this potential drop is actually responsible for the oxygen vacancy formation reaction. In other words, the thinner the film, the easier oxygen vacancy formation occurs. However, this conclusion is dragged out when the oxygen vacancies are the dominant defect within the film.

In conclusion, the PDM describes metal/film/solution system under a steady state. Point defects like oxygen, cation, anion vacancies and interstitial cations can be generated, transported and consumed under the influence of concentration and potential gradient in the oxide and its boundaries with metal and solution.

3.1.B.4 Corrosion Kinetics

The thickness of the oxide layer and average crystallite size increase with exposure time to the primary PWR water environment [4].

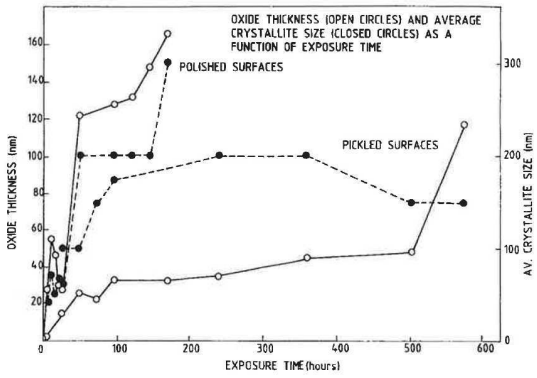

Figure 3.7: Oxide thickness (○) and average crystallite size (●) as a function of exposure time: upper zone polished surface; lower zone pickled zone [4].

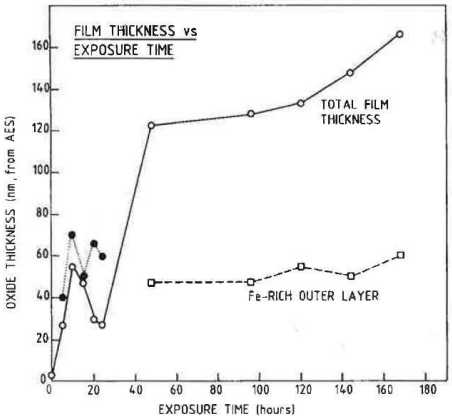

Figure 3.8: Oxide thickness versus exposure time (polished surface), crystallite size has been taken into account after 24 hours in same scales for thickness [4].

Fig.3.7 & Fig.3.8 show the increase of thickness and average crystallite size of 304 with exposure time under high temperature coolant. Due to the similarity of composition between 304 and 316, the conclusion obtained on 304 can also be adapted to 316L. In the first 10 hours, the initial nucleation and growth of both outer and inner layers take place very rapidly. As a result, both thickness and crystallites size increase sharply and reach a first maximum. Between 10 to 24 hours, the dissolution and the growth of the outer oxide film compete with each other, thus the curve somewhat decreases. From 24 to 48 hours, the thickness and crystallite sizes increase sharply again. Afterwards, the increase of nucleation and growth of the oxide film is stabilised. At this time, the overall growth of the oxide can be considered as a dynamic balance between precipitation and dissolution.

Tapping *et al.* [4] have estimated an expression for the corrosion rate, Eq.3.2 where d is the

equivalent thickness of the oxide, k_p is the appropriate rate constant, t is the duration of exposure and $n = 0.53$:

$$d = k_p t^n \tag{3.2}$$

Since the value of n was close to 0.5, Tapping *et al.* [4] considered that the growth kinetic of the oxide film has a parabolic character. Thereby, Terachi *et al.* [10] have used the parabolic equation, as written in Eq.3.3, in which d and t have the same definitions, whilst k_p is the parabolic rate constant.

$$d^2 = 2k_p t \tag{3.3}$$

Indeed, this equation corresponds to a growth mechanism with a rate limited by diffusion. The formation of the outer layer is considered as a re-deposition process of iron, nickel and chromium dissolved in solution due to general corrosion of stainless steels. It grows with outward diffusion of metal. Reversely, the inner layer is a protective, mostly chromium oxide, formed spontaneously on the metal surface. It grows with inward diffusion of oxygen.

3.1.C The Electronic Properties of Oxide Film

The oxide film formed on the austenitic stainless steel is often regarded as semiconductor under primary PWR conditions.. Many studies have been done in this domain and hence the electronic properties have been well described [3, 7, 13, 30–32].

The characterisation of electronic properties, also called semiconducting properties, can be interpreted by capacitance measurements (Mott-Schottky approach) and photoelectrochemical measurements [30].

3.1.C.1 Capacitance mesurements (Mott-Schottky approach)

The capacitance behaviour of a passive film-electrolyte interface is similar to the one of a semiconductor-electrolyte interface, and the semiconductor-electrolyte interface is equivalent to that of a semiconductor-metal Schottky junction. The effect of the applied electrochemical potential **U** on capacitance value is described by the **Mott-Schottky** equation [33]:

$$\frac{1}{C^2} = \frac{1}{C_H^2} + \frac{1}{C_{SC}^2} = \frac{2}{\varepsilon\varepsilon_0 q N_q}\left(U - U_{FB} - \frac{kT}{q}\right) \tag{3.4}$$

The measured capacitance includes two parts: C_{SC}, space charge capacitance, is related to the applied potential (**U**) through the classical Mott-Schottky equation; the other is C_H, the contribution of the Helmholtz layer capacitance, which can not be neglected if the passive film is considered as heavily doped. In Eq.3.4, N_q is the density for donor and acceptor, ε the dielectric constant of the passive film, ε_0 the vacuum permitivity, q the elementary charge (-e for electrons and +e for holes), k the Boltzmann constant, T the absolute temperature and U_{FB} the flat band potential. From the slope and the intercept given by the plot between C^{-2} and U, the doping density and the flat band can both be determined, respectively. Furthermore, the characteristics of the semiconductor can also be obtained.

Noting that for the study of electronic properties, **U** is usually used as the applied potential while in most corrosion studies, **E** is always regarded as the corrosion potential.

3.1.C.2 Photoelectrochemical measurements

The photoelectrochemical behaviour of the oxide film is examined by determining the photocurrent, generated under illumination, as a function of the incident light energy [7, 13]. The Gärtner model [34] is the most used calculation together with some simplifications [35], such as neglecting the contribution to the photocurrent of the hole-electron pair formed in the bulk region. Therefore, the quantum efficiency η, the ratio between the photocurrent (I_{ph}) and the incident photon flux Φ_0 can be expressed by the Eq.3.5:

$$\eta = \frac{I_{ph}}{\Phi_0} = qAw\frac{(h\nu - E_g)^n}{h\nu} \tag{3.5}$$

where A is a constant, q the elementary charge, w the space charge layer thickness, E_g the band gap energy and $h\nu$ the photon energy. The value of n depends on the type of transition between the valence band and the conduction band. It is actually corresponds to indirect transitions in crystallised solids and to non-direct transitions in amorphous materials. In the case of passive films, the value of n is linked to indirect transitions in crystalline band structure model, and the most appropriate value is equal to 2 obtained by the analysis of the photocurrent spectra.

It has been pointed out that the photocurrent spectra depends on the oxidation time [36]. The increase oxidation duration can cause a higher disordered structure of the oxide and results in a decrease of photocurrent.

3.1.C.3 The Electronic Structures

Fig.3.9 shows the basic electronic properties of the oxide film formed on 316L in a high temperature environment, (a) is for the capacitance measurement and (b) is for the photoelectrochemical behaviour, they describe:

- Fig.3.9(a): The positive slope in the region above -0.5 V indicates n-type semiconductiong properties; otherwise, the negative slope in the region below this potential meaning p-type semiconducting properties. Linking the two types of spinel oxide to the electronic properties, it has been demonstrated by Hakiki *et al.* [12] that the inner Cr-rich layer is p-type and outer Fe-rich layer on the other hand is n-type. They have well described the capacitance behaviour:

  1. the oxide film can take up ions and electrons from the metallic substrate, and cause a space charge region raised up at the metal/oxide film interface;
  2. the oxide film can produce a second space charge region on contact with the electrolyte.

  Therefore, this electronic structure is often regarded as a classical heterojunction [33]. The existence of both positive and negative slopes in the capacitance plot demonstrates the double structure of the oxide film formed on the 316L stainless steel. At about 0 V, another change can be noticed, which is considered as an important feature of the Mott-Schottky plot. It implies the

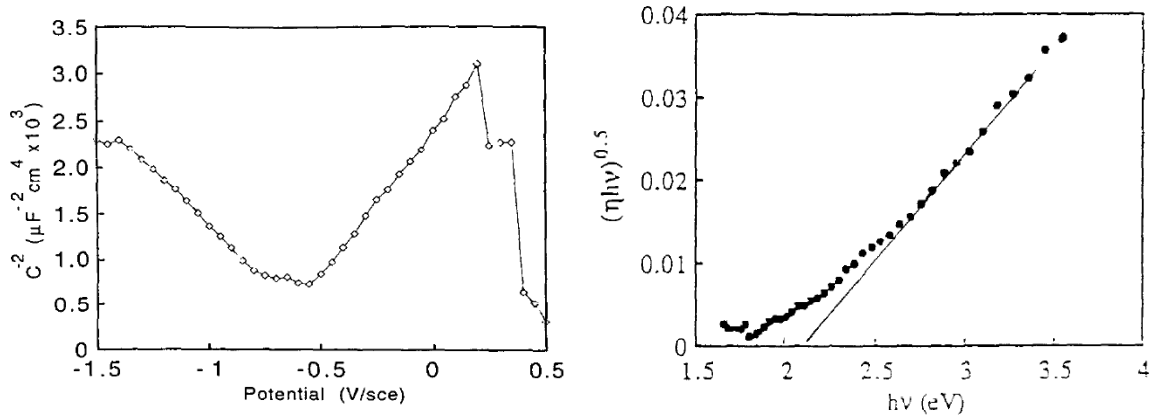

(a) (b)

Figure 3.9: Electronic characteristic of the oxide film formed on 316L austenitic stainless steel after 2000 hours exposure at 350°C under a simulated primary PWR environment : (a) Plot of $1/C^2$ (Mott Schottky plot) as a function of applied potential U, at 1580 Hz; (b) Plot of $(\eta h\nu)^{0.5}$ versus the incident light energy $h\nu$ [7].

.

existence of a second donor level for the n-type, formed by Fe^{2+} ions placed in the octahedral sites of the unit cell of the spinel oxide.

- Fig.3.9(b): The band gap energy obtained from the intercept of the straight line with the photon energy axis, which is about 2.3 eV for the passive film at room temperature, 2 eV for the thick passive film formed at high temperature. This slight difference here may mostly due to the higher iron oxide content [7]. The best fit for the band gap energy is a Fe-Cr oxide, $FeCr_2O_4$, however its theoretical value is actually 3.0 eV [37]. It is explained that the decrease may due to the presence of Fe(II) in the $FeCr_2O_4$ [38].

Furthermore, the n-type Fe-rich oxide and the p-type Cr-rich oxide are represented as inverse and normal spinel oxides, respectively. They are not immiscible, thus a significant difference can be noticed between inner and outer layer [5].

Based on the thesis study of Marchetti-Sillans [24], it was demonstrated that Cr_2O_3 and $Ni_{1-x}Fe_xCr_2O_4$ formed under primary PWR conditions are n-type semiconductors.

As mentioned, the electronic structure of oxide film can be regarded as a p-n heterojunction. It is composed of a p-type Cr-rich oxide at the metal/film interface and a n-type Fe-rich oxide at the oxide/electrolyte interface. Fig.3.10 represents this electronic structure in two cases, one is for applied **U** less than flat band potential, the other is the inverse case:

- $\mathbf{U} < \mathbf{U}_{FB}$: Inner chromium rich layer is served as Schottky barrier showing the p-type semiconductivity, which means the inner layer is in a dominant position while outer iron rich layer is in a condition of accumulation ohmic contact;

- $\mathbf{U} > \mathbf{U}_{FB}$: Outer iron rich layer take the dominant, thus the oxide act as the n-type semiconductor whilst inner layer is in the condition of accumulation ohmic contact.

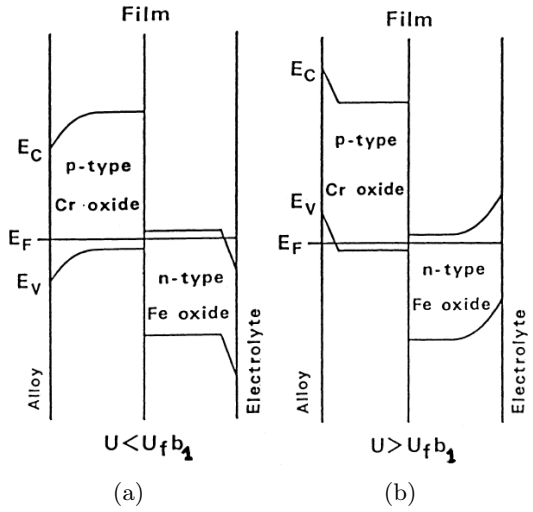

Figure 3.10: Schematic sketch of the electronic structure model of oxide film formed on 316L: (a) U $<$ U_{FB} (≈ -0.5 V); (b) U $>$ U_{FB} (≈ -0.5 V) [13].

3.1.C.4 Difference between Thick and Thin Passive Films

Considering the semiconducting properties of oxide film, one often distinguishes either the passive film as thick or thin, even though they show very similar electrochemical behaviours, as portrayed in Fig.3.11. For the same alloy, the passive oxide film is thicker when it is formed at high temperature than at room temperature under the same environment. In general, chromium oxide is often referred as the passive film for stainless steel.

One explanation for the difference between these passive oxide film is linked to their carrier concentration, or doping density, in which thin passive film formed at room temperature is much higher than the thicker one formed at higher temperature like in primary PWR conditions [13].

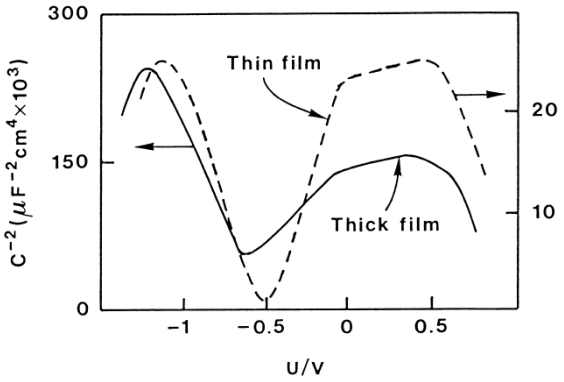

Figure 3.11: Plot of $1/C^2$ as a function of applied potential U on stainless steel: an thick passive film formed at high temperature in aqueous environment; a thin passive film formed at 0.6 V/SCE in borate buffer solution at room temperature [13].

Another explanation [31] relates this difference to the iron ions transport process through the inner chromium layer from the alloy. For oxide film, both Fe^{2+} can transport over tetrahedral and octahedral sites in the inner spinel oxide. However, when Cr content is high, which is the case for thin

passive film, chromium will certainly occupy most of the sites in the spinel and leave the transport of iron only through the grain boundaries. Nevertheless, the oxygen transport is always favoured by both passive films.

In addition, the transport of iron ions also links with the conductivity in the inner layer. The hopping conduction in the octahedral sites caused by Fe^{2+} may turning back the normal band conduction with a high content Cr in the spinel. These may explain the slight difference in semiconducting behaviours between the thick and thin passive films.

Briefly, studying the electronic structure is a good way to get a better understanding of the oxide film formed on the alloy. In our case, the oxide film formed on austenitic stainless steel 316L under primary PWR conditions reveals semiconducting properties, reflected as a p-n heterojunction.

3.1.D Influence of Different Parameters on The Oxide

Many parameters can influence the oxide film formed on 316L under PWR primary conditions. Some of them have direct effect on the oxide film, others may affect the electrochemical behaviour formerly and then influence the oxide film afterwards.

However, the basic double layer structure, the main composition and the basic electronic structure for both inner and outer layer will not change tremendously.

3.1.D.1 Influence of Boron and Lithium

The presence of boron and lithium in the primary PWR water are well-known for their role in neutron capture and adjusting pH, respectively. Concerning the oxide film formed on the 316, their influences are not so noticeable.

Boron The presence of boron dose not affect the oxide formed on stainless steel such as 316L [39]. As shown in Fig.3.12 [10], the oxide structure were considered as the same for both [B]=500 ppm and [B]=2300 ppm, which can lead to a different pH for both cases. Nevertheless, a NanoSIMS analysis [40] has otherwise demonstrated the boron tends to accumulate in the Cr-rich oxide, next to the interface of inner and outer layer. The absence of boron traces in other analysis [25] may be explained by the preparation process which can somewhat influence the outer part of oxide layer. Indeed, their extremely low concentration in the oxide film may also be another explanation.

Lithium The presence of lithium atoms on the oxide of stainless steel on the other hand has been proven by using the technique of Atom-Probe Tomography (APT) [25]. In Fig.3.13, the rose points represent the lithium atom detected by APT: they can be traced throughout the oxide to the oxide-metal interface. The presence of Li atom can be correlated to the CrO_2, as demonstrated in Fig.3.13 (d), nevertheless the concentration of Li was quite low, 200ppm. It was considered that Li atoms incorporate into the Cr-rich oxide and it may be explained by the changes in oxide conductivity when varying the Li content in the water [41].

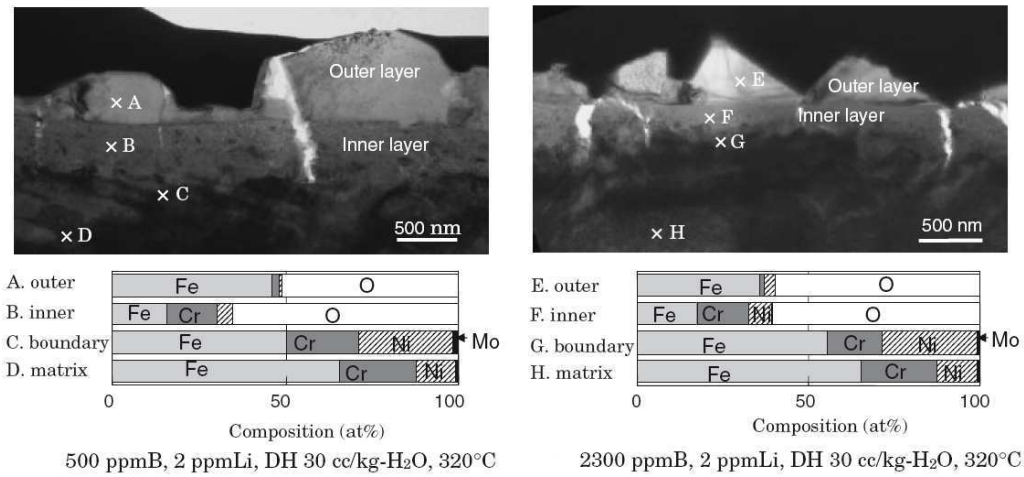

Figure 3.12: TEM images and EDS analysis on oxide film formed on 316 stainless steel under primary PWR water with 2 ppm Lithium and 30 cc/kg dissolved hydrogen at 320°C: [B] = 500 ppm (left) and [B] = 2300 ppm (right), [10].

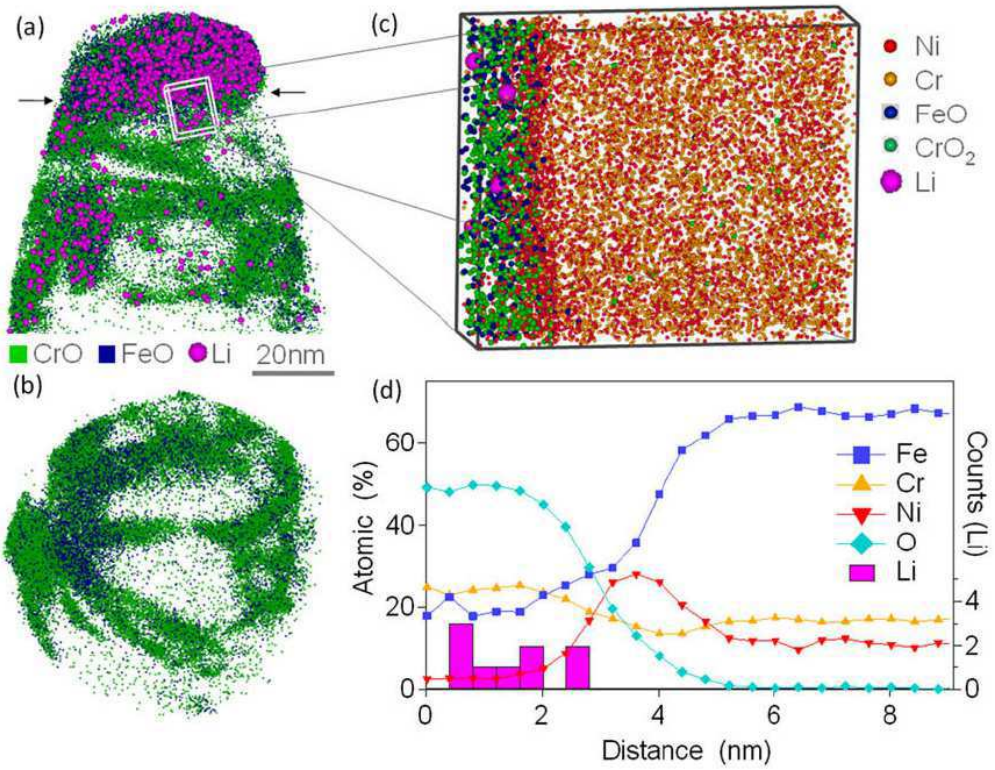

Figure 3.13: APT reconstruction demonstrating "atom by atom" on oxide formed on stainless steel 316L under primary PWR condition: (a) the cap and sub-interface oxides; (b) top-view of sub-interface region removing the cap oxide; (c) sub-volume showing the detected species taken form the cap-oxide-metal interface, square region in figure(a); (d) concentration profile across the oxide-metal interface using Proxigram analysis [25].

3.1.D.2 Influence of pH

Recent studies [42, 43] were performed on the oxide film formed on the nickel-based alloy and the stainless steel 304 at high temperature in aqueous solution and borated and lithiated water, respectively. For the stainless steel under primary PWR water, they show that in the safe E-pH zone ($pH_{300°C}$ between 7.7 and 9.1), the density and the size of crystallite (Fe-rich oxide) decrease with the increasing pH while the composition of the inner protective layer (Cr-rich oxide) is nearly not affected.

However, the influence of pH cannot be simply dragged out, because it depends on other parameters, such as temperature, the aqueous chemistry, etc.

According to Montemor *et al.*, chromium decreases in the oxide film formed on 316L and nickel based alloy in high temperature aqueous environment, from pH 8 to 10 [13]. They say that the pH effect does not change the double layer structure of oxide film. However, the composition may be somewhat affected. Iron content in the oxide film seems to increase with the increasing pH. Consequently, the chromium concentration decreased in the oxide film leads the oxide film less protective. The same conclusion was made for alkaline media at room temperature, in which pH varies from 9 to 13 [44].

Carmezim *et al.* [45] have studied the electrochemistry, the composition and the semiconducting properties of the passive film on austenitic stainless steel 304 at room temperature under different environments contain NaOH, KOH and H_2SO_4 separately in order to achieve different pH, 4.5, 8 and 0.6. They demonstrate that:

- Corrosion potential (E_{corr}) becomes more anodic as pH decreases. Corrosion current depends on pH slightly and it increases with the decreasing pH.
- Chromium oxide strongly depends on the acidic condition, the content of Cr(III) oxide in the oxide film decrease dramatically with the increasing pH, revealing that an enrichment of chromium oxide in a more acid environment. Subsequently, iron oxide enriches when the solution is less acid. In other words, the ratio of Cr/Fe increase significantly with the decreasing of pH, at pH = 0.6, the film is nearly all chromium oxide.
- The capacitance behaviours are different at pH= 4.5 and 8, and the difference is mainly related by the donor density, N_D, it augments with the pH. Therefore, the film is enriched in iron oxide with the increasing pH while the chromium oxide gradually decreases, which is in accordance with the composition study. Nevertheless, pH at 0.6 seems to be too acid to perform a capacitance measurement.

In brief, the influence of pH can be based on the different temperatures and various environments.

3.1.D.3 Influence of surface state

Surface state is an important parameter which can affect the oxide film, more precisely, the substructure under the oxide film. The presence of a recrystallised area under oxide layer has been reported [46]. The surface state, either polished or ground can influence this recrystallised area.

The metal under the oxide layer is recrystallised in a fine elongated nano-grains structure, as pictured in Fig.3.14. The study was done for 304L, but it can also be adapted to our case, 316L. When the surface is rough, the recrystallised area is larger and the oxide layer is relatively thinner.

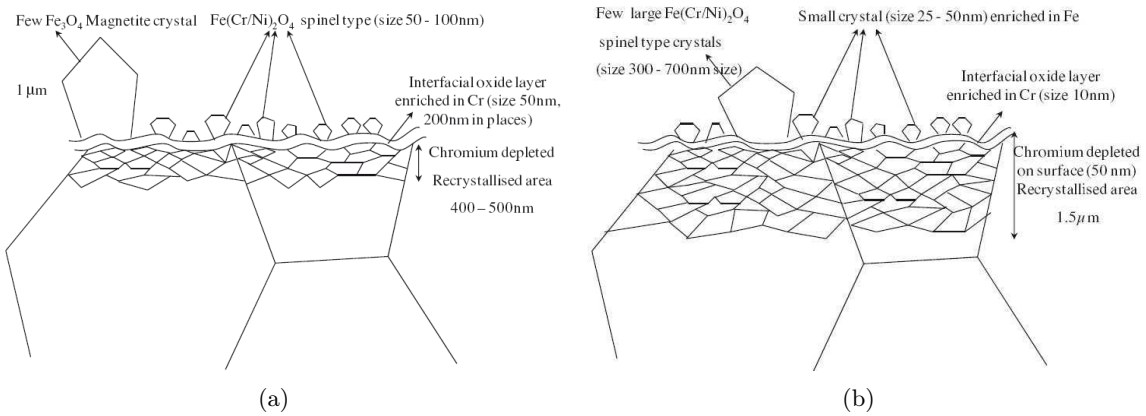

Figure 3.14: Diagrammatic sketch of the oxide formed on a 304L sample under simulated PWR primary water at 340°C for 500 hours: (a) polished surface; (b) ground surface [46].

.

As already shown by Tapping *et al.* in Fig.3.7 [4], the thickness of oxide layer is much higher for polished samples than pickled ones at same exposure time.

3.1.D.4 Influence of Chromium Content

The chromium content in stainless steel causes several related consequences:

- the size of crystal formed on the outer layer;
- the thickness of oxide film;
- the chromium content in the protective oxide scale;
- the corrosion rate.

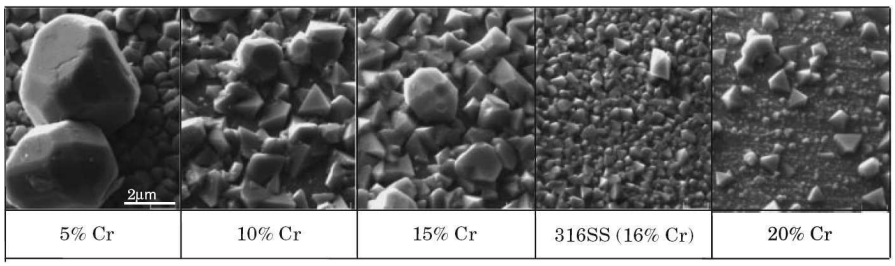

Figure 3.15: SEM images of oxide film after immersion in the primary PWR water at 320°C for 380 hours [10].

Fig.3.15 demonstrates that bigger size of crystal for lower content of chromium. At 5% of Cr, the big crystals may have 4 to 5 μm, and for 316L which has nearly 16% of Cr, the crystal sizes seem to be less than 1 μm. Fig.3.16 shows the relationship between the total oxide film thickness and Cr content which appears to be linear decrease. Other than the morphology and thickness, Fig.3.17 shows that the structure of the spinel oxide may also be affected by chromium content. The peaks shift gradually from Fe_3O_4 to $FeCr_2O_4$ with the increase of Cr% in the alloy.

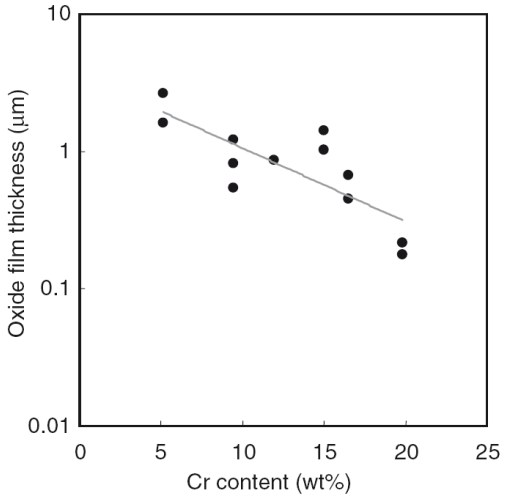

Figure 3.16: Oxide film thickness as a function of Cr content: formed under primary PWR water at 320°C for 380 hours [10].

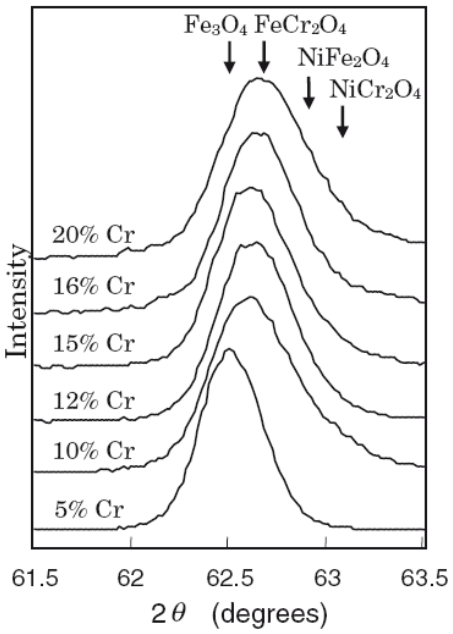

Figure 3.17: XRD analysis of 316L formed under PWR simulated conditions, 320°C, 380 hours: diffraction peaks of the spinel structure for different Cr% content alloy [10].

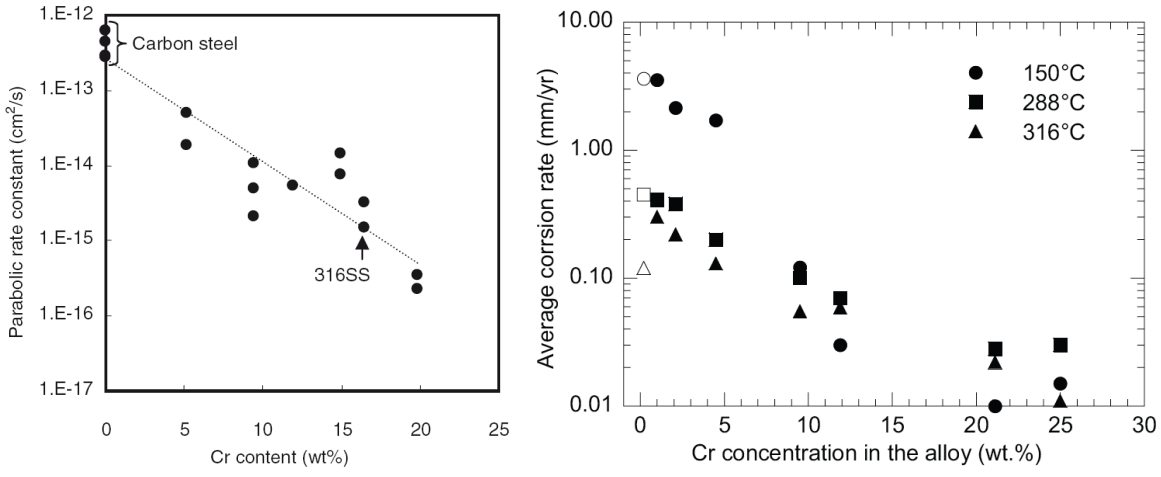

Figure 3.18: The effect of chromium content on the corrosion rate : (a) the parabolic rate constant as a function of Cr% in the alloy under simulated PWR primary condition at 320°C for 380 hours [10]; (b) average corrosion rate of steels as a function of Cr%, in boric acid solution at different temperatures [39].

.

Fig.3.18 (a) & (b) on the other hand give the proof that average corrosion rate decreases with chromium content in the alloy [10, 39]. (a) demonstrates the relationship between Cr% and k_p, which is the parabolic constant in the Eq.3.3. (b) shows directly the corrosion rate of various steels at different temperatures all decrease with chromium content in the alloy. In other words, more chromium in the alloy results in a lower global corrosion rate.

Briefly, the increase of Cr content in the alloy leads to a decrease of oxide film thickness. And the chromium content of the protective oxide scale increased with chromium content in the alloy [10]. Furthermore, the inner chromium-rich layer may not be a continuous and compact structure when Cr% in the alloy is lower than 10% [47]. In summary, the increase of Cr content in the alloy mitigate the corrosion rate. Therefore, in the aspect of corrosion, it is a beneficial effect.

3.1.D.5 Influence of Temperature

Temperature is always an important parameter which has a strong effect on the oxide formed. With increasing temperature, the double structure of the oxide film is not affected while the thickness will increase sharply.

Secondly, temperature influences the open circuit potential. With an increase of temperature, the open circuit potential may shift either to a more negative or more positive value until it reaches a steady state, respectively. It has been shown that in lithiated water containing H_2, the open circuit potential goes down [3] while it goes up in a borate buffer solution [31].

Fig.3.19 (a) & (b) illustrates the temperature influence on semiconducting properties [3, 31], (a) is for capacitance measurements and (b) is for photoelectrochemical results.

Temperature (°C)	ambient	50	150	250	350	450
N_D (10^{20} cm^{-3})	2.5	2.6	1.5	0.9	0.5	0.3
N_A (10^{20} cm^{-3})		2.8	2.7	2.3	2.3	2.2

Table 3.3: Donor and Acceptor densities (N_D & N_A) of oxide film formed on 304 stainless steel at different temperature, using the dielectric constant $\varepsilon = 12$ for the calculation [3, 31].

In Fig.3.19(a), it can be noticed that:

- The electronic structure for the oxide film formed on austenitic stainless steel does not changed with the increasing temperature: inner layer, chromium rich oxide, with a p-type semiconductivity; outer layer, iron rich oxide, n-type semiconductor. It is still a classical p-n heterojunction, the flat band energy stays at -0.5 V.
- According to the plot and Eq.3.4, estimation of donor and acceptor densities can be done, as exhibited in Tab.3.3. The donor density, N_D, depends on the temperature during the oxide formation, whereas the acceptor density appears to be indifferent. Note that the N_D for passive film is actually close to the one for oxide film formed at 50°C.
- Due to the decrease of N_D, the transport of Fe^{2+} seems to be less important through the oxide film and result in an increase of Fe^{3+} content in the film. In another word, the ratio of Fe^{3+}/Fe^{2+} increases with the temperature of oxide formation.

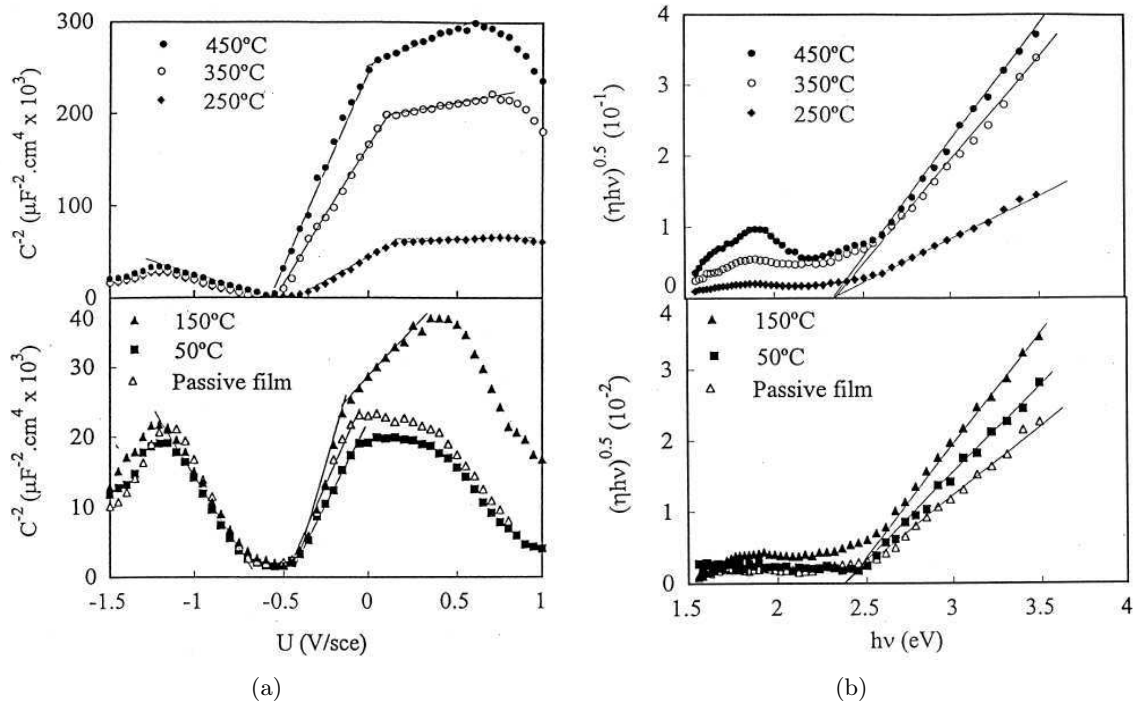

(a) (b)

Figure 3.19: The effect of temperature on electrochemical behaviour of oxide formed 304 stainless steel in the temperature range from 50 to 450°C, with the presence of passive film formed at 0.8 V/SCE in borate buffer solution : (a) plot of $1/C^2$ as a function of applied potential U; (b) plot of $(\eta h\nu)^{0.5}$ versus the incident light energy $h\nu$ [31].

- The break at 0 V remains with the increasing temperature, it is considered as a second donor level formed by Fe^{2+} ions placed in the octahedral sites in the spinel as mentioned previously. The oxide film can be thought as a semiconductor electrode containing multiple donor level in the bandgap. The changes in the slopes from 150°C to higher temperature, imply that a decrease of the concentration of Fe^{2+}_{oct} in the oxide film, especially between 150 to 250°C.

- The thickness of space charge layer, W, can also be estimated by the expression:

$$C = \varepsilon\varepsilon_0/W$$

  where the definition for C, ε, ε_0 are the same as in Eqs.3.4 & 3.5. It has been concluded that the space charge layer in the outer region is closely related to the thickness of iron oxide, meaning the outer oxide layer. Meanwhile, the space charge layer is independent of either the thickness and the temperature. It seems that the inner thickness is not relevant with the temperature of oxide formation.

The quantum efficiency (η) increases with the temperature during the oxide formation, shown in the Fig.3.19(b). As expressed in Eq.3.5, no wonder it augments with the increase of space charge layer, W, and it is the case when temperature rises. The band gap energy is the same for all the temperatures, 2.3 eV, which is also the same value for thin passive film. However, a peak become more significant at about 1.9 eV with the increasing temperature which is associated with transitions

from the valence band to the second donor level in the bandgap. Together with the capacitance results, the second donor level is formed by Fe^{2+} place in the octahedral sites in unit cell of the spinel oxide. The intenser peaks imply that the content of Fe^{2+}_{oct} in the oxide film decreases with the increasing temperature. It is in agreement with the capacitance measurements.

The explanation for the increase of quantum efficiency (η) is related to the donor density. The decrease of donor density with temperature also decrease the film defects, and subsequently decrease the electron-hole recombination processes. Therefore, the quantum efficiency (η) become more significant at higher temperature.

3.1.D.6 Influence of Dissolved Hydrogen

The dissolved hydrogen plays an important role on the oxide formation under PWR conditions. In general, it can be distinguished into two parts: the oxide film itself and the electrochemical behaviours of 316L .

The structure and composition of oxide film is not affected by the dissolved hydrogen in the solution, nevertheless the thickness and the corrosion rate of oxide layer appear to increase with dissolved hydrogen [10].

Cation diffusion in the oxide needs to be brought into consideration. According to Dieckmann [48, 49], cation vacancies and cation interstitials are the majority defects at high and low oxygen activities, respectively. The oxygen activity dependence of the tracer diffusion coefficient in magnetite-based spinels can be written as Eq.3.6.

$$D^*_{Me} = D^0_{Me(v)} P_{O_2}^{2/3} + D^0_{Me(I)} P_{O_2}^{-2/3} \tag{3.6}$$

Based on this diffusion equation, V-shaped curves can be obtained in D^*_{Me}. Fig.3.20 illustrates the diffusion rate of Fe at 320°C. And as concluded by Dieckmann, the diffusion of Cr and Fe are governed by cation vacancies at high oxygen activities; otherwise, they are governed by cation interstitials at low oxygen activities. However, in the same conditions, the diffusion of Fe is much more significant than that of Cr.

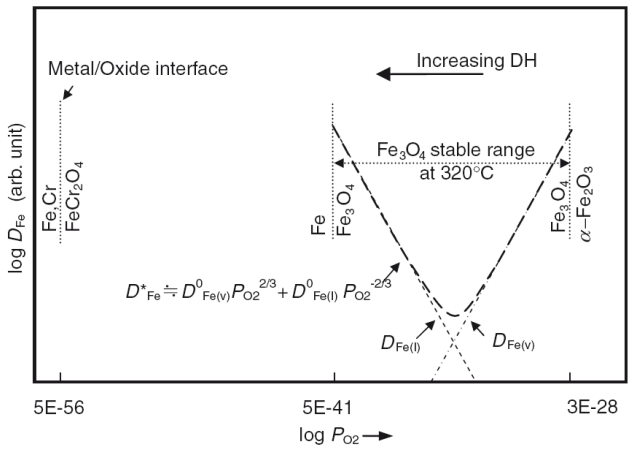

Figure 3.20: Diffusion rate of Fe in spinel oxide versus oxygen partial pressure, calculated for metal/oxide and oxide/oxide interfaces at 320°C [10].

As explained, when the partial pressure is relatively low, $D_{Fe(I)}$ takeover the dominant position for iron cation diffusion in the spinel which is actually enhanced by the increasing dissolved hydrogen. Therefore, the corrosion rate increased by dissolved hydrogen might be caused by this augmented interstitial iron diffusion in the spinel.

From the point view of electrochemical behaviour, there is no direct study the effect of dissolved hydrogen on stainless steel. By comparing with the low-alloy steel [50], and the Alloy 600 [51], several points should be noticed:

- With the increase of dissolved hydrogen, the corrosion potential, E_{corr} becomes more negative;
- With the increase of dissolved hydrogen, cathodic process can be promoted and result in a higher critical and passive current. Therefore, the protective performance of the oxide film can drop dramatically;
- With the increase of dissolved hydrogen, ion diffusion is much easier and the iron release rate may increased as a consequence, and the corrosion may be accelerated subsequently;
- With the increase of dissolved hydrogen at high temperature, more H_2 diffuses through the porous outer layer and comes into the inner protective layer. The more it reacts with, the less stable the oxide film will be. The decrease of stability of oxide film may also enhance the corrosion rate.

3.1.D.7 Influence of other parameters

Other parameters than those detailed before (boron, lithium, pH, dissolved hydrogen, etc.), have influence on the oxide film formed on 316L under primary PWR conditions, such as the dissolve oxygen, Mo, Zn, etc.

Dissolved Oxygen With the increase of dissolved oxygen in high temperature water, spinel oxide seems to be less stable. Furthermore, Cr content in the oxide film is certainly decreased with the increasing dissolved oxygen and the inner layer become less protective due to this Cr dissolution subsequently [52].

Mo For austenitic stainless steel 316L, the content of Mo in the substrate alloy is about $2 \sim 3\%$. Mo is beneficial to promote the corrosion resistance in chloride environments. The presence of Mo brings an enrichment of chromium oxide in the film between 250°C and 450°C [53]. Metallic Mo is also in the oxide/ film interface: it can act as a diffusion barrier for Fe and Cr ions in the oxide [54]. Moreover, Mo affects the oxide capacitance. With the presence of MoO_4^{2-} in the outer layer even in very low concentration, the number of donors in the iron oxide decrease and hence the conductivity. Besides, it ameliorates the defect structure cause by Fe^{2+} of the inner chromium oxide layer [53, 55]. Overall, Mo is a positive effect to against corrosion in chloride environments.

Zn Zn is introduced in the primary PWR water. It has been proved that Zn has a positive effect on the release of cations in the primary medium. It can both incorporate in the inner layer and

probably form a new Zn-rich phase in the outer region. The thickness of the oxide film decrease dramatically with the presence of Zn. Due to the Zn hydrolysis reaction, pH can be changed, and results in an important decrease of iron transport in the inner layer. Briefly, Zn is a beneficial element to decrease uniform corrosion and thus to decrease the contaminations of primary circuits by corrosion products [56].

Under primary PWR conditions, more impurities can be found, like chloride, sulphate, radiolytic products which are quite aggressive even though the concentrations are relatively low, few ppb, in order to avoid corrosion risks. With no doubt, the existence of chloride and sulphate can accelerate the corrosion process and in favour of the non-protective rust formation on the outer region [57]. The presence of the radiolytic products, such as hydrogen peroxide, only makes the corrosion issues more seriously, enhances the probabilities of pitting and cracking corrosion [58].

In summary, the oxide of 316L formed under primary PWR water is a double oxide, chromium rich, continuous inner layer and an outer layer is iron rich and porous. It can be regarded as a semiconductor with a classic p-n heterojunction electronic structure. The oxide is sensitive to various parameters during the oxidation process, like temperature, stress, pH, redox and so on.

The oxide film formed on 316L well resists the corrosion, and it is actually the case without considering irradiation. However, in presence of irradiation, this situation can be modified, which will be explained in the following section.

3.2 Stress Corrosion Cracking (SCC)

What is stress corrosion cracking? It is the interaction between corrosion and mechanical stress, and it may produce failures by cracking. This type of failure is called **Stress Corrosion Cracking**, SCC. It has been studied for decades, many processes have been made in order to get a better understanding of this failure. However, the mechanisms of SCC are still under discussion.

Why is SCC so important? SCC is an insidious and tricky corrosion. It can bring a markable loss of mechanical strength with little metal loss. In consequence, the damage of SCC is not evident from inspection, but it can trigger mechanical fast fracture and catastrophic failure of components and structures. However, the occurrence of SCC acquires at least several parameters simultaneously: a susceptible material, an environment which can cause SCC for this material and a sufficient tensile stress to induce SCC.

There exists several basic models for the mechanism of SCC, for example:

- **Active Path Dissolution:** The probability of the accelerated corrosion is higher along a path than the bulk material which is basically being passive. This path, often refers to the grain boundary, where segregation of impurity elements can make the passivation more difficult to occur. It implies that the whole surface of the material may still remains passive and the grain boundaries have already been corroded. In the way, SCC may occur even without stress by intergranular corrosion.

- **Hydrogen Embrittlement:** Hydrogen atoms can diffuse and dissolve in the metal, subsequently they will assist in the fracture of metal, start with cracks and develop to some mechanical defects. The cracking under this process may be either trans- or inter- granular. Nevertheless, in the case of austenitic stainless steel, the coefficient of diffusion of hydrogen is relatively low, thus it is thought as immune form the embitterment of hydrogen.

- **Internal Oxidation:** This mechanism of is actually concerned for IGSCC, proposed by Scott and Le Calvar [59]. It occurs when atomic oxygen dissolves into an alloy at the external oxide-metal interface and diffuses into the metal matrix to oxidise a more reactive alloying element than the solvent metal. Under certain temperature range, it becomes intergranular internal oxidation. In the case for cracking, the morphology of nickel separated from chromium oxide, formed ahead of resolvable crack tips and result in the absence of solution impurities [60].

There are many types of SCC. The most discussed in recent decades, without any doubt, are the IGSCC[1] and IASCC[2]. The former one is the SCC without considering irradiation effects. IASCC is otherwise with the presence of irradiation. Recently, a new name, EAC has comes into sight, which is actually meaning Environmentally Assisted Crack. In fact, it includes all the type of SCC together and considers their effects in the same picture, which is exact the case for primary PWR conditions.

Austenitic stainless steels are not susceptible to SCC without the presence of pollution (chloride for instance), oxygen (or oxidising species) or irradiation in the primary PWR water. Surely, dissolved oxygen is eliminated under the primary PWR conditions, for the sake of radiolysis and also in the aspect of preventing SCC.

3.2.A IASCC - Irradiation Assisted Stress Corrosion Cracking

3.2.A.1 Introduction

The existence of IASCC, except in nuclear reactors, is rare. During the recent two decades, many scientists have contributed to this essentially complex subject [61–67]. IASCC, a special case of IGSCC, can be referred as intergranular cracking showing little or no ductility which can occur in heavily irradiated structural components of nuclear reactor cores and/ or under irradiation [62]. IASCC is actually IGSCC combined with the presence of irradiation effects. The irradiation effects can be roughly considered into two major parts: effects on the metallic materials and on the water environment. More precisely, irradiation-induced changes in microstructures and microchemical content of alloys and also the environmental changes due to irradiation (radiolysis phenomenon) [65].

Fig.3.21 illustrates the different processes participated in the IASCC:

- **Radiation & Water:** the couple of radiation and water brings about water radiolysis which has been well explained in the previous chapter, Chapter 2.

[1] **IGSCC:** Inter-Granular Stress Corrosion Cracking.
[2] **IASCC:** Irradiation Assisted Stress Corrosion Cracking.

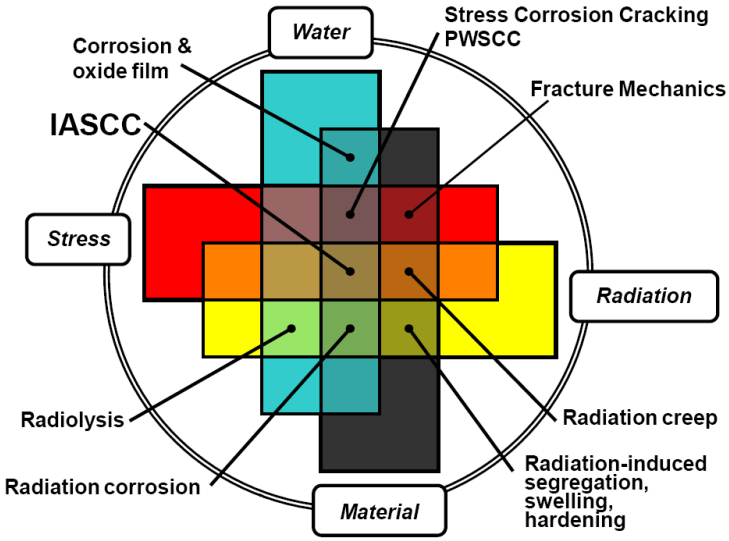

Figure 3.21: Diagram of different processes involved in radiation-induced stress corrosion cracking [68].

- **Radiation & Material:** the radiation damage on materials can lead to changes in mechanical and metallurgical properties and subsequently in their resistances to SCC. It is generally thought as the most important factor for IASCC.

- **Radiation & Stress:** the combination of radiation and stress, often included in the *radiation & material*, which is linked to the applied stress. The applied stress can be affected by the dimensional changes due to creep or swelling induced by irradiation.

- **Radiation & Water & Material:** the presence of these three factors result in radiation corrosion. Indeed, the radiolytic products, the impurities in the water, may constitute an aggressive environment and accelerate the process of general corrosion. Moreover, without the presence of stress, the occurrence of IASCC may also possible.

- **Radiation & Water & Material & Stress:** when all the factors get together, it may lead to the IASCC.

The mechanism of IASCC, the main influence parameters, the crack growth rates and so on, have not been clarified yet. However, the effect of neutron fluence on IASCC has been established for a long time, as illustrated in Fig.3.22. One important point is related to the fact that the cracking is observed in BWR oxygenated water at fluence above 5×10^{20} n/cm^2 (E $>$ 1 MeV)[3] while a higher threshold about 2×10^{21} n/cm^2 (E $>$ 1 MeV) is needed in PWRs. This observation emphasises the role of the environment.

The specific radiation-induced microstructural and microchemical changes can promote IASCC susceptibility. Metallurgical, mechanical and environmental aspects which are considered to take part in the process for cracking propagation, as illustrated in Fig.3.23. It can be roughly separated into two aspects: the radiation damages on materials and the environmental changes.

[3]Another unit for fluence: **dpa**, meaning displacement per unit atom.

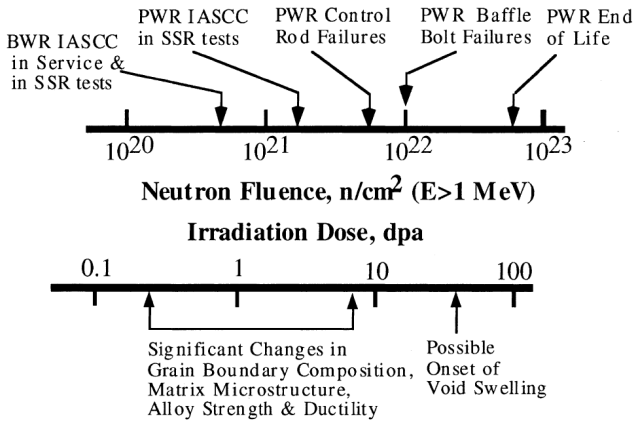

Figure 3.22: Neutron fluence effects on IASCC susceptibility of type 304SS in LWR environments [66].

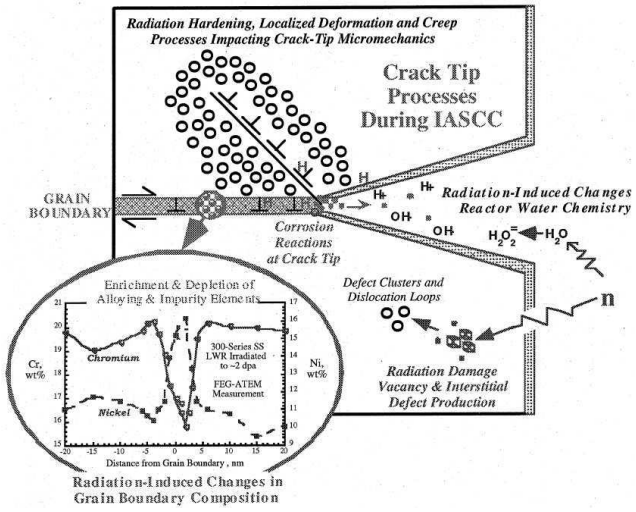

Figure 3.23: Schematic illustrating the different potential parameters on crack advance during IASCC of austenitic stainless steel [66].

3.2.A.2 Radiation Damages on Materials

Usually, radiation damages on materials are regarded as the most important factor for IASCC [62, 64, 66, 67].

The displacement of atoms from their lattice position caused by ionisation radiation is the basis for changes in the material, and results in creation of point defects in materials. Each displaced atom produces a *Frenkel pair*: one vacancy, one self-interstitial atom. The production, annihilation and migration of the point defects lead to changes in microstructure and microchemistry of the material.

- **Microstructural evolution:** starts by the partitioning of vacancies and self-interstitial atoms, and former clusters, dislocation loops and cavities.
- **Microchemical evolution:** caused by the migration of vacancies and self-interstitial atoms to sinks, like grain boundaries, dislocations, precipitations, or surfaces of second phase particles, and gives the local composition change.

Microstructure The mechanism of the microstructural evolution is not easy to predict: the cascade events as atomic displacement and cluster dissolution is rather rapid while the persistent growth of partitioned defect aggregates (the growth of interstitial loop and cavity, network dislocation development, etc.) are slower.

Material composition, thermomechanical treatment, irradiation temperature and dose rate may influence the changes in microstructure. For austenitic stainless steel:

- **Temperature:** is a significant parameter for microstructure evolutions:
  1. *Under* $300°C$, the change is dominanted by small clusters whose diameter is less than 4 nm and large dislocation loops with a diameter between 4 to 20 nm.
  2. *Between* 300 *and* $700°C$, the change is controlled by large faulted loops and network dislocations.
- **Dose** At high dose, cavities/voids[4] represents at the temperature above 350°C [67].

When the temperature is above 350°C, a second phase particles may be formed due to the irradiation, it is known as the radiation-induced precipitation. Nevertheless, the fabrication procedure may have an influence on the IASCC as well [63].

An irradiation at moderate dose and temperature below 350°C, leads to dislocation structure. Otherwise, cavities and voids become dominant at higher dose and higher temperature.

Microchemistry The microchemical evolution during the irradiation is due to *radiation-induced segregation* (RIS) [69]. It is often regarded as the precursor of IASCC. The RIS process is driven by the flux of radiation-produced defects to various sinks including grain boundaries, dislocations, or precipitates on the surfaces, and result in local composition change [70]. RIS is actually controlled by the strength of defect-solute interaction and the kinetics of back diffusion.

Most interstitials annihilate with the vacancies quickly during the irradiation. Major alloying and additional elements in stainless steel are fast diffusing species, such as Cr, Fe and Mo, they are depleted. Meanwhile, Ni as the slowest diffusing species, is enriched on the grain boundary. This is call *Inverse Kirkendall Segregation*, as represented in Fig.3.24 (a). Impurities elements, P and especially Si can bind with interstitials and migrate preferentially into sinks. That is *Interstitial Association segregation*, as delineated in Fig.3.24 (b).

Fig.3.25 illustrates the Cr depletion and Si enrichment on the grain boundary with fluence. Commonly, at 5 dpa, most stainless steel, shows a sharp decrease in Cr to nearly 13%wt, an increase in Si up to about 4% [69]. Therefore, Ni-silicide precipitation has often been observed at the region near sinks in irradiated stainless steel at high temperatures ($>$ 380°C) and high doses ($>$ 20 dpa). Without any doubt, the high concentration of Si at grain boundaries increases the susceptibility to IASCC. Furthermore, the Cr depletion, as stated for the IGSCC, is the major cause for the decrease of resistance to corrosion.

The predominant factors on microchemistry are still the temperature and dose. Mobility reduced at low temperature while back diffusion happens at high temperature. Therefore, in the intermediate

[4]clusters of vacancies and/ or gas bubbles

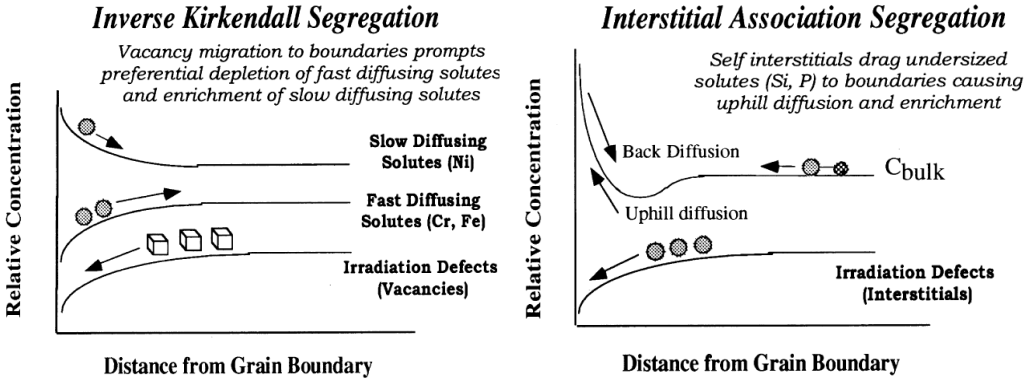

Figure 3.24: Diagrammatic sketch of solute-defect interactions on radiation-induced segregation (RIS): (a) Inverse Kirkendall segregation; (b) Interstitial Association segregation [66].

.

temperature, RIS comes to a maximum. For a specific dose, more RIS at lower dose rate. Between low and moderate dose, 0.1 - 5 dpa, RIS promotes a sharp change in interfacial composition.

Other elements segregate, like P, S, B and so on. However their effects are not significant, but they are still under debate.

Others: radiation hardening, yield strength, creep... The point defect cluster and precipitates produced by irradiation, act as obstacles to dislocation motion, leading to an increase in tensile strength and a reduction in ductility and fracture toughness of the materials. Cavities/ voids, Frank loops, small loops and bubbles can all serve as barriers to dislocation motion. The yield and ultimate stresses increase with irradiation and ductilities decrease [67]. It has been pointed out that hardening, yield strength and creep induced by radiation play an important role in IASCC [62]. It is suggested that a threshold hardening level may exist for the occurrence of IASCC, which corresponds to significant ductility loss and heterogeneous deformation mode [71].

In short, radiation perturbs the materials microstructure and microchemistry and leads to changes the threshold conditions for intergranular cracking. *Mechanistic factors*, deformation and fracture, are essential to interpret IASCC failure, followed by grain boundary chemistry. The third underpinning discipline will be the evolution of corrosion science due to the radiation-induced environmental change.

3.2.A.3 Environmental Change

As mentioned in the Chapter 2, both radical and molecular products can be produced during the water radiolysis. Their yields are dependent of mostly LET and temperature. Briefly, solutes reacting with e^-_{aq} or $H^\bullet$, reduce the yield of H_2, whereas those reacting with $HO^\bullet$ reduce the yields of H_2O_2 and O_2 subsequently.

The corrosion potential E_{corr} decreases with the presence of H_2 and increases with O_2. Therefore, the corrosion or redox potentials can be significantly shifted due to the radiolysis. It seems that the environmental changes induced by irradiation are quite clear. Under the consideration of water

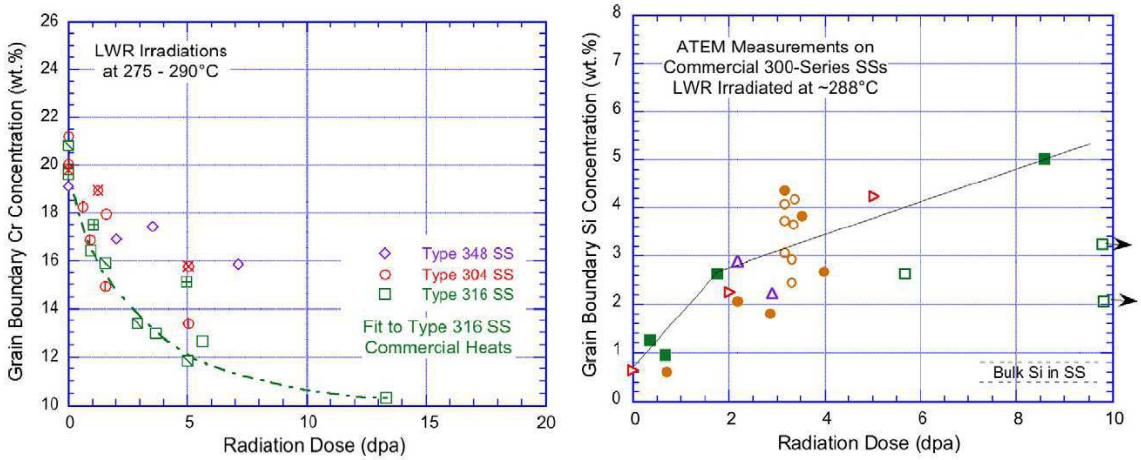

(a) (b)

Figure 3.25: Grain boundary compositions of different stainless steels versus the radiation dose: (a) Cr concentration; (b) Si concentration [67].

.

radiolysis, excess hydrogen is added/dissolved in the primary circuits of PWRs in order to suppress the oxidising species. Thus, the corrosion potential remains at a relatively low, reductive value.

However, things are not so simple in the case of IASCC. For example, the segregation of Si at the grain boundaries can increase the reducing potential in highly irradiated stainless steel, and thus enhances the susceptibility to IASCC [67]. Under this circumstance, a review on electrochemical corrosion potential (ECP) is quite necessary.

3.2.A.4 Electrochemical Corrosion Potential (ECP)

Electrochemical Corrosion Potential (ECP) measurement is a method to predicting the evolution of SCC occurred in nuclear reactors. Based on the tests have done in BWRs, it is believed that a ECP < -230 mV (SHE) can achieve potential SCC mitigation. Above -230 mV (SHE), the crack growth rate increases as the ECP increases. ECP measurement is largely employed in BWRs but not PWRs. It is mainly due to the absence of dissolved oxygen in PWRs. However, it has been pointed out that zero dissolved oxygen does not necessarily mean the ECP is less than -230 mV (SHE). A higher ECP value ($-50 \sim +50$ mV (SHE)) may also be obtained without the presence of dissolved oxygen [72].

ECP is actually a measure of the reduction/oxidation (redox) reactions which occur on the metal/solution interface. These reactions depend directly on the dissolved oxygen, hydrogen, and hydrogen peroxide concentration of the water, as indicated in Eqs.3.7, 3.8 and 3.9. It is also worth mentioning the anodic main reaction written in Eq.3.10.

$$H_2 \rightleftarrows 2H^+ + 2e^- \tag{3.7}$$

$$O_2 + 4H^+ + 4e^- \rightleftarrows 2H_2O \tag{3.8}$$

$$H_2O_2 + 2H^+ + 2e^- \rightleftarrows 2H_2O \tag{3.9}$$

$$M \rightarrow M^{n+} + ne^{-} \tag{3.10}$$

According to Macdonald [73], ECP is a mixed potential, can be calculated in MPM (Mixed Potential Model) as a crossing point between anodic and cathodic polarisation curves, and the redox species can be calculated by the **Butler-Volmer** equation, Eq.3.11.

$$i_{R/O} = \frac{e^{(E-E_{R/O})/b_a} - e^{-(E-E_{R/O})/b_c}}{\frac{1}{i_{o,R/O}} + \frac{e^{(E-E_{R/O})/b_a}}{i_{l,a}} - \frac{e^{-(E-E_{R/O}/b_c)}}{i_{l,c}}} \tag{3.11}$$

where E is the potential of electrode, $E_{R/O}$ the equilibrium potential for redox reaction, $i_{o,R/O}$ the exchange current density, $i_{l,a}$ and $i_{l,c}$ the mass transfer limited current densities or limiting current densities ofr anodic and cathodic reactions, b_a and b_c are the respective Tafel constants [74].

Meanwhile, the calculation of ECP in corrosive environments based on the conservation of charge at the interface, the net current is zero, as shown in Eq.3.12:

$$\sum_{j=1}^{n} i_{R/O,j}(E) + i_{corr}(E) = 0 \tag{3.12}$$

where E is the potential, $i_{R/O,j}$ is the partial current density due to the jth redox couple in the system and i_{corr} is the corrosion current density of the substrate.

As suggested by MacDondald, the key to understanding and predicting SCC lies in developing an understanding of origin and properties of the coupling current, as depicted in Fig.3.26. The coupling current enables direct interrogation of the processes that occur at the crack tip and provides information of crack tip dynamics in different systems.

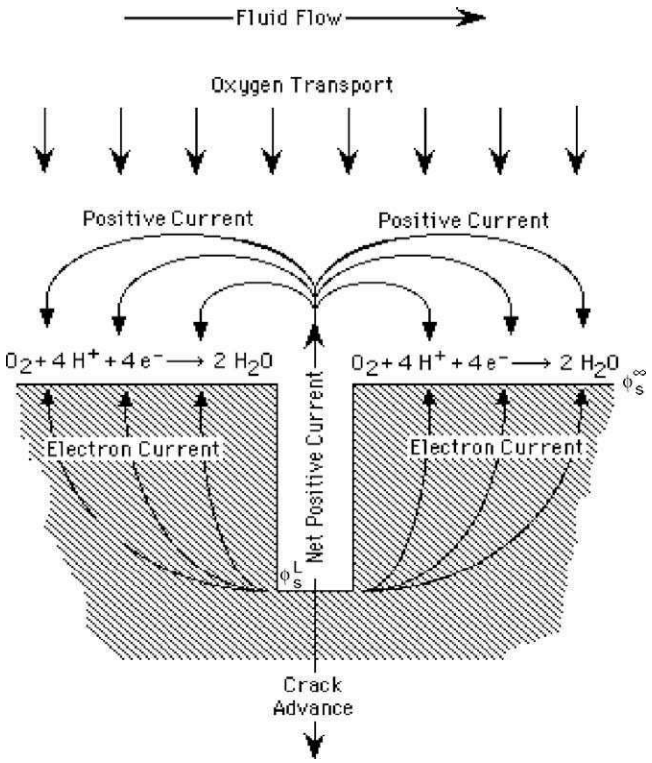

Figure 3.26: Coupling of crack internal and external environments [75].

Therefore, for IGSCC, shifting the ECP to a sufficiently negative value reduces the coupling current and thus the crack growth rate of IGSCC becomes negligible to a certain extent.

Concerning IASCC, Macdonald [74] has developed a code, CEFM, combining with the raidolysis model and mixed potential model, to predict coolant chemistry, ECP, and crack growth rate for any location in the coolant circuit for BWRs. Urquidi-Macdonald and Macdonald*et al.* [76] have developed a code, PWR-ECP, comprising chemistry, radiolysis, and mixed potential models to calculate radiolytic species concentrations and the corrosion potential of structural components at closely spaced points around the primary coolant circuits of PWRs.

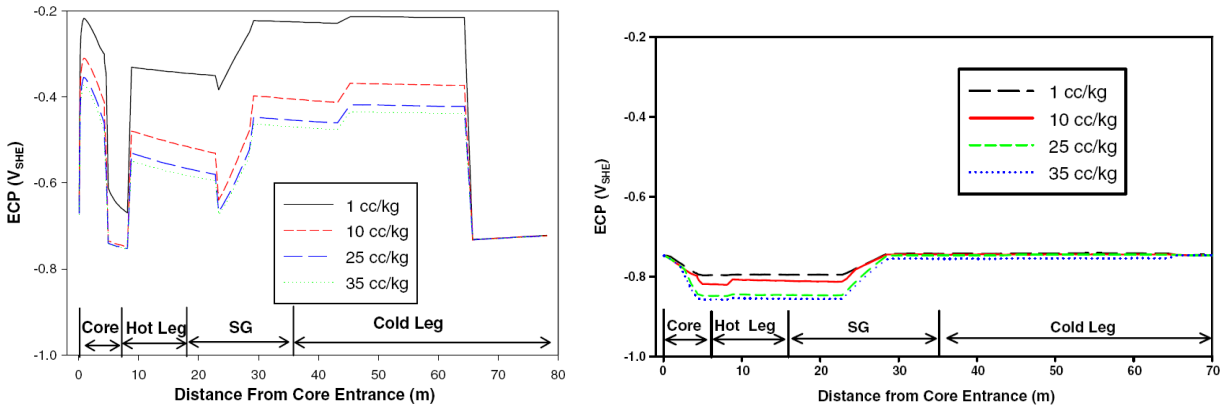

Figure 3.27: Calculated ECP in the primary circuit of a PWR, concentration of O_2 = 5 ppb, concentration of H_2 varied (1, 10, 25, 35 cc/kg): (a) Model uses *high* set of radiolytic yields; (b) Model uses *low* set of radiolytic yields [76].

.

Fig.3.27(a) & (b) illustrate the ECP in primary circuit of a PWR at constant O_2 concentration(5 ppb) and various H_2 concentration. It clearly shows that the sensitivity of the predicted ECP to the assumed values of radiolytic yields. No matter what the H_2 concentration is, the ECPs for *high* set radiolytic yields are always more positive than the ones at *low* set. Secondly, it also demonstrates that with the increasing concentration of H_2, ECP will be shifted to a more negative value.

For the calculation of ECP, only electro-active species presented at the highest concentrations will have a significant impact on ECP. Therefore, in the primary circuit of PWRs, for one thing, it traces back to the radiolytic yields, H_2O_2, $HO^{\bullet}$, $e^-_{aq}$and $H^{\bullet}$. For another, the dissolve hydrogen, added on purpose in the primary circuit, also needs to be take into account.

On the other hand, according to Ishigure *et al.* [77], the radiolysis in the diffusion layer give significant effects on the limiting current densities of the redox reactions of H_2O_2 and H_2, depending on factors as dose rate, flow rate and water chemistry. As a result, ECP can be increased importantly in hydrogen water chemistry conditions.

Briefly, measuring ECP is a good way to get a better understanding of the SCC circumstance, corrosion issues and radiolysis.

3.3 Summary

In this chapter, we have talked about the corrosion issues of 316L under primary PWR conditions. Its protective passive film is a double oxide film structure formed, chromium rich, continuous inner layer and iron rich, discontinuous outer layer. The oxide film also shows semiconducting properties, with a classic p-n heterojunction electronic structure.

With no doubt, parameters of PWR chemistry (pH, dissolved hydrogen, temperature, etc.) can influence the oxide film. Combining all the influences together as in real PWR conditions, stress corrosion cracking may occur, especially IASCC, which may be induced by irradiation. Indeed, with the presence of irradiation, corrosion issue always becomes more complex.

This is actually the starting point of the thesis study, by including material, water radiolysis and corrosion issues into the same picture.

References

[1] Evans U. R. *The corrosion and oxidation of metals.* Edward Arnold, Londron, 1960.

[2] D.H. Lister and R.D. Davidson and E. McAlpine. The mechanism and kinetics of corrosion product release from stainless steel in lithiated high temperature water. *Corrosion Science*, 27(2):113 – 140, 1987.

[3] Szklarska-Smialowska Z. and Chou Kuo-chin and Xia Zaizhu. The Compostion and Properties of Oxide Films on Type 304 Stainless Steel on Exposure to Lithiate Water at 100-350°C. *Corrosion Science*, 32(5–6):609 – 619, 1991.

[4] Tapping R.L. and Davidson R.D. and McAlpine E. and Lister D. H. The composition and morphology of oxide films formed on type 304 stainless steel in lithiated high temperature water. *Corrosion Science*, 26(8):563 – 576, 1986.

[5] S.E. Ziemniak and M. Hanson. Corrosion behavior of 304 stainless steel in high temperature, hydrogenated water. *Corrosion Science*, 44(10):2209 – 2230, 2002.

[6] Kim Y. J. Characterisation of the Oxide Film Formed on Type 316 Stainless Steel in 288°C Water in Cyclic Normal and Hydrogen Water Chemistries. *CORROSION*, 51(11):849–860, 1995.

[7] Da Cunha Belo M. and Walls M. and Hakiki N. E. and Corset J. and Picquenard E. and Sagon G. and Noël D. Composition, structure and properties of the oxide films formed on the stainless steel 316L in a primary type PWR environment. *Corrosion Science*, 40(2–3):447 – 463, 1998.

[8] Takeda Y. and Shoji T. and Bojinov M. and Kinnunen P. and Saario T. In situ and ex situ characterisation of oxide films formed on strained stainless steel surfaces in high-temperature water. *Applied Surface Science*, 252(24):8580 – 8588, 2006.

[9] Cheng, Xuequn and Feng, Zhicao and Li, Chengtao and Dong, Chaofang and Li, Xiaogang. Investigation of oxide film formation on 316L stainless steel in high-temperature aqueous environments. *ELECTROCHIMICA ACTA*, 56(17):5860–5865, JUL 1 2011.

[10] Terachi T. and Yamada T., Miyamoto T., Arioka K., Fukuya K. Corrosion Behavior of Stainless Steels in Simulated PWR Primary Water - Effect of Chromium Content in Alloys and Dissolved Hydrogen -. *Journal of NUCLEAR SCIENCE and TECHNOLOGY*, 45(10):975–984, 2008.

[11] Féron D., Herms E., Tanguy B. Behavior of stainless steel in pressurized water reactor prirmary circuits. *Journal of Nuclear Materials*, 427:364–377, 2012.

[12] Hakiki N.E., Boudin S., Rondot B. and Da Cunha Belo M. The electronic structure of passive film formed on stainless steel. *Corrosion Science*, 37(11):1809–1822, 1995.

[13] Montemor M.F. and Ferreira M.G.S. and Hakiki N.E. and Da Cunha Belo M. Chemical composition and electronic structure of the oxide films formed on 316L stainless steel and nickel based alloys in high temperature aqueous environments. *Corrosion Science*, 42(9):1635 – 1650, 2000.

[14] Terachi T. and Fujii K., Arioka K. Microstructural Characterization of SCC Crack tip and Oxide Film for UNSS 316 Stainless Steel in simulated PWR Primary Water at 320°C. *Journal of NUCLEAR SCIENCE and TECHNOLOGY*, 42(2):225–232, 2005.

[15] Terachi T. and Totsuka N., Yamada T., Nakagawa T., Deguchi H., Horiuchi M., Oshitani M. Influence of dissolved hydrogen on structure of oxide film on Alloy 600 formed in primary water of pressurized water reactors. *Journal of NUCLEAR SCIENCE and TECHNOLOGY*, 40(7):509–516, 2003.

[16] Lobnig R. E., Schmidt H.P., Hennesen K. and Grabke H. J. Diffusion of Cations in Chromia Layers Grown on Iron-Base Alloys. *Oxidaation of Metals*, 37:81–93, 1992.

[17] Carrette F., Lafont M. C., Chatainier G., Guinard L., Pieraggi B. Analysis and TEM examination of corrosion scales grown on Alloy 690 exposed to pressurized water at 325°C. *Surf. Interface Anal.*, 34:135–138, 2002.

[18] Soulas R., Cheynet M., Rauch E., Neisius T., Legras L., Domain C., Brechet Y. TEM investigations of the oxide layers formed on a 316L alloy in simulated PWR environment. *J Mater Sci*, 48:2861–2871, 2013.

[19] Jean-Philippe Berge. *Influence des traitement de surface sur la résistance á la corrosion des aciers inoxydables*. PhD thesis, Faculté de Université de Paris, 1968.

[20] Beverskog G. and Puigdomenech I. Revised pourbaix diagrams for iron at 25-300°C. *Corrosion Science*, 38(12):2121–2135, 1996.

[21] You D. Présentation du module de chimie pour pactole: Phreeqc-cea, private communication. Technical report, CEA, 2004.

[22] You D. Comportement thermodynamique des ferrites de nickel, de cobalt et de fer dans les réacteurs á eau pressurisée, private communication. Technical report, CEA, 1997.

[23] Beverskog G. and Puigdomenech I. Revised pourbaix diagams for nickel at 25-300°C. *Corrosion Science*, 39(5):969–980, 1997.

[24] Loïc Marchetti-Sillans. *Corrosion généralisée des alliages á base nickel en milieu aqueux á haute température: apport á la compréhension des mécanismes*. PhD thesis, Ecole Nationale Supérieure des Mines de Saint-Etienne, 2007.

[25] Sergio Lozano-Perez, David W. Saxey, Takuyo Yamada, Takumi Terachi. Atom-probe tomography characterization of the oxidation of stainless steel. *Scripta Materialia*, 62(11):855 – 858, 2010.

[26] Perrin S., Marchetti L., Duhamel C., Sennour M., Jomard F. Influence of Irradiation on the Oxide Film Formed on 316L Stainless Steel in PWR Primary Water. *Oxid. Met.*, 2013.

[27] Macdonald D. D. The Point Defect Model for the Passive State. *J. Electrochem. Soc.*, 139(12), 1992.

[28] Macdonald D. D. Passivity-the key to our metals-based civilization. *Pure Appl. Chem.*, 71(6), 1999.

[29] Macdonald D. D., Al Rifaie M., Engelhardt G. R. New Rate Laws for the Growth and Reduction of Passive Films. *J. Electrochem. Soc.*, 148(9), 2001.

[30] Wilhelm S. M. and Hackerman N. Photoelectrochemical Characterization of the Passive Films on Iron and Nickel. *J. Electrochem. Soc.*, 128(8):1668–1674, 1981.

[31] Hakiki N.E. and Montemor M.F. and Ferreira M.G.S. and Da Cunha Belo M. Semiconducting properties of thermally grown oxide films on AISI 304 stainless steel. *Corrosion Science*, 42(4):687 – 702, 2000.

[32] Feng Zhicao and Cheng Xuequn and Dong Chaofang and Xu Lin and Li Xiaogang. Passivity of 316L stainless steel in borate buffer solution studied by Mott-Schottky analysis, atomic absorption spectrometry and X-ray photoelectron spectroscopy. *Corrosion Science*, 52(11):3646 – 3653, 2010.

[33] De Gryse R., Gomes W. P., Cardon F. and Vennik J. On the Interpretation of Mott-Schottky Polts Determined at Semiconductor/Electrolyte Systems. *J. Electrochem. Soc.*, 122 (5):711–712, 1975.

[34] Gärtner W. W. Depletion-Layer Photoeffects in Semiconductors. *Phys. Rev.*, 116(1):84–87, 1959.

[35] Butler M. A. Phtotelectrolysis and physical properties of the semiconduting electrode WO_3. *J. Appl. Phys.*, 48(5):1914–1920, 1977.

[36] Hamadou L., Kadri A., Boughrara D., Benbrahim N., Petit J. P. Influence of oxidation time on semiconductive behaviour of thermally grown oxide films on AISI 304L. *Applied Surface Science*, 252, 2006.

[37] Di Quarto F., Sunseri C., Piazza S., Romano M.C. Semiempirical Correlation between Optical Band Gap Values of Oxides and the Difference of Electronegativity of the Elements. Its Importance for a Quantitative Use of Photocurrent Spectroscopy in Corrosion Studies. *J. Phys. Chem. B*, 101(14):2519–2525, 1997.

[38] Sudesh T. L., Wijesinghe L. and Blackwood D. J. Electrochemical & optical characterisation of passive films on stainless steels. *J. Phys.: Conf. Ser.*, 28:74–78, 2006.

[39] Park J. H., Chopra O. K., Natesan K. and Shack W. J. Boric acid corrosion of light water reactor pressure vessel materials. In *Proceedings of the 12th International Conference on Environmental Degradation of Materials in Nuclear Power System - Water Reactors*, 2005.

[40] Lozano-Perez S., Schröder, Yamada T., Terachi T., English C. A., Grovenor C. R. M. Using NanoSIMS to map trace elements in stainless steels from nuclear reactors. *Applied Surface Science*, 255:1541–1543, 2008.

[41] Andresen P. L., Emigh P. W., Morra M. M., Hickling J. Effects of PWR Primary Water Chemistry and Deaerated Water on SCC. In Allen T. R., King P. J. and Nelson L., editor, *Proceedings of the 12th International Conference on Environmental Degradation of Materials in Nuclear Power System - Water Reactors*, pages 989–1008, 2005.

[42] Huang J. B., Wu X. Q., Han E. H. Influence of pH on electrochemical properties of passive films formed on Alloy 690 in high temperature aqueous environments. *Corrosion Science*, 51:2976–2982, 2009.

[43] Sun H., Wu X. Q., Han E. H., Wei Y. Z. Effects of pH and dissolved oxygen on electrochemical behavior and oxide films of 304SS in borated and lithiated high temperature water. *Corrosion Science*, 59:334–342, 2012.

[44] Freire L. and Carmezim M. J. and Ferreira M. G. S. and Montemor M. F. The passive behaviour of AISI 316 in alkaline media and the effect of pH: A combined electrochemical and analytical study. *Electrochimica Acta*, 55(21):6174 – 6181, 2010. IMPEDANCE SPECTROSCOPY AND TRANSFER FUNCTIONS.

[45] Carmezim M. J. and Simões A. M., Montemor M. F., Da Cunha Belo M. Capacitance behaviour of passive films on ferritic and austenitic stainless steel. *Corrosion Science*, 47(3):581 – 591, 2005. Corrosion, Electrodeposition and Surface treatment of the 54th Annual Meeting of the ISE.

[46] Cissé, S., Laffont L., Tanguy B., Lafont M. C., Andrieu E. Effect of surface preparationon the corrosion of austenitic stainless steel 304L in high tmeperature steam and simulated PWR primary water. *Corrosion Science*, 56:209–216, 2012.

[47] Delabrouile F. and Legras L., Vaillant F., Scott P., Viguier B., Andrieu E. Effect of the chromium cotent and strain on the corrosion of nickel based alloys in primary water of pressurized water reactors. In Allen T. R., King P. J. and Nelson L., editor, *Proceeding of the 12th International Conference on Environmental Degradation of Materials in Nuclear Power System - Water Reactors* -, pages 903–909, 2005.

[48] Dieckmann R. Point defects and transport properties of binary and ternary oxides. *Solid State Ionics*, 12, 1984.

[49] Töpfer J., Affarwal S., Dieckmann R. Point defects and cation tracer diffusion in $(Cr_xFe_{1-x})_{3-\delta}O_4$ spinels. *Solid State Ionics*, 81, 1995.

[50] Berge P., Ribon C., Paul P. S. Effect of hydrogen on the corrosion of steels in high temperature water. *Corrosion*, 33(5), 1997.

[51] Qiu Y. B., Shoji T., Lu Z. P. Effect of dissolve hydrogen on the electrochemical behaviour of Alloy 600 in simulated PWR primary water at 290°C. *Corrosion Science*, 53, 2011.

[52] Kuang W. J., Wu X. Q., Han E. H. Influence of dissolve oxygen concentration on the oxide formed on 304 stainless steel in high temperature water. *Corrosion Science*, 63, 2012.

[53] Montemor M.F. and Simões A. M. P., Ferreira M.G.S. and Da Cunha Belo M. The role of Mo in the chemical composition and semiconductive behaviour of oxide films formed on stainless steels. *Corrosion Science*, 41:17–34, 1999.

[54] Mathieu H. J., Landolt D. An investigation of thin oxide films thermally grown in situ on $Fe_{24}Cr$ and $Fe_{24}Cr_{11}Mo$ by auger electron spectroscopy and X-ray photoelectron spectroscopy. *Corrosion Science*, 26(7), 2012.

[55] Taveira L. V. and Montemor M. F., Da Cunha Belo M., Ferreira M. G., Dick L. F. P. Influence of incorporated Mo and Nb on the Mott-Schottky behaviour of anodic films formed on AISI 304L. *Corrosion Science*, 52:2813–2818, 2010.

[56] Betova I., Bojinov M., Kinnunen P, Lundgren K. Saario T. Influence of Zn on the oxide layer on AISI 316L(NG) stainless steel in simulated pressurised water reactor coolant. *Electrochimica Acta*, 54, 2009.

[57] Pérez F. R., Barrero C. A., Hight Walker A. R., García, Nomura K. Effects of chloride concentration, immersion time and steel composition on the spinel phase formation. *Materials Chemistry and Physics*, 117, 2009.

[58] Bellanger G. . Localized corrosion of 316L stainless steel in tritiated water containing aggressive radiolytic and decomposition products at different temperatures. *Journal of Nuclear Materials*, 374(1–2):20 – 31, 2008.

[59] Scott P. M., Le Calvar M. Some possible mechanisms of intergranular stress corrosion cracking of Alloy 600 in PWR primary water. In *Proc. 6th Int. Symp. on Environmental Degradation of Materials in Nuclear Power System - Water Reactors*, pages 657–665, 1993.

[60] Scott P. M. An Overview of Internal Oxidation as a Possible Explanation of Intergranular Stress Corrosion Cracking of Alloy 600 in PWRs. In Ford P. N., Bruemmer S. M. and Was G. S., editor, *Proceedings of the 9th International Symposium on Environmental Degradation of Materials in Nuclear Power Systems - Water Reactors*, pages 3–14, 1999.

[61] Jacobs A. J., Wozadlo G. P. Irradiation-Assisted Stress Corrosion Cracking as a Factor in Nuclear Power Aging. *J. Mater. Eng.*, 9:345–351, 1988.

[62] Scott P. M. A review of irradiation assisted stress corrosion cracking. *Journal of Nuclear Materials*, 211:101–122, 1994.

[63] Chung H. M., Ruther W. E., Sanecki J. E., Hins A., Zaluzec N. J., Kassner T. F. Irradiation-assisted stress corrosion cracking of austenitic steels: recent progress and new approaches. *Journal of Nuclear Materials*, 239:61–79, 1996.

[64] McNeil M. B. Irradiation assisted stress corrosion cracking. *Nuclear Engineering and Design*, 181:55–60, 1998.

[65] Shoji T., Suzuki S. I., Raja K. S. Current status and future of IASCC research. *Journal of Nuclear Materials*, 258-263:241–251, 1998.

[66] Bruemmer S. M., Simonen E. P., Scott P. M., Andresen P. L., Was G. S., Nelson J. L. Radiation-induced material changes and susceptibility to intergranular failure of light-water-reactor core internals. *Journal of Nuclear Materials*, 274:299–314, 1999.

[67] Chopra O. K., Rao A. S. A review of irradiation effects on LWR core internal materials - IASCC susceptibility and crack growth rates of austenitic stainless steels. *Journal of Nuclear Materials*, 409:235–256, 2011.

[68] Vankeerberghen M. IASCC Modelling: phenomenological approach. In *Training symposium on Irradiation Effects in Structural Materials for Nuclear Reactors*, pages STR–6.1–1 – STR–6.1–5, 2012.

[69] Bruemmer S. M. In *Proc. 10th Int. Symp. on Environmental Degradation of Materials in Nuclear Power System - Water Reactors*, volume paper no. 0008V, 2001.

[70] Bruemmer S. M. Grain Boundary Composition and Effects on Environmental Degradation. *Materials Science Forum*, 294-296, 1999.

[71] Fukuya K., Nakano M., Fujii K., Torimaru T., Kitsunai Y. Separation of Microstructural and Micorchemical Effects in Irradiation Assisted Stress Corrosion Cracking using Post-irradiation Annealing. *Journal of NUCLEAR SCIENCE and TECHNOLOGY*, 41:1218–1227, 2004.

[72] Hettiarachchi S. Advances in Electrochemical Corrosion Potential Monitoring in Boiling Water Reactors. In Allen T. R., King P. J. and Nelson L., editor, *Proceedings of the 12th International Conference on Environmental Degradation of Materials in Nuclear Power System - Water Reactors*, pages 3–17, 2005.

[73] Macdonald D. D. *Corrosion*, 48:194, 1992.

[74] Macdondald D. D. The Electrochemistry of Stress Corrosion Cracking in Water-Cooled Reactor Coolant Circuits. In *Presentation at OLI Systems INC, Morris Plains, NJ*, 2007.

[75] Maeng W. Y., Macdondald D. D. The effect of acetic acid on the stress corrosion cracking of 3.5NiCrMoV turbine steels in high temperature water. *Corrosion Science*, 50:2239–2250, 2008.

[76] Mirna Urquidi-Macdonald, Jonathan Pitt, and Digby D. Macdonald. The impact of radiolytic yield on the calculated ECP in PWR primary coolant circuits. *Journal of Nuclear Materials*, 362(1):1 – 13, 2007.

[77] Ishigure K., Nukii T., Ono S. Analysis of water radiolysis in relation to stress corrosion cracking of stainless steel at high temperatures - Effect of water radiolysis on limiting current densities of anodic and cathodic reactions under irradiation. *Journal of Nuclear Materials*, 350:56–65, 2006.

Part II

Experimental

Chapter 4

Description of the Experiments and the Analyses

The thesis aims to investigate the corrosion of stainless steel 316L under radiolysis at high temperature and high pressure as in nuclear pressurised water reactors (PWRs).

The present approach uses either proton or electron beam to control the production of radiolytic species on a 316L/PWR water interface in a high temperature and high pressure (HTHP) electrochemical cell, so called HTHP cell. Meanwhile, another Teflon® cell, is used with proton beam on a 316L/ PWR water interface, working at room temperature and atmospheric pressure.

4.1 Accelerators - Beams

Two types of beams have been employed in this study, proton and electron beams from Cyclotron and SIRIUS Pelletron accelerators, respectively.

4.1.A Cyclotron - Proton Beam

The proton beam we used is delivered by Cyclotron in **CEMHTI** (Conditions Extremes et Matériaux: Haute Température et Irradiation) laboratory of CNRS Orléans in France. The Cyclotron in CEMHTI is a Cyclotron with variable energy. It routinely provides high energy beams of light particles (neutrons, protons, deuterons, tritons and alpha) since 1976. It is part of the French national network EMIR (Etude des Matériaux sous Irradiation). Fig.4.1 shows the scheme of the Cyclotron while Tab.4.1 lists the different ion beams, their energy range and maximum flux, which can be delivered by the Cyclotron.

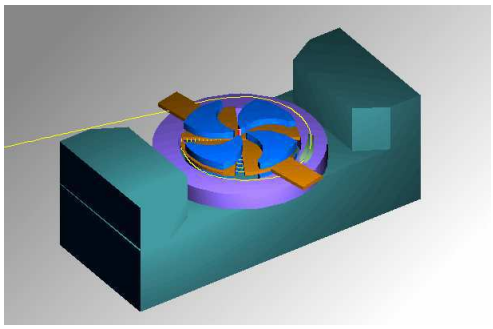

Figure 4.1: Schematic image of a cyclotron accelerator.

Ions	Energy Range (MeV)	Maximum Intensity (μA)
Proton	$5 \sim 38$	40
Deuterons	$5 \sim 25$	40
Alphas	$10 \sim 50$	15
Helions	$10 \sim 50$	15

Table 4.1: Cyclotron with variable Energy: different beams with their corresponding energy range and maximum intensity.

In our case, we use a 23 MeV proton beam in order to let the protons penetrate the 316L disc and irradiate the PWR water, which has been calculated to be about 6 MeV emerging at this solid/ solution interface.

Concerning the flux, it varies five orders of magnitude from 6.6×10^7 to 6.6×10^{11} $H^+m^{-2}s^{-1}$, corresponding to an intensity from 3pA to 30 nA. With the calculation of SRIM (*The Stopping and Range of Ions in Matter*), it can be sured that 100% of the protons penetrate the disc. The main path in the solution is about $480 \sim 500$ μm.

4.1.B SIRIUS Pelletron - Electron Beam

The electron beam we used comes form SIRIUS irradiation facility of the laboratory **LSI** (Laboratoire des Solides Irradiés) at École Polytechnique, Palaiseau in France. It is a high energy electron Pelletron accelerator from the National Electrostatics Corporation (NEC). The maximum energy of the accelerator is 2.5 MeV. It has different irradiation lines, and allows different *in situ* measurements during the irradiation. It is also part of the French national network EMIR. Fig.4.2 shows a picture of SIRIUS Pelletron Accelerator.

Figure 4.2: Picture of NEC Pelletron Accelerator.

In our case, due to the thickness of the 316L stainless steel disc for electron irradiation experiments was varied, the energy of the beam was consequently changed in order to obtain a 0.6 MeV energy at the 316L/ PWR water interface.

4.2 HTHP Cell

A specific cell has been designed in order to measure the electrochemical potential at a solid/ solution interface, under irradiation in primary PWR media [1]. The primary PWR relevant media means:

- **PWR water:** containing 1000 ppm boron, 2 ppm lithium, dissolved hydrogen and no or nearly no dissolved oxygen;
- **High temperature:** around 280 $\sim$ 320 °C;
- **High pressure:** about 90 $\sim$ 100 bar.

Therefore, this cell is so-called **HTHP Cell**. The description of the cell includes the 316L/ PWR water interface and the design of the cell.

4.2.A Cell Interface

4.2.A.1 Stainless Steel 316L - Working Electrode

Composition The disc of stainless steel 316L is made of and manufactured from a 316L stainless steel bar. The composition is indicated in Tab.4.2. Comparing with the composition range shown in the literature, the 316L stainless steel has relatively lower composition of Cr, Ni and Mo, but

with impurities, such as Cu and Co, and a carbon content just at the upper limit of the standard (UNSS31603).

Cr	Ni	Mo	Mn	Cu	Si	Co	N	P	C	S	Fe
16.6	10.2	2.21	1.82	0.43	0.3	0.11	0.056	0.033	0.03	0.028	68.183

Table 4.2: Composition of 316L stainless steel bar (%mass.).

Polishing & Cleaning After manufacturing, all 316L stainless steel discs are mechanically polished, followed by a cleaning process.

Both faces of the 316L disc are polished. The front face of the disc, which is actually the surface in contact with PWR water, is first polished with STRUERS SiC paper up to grade 4000 (grain size is about 3 μm), and finished by using PRESI Mecaprex compounds diamond 1 μm. Therefore, the grain size for the front face is 1 μm after polishing. The back face of the disc, which is first stricken by the beam, is also polished with SiC paper up to grade 1200(grain size, 10 μm).

Afterwards, the discs were cleaned by ultrasonics (TRANSSONIC TS 540) in a 1 : 1 ethanol/acetone solution during $3 \sim 4$ min and then rinsed with demineralised water.

At the end of the preparation process, a wire with a diameter about 0.5 mm of 316L stainless steel is welded on the edge of the disc. This wire is served as the electrical connection part of the working electrode, 316L disc.

After this first stage of preparation, all the discs before mounting on the cell have a diameter of 26mm and a thickness varies from 0.6 to 0.9 mm. The thickness is chosen on one hand to endure the high pressure inside the device and on the other hand to let either proton or electron beams to pass through the 316L disc. It needs to recall that for all the electron irradiation experiments, due to the small variation of the thickness after polishing, the energy of the beam was adjusted in order to achieve an energy around 0.6 MeV at the 316L/ PWR water interface.

Different Zones Once we have mounted the specimen 316L on the cell, the disc can be identified into three zones, as illustrated in the Fig.4.3:

- *Zone 1: central zone*, about 6 mm in diameter, which is in **direct** contact with PWR water. During the irradiation experiments, it is the irradiated interface.

- *Zone 2: confined zone*, which is in contact with **confined** PWR water but outside the irradiation area and within the seal ring[1].

- *Zone 3: outer zone*, which is an unirradiated interface with no contact with PWR water outside the seal system.

[1]The inner diameter of the seal ring is about 14 mm whilst the outer is nearly 16 mm.

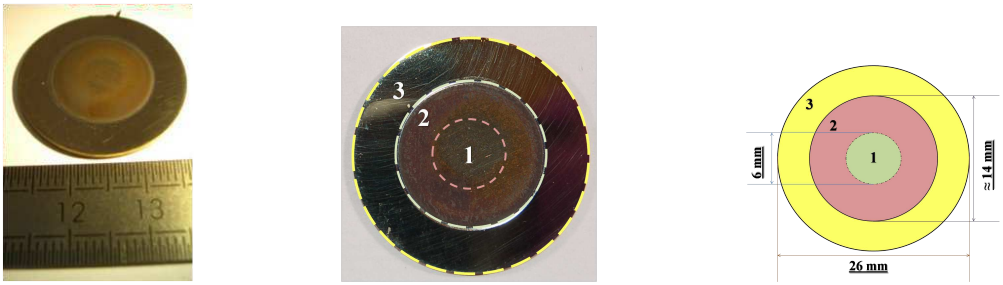

(a) (b) (c)

Figure 4.3: 316 stainless steel disc for HTHP cell: (a) a photo of an irradiated 316L stainless steel disc; (b) a photo indicated three different zones; (c) schematic layout of three different zones.

.

4.2.A.2 PWR Water

Boron & Lithium Boric acid (CHEM-LAB® Boric acid v.p., As $< 0.0005\%$, MW $= 61.83$ g/mol) and lithium hydroxide monohydrate (Fluka® $LiOH.H_2O$, As $> 99\%$, MW $= 41.96$ g/mol) are used to prepare PWR water. For 1 L of PWR water, 5.72 g of boric acid and 0.012 g of lithium hydroxide monohydrate are introduced in high purity (Milli-Q) water at 25 °C in order to achieve 1000 ppm [B] and 2 ppm [Li] solution.

Afterwards, at 25°C, we measure the pH of PWR water by Metrohm® 744 pH Meter, it is around $6.3 \sim 6.4$. Using the code PHREECQ-CEA, we estimated that the pH of the PWR water is about 7.0 at 300°C.

Dissolved Hydrogen Before introducing into the HTHP cell, the PWR water is degassed by an MESSER Ar/5% H_2 (H_2 0.985 mol%, Incertitude Rel.2%) gas mixture for one hour. After the introduction, the initial pressure in the cell is fixed at $P_{tot} = 1.5$ bar with this Ar/5% H_2 gas mixture.

Knowing the initial composition of the atmosphere, the gaseous volumes and the Henry's constants[2] at 25°C and 300°C, it is possible to calculate the theoretical ratio of $[H_2]/[O_2]$ (in ppb) in the solution. The ratio exceeds 2.0×10^5 at 25°C and 2.0×10^3 at 300°C. This ratio enables us to use a platinum wire to be a pseudo-reference electrode in the HTHP cell. The criterion for which the $[H_2]/[O_2]$ ratio should exceed eight to ensure the platinum as a reliable pseudo-reference electrode is thus satisfied [1, 2] before irradiation. In another word, the initial dissolved hydrogen in the water and the low oxygen concentration ensure that the platinum wire can be considered as a pseudo-reference electrode.

4.2.B Cell Design

The HTHP cell is designed to record the free corrosion potential of the 316L electrode (disc of the cell) in PWR water under irradiation. The device is shown in Fig.4.4 and schematised Fig.4.5:

- **Front Part:** is linked to the beam. The beams first arrive at 316L, penetrate through and then diffuse in the PWR water.

[2] *Henry's law:* "At a constant temperature, the amount of a given gas that dissolves in a given type and volume of liquid is directly proportional to the partial pressure of that gas in equilibrium with that liquid."

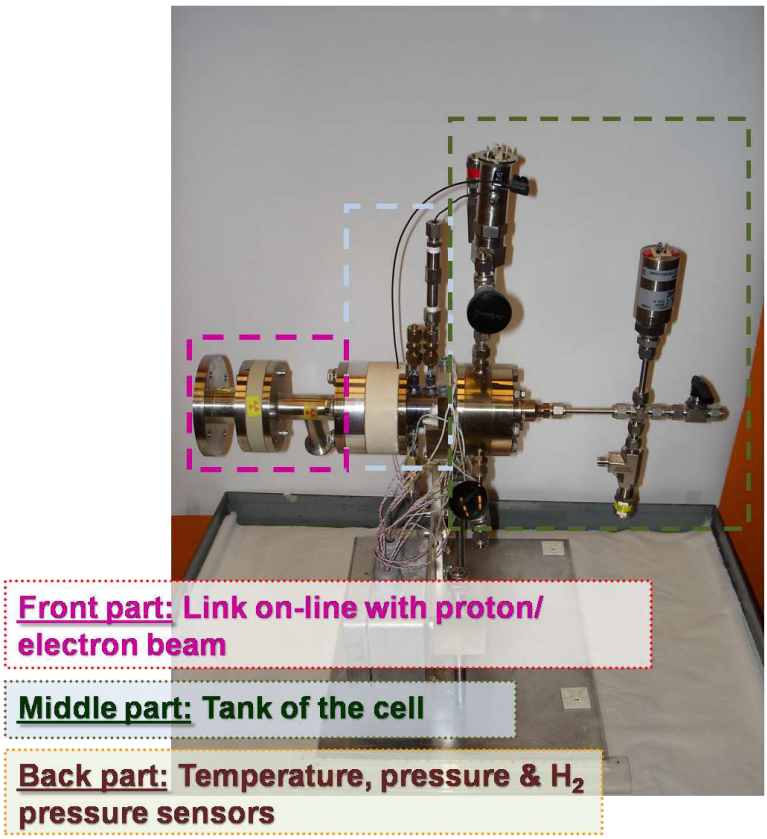

Figure 4.4: Photo of high temperature and high pressure (HTHP) electrochemical cell.

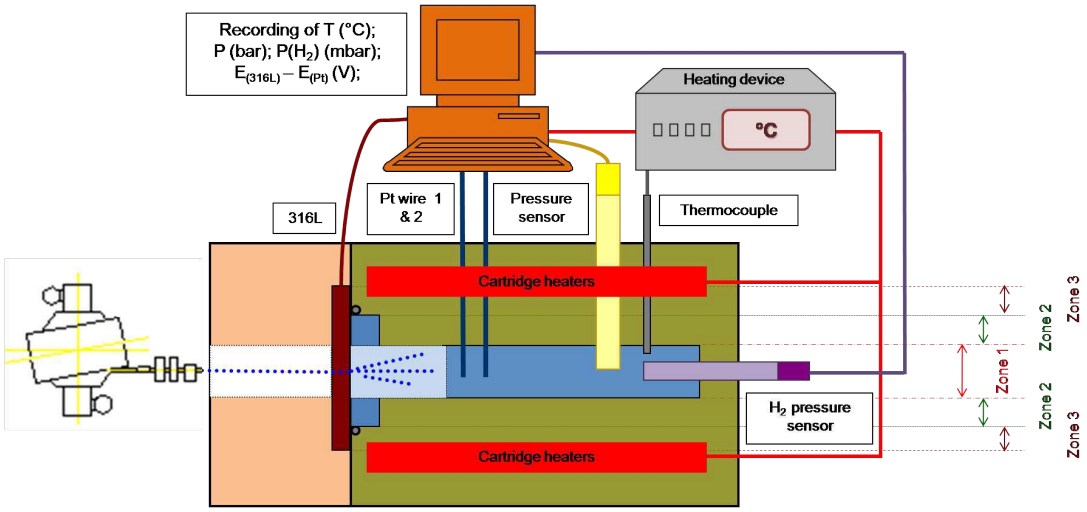

Figure 4.5: Schematic layout of high temperature and high pressure (HTHP) electrochemical cell, working at the range [25°C, 1 bar] - [300°C, 90 bar].

- **Middle Part:** is the tank of PWR water, made of a zirconium alloy which has been oxidised in air at 500°C in order to develop an electrical isolating layer of ZrO_2. The volume of the tank is approximately 20 $\sim$ 25 mL. 6 cartridge heaters are inserted to surround the tank, controlled by heating devices, which allow the increase of temperature up to 300°C. The tank is closed with the target material, 316L stainless steel disc. The disc is maintained straight, and tightly fixed by 6 screws, using two stainless steel rings on both surfaces.

- **Back Part:** is associated to all types of sensors. They are connected to a computer which can record the data in real time. Two platinum wires can be used as reference electrodes, thermocouple, pressure and hydrogen pressure sensors record the detailed informations about the conditions of experiments. All the sensors, especially the platinum wires are located few centimetres away from the irradiation zone in order to avoid the possible direct irradiation effects on them.

In short, during the experiment, with or without irradiation, the HTHP cell records temperature, pressure, hydrogen pressure and the potential difference between 316L and the platinum, as listed in Tab.4.3.

Parameters	Ranges
Temperature (°C)	[20, 300]
Pressure (bar)	[1, 90]
Hydrogen Pressure (mbar)	[0, 400]
Measurement	Accuracy
Potential difference (E_{316L} - E_{Pt}) (mV)	1

Table 4.3: Recording parameters of HTHP cell and their ranges.

4.3 Teflon® Cell

Another specific cell has been used at room temperature. It is designed to measure the electrochemical potential of a 316L stainless steel electrode under irradiation at room temperature and atmospheric pressure. The cell is mainly made of Teflon, thus is named **Teflon® Cell** [3–5], as shown in Fig.4.6 (a).

4.3.A Interface Description

4.3.A.1 Stainless Steel 316L - Working Electrode

Composition The 316L discs (Fe/Cr18/Ni10/Mo3) used for Teflon cell are high purity materials provided by Goodfellow. The diameter is 8 mm and the thickness is 200 μm (see Fig.4.6 (c)).

There are two procedures for the discs preparation, one is at room temperature, the other is prepared at high temperature (300°C) in a stainless steel autoclave.

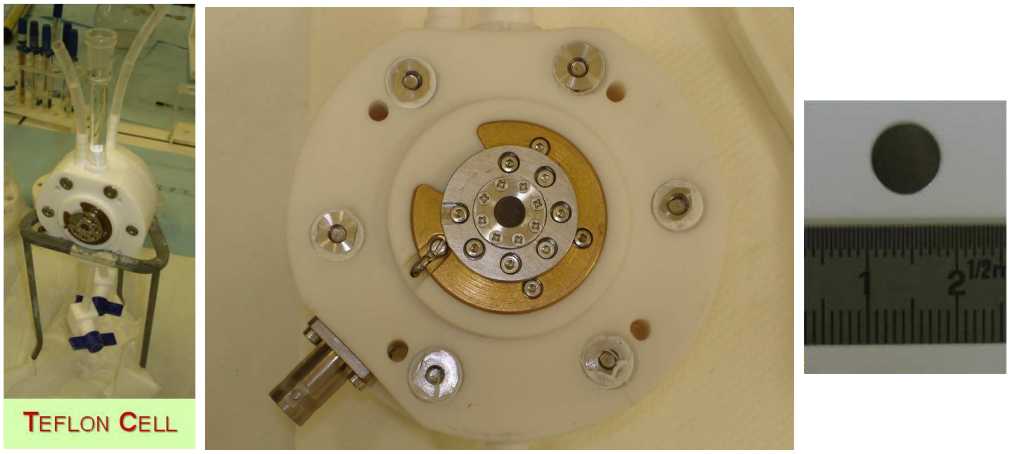

(a) (b) (c)

Figure 4.6: Teflon cell: (a) picture of Teflon cell; (b) top-view of Teflon cell (back face of the disc); (c) Good Fellow 316L stainless steel disc.

.

Preparation Procedure at room temperature (Ox25°C discs for Telfon® Cell) The standard procedure for the surface preparation of the 316L discs is listed below: all the discs are

1. degreased with a 1 : 1 ethanol/acetone solution;
2. rinsed in high purity water;
3. etched in $HF(2_{V/V})$: $HNO_3(30_{V/V})$ solution;
4. rinsed in high purity water;
5. left in air for 8 days (in a specific storage box).

Then, the 316L stainless steel discs prepared at room temperature, so called Ox25°C discs, are ready for mounting on the Teflon® cell.

Passivation Procedure at 300°C (Ox300°C discs for Teflon® Cell) Another procedure to prepare the 316L stainless steel disc is to passivate them in an autoclave with PWR water (1000 ppm [B] added as boric acid and 2 ppm [Li] added as lithium hydroxide monohydrate) at 300°C and under 1.5bar Ar/5% H_2 gas mixture for a certain duration, as pictured in Fig.4.7.

Both 8 mm and 26 mm stainless steel discs have been prepared by this method. Two experiments have been done, one is for 3 days at 300°C, the other is for 7 days at 300°C. However, these discs are only used for the experiments of Teflon® cells. Noting that a specific designed Teflon cell have been used for the 26 mm stainless steel disc.

4.3.A.2 PWR Water

The PWR water for Teflon® cell is nearly the same as the one used in HTHP cell except for the dissolved hydrogen, see previous section 4.2.A.2. Due to the fact the tank is not sealed, it is not

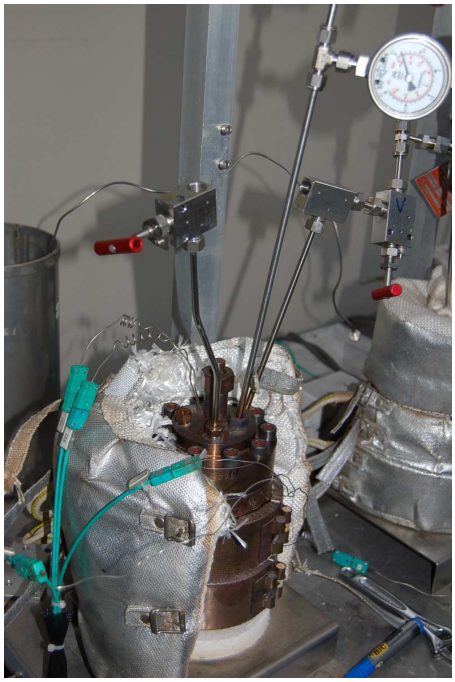

Figure 4.7: Picture of an autoclave used to prepare the Ox300°C stainless steel discs.

possible to maintain a constant dissolved hydrogen concentration. That's why the PWR water we used for the Teflon cell is without dissolved hydrogen inside.

4.3.B Cell Description

The Teflon cells used for electrochemical measurements have either two or three electrodes, pictured in Fig.4.6 (a). The working electrode is always the disc of stainless steel 316L. The reference electrode is either a saturated calomel electrode (SCE) or a mercury sulphate electrode (Hg/Hg_2SO_4).[3] In some cases, a third counter electrode is used for the measurements, which is made of an Au wire. The volume inside the cell is approximately 20ml.

The disc is mounted on a Teflon® gasket using a stainless steel ring fixed by screws, acting as an irradiation window, as shown in Fig.4.6 (b). The disc needs to be fixed properly, otherwise the PWR water will leak and then will interfere with the measurements.

The disc back face, shown in the Fig.4.6 (b), is first stricken by the proton beam and its front face, cannot be seen on the figure, is leached by the aqueous solution. The 316L disc/ PWR water interface is fully irradiated, in a diameter of 6 mm in the centre of the disc and the surface is about 0.283 cm^2, which is defined by the ring used for mounting. The thickness of the water layer at the interface is $1 \sim 2$ cm. The energy of the proton beam sent by Cyclotron is 12 MeV, and thus the energy at the interface of 316L/ PWR water is about 6 MeV. With a 480 μm penetration range, proton beam is thus stopped in PWR water.

[3] SCE is +0.241 V versus standard hydrogen electrode (SHE) at 25°C; while mercury sulphate electrode is +0.680 V vs. SHE.

4.4 Experiment Procedure

For both the HTHP cell and the Teflon® cell, two different types of experiments are carried out: ones are the experiments without irradiation, served as the reference. The other ones are the experiments with irradiation.

Before explaining the experiments in detail, a summary of the beam conditions is illustrated in Fig.4.8 and indicated in Tab.4.4.

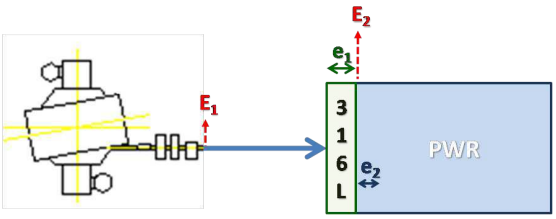

Figure 4.8: Simplified sketch indicates all the parameters of the beam conditions: E_1, the energy of the beam; E_2, the energy of at the 316L/ PWR water interface; e_1, thickness of the 316L stainless steel discs; e_2, penetrating path in the PWR water.

Beam	Cell	E_1 (MeV)	e_1 (mm)	E_2 (MeV)	e_2 (μm)
Proton	HTHP	23	~ 1	6	< 480
	Teflon®	12	0.2	6	480 - 500
Electron	HTHP	varied	varied	0.6	480 - 500

Table 4.4: Overview of all the parameters of the beam conditions: E_1, the energy of the beam; E_2, the energy of at the 316L/ PWR water interface; e_1, thickness of the 316L stainless steel discs; e_2: penetrating path in the PWR water.

4.4.A HTHP Cell

4.4.A.1 Standard Procedure

The general procedure for mounting a complete HTHP cell:

1. Install a new 316L stainless steel disc on the cell and fix with six screws. Using two stainless steel gaskets on both sides of the disc to ensure the tank and the cell are well sealed. Afterwards, check and assure the electrical isolation of the cell by using a ohmmeter.

2. Pump the HTHP cell into vacuum and then fill in with the helium gas for about $10 \sim 15$ bar. Using Adixen® ASM 142 helium leak detector to detect the leak of He gas. If there is no leak, the cell is ready for the introduction of PWR water. If not, it needs to restart from the beginning with another new proper disc.

3. Prepare the PWR water in a stainless steel vessel under pressure: introduce about 22 g of PWR water, degassed by Ar/5% H_2 gas mixture for about one hour and then the initial pressure in the vessel is fixed at about 1.5 bar with this gas mixture.

4. Pump the HTHP cell into vacuum again, then introduce the degassed PWR water into the cell.

5. Connect the HTHP cell with the heating device and all the sensors to the computer.

At this stage, the HTHP is ready for experiments. Nevertheless, we cover the whole HTHP with isolating materials in order to make the heating efficient.

We record all the data with the software Aglient BenchLink Data Logger 3: the temperature, the total pressure, the hydrogen pressure and the potential difference between the 316L disc and the platinum wires.

4.4.A.2 Reference Experiments

The reference experiments for HTHP cell are performed at the LECA laboratory, CEA Saclay.

When the HTHP cell is well prepared, we heat the cell gradually until 300°C. This process takes more or less 4 hours before the temperature and the pressure become stable at 300°C. Once they are stable, the HTHP is maintained at 300°C for the rest duration before cutting off the heating. The cooling off process is quicker: it takes about 2 hours to reach room temperature.

Three reference experiments have been achieved. The main difference among them are the duration which are 3, 5, 7 days, respectively. However, the initial conditions for these experiments may also be a little bit different, for instance, the dissolved hydrogen concentrations at 300°C.

The details about these three reference experiments are given in Tab.4.5.

Specimens	Duration (h)	Thickness (mm)	Hydrogen Pressure at 300°C (mbar)
LE11-02 ref	72	0.655	133(s) - 166(e)
LE12-04 ref	120	0.94	33*(s)
LE11-03 ref	168	0.625	33(s) - 80 (e)

Table 4.5: List of reference experiments with detailed conditions: duration, initial thickness of the 316L disc and hydrogen pressure. (s): the initial hydrogen pressure, first measured at 300°C by the sensor; (e): the hydrogen pressure measured at 300°C in the end of the thermal treatment. *: estimated value, around $30 \sim 35$ mbar.

4.4.A.3 Irradiation Experiments

Both proton and electron beams have been used for the irradiation experiments of HTHP cell, performed at the CEMHTI laboratory (Orléans, France) and LSI laboratory (Palaiseau, France), respectively.

A pre-heating oxidation treatment for all the irradiation experiments is preformed in order to produce an oxide at 300°C on all the 316L stainless steel discs before irradiation. This pre-heating process takes about $2 \sim 3$ hours at 300°C. Then, we cut off the heating, and leave the HTHP cell to cool down. In other word, before all the irradiation experiments, the interface, both 316L disc and PWR water have been treated at 300°C for few hours ($2 \sim 3$ h).

There are two kinds of irradiation experiments: one is discontinuous, the other is continuous. They are performed for different purposes: the discontinuous experiments are mainly for electrochemical behaviours of 316L under irradiation, the continuous ones on the other hand are for irradiation effects on the surface of 316L.

- **Discontinuous irradiation experiments:** after a pre-heating oxidation treatment at 300°C as described above, the HTHP cell is mounted on-line with the accelerator (Cyclotron or Pelletron). The irradiation (proton or electron) normally starts after the cell has been heated up to 300°C.

It lasts for a certain duration, which is variable, from 20 min to several hours, but more often 1 hour. Afterwards, we repeat the irradiation experiment (*beam start-on-stop*) again, and again. Meanwhile, we may change the conditions before each irradiation: temperature and hydrogen pressure. At the end of experiment, we cut-off the heating and leave the cell to cool down to room temperature. The *beam start-on-stop* process of irradiation is referred as discontinuous, or can also be considered as sequential.

- **Continuous irradiation experiments:** the beginning of the experiment is as same as the previous one: the irradiation starts after the HTHP cell is heated up to 300°C and the beam stays *on* for a quite long period without any stop. The beam is stopped before cutting-off the heating and the cell is cooled down to room temperature. This kind of experiments is called continuous irradiation experiments.

All the conditions for proton and electron experiments under irradiation are listed in the Tab.4.6.

Proton Experiments					
Specimens	Energy (MeV)	Flux (nA)	Irradiated Duration (h)	Thickness (mm)	Hydrogen Pressure at 300°C (mbar)
LE11-01 irr (D)	23/12	3×10^{-3} - 30	13.5	~ 1	29(s, L) - 390(s, H)
LE11-01 irr (D)	23/12	3×10^{-3} - 10	13.5	~ 1	29*
Electron Experiments					
Specimens	Energy (MeV)	Flux (nA)	Irradiated Duration (h)	Thickness (mm)	Hydrogen Pressure at 300°C (mbar)
LE11-04 irr (D)	1.5/0.6	168 & 465	177	0.62	190(s)
LE12-05 irr (C)	1.8/0.6	920 $\sim$ 600	65	0.95	29(s)- 53(e)
LE12-07 irr (D)	1.75/0.6	1100	107	0.88	32(s, L) -187 (s, H)

Table 4.6: List of irradiation experiments with detailed conditions: energy, flux, duration under irradiation, thickness of 316L disc and hydrogen pressure at 300 °C. (L): low hydrogen pressure; (H): high hydrogen pressure; (D): discontinuous irradiation experiment; (C): continuous irradiation experiment, (s): the initial hydrogen pressure, first measured at 300°C by the sensor; (e): the hydrogen pressure measured at 300°C in the end of the thermal treatment. *: estimated value.

4.4.A.4 Analysis After Experiments

After the experiments, we cool down and deinstall the HTHP cell, collect and analyse the interface afterwards, including both the 316L stainless steel discs and the PWR water.

- 316**L stainless steel:** many surface observations have been done for the solid interface in order to understand the irradiation effects on the materials.
- **PWR water:** solution analyses have been done so that a better understanding on the chemical changes due to the irradiation.

Tab.4.7 indicates all the techniques used for the surface characterisations of 316L stainless steel and the solution analysis of PWR water, respectively. It is worth mentioning that the proton irradiated

316L disc is not available for the analysis because it was activated by the proton beam. Therefore, all the 316L surface characterisations have been performed on the electrons irradiated discs. See Appendix D for the descriptions of the different techniques.

316L Stainless Steel	
Settings	Techniques
Morphology	SEM
Chemistry & Compositions (extreme surface $<$ 10 nm)	XPS
Chemistry & Compositions (localised) & Structure	TEM
Structure	Raman Spectroscopy
Oxygen concentration	NRA
Elemental depth profiling	GD-OES
Topography & Electronic properties	CS-AFM
PWR water	
Settings	Techniques
Cations	ICP-AES
pH	pH meter

Table 4.7: List of techniques used for interface characterisation: 316L stainless steel and PWR water.

4.4.B Teflon® Cell

4.4.B.1 Standard Procedure

Only proton beam has been used for the Teflon® cell, thus all these experiments are performed in CEMHTI laboratory, CNRS Orléans. The general procedure for mounting a complete Teflon® cell in the following:

1. Mount a new 8 mm 316L stainless steel disc on the Teflon® cell and fix with screws. Using a voltammeter to ensure there is no electrical contact between the 316L disc and the cell itself.

2. Fill the cell with demineralised water for 10 min in order to clean the cell and verify whether the cell is well sealed or not.

3. Empty the cell and refill it with PWR water and leave it still for at least 12 hours so that a electrochemical balance between the PWR water and the 316L can be achieved before mounting on-line with the cyclotron.

After mounting on-line with the beams, the reference electrode (either SCE or Hg/Hg_2SO_4) is put inside the cell, and connected (both reference and working potential) to a computer. For the potential measurements, a GAMRY® potentiostat is used. It is worth mentioning, in this study, the term *potential* is used for *free exchange potential* and the values are measured either in mV/SCE or in $mV/Hg/Hg_2O_4$ depending on the reference electrode used for the specific experiment. Nevertheless, they will all be represented in mV/SHE in order to simplify the comparison.

4.4.B.2 Irradiation Experiments

Three different types experiments have been proceeded with Teflon® cell with different purposes:

- **For electrochemical behaviour:** the process is quite the same as the discontinuous/sequential irradiations (*beam start-on-stop* repeating) used for the HTHP cell. However, no man-made changes in chemical conditions of the cell during the experiment. It means that same PWR water is used for the whole sequential irradiations at room temperature and atmospheric pressure. Meanwhile, the flux of the beam can be variable.
- **For impedance measurements:** Under continuous proton irradiation, measurements of impedance have been performed at imposed potential and at frequency between 10^4 Hz and 10^{-3} Hz.
- **For solution analysis:** under irradiation, the solution chemistry evolves. In order to understand this evolution, a specific analytical procedure is designed, as indicated in the three steps below and illustrated in Fig.4.9:
  1. Mount a proper Teflon® cell (with a new 316L stainless steel disc) on line with the Cyclotron, and then fill it with proper PWR water.
  2. Start the irradiation (6 MeV at the interface, constant flux 30 nA) for a certain duration (20, 30, 40, 60 min), then stop the beam.
  3. Collect the irradiated PWR water, and then refill the same Teflon® cell (without changing the 316L stainless steel disc) with a new proper PWR water.
  4. Afterwards, back to step 2, start the irradiation under the same conditions. This process can be repeated for n times.

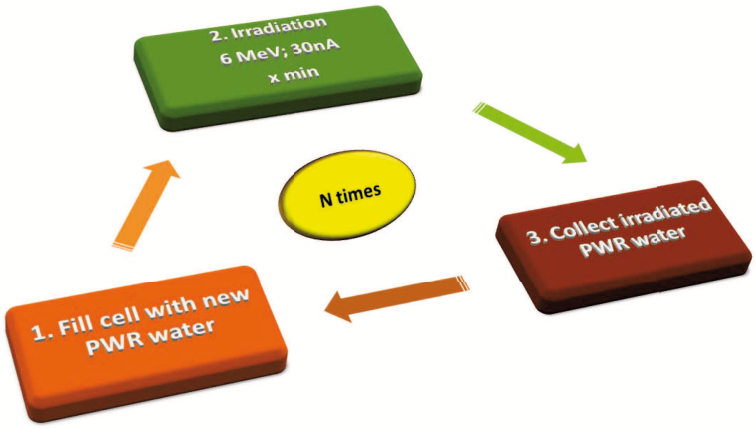

Figure 4.9: Layout of the three steps for the solution analysis experiments.

The PWR water has been analysed by different techniques, as listed in Tab.4.8. See Appendix D for the descriptions of the different techniques.

For both impedance measurements and solution analysis, we have also done the reference experiments, respectively. It means the exactly same process without irradiation.

Settings	Techniques & Methods
Cations ([Fe], [Cr], [Ni], [Zn])	ICP-AES
Anions ([F^-], [Cl^-], [NO_3^-], [SO_4^{2-}])	Ion Chromatography
pH	pH meter
[H_2O_2]	UV Spectrometer (Ghormley method)

Table 4.8: Different techniques and methods used for analysing different parameters of irradiated PWR water.

4.5 Summary

In brief, two types of irradiation have been used for the thesis study, proton and electron. They both have their own advantages. Compared to the electron beam, the proton beam used in this thesis is much closer to the recoil protons generated by the PWR flux of fast neutrons in water. However, a part of the experimental device used in this thesis, including the 316L stainless steel discs, will be activated by the proton beam. Therefore the surface observation of 316L is only possible after a long time, longer than the period of the thesis.

That is one of the reasons for introducing the electron beam. By using electron beam, both 316L disc and PWR water can be analysed in a minimum time delay after irradiation. The other reason is that the electron beam used here has energy comparable to those of the Compton electron and Beta electron that exist in PWR's reactor core due to the gamma and beta radioactivity. These two types of beam are known, from the literature, to generate different features of the radiation damage in the discs and radiolysis in water. It is consequently possible to investigate in this thesis whether the electrochemical behaviour of a 316L and PWR water interface depends on these types of irradiations or not.

Secondly, two types of experimental device have been used. They have both electrochemical working cells, one is for high temperature and high pressure, the HTHP cell; the other is used at room temperature and atmospheric pressure, the Teflon® cell. Both cells allow an *in situ* electrochemistry measurement, which is a major input of the study.

With the HTHP cell, the environmental conditions allow to reproduce the exposure conditions of the primary circuit of PWR. Regardless the difficulty of mounting the HTHP cell, it takes a long preparation time. More inconveniently, we can irradiate only one specimen for one irradiation seance due to this long time preparation work. That is the reason why we did not perform many irradiation experiments with HTHP cell. Therefore, Teflon® cell was introduced as an additional and easier experiment at room temperature. The irradiated interface of Teflon® cell is convenient to change, either the PWR water used inside the cell or the cell itself, meaning the 316L stainless steel disc. Therefore, we can repeat the irradiation experiments easily to make sure of the reproducibility of the data. Another advantage of using Teflon® cell is that a counter electrode can be easily inserted into the cell. Furthermore, without the restriction of high temperature, a real reference electrode can also be used. As a result, the Teflon® cell can be used to perform other electrochemical measurements, like measuring electrochemical impedance.

By using these two beams together with the two electrochemical cells and the ex-situ multiple techniques of surface and film analysis for the discs and solutes for the solution, we expect to achieve

the main purpose of the study: the PWR water radiolysis effect on the electrochemical behaviour of stainless steel 316L when submitted to irradiation damage.

References

[1] Muzeau B., Perrin S., Corbel C., Simon D. and Fron D. Electrochemical behaviour of stainless steel in PWR primary coolant conditions: Effects of radiolysis. *Journal of Nuclear Materials*, 419(1–3):241 – 247, 2011.

[2] Lin C. C., Smith F. R., . Electrochemical Potential Measurements Under Simulated BWR Water Chemistry Conditions. *Corrosion*, 48(01):16–28, 1992.

[3] E. Leoni and C. Corbel and V. Cobut and D. Simon and D. Féron and M. Roy and O. Raquet. Electrochemical behaviour of gold and stainless steel under proton irradiation and active redox couples. *Electrochimica Acta*, 53(2):495 – 510, 2007.

[4] Alecu Catalin G. *Studies of Electrochemical Corrosion Processes of UO_2 and Mixed Oxide Fuels in Aqueous Solutions in the View of Final Storage of Spent Nuclear Fuel*. PhD thesis, Ruprecht-Karls-Universität Heidelberg, 2008.

[5] Mendes E. *Comportement des interfaces UO_2/H_2O de haute pureté sous saisceau d'ions He^{2+} en milieu désaéré*. PhD thesis, Université de Paris-Sud, Facuulté des Sciences d'Orsay (Essonne).

Part III

High Temperature and High Pressure – Results & Discusions

Chapter 5

Reference Experiments

Reference interfaces are investigated in this chapter in order to examine the properties of the interface between 316L and PWR water from the thermal treatment in various conditions. These conditions are similar to the ones performed on irradiated interfaces which will be represented in the next chapter. Therefore, the information of these reference experiments are essentially important because they are the basis for further interpretations and reflections of the irradiation effects.

As stated previously (Ch.4.4.A.2), three reference experiments of different durations (72, 120, and 168 hours) in the HTHP cell with PWR water under 300°C and $\sim$ 90 bars have been performed, as indicated in Tab.5.1. In order to keep in mind the experimental conditions, the interfaces are noted with a name that includes the duration and initial hydrogen pressure in bracket.

Specimens	Duration (h)	Thickness (mm)	Hydrogen Pressure* (mbar)
LE11-02 ref	72	0.655	133(s) - 166(e)
LE12-04 ref	120	0.94	33*(s)
LE11-03 ref	168	0.625	33(s) - 80 (e)

Table 5.1: List of reference experiments with detailed conditions: duration, initial thickness of the 316L and hydrogen pressure. (s): the initial hydrogen pressure, first measured at 300°C by the sensor; (e): the hydrogen pressure measured at 300°C in the end of the thermal treatment. *: estimated value, around 30 $\sim$ 35 mbar.

The results for the reference interfaces can be divided into three parts:

- ***In-situ* electrochemical behaviour:** by recording the free potential evolution between 316L and Platinum in-situ, we may establish the relationships of the free potential with temperature and hydrogen pressure ($[200 - 300]$°C), respectively.

- ***Ex-situ* analysis:** including the interface (316L stainless steel) and the aqueous solution (PWR water):

    1. 316**L stainless steel disc:** by using different kinds of analytical techniques in order to study the properties of the oxide film, such as morphology, chemical composition, structure and etc, which may also be compared with the literature. Furthermore, it gives a general understanding of the oxide which can be considered as the initial state of our 316L without irradiation.

    2. **PWR water analysis:** by analysing dissolved cations and pH of the solution, comparison between before and after experiment can be made, which may tell the chemical evolution of the PWR water during the thermal treatment.

5.1 Electrochemical Behaviours

As described in Chapter 4, the electrochemical potential between 316L and platinum is followed and recorded during the experiment. The measurements of reference experiments may provide a global version for the evolution of the free potential and hydrogen pressure while it is being heated, at 300°C constantly and cooled down.

The electrochemical measurements of LE11-03 ref (168hr, 33_smbar) are illustrated in Fig.5.1, which is an interface oxidised at 300°C for 168 hours in the HTHP cell. The figures show the three stages of the reference experiment: Fig.5.1 (a) heating up to 300°C, Fig.5.1 (b) staying at 300°C and Fig.5.1 (c) cooling down to room temperature.

5.1.A Free Potential versus Temperature

The relationship between free potential and temperature are shown in all the bottom figures of Fig.5.1 (a), (b) and (c). It needs to be emphasised that the word *free potential* here is referred to the potential difference between 316L stainless steel and the platinum wire.

Based on the three figures, it underlines that:

- The free potential evolves inversely with the temperature. It decreases while the temperature increases and it increases while the temperature decreases. It seems that the potential decreases gradually but increases sharply, as shown in the Fig.5.1 (a) & (c), respectively. However, it is due to the fact that the heating process is performed gradually while the cooling process is done rapidly, as demonstrated in Fig.5.1 (d).

- The free potential stabilises at 300°C when a constant temperature is established, as shown in the Fig.5.1 (b). The free potential has an increase for the first twenty hours, afterwards it can be considered as constant, only a small increase of a few mV can be observed. It reveals probably that once the oxide film is well developed under steady state conditions, the electrochemical properties are also stable.

It is also worth mentioning that the potential has dropped for about 300 mV between the beginning and the end of the experiment. More precisely, the free potential was about 0.4 V_{Pt} at room temperature before heating and it became 0.1 V_{Pt} after cooling. Indeed, it can be attributed to the evolution of the passive layer due to the heating process as well as the chemistry of the media. Though it is rather constant with a small increase of hydrogen at 300°C. The **thermal ageing effect** has probably a direct and major influence on the free potential between the 316L and the Platinum.

5.1.B Hydrogen Pressure versus Temperature

The relationship between hydrogen pressure and temperature are shown in all the top figures of Fig.5.1 (a), (b) and (c). It needs to be pointed out that the sensors of hydrogen pressure is considered only functioning from 200 to 300°C, because the diffusion of hydrogen (through the membrane of the sensor) is more efficient at these temperatures. Otherwise, it takes quite longtime, like days or weeks, for showing the proper values at low temperature (< 200°C). In addition, the value of hydrogen pressure shown in Fig.5.1 (a) is the one indicated in the Tab.5.1: it is the initial hydrogen at 300°C in the HTHP cell.

It is clear that the hydrogen pressure increases with time at 300°C, as illustrated in Fig.5.1 (b). Besides, it seems to be indifferent of the change of the temperature, based on the fact that it remains nearly constant in Fig.5.1 (a) & (c).

The increase of hydrogen may be explained by:

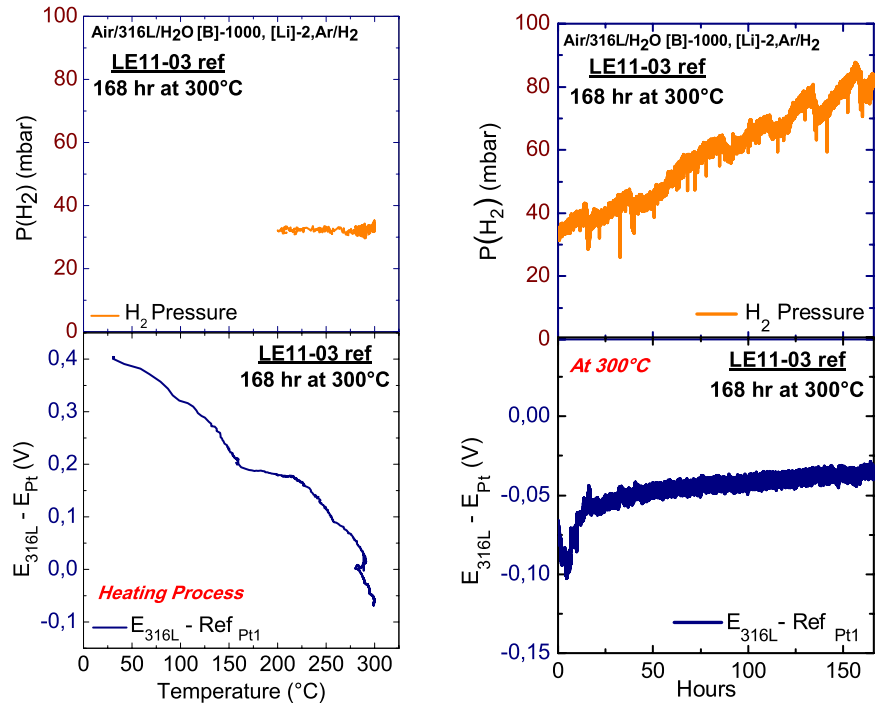

(a) Heating (b) At 300°C

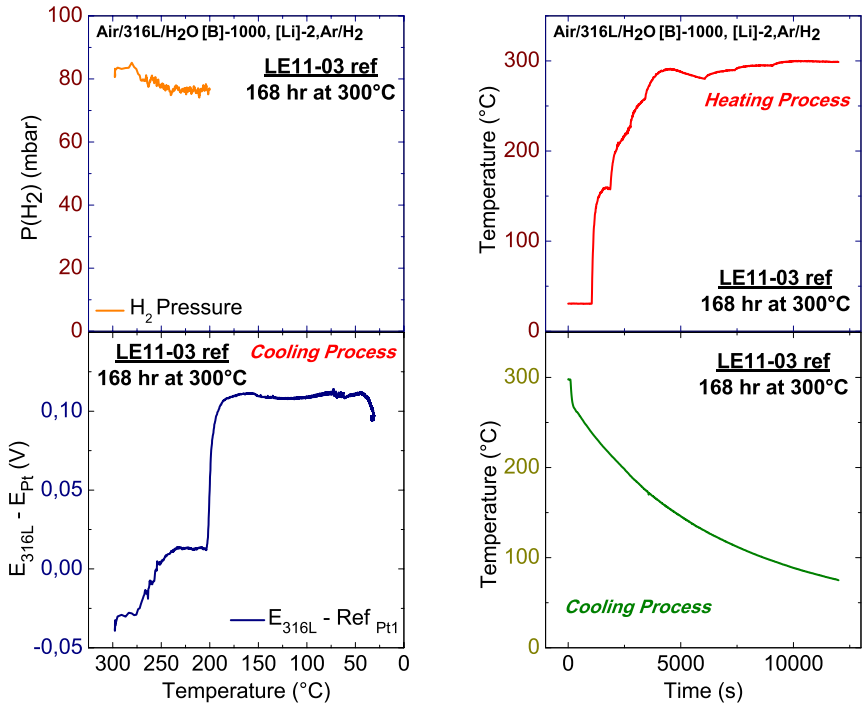

(c) Cooling (d) Temperature evolutions

Figure 5.1: Electrochemistry and hydrogen measurements of LE11-03 ref (168hr, 33_smbar), hydrogen pressure (*on the top*) and free potential between 316L and platinum (*at the bottom*) versus temperature: (a) heating process; (c) cooling process. (b): Electrochemistry (*at the bottom*) and hydrogen evolution (*on the top*) at 300°C for 168 hours. (d): Heating (*on the top*) and cooling (*at the bottom*).

1. the cathodic reaction of the corrosion, Eq.5.1, which produces H_2. An approximative calculation for the quantity of produced hydrogen inside the tank has been done in Appendix A.

$$H_2O + e^- \rightleftharpoons \frac{1}{2}H_2 + OH^- \tag{5.1}$$

2. the other possibility of the increase is addressed to the diffusion of hydrogen takes more time than expected, thus it increases continuously during the experiment.

Above all, the most evident electrochemical behaviours can be observed on the reference experiment is the **thermal ageing effect**. The free potential between 316L and Pt decreases after the thermal treatment, which may also be considered as an evolution of the electrochemical properties of the oxide film. Meanwhile, several remarks should be pointed out:

- The measurement of the free potential between 316L and Pt is via the platinum wire and a 316L wire welded on the edge of the 316L disc. Therefore, the measured value is actually average.
- Usually, the difference of potential between 316L and Pt (E_{316L} - E_{Pt}) should be negative, because Pt is a noble metal which has a higher oxidative potential. Oppositely, the one we measured here is positive. It may be explained by a presence of very few oxygen at the beginning of the experiment in the HTHP cell [1].

5.2 Characterisation of Reference 316L Oxide Films

The surface of 316L stainless steel can be characterised by many different techniques and methods, giving us information about the oxide film: morphology, chemical composition, structure and etc. As explained in the literature, the oxide formed on 316L stainless steel under primary PWR conditions are a bi-layer oxide, the inner layer is rich in chromium while the outer is mostly iron oxide. However, it needs to be pointed out that not all the techniques allow us to analyse both layers, some of them may only show the outer layer, some of them may consider the bi-layer as a whole. Therefore, combining different results form different techniques together may give us a complete idea on the oxide film formed on 316L stainless steel under our simulated PWR conditions.

Three 316L stainless steel discs have been used for the analysis, they are LE11-02 ref (72hr, 133_smbar), LE12-04 ref (120hr, 33_smbar) and LE11-03 ref (168hr, 33_smbar), corresponding to different durations at 300°C and different hydrogen pressures with PWR water in the HTHP cell, respectively.

5.2.A Surface Morphology

Surface morphology is one of the basic characterisations for studying oxide films formed on metal surfaces. The photo in Fig.5.2 (a) shows the front face of the 316L stainless steel discs which have been used for the reference experiments. Inside of the sealed mark, the surfaces are in contact with PWR water, thus the time spent under 300°C have made them to be dark brown due to the formation of the oxide layer at high temperature.

Fig.5.2 (c) shows the optical image of the a selected zone of LE11-02 (72hr, 133_smbar) which is identified in Fig.5.2 (b), it crosses the discs from side to side. The image clearly indicates the fact

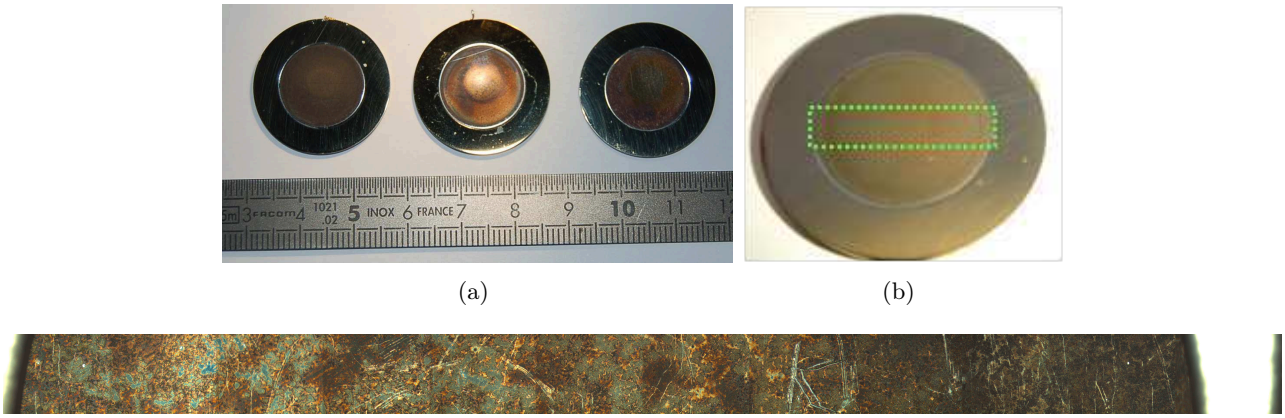

(a) (b)

(c)

Figure 5.2: Photos of 316 stainless steel discs of the reference experiments: (a) from left to right: LE11-02 ref (72hr, 133$_s$mbar), LE12-04 ref (120hr, 33$_s$mbar) and LE11-03 ref (168hr, 33$_s$mbar); (c) an optical image for a selected zone of LE11-02 ref (72hr, 133$_s$mbar) indicated in (b) with a 10x objective.

that the surface is inhomogeneous. It exhibits two different colours: dark red and green. Generally, the dark red zone is considered to be the iron oxides (magnetite is dark and hematite is red). Further approach will demonstrate this observation in the following sections.

5.2.A.1 Micrographs Characterisation

SEM, *Scanning Electron Microscope*, is the most commonly used electron microscope for the characterisation of surface morphology. It clearly visualises the outer layer of the oxide film, by showing their geometry and crystalline form. Along with the analysis of **EDX**, *Energy-Dispersive X-ray Spectroscopy*, an identification of chemical elements of the specimen can also be achieved.

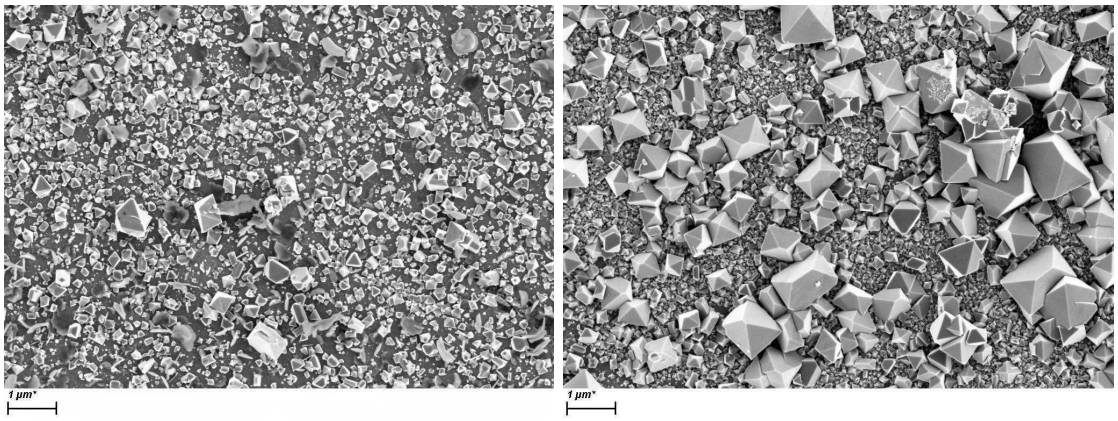

(a) zone 1 (b) zone 2

Figure 5.3: SEM micrographs of LE11 − 02 ref (72hr, 133$_s$mbar), SEM under the conditions: EHT = 2kV, Mag = 10kX, WD = 2.0 mm. (a) *zone* 1, the 6 mm in the centre of the 316L disc; (b) *zone* 2, the surrounding zone inside of seal mark.

Figs.5.3, 5.4 and 5.5 portray the SEM micrographs for LE11-02 ref (72hr, 133$_s$mbar), LE12-04

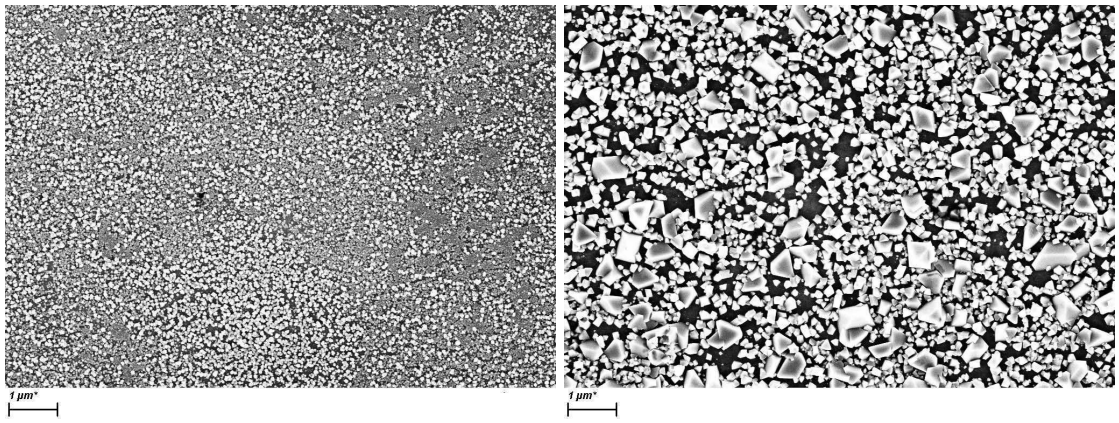

(a) zone 1 (b) zone 2

Figure 5.4: SEM micrographs of LE12 − 04 ref (120hr, 33$_s$mbar), SEM under the conditions: EHT = 5kV, Mag = 10kX, WD = 2.0 mm. (a) *zone* 1, the 6 mm in the centre of the 316L disc; (b) *zone* 2, the surrounding zone inside of seal mark.

ref (120hr, 33$_s$mbar) and LE11-03 ref (168hr, 33$_s$mbar), respectively. All the figures are in the same magnification. Figures (a) show zone 1 which is on direct contact with PWR water while figures (b) is related to zone 2, the surrounding area in contact with a confined layer of PWR water:

- In all the micrographs, the precipitates, which have the geometry form of crystallites, are discontinuously situated on the observed surface. For consistency purpose, **crystallites** will be used when referring to these types of precipitates in this manuscript. This is in accordance with the literature [2, 3] for describing the form of the outer layer.

- Comparing (a) with (b) in each figure, the density and the size of the crystallites are always less and smaller in the centre of the disc (a, zone 1) than in the confined zone (b, zone 2). The PWR water in contact with the zone 2 is confined and small, which can be considered as several layers of water. The dissolution of the crystallite occurs in both zones, but the solubilisation of cations caused by general corrosion of stainless steel can reach the limit rapidly in confined zone. Consequently, it comes to saturate more quickly and favours the nucleation/ precipitation of crystallites. This observation shown here is linked to the geometry of the HTHP cell, which results in a confined zone. Therefore, it is named **Confined Effect** in the thesis study.

- The density and the size of the crystallites are different for each surface. There are more and bigger crystallites in the figure 5.3 for LE11-02 ref (72hr, 133$_s$mbar). Among the three, it has the shortest duration at 300°C but the highest hydrogen pressure. Therefore, it is no longer comparable with the other two cases. For LE12 − 04 ref (120hr, 33$_s$mbar) and LE11-03 ref (168hr, 33$_s$mbar), Figs.5.4 and 5.5, exhibit a clear decrease in density while a slight diminution of size of the crystallites with the duration at 300°C. Actually, in zone 1, the crystallites are extremely little both in density and in size while several relatively big crystallites may be left on the surface. It means that the dissolution of crystallites occurs after their formation, probably linked to a decrease of the uniform corrosion rate of stainless steel.

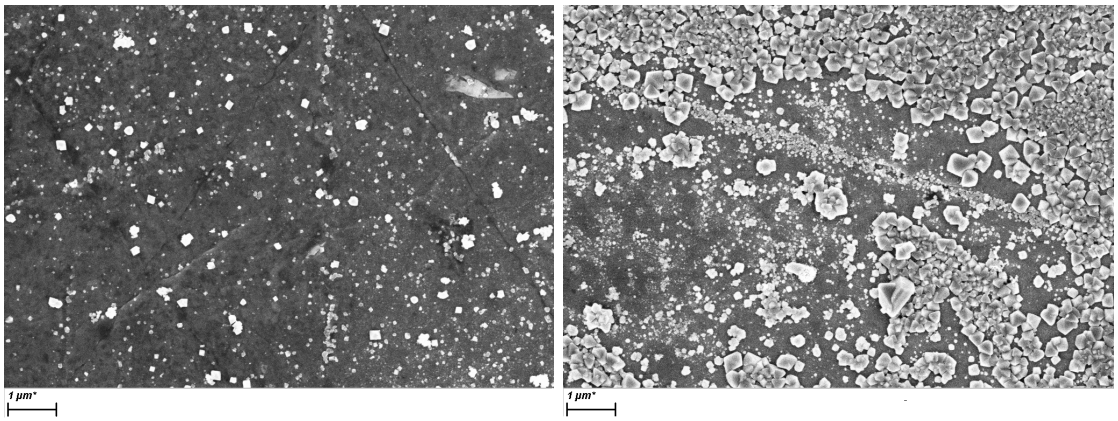

(a) zone 1 (b) zone 2

Figure 5.5: SEM micrographs of LE11 − 03 ref (168hr, 33_smbar), SEM under the conditions: EHT = 5kV, WD = 6.2 mm, Mag = 10kX. (a) *zone* 1, the 6 mm in the centre of the 316L disc; (b) *zone* 2, the surrounding zone inside of seal mark.

With the SEM micrographs, it may be concluded that the outer layer of the 316L oxide film formed under a simulated primary PWR condition in the HTHP cell is discontinuous crystallites with different sizes. The design (or the geometry) of the HTHP cell gives a **confined effect** on precipitation of the crystallites on the surface.

5.2.A.2 EDX Analysis

EDX analysis is one way to determine the chemical elements. Figs.5.6 shows an EDX analysis of zone 1 on LE11-03 ref (168hr, 33_smbar), with the analysing spots indicated in (a) and (c), and their corresponding spectra are in (b) and (d), respectively.

From the two spectra, we can identify the same elements for both areas, Fe, Cr, Ni, O, Mo, Si which are normal for a 316L. However, two elements, Zn and Al, appear to be quite surprising, because they are not the bulk elements of the 316L. Considering the intensity of the detected peaks, it reveals that the quantities for both Zn and Al are quite little, especially for Al, which can barely be detected in Fig.5.6 (b). These peaks are due to some contaminations of the surface.

As indicated in the caption of Fig.5.6, the energy (EHT) and the working distance (WD) used are considered to be the best choice for the EDX analysis of our 316L stainless steel discs. But with this conditions, the analysed volume has a shape of a *droplet* with a depth of 1 μm, which is much thicker than the oxide film (tens or hundreds of nanometers) normally formed on the stainless steel at high temperature [4]. Instead of analysing the oxide film on the surface, it may bring more information about the bulk elements, like Fe which is the major elements for 316L. Therefore, the quantification results from EDX (of SEM), are not adapted for the characterisation of the oxide film formed on the 316L stainless steel at 300°C.

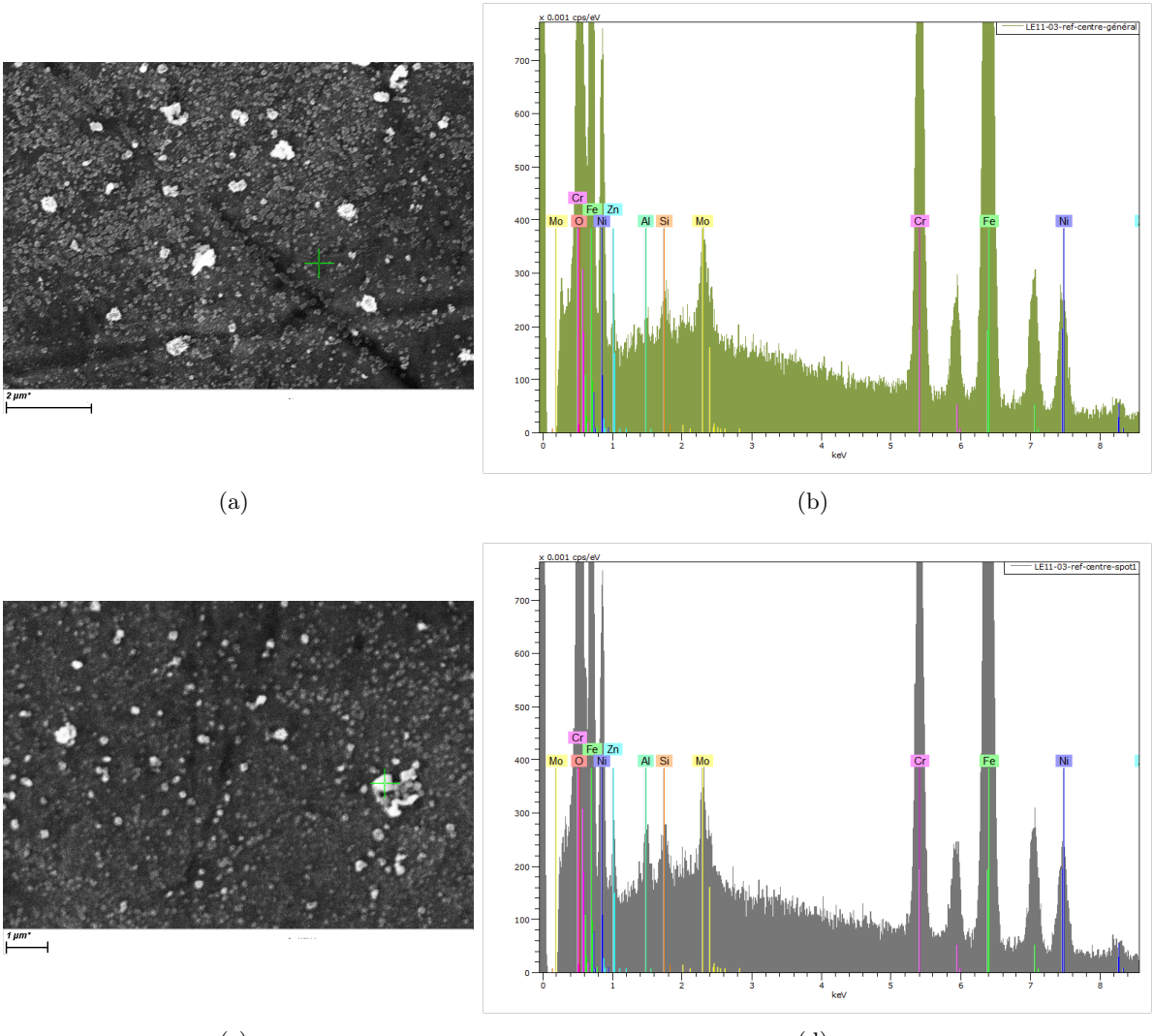

Figure 5.6: EDX analysis of two different spots on LE11-03 ref (168hr, 33$_s$mbar), SEM under condition EHT = 15 kV, WD = 6.3 mm, Mag = 10.32 kX for (a) and 10 kX for (c). (a) matrix area indicated by the green cross; (b) spectrum of the matrix area; (c) a crystallite indicated by the green cross; (d) spectrum of the crystallite.

5.2.B Composition - XPS Analysis

XPS, *X-ray Photoelectron Spectroscopy*, is a basic techniques for determining the chemical composition of an oxide films formed on metal surface. It provides a reasonable quantification and chemically specific information for each element detected, through the chemical shift. It is a highly surface-sensitive technique. Therefore, all the informations obtained are only valid for a depth less than 10 nm. If the crystallites are small enough compared to the analysed surface, the results may conclude both layers, the inner and the outer. Otherwise, the outer iron oxide will be mainly being analysed.

Briefly, by running the XPS analysis, we may have access to the following information:

- identification of the chemical elements on the analysed surface;
- chemical state determination of each element detected;
- relative quantification all the elements detected.

Instead of exhibiting all the XPS analysis results for the three reference 316L stainless steel discs, LE12-04 ref (120hr, 33_smbar) has been chosen as the example to demonstrate the interpretation based on two reasons:

1. a high similarity of the spectra, there is no difference in the elements identification for the three reference discs;
2. it is the reference experiment with a middle duration under simulated primary PWR conditions in the HTHP cell.

However, a short comparison of three reference discs will be made at the end of this section.

A line scan has been performed through the whole PWR water contacted zone of the 316L stainless steel disc, one scan on a spot zone of 650 μm every 1 mm, as shown in Fig.5.7. Fifteen scans have done from position (0 mm) on one board to position ($\approx$ 14 mm) on the other board. Among them, the central positions between 4 mm and 10 mm are representing zone 1 and the rest is zone 2.

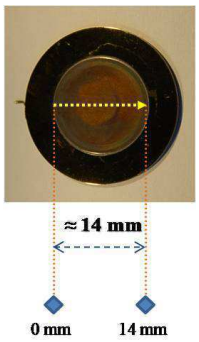

Figure 5.7: Schematic image of the line scan analysis: from side (0 mm) to side (14 mm), crossing the whole PWR water contacted zone.

5.2.B.1 Survey Scan - Element Identification

Fig.5.8 show two survey scans for position 7 and 3, in the zone 1 and the zone 2, respectively. Actually, all survey scans are alike, thus the two selected ones may be represented for the whole zone. Both scans have demonstrated the same elements: Mo 3d (225-235 eV), C 1s ($\sim$ 285 eV), O 1s ($\sim$ 530 eV), Cr 2p (570-590 eV), Fe 2p (700-740 eV), Ni 2p (845-880 eV) and Zn 2p (1015-1050 eV).

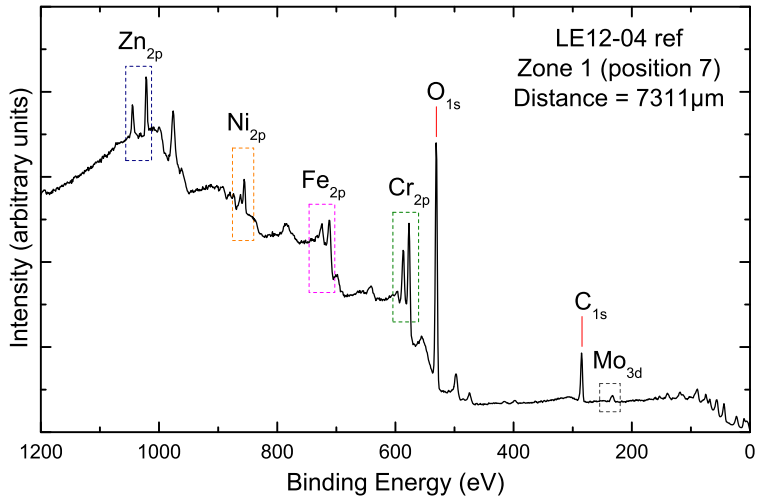

(a)

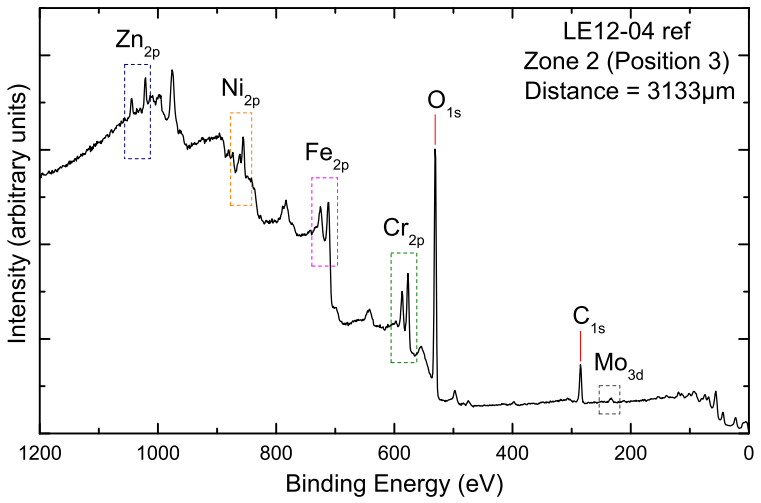

(b)

Figure 5.8: Survey spectra of 316L stainless steel discs, LE12-04 ref (120hr, 33$_s$mbar), 120 hours under simulate primary PWR conditions in the HTHP cell : (a) position 7 in the zone 1 (central zone); (b) position 3 in the zone 2 (confined zone).

All the elements identified on the spectra are reasonable for 316L stainless steel, except for the Zinc. Iron, chromium, nickel and oxygen imply the basic composition of the oxide formed. Carbon is a common contamination element on the oxide surface. On the contrary, the presence of zinc is not expected because it is not a constitutive element for 316L stainless steel. However, in Fig.5.8, the peaks of Zn 2p are clear and intense enough to demonstrate its presence, and it also in agreement

with EDX analysis.

5.2.B.2 Element Scan - Chemical States Determination

A further high resolution scan has been done for each detected elements on the survey scan. The peak of C 1s is found at 284.8 eV on its high resolution spectrum. Considering the incertitude of the XPS spectra, ± 0.3 eV, it is not necessary to adjust the C 1s spectrum to 285 eV. Thus, for all the spectra shown below, no adjustment have been made.

The fact that no metal peak can be observed on all the spectra, elucidates that no bulk elements have been analysed by XPS. It reveals that the thickness of the oxide film is more than 10 nm. In order to get more details on the oxide composition, peak assignments for each elements are necessary. Shirley backgrounds were applied for all the spectral curve fitting works.

No difference can be observed between position 7 (zone 1) and position 3 (zone 2) on all the high resolution spectra. It elucidates that the nature of the oxide remains the same for the whole PWR water contacted zone.

Chromium Oxide The peaks observed for Cr $2p_{3/2}$ oxide are asymmetric and broad, the position of the main peaks are around 576.2 ∼ 577.5 eV, shown in Fig.5.9 (a) & (b).

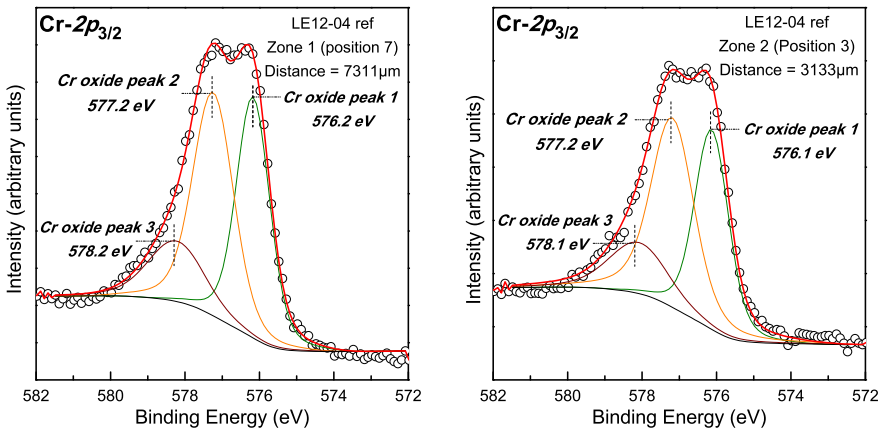

Figure 5.9: Cr $2p_{3/2}$ spectra of LE12-04 ref (120hr, 33_smbar), 120 hours under simulate primary PWR conditions in the HTHP cell: (a) zone 1 (central zone); (b) zone 2 (confined zone).

The high-resolution spectra of Cr $2p_{3/2}$ are difficult for the peak assignments due to the multiplet splitting. According to Biesinger and Payne [5–7], they all chose to fit the spectra with 5 peaks representing the multiplet splitting of the Cr^{3+} cations. However, Marchetti-Sillans [8] proposed a simple spectral curve fitting by using only 3 peaks. It is the minimum and necessary amount of peaks to fit the Cr $2p_{3/2}$ spectra. In the light of his work and the reference in our laboratory [9], Fig.5.10 (a), we refine the spectra with 3 peaks as demonstrated in Fig.5.9. A slight difference of binding energy for the 3 peaks can be linked to the different XPS machine and the different C 1s values.

Based on Biesinger *et al.* [5, 6] and Payne *et al.* [7], the spectra obtained (Fig.5.9) are probably Cr_2O_3 (chromium(III) oxide) and $FeCr_2O_4$ (chromite) rather than $NiCr_2O_4$ due to the line shape and

the peak position. For either Cr_2O_3 or $FeCr_2O_4$, the oxidation state is Cr(III).

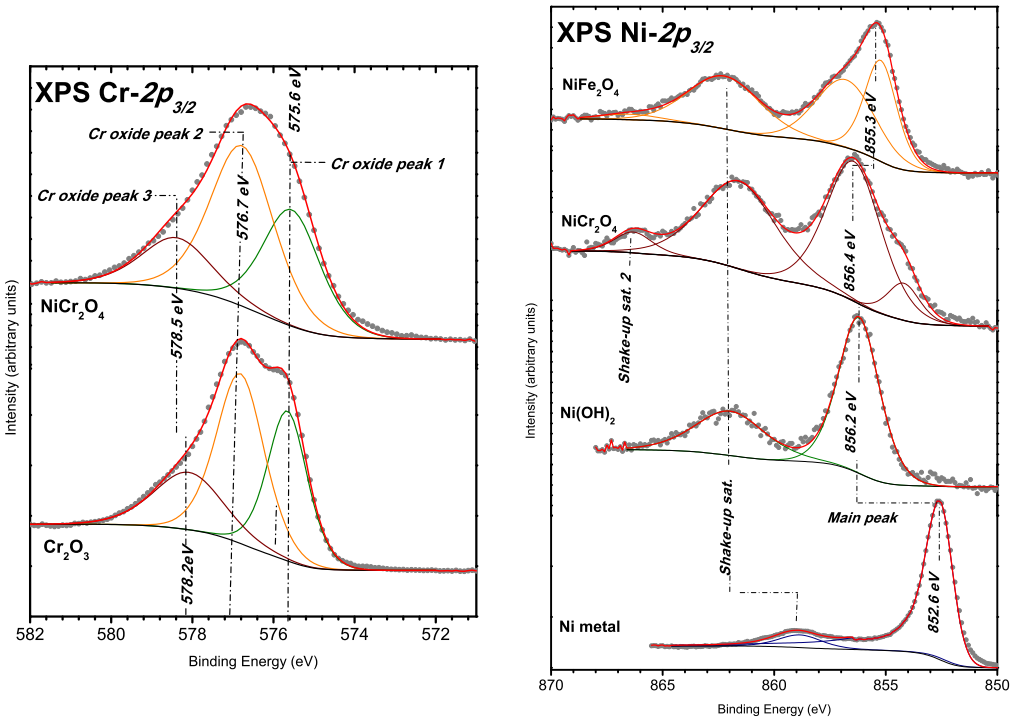

(a) (b)

Figure 5.10: Reference spectra of Cr $2p_{3/2}$ and Ni $2p_{3/2}$: (a) Cr $2p_{3/2}$, including $NiCr_2O_4$ (top) and Cr_2O_3 (bottom); (b) Ni $2p_{3/2}$, including $NiFe_2O_4$, $NiCr_2O_4$, $Ni(OH)_2$ and metallic Ni, in order from top to bottom [9].

Iron Oxide In Fig.5.11 (a) & (b), the main peaks observed for Fe $2p_{3/2}$ oxide are asymmetric, the position of the peaks are about 711.2 ± 0.3 eV. The interpretation of Fe $2p_{3/2}$ spectrum is complex because of the overlapping binding energy and multiplet splitting.

As for the refinements of Cr $2p_{3/2}$ spectra [8], instead of using 4 or 5 peaks may or may not corresponding to the different multiplet splitting, a minimum and necessary amount of peaks, 2 peaks are applied for the spectral curve fitting of Fe $2p_{3/2}$, shown in Fig.5.11.

An Auger peak of Ni appears to have the same binding energy with Fe $2p_{3/2}$, and hence leads to the overlapping of binding energy. It may leads to a slight error on the quantification work of Ni oxide. However, we neglect this Auger peak based on two reasons. On one hand, this Auger peak of Ni is quite weak. On the other hand, speaking of an oxide formed on 316L stainless steel, the quantity of Ni oxide is not comparable with the ones of Cr and Fe, thus it should not influence the global version for the quantification afterwards.

On the basis of Grosvenor *et al.* [10] and Biesinger *et al.* [6], the multiplet peaks of Fe(II) oxide ($\sim$ 709 eV) were found at a lower binding energy than the ones of Fe(III) oxide (710 $\sim$ 711 eV). The obtained spectra (Fig.5.11) are closer to the spectrum of $NiFe_2O_4$ (Fe(III) oxide) than the one of $FeCr_2O_4$ (chromite, Fe(II) oxide). It seems that the oxidation state of Fe(III) is favoured over Fe(II).

According to the literature in Chapter 3, $NiFe_2O_4$ and Fe_3O_4 are the main constituent of the

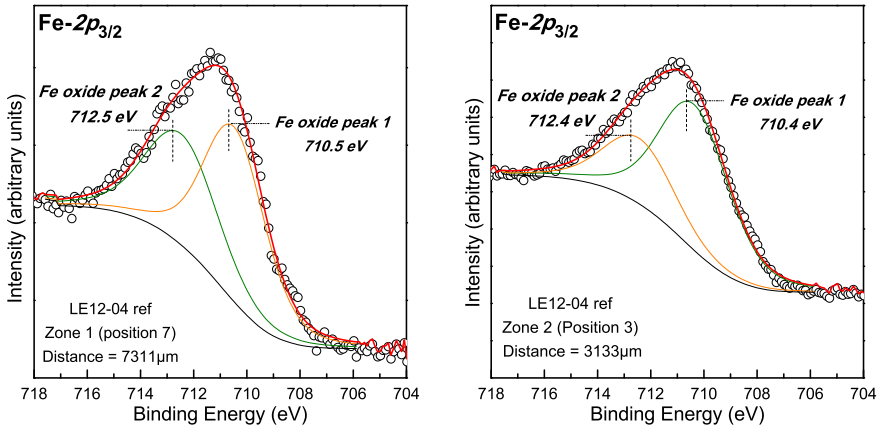

(a) (b)

Figure 5.11: Fe $2p_{3/2}$ spectra of LE12-04 ref (120hr, 33_smbar), 120 hours under simulate primary PWR conditions in the HTHP cell: (a) zone 1 (central zone); (b) zone 2 (confined zone).

crystallites formed on the 316L stainless steel, which contain both Fe(III) and Fe(II) oxides. It is likely that the concentration of Fe(III) is much more higher than the Fe(II) one. Subsequently, it may not be well represented by the XPS spectra.

Overall, one thing can be concluded: the majority of the iron oxide analysed has an oxidation state of III. Coupled with literature, the most reasonable oxide detected is (Ni,Fe)Fe_2O_4. In other words, it can be considered as the oxide Fe_3O_4 with the presence of Ni.

Nickel Oxide Two peaks can be observed for a Ni $2p_{3/2}$ spectrum, the first at about 855.3 ± 0.3 eV, and the second at about 862.0 ± 0.3 eV which happens to be the shake-up structure. In some circumstances, the shake-up peak may imply the oxidation state. In this study, it mainly serves for the quantification use. The first peak is the main peak, and the binding energy is about 855.3 ± 0.3 eV, as shown in Fig.5.12 (a) & (b). As stated, a minimum and necessary amount of peaks are used for the spectral curve fitting based on the reference of Marchetti-Sillans [8]. The first peak is asymmetric and fitted with two peaks while the second peak is fitted with only one.

Biesinger *et al.* [6, 11, 12] have achieved a large body of work by using XPS for the chemical state identification of the Ni oxide and metallic Ni. Thanks to their work, the main peak found at 855.3 eV is associated to $NiFe_2O_4$, not to $NiCr_2O_4$. The interpretation can also be confirmed by the reference obtained in our lab, as demonstrated in Fig.5.10 (b) [9]. The line shape of the spectrum (Fig.5.12) shows a high similarity to the reference spectrum of $NiFe_2O_4$ powder. It confirms the presence of Ni in the (Ni,Fe)Fe_2O_4, referred as the crystallites of the outer oxide layer. The oxidation state for Ni is the typical one, Ni(II).

Zinc Oxide and Molybdenum Oxide For the spectra Zn $2p_{3/2}$ and Mo 3d oxide (Fig.5.13), the peak assignments appear to be unnecessary because the chemical states are clear for both oxides. According to Biesinger *et al.* [13], the peak at 1021.7 eV represents for the ZnO with O 1s for ZnO found at 530.4 or 530.6 eV. Therefore, the spectrum of zinc clarifies the presence of zinc oxide, with

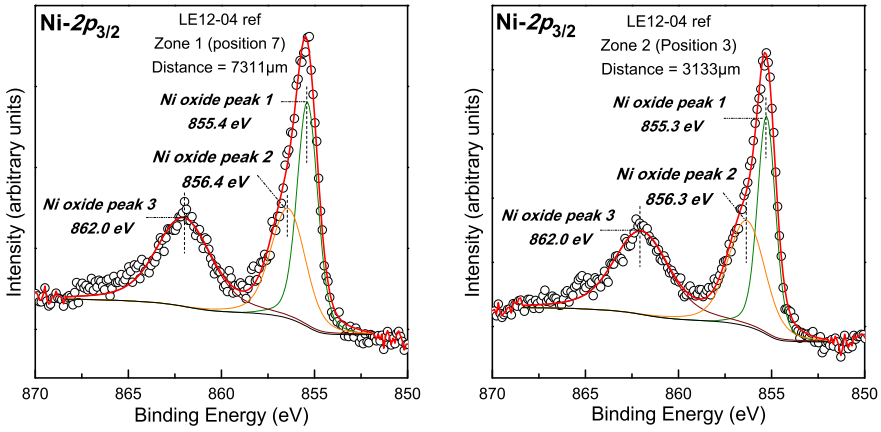

(a) (b)

Figure 5.12: Ni $2p_{3/2}$ spectra of LE12-04 ref (120hr, 33_smbar), 120 hours under simulate primary PWR conditions in the HTHP cell: (a) zone 1 (central zone); (b) zone 2 (confined zone).

its typical oxidation state II. However, under the primary PWR conditions, it is more likely to be a spinel oxide, such as $ZnFe_2O_4$ and $ZnCr_2O_4$. More precisely, it may be in the form of $(Zn,Fe)Fe_2O_4$ or $(Zn,Fe)Cr_2O_4$. They are both protective oxide film, which are favoured to be formed. Nevertheless, no reference can be found on the zinc spinel oxide.

For the Mo oxide spectrum, based on the binding energy database, the peaks at 232.4 eV and 235.4 eV are referred to Mo $3d_{5/2}$ and Mo $3d_{3/2}$ oxide, respectively. The oxidation state is Mo(VI).

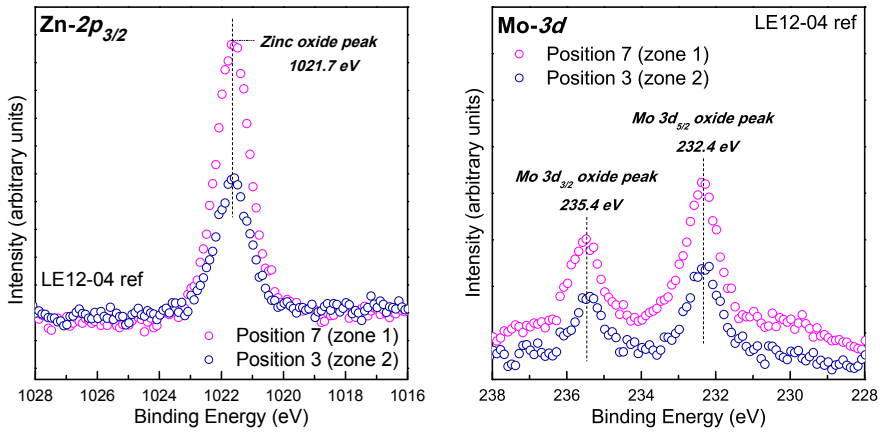

(a) (b)

Figure 5.13: Zn 2p (a) and Mo 3d (b) spectra of 316L stainless steel discs LE12-04 ref (120hr, 33_smbar), 120 hours under simulate primary PWR conditions in the HTHP cell. Rose ○: zone 1 (central zone), blue ○: zone 2 (confined zone).

Oxygen The interpretation of oxygen spectra may serve as a confirmation for the chemical states determination of different oxides. As demonstrated in Fig.5.15, absorbed hydroxide and/ or organic oxide results in the asymmetry of the oxygen peak, which is not the case for LE12-04 ref (120hr,

33_smbar), Fig.5.14. Therefore, it excludes the presence of absorbed hydroxide and organic oxide.

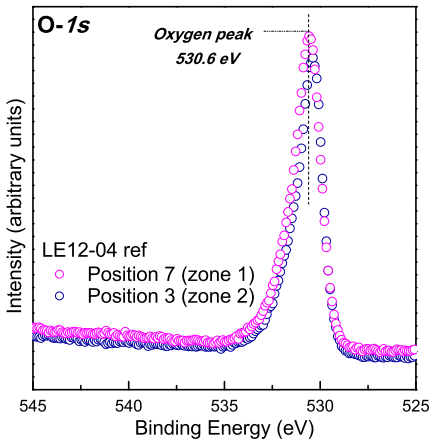

Figure 5.14: O 1s spectrum of LE12-04 ref (120hr, 33_smbar). Rose ○: zone 1 (central zone), blue ○: zone 2 (confined zone).

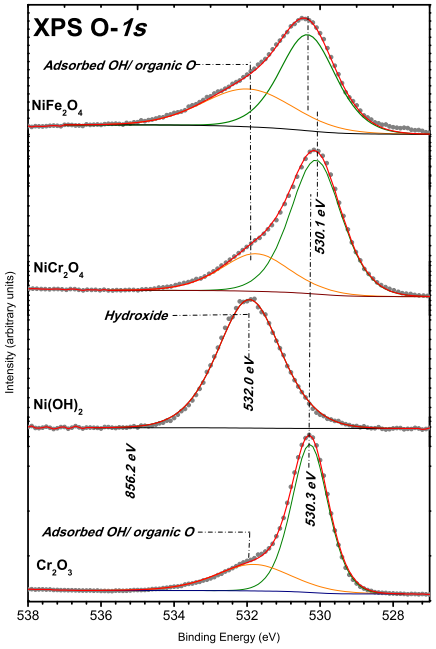

Figure 5.15: Reference spectra of O 1s: including $NiFe_2O_4$, $NiCr_2O_4$, $Ni(OH)_2$ and Cr_2O_3 in order form top to bottom [9].

The main peak for O 1s spectrum of LE12-04 ref (120hr, 33_smbar) is found at 530.6 eV in Fig.5.14. For the oxide and the hydroxide, most oxygen peaks have binding energies around 530 eV [5, 6], except for the $Ni(OH)_2$ which has a binding energy around 532 eV [9, 12], as shown in Fig.5.10 (b). Besides, the line shape of the O 1s spectrum for $Cr(OH)_3$ is different from Fig.5.14 [5]. Thus, it eliminates the presence of both nickel and chromium hydroxide. No further literature was found on the oxygen spectrum of iron hydroxide, though FeOOH is not stable under primary PWR conditions. To sum up, the oxygen spectra of LE12-04 ref (120hr, 33_smbar) correspond to an oxide and not to an hydroxide.

In short, by interpreting the high resolution spectra of each element detected, we obtained the following information:

- the oxide film on 316L stainless steel under stimulated primary PWR conditions is mainly formed by oxide and not hydroxide;
- the oxide film is composed of Fe (II, III), Cr (III), Ni (II), Zn (II) and Mo (VI);
- the majority of the oxide can be described as $(Ni,Fe)(Fe,Cr)_2O_4$.

Actually, no further comments can be made on the XPS results due to the limitations of the technique. There are not enough details to identify the Zn (II) oxide. Also, it is difficult to distinguish the Fe (II) and Fe (III) oxides.

5.2.B.3 Quantification

After interpreting the high resolution spectra of XPS analysis, a quantification work can also be performed, as shown in Fig.5.16, which gives the atomic percentage of each element. The values are standardised at 100% for the analysed elements (Cr, Ni, Fe, Zn and Mo).

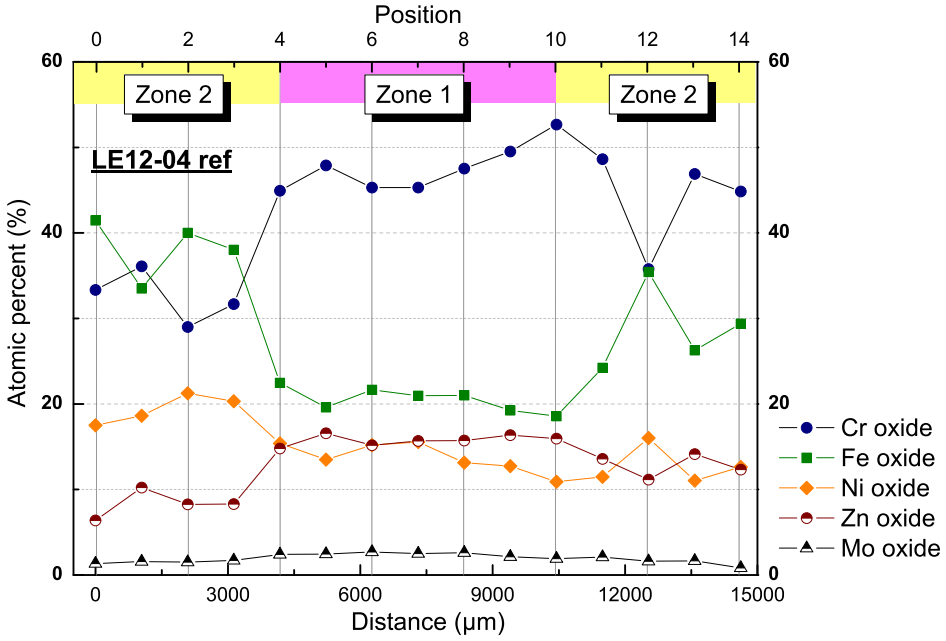

Figure 5.16: The quantification results of oxide film formed on LE12-04 ref (120hr, 33_smbar): 120 hours under simulated primary PWR conditions in the HTHP cell, error bar: ±5%. Distance is the diameter of the disc as represented in Fig.5.7.

It clearly demonstrates that:

- The majority of the oxide detected is rich in chromium oxide ($30 \sim 54\%$), and a strong enrichment ($45 \sim 55\%$) can be found in the zone 1 (central zone), from position 4 to 10. Oppositely, there is a relative enrichment for iron ($20 \sim 40\%$) oxide in the zone 2 (confined zone), from position 0 to 4 and position 10 to 14. The three oxides are mainly responsible for the oxide film analysed, which is also in accordance with the literature of the oxide film formed on the 316L stainless steel under simulated primary PWR conditions [14, 15].

- The evolution of iron and nickel oxide are similar, meaning that they are following each other from side to side across the LE12-04 ref (120hr, 33_smbar) disc. Actually, this tendency can be explained by the existence of (Ni,Fe)Fe_2O_4. (Ni,Fe)Fe_2O_4 has been analysed in the zone 2 (confined zone). The reason should be linked back to the surface morphology of zone 2. As demonstrated, more crystallites observed on the surface, Fig.5.4, more (Ni,Fe)Fe_2O_4 can be analysed by XPS. Therefore, a preliminary conclusion can be drawn: (Ni,Fe)Fe_2O_4 appears to be the corresponding oxide for the crystallites.

- The presence of zinc oxide was not expected, the maximum can be up to 16% in the zone 1. It seems that the evolution of zinc oxide is also following the chromium oxide. Zn can be presented

in the spinel oxide (AB_2O_4), in the sites of A^{2+} cations, such as $Zn(Fe,Cr)_2O_4$. As a matter of fact, it is thought that zinc is just a minor contamination element which comes from HTHP cell. However, with the high quantity demonstrated which is almost the same as the nickel oxide, the presence of zinc oxide on the oxide film is not negligible.

5.2.B.4 Comparison of Three Reference 316L Discs

The quantification of the oxide layer composition for three reference discs, LE11-02 ref (72hr, 133_smbar), LE12-04 ref (120hr, 33_smbar) and LE11-03 ref (168hr, 33_smbar) are shown in Tabs.5.2 & 5.3.

For LE11-02 ref (72hr, 133_smbar), two spot analyses were performed in zones 1 and 2, respectively. Only Cr, Fe and Ni oxide have been taken into consideration for the quantification, as the Zn and Mo peaks are relatively weak. LE11-03 ref (168hr, 33_smbar) was analysed in the same way of LE11-02 ref. Due to the importance of the zinc peak, it has been taken into account for the quantification work. For LE12-04 ref (120hr, 33_smbar), with an upgrade of the XPS machine, a better line scan was provided for the analysis, as explained in the previous paragraphs. Therefore, the percentages indicated in the tables are the average values calculated for each position in both zones.

Before discussing the results, we assume that a ±5% incertitude needs to be taken into account for the quantification values based on the uncertainty of spectra interpretation. Also, it should be pointed out that all the quantification results are relative [1].

Atomic percent (%) in zone 1					
	Cr	Fe	Ni	Zn	Mo
LE11-02 ref*	25.1	41.3	33.6	/	/
LE12-04 ref	47.6	20.5	13.8	15.7	2.4
LE11-03 ref	62.5	8.7	8.3	20.5	/

Table 5.2: The quantification results of zone 1 for LE11-02 ref (72hr, 133_smbar), LE12-04 ref (120hr, 33_smbar) and LE11-03 ref (168hr, 33_smbar), error bar: ±5%. * is meant for the first time analysis.

Atomic percent (%) in zone 2					
	Cr	Fe	Ni	Zn	Mo
LE11-02 ref*	21.1	49.8	29.1	/	/
LE12-04 ref	38.3	33.5	16.1	10.6	1.5
LE11-03 ref	32.9	32.3	27.7	7.1	/

Table 5.3: The quantification results of zone 2 for LE11-02 ref (72hr, 133_smbar), LE12-04 ref (120hr, 33_smbar) and LE11-03 ref (168hr, 33_smbar), error bar: ±5%. *: is meant for the first time analysis.

- **LE11-02 ref (72hr, 133_smbar):** Actually, the major elements detected are iron and nickel oxides in both zones. It is due to the fact that there are a lot of big crystallites on the surface as shown on the SEM micrographs, and thus the XPS results only reveal the constituents of the crystallites which are iron and nickel oxide.

- **LE11-03 ref (168hr, 33_smbar):** A difference can be noticed between zones 1 and 2. However, it can totally trace back to the surface morphology. Lack of the crystallites on the surface of zone 1 results in the high content of chromium oxide, extremely low content of iron and nickel oxide, and possibly also responsible for the high percentage of zinc oxide[2]. In zone 2, with the

[1] It means that an increase of element A certainly brings a decrease of element B in the same disc.
[2] The analysis in this case concerns the inner oxide layer

recovery of the crystallites, a drop on chromium oxide and an increase of iron and nickel oxide are observed.

- **Duration:** Comparing LE12-04 ref (120hr, 33_smbar) with LE11-03 ref (168hr, 33_smbar), it shows that with an increase of the duration in simulated primary PWR conditions (300°C, with PWR water degassed with Ar/H_2 5%) in the HTHP cell:

  Zone 1: chromium and zinc oxide increase sharply while iron and nickel oxide decrease dramatically.

  Zone 2: the quantity of chromium, iron, zinc oxides more or less remained in the same range. An increase of nickel oxide content can be noticed, however the explanation should not be linked to the duration, but to the relative quantification results of LE11-03 ref itself.

  It reveals that the quantification results of XPS are totally in agreement with the surface morphology observed by SEM, Figs.5.3 (a), 5.4 (a), 5.5 (a) for zone 1, and Figs.5.3 (b), 5.4 (b), 5.5 (b) for zone 2. Less crystallites covered on the surface for a longer duration, more chromium and zinc oxide and less iron and nickel oxide can be analysed by XPS. For the same reason, more and bigger crystallites result in more iron and nickel oxide, which is probably referred to a spinel oxide $(Ni,Fe)Fe_2O_4$.

5.2.C Structure - Raman Spectroscopy Analysis

Raman spectroscopy is used to analyse the crystal structure of the oxide film. All the spectra were obtained by using a 532 nm laser. Using the objective lens of Raman, it exhibits the whole PWR water contacted surface with two different colours, as pictured in Fig.5.17. Two individual scans have been done for each colour in zones 1(central zone) and 2 (confined zone), respectively, shown in Figs.5.18 (a) & (b).

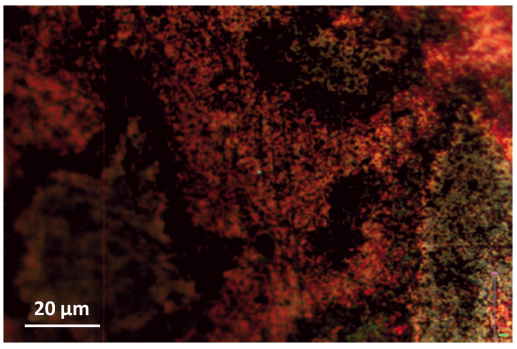

Figure 5.17: Optical image taken by the Raman objective lens for LE11-02 ref (72hr, 133_smbar), showing two areas with either dark red or green/ grey colour.

All the obtained Raman spectra are alike, five peaks can be found in each spectrum, with the main peak around 700 cm^{-1} which is relatively sharp and symmetric. One main difference should be noticed: the signals of peaks 1, 2 and 3 for the dark red area are less intensive than the green/ grey one. Oppositely, peak 5 is more visible for the dark red area.

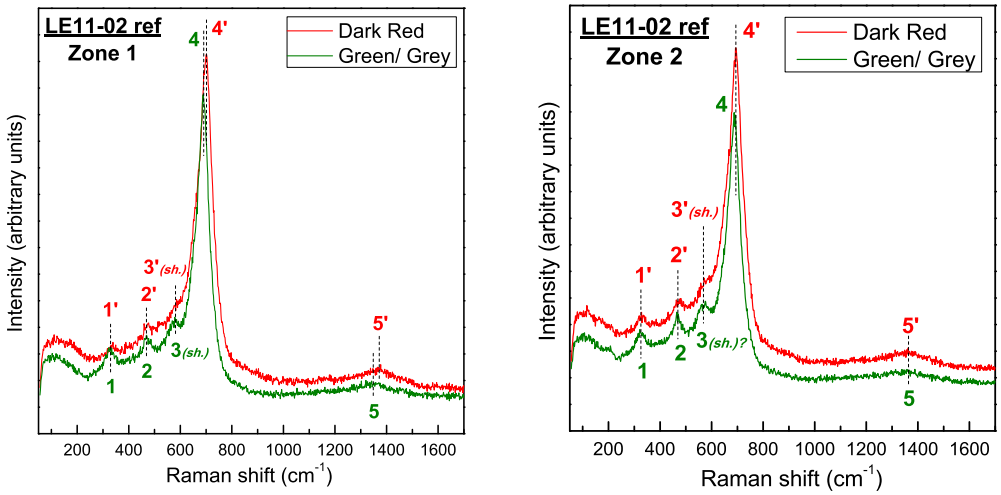

(a) (b)

Figure 5.18: Raman spectra of LE11-02 ref (72hr, 133$_s$mbar), zone 1 (central zone) in (a) and zone 2 (confined zone) in (b).

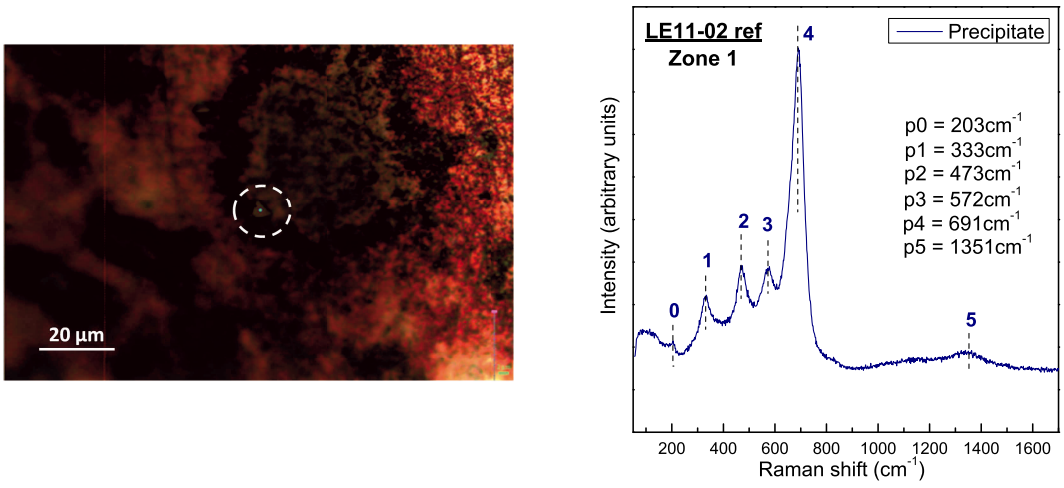

(a) (b)

Figure 5.19: Raman analysis on a crystallite in zone 1 (central zone): (a) the objective photo on the analysed crystallite; (b) Raman spectrum of the crystallite.

Fig.5.19 illustrates a spectrum of a crystallite found in zone 1 with the values of the Raman wavenumbers. It is obvious that the intensity of the crystallite spectrum is the strongest among all. An extremely slight peak 0 at 203 cm^{-1} can be detected.

In fact, no reference wavenumbers of spectra can be found for the oxide film formed on 316L stainless steel under primary PWR conditions. However, a well detailed interpretation was carried out, see Appendix B.

In conclusion, the Raman spectroscopy results show that the oxide film formed on 316L stainless steel under primary PWR conditions is a mixed spinel oxide with a co-existence of $NiFe_xCr_{2-x}O_4$ with a $x > 0.9$, and $Fe_{3-x}Cr_xO_4$ with a $x \gtrapprox 1.4$: more probably, $NiFe_xCr_{2-x}O_4$ for the green/ grey area while $Fe_{3-x}Cr_xO_4$ for the dark red one, and the crystallites are close to a $NiFe_xCr_{2-x}O_4$.

5.2.D Quantification of Oxygen - NRA Analysis

NRA, *Nuclear Reaction Analysis*, provides a way to analyse the quantity of oxygen atoms on the oxide film, in terms of *atoms per* cm^2. The reaction used for the analysis is $^{16}O(d,p)^{17}O$. It estimates the oxygen atom for the whole oxide layer, including the outer and the inner. The inner oxide layer is protective, and thus its evolution is important. Though, the existence of the crystallites, as the outer layer on the surface makes the analysis become complicated. However, this technique can give us a general idea on the homogeneousness of the oxide film. Analysis details is included in Appendix D.

Two analyses have been carried out for the 316L stainless steels, one spot in the zone 1 and the other in the zone 2, as shown in Figs.5.20 (a) & (b).

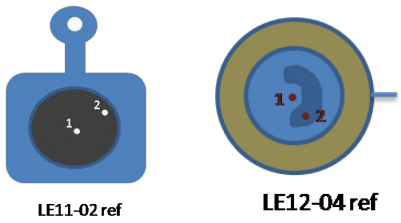

(a) (b)

Figure 5.20: Sketch of LE11-02 ref (72hr, 133_smbar) and LE12-04 ref (120hr, 33_smbar). Spots 1 and 2 indicate the analysed spots in zones 1 (central zone) and 2 (confined zone), respectively.

Specimens	N oxygen atom (10^{15} at/cm^2)	
	zone 1 (spot 1)	zone 2 (spot 2)
LE11-02 ref	1078	1232
LE12-04 ref	465	1204

Table 5.4: NRA estimated the quantity of oxygen atoms (atoms per cm^2) of LE11-02 ref (72hr, 133_smbar) and LE12-04 ref (120hr, 33_smbar), error bar: ±10 %.

Tab.5.4 indicates the estimated quantity of oxygen atoms on the oxide film of the two reference discs, LE11-02 ref (72hr, 133_smbar) and LE12-04 ref (120hr, 33_smbar).

- **LE11-02 ref (72hr, 133_smbar):** Nearly no difference can be noticed between the zone 1 and

the zone 2. Furthermore, considering the incertitude of the analysis, we may say that the zone 1 and 2 have the same range of the oxygen atoms.

- **LE**12-04 **ref (**120**hr,** 33_s**mbar):** There is a significant difference of the concentration between the two zones. It is probably due to the surface morphology, the sizes and the densities of crystallites. Nevertheless, it reveals that the oxide film is quite heterogenous on different spots.

Generally, the growth of the inner layer is linked to the duration spent under the environment. However, for the outer layer, it depends more likely on its size and density under the circumstance and on the competition between dissolution and deposition. In short, the NRA results are in agreement with the morphology observation, Figs.5.3 & 5.4.

5.2.E TEM Analysis

TEM, *Transmission Electron Microscopy*, is a powerful technique for studying the whole oxide film, which gives information on the morphology, the composition, the crystal structure of the oxide film and even the defects in the oxide. However, it is a localised analysis for an area about $10\mu m^2$.

An analysis has been performed on the zone 1 of LE11-02 ref (72hr, 133_smbar), which corresponds to a high hydrogen environmental condition during the experiment.

5.2.E.1 Morphology

As clearly illustrated in Fig.5.21, the oxide film formed on 316L stainless steel under primary PWR conditions has a double-layer structure: a continuous inner layer and the discontinuous outer layer [16, 17]. The continuous inner layer has a granular appearance and the thickness of the oxide layer is extremely irregular, form 30 to 280 nm.

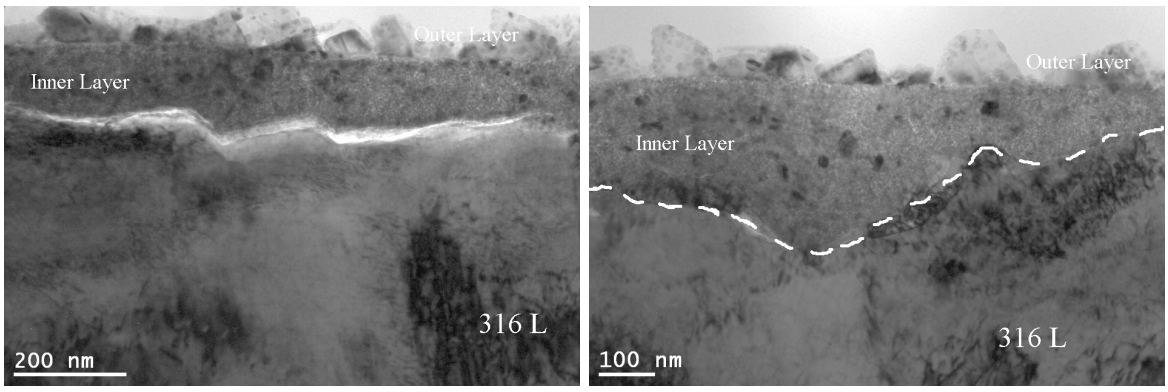

(a) (b)

Figure 5.21: Two TEM micrographs on LE11-02 ref (72hr, 133_smbar): (a) and (b) different spots.

The sets of TEM micrographs are shown in Fig.5.22 & 5.23 for the inner and outer layer of the oxide film formed on LE11-02 ref (72hr, 133_smbar). Surprisingly, a dispersion of **second phase** particles can be found for both layers.

For the inner layer, the existence of the *second phase* is indicated in Fig.5.22 (a) and enlarged in (b). A detachment of inner layer and the substrate (316L) can be observed in Fig.5.22 (c). Fig.5.22

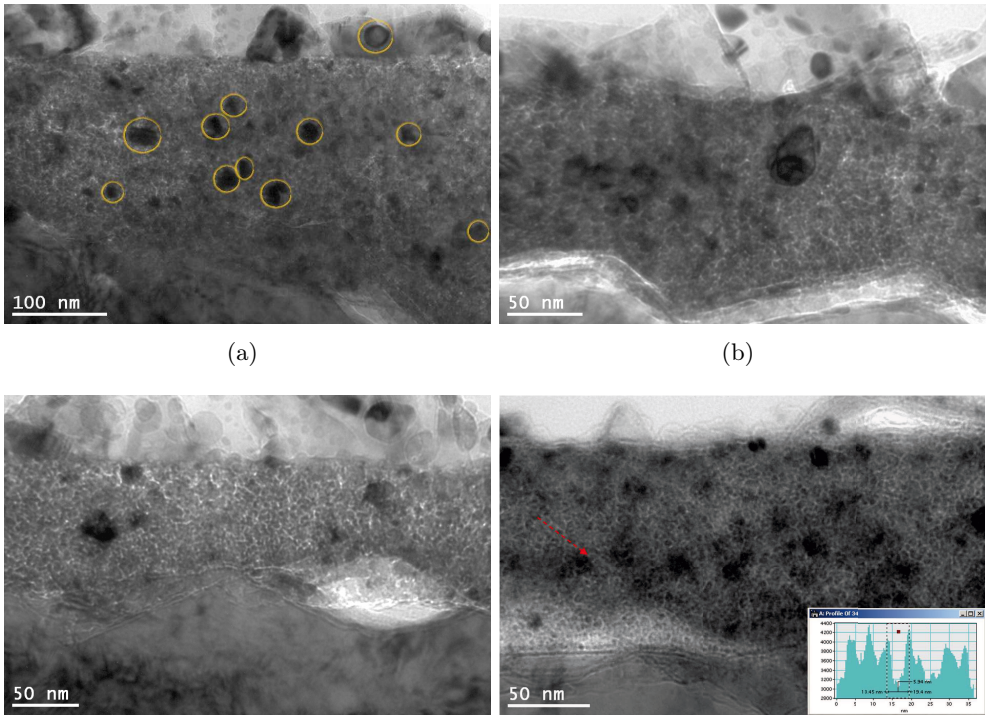

(a) (b)

(c) (d)

Figure 5.22: TEM micrographs on the inner layer of the oxide film formed on LE11-02 ref (72hr, 133$_s$mbar): (a), (b), (c) and (d), different spots of the inner layer.

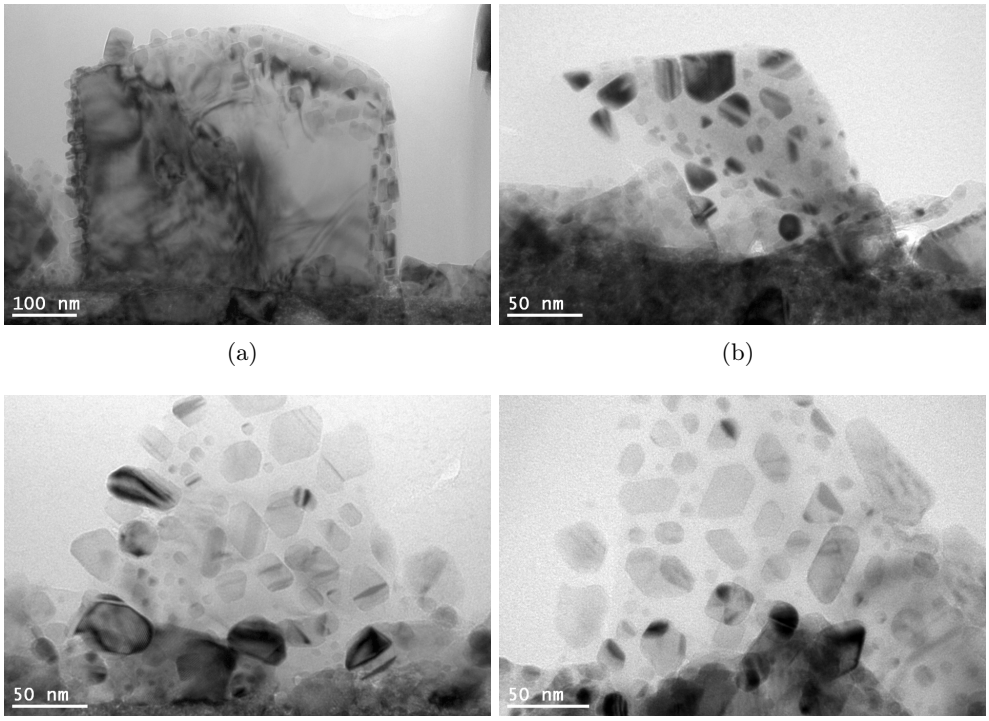

(a) (b)

(c) (d)

Figure 5.23: TEM micrographs on the outer layer of the oxide film formed on LE11-02 ref (72hr, 133$_s$mbar): (a), (b), (c) and (d), different spots of the outer layer.

(d) is taken in under-focus mode (*Fresnel contrast*) in order to estimate the mean grain size of the inner layer with the assistance of the profile spectrum (insert image) of the red arrow mark. It reveals that the inner layer is composed of nano-grains with an average size of about 5 nm.

There are crystallites with different sizes on the outer layer. It also exists the *second phase* presented everywhere on the analysed sample, as shown in the four images of Fig.5.23.

In brief, the TEM micrographs clarify the double-layer structure of the oxide film formed on 316L under primary PWR conditions. Moreover, it exhibits the irregularity of the thickness of the inner layer. The evolution of the thickness may not only come from the outer crystallites but also from the continuous inner layer. In addition, *second phases* are observed in both layers, which have not be found in the literature.

5.2.E.2 Composition

The composition of the oxide layer is analysed by the EDX device, equipped with the TEM microscope. Fig.5.24 illustrates the elemental identification for the observed *second phase* while Fig.5.25 shows the compositional profiles for the line-scans.

In Fig.5.24, it shows four spot EDX analyses on both inner (figures (a) & (b)) and outer (figures (c) & (d)) layers. Some of the spots are aiming at the *second phase*, others are meant for the generality of the inner or outer layer. It clearly reveals that:

- **Inner layer:** it is an oxide mainly composed by chromium and iron, as demonstrated by the insert quantification tables of spectra 2 and 4 in the figure (b). Furthermore, the chromium content increases while the iron content decreases from the spot 4 to the spot 2. It implies that the more iron participates in the oxide near the outer layer interface. Mo may poorly participate in the formation in the inner layer. However, Ni is only observed in the spectra 1 and 3 but not 2 and 4. It elucidates that Ni is the major component of the *second phase*. In short, the composition of inner oxide layer is $Fe(Fe, Cr)_2O_4$, where the proportion of Fe^{3+} depends on the depth, together with a *second phase* where Ni is the major component.

- **Outer layer:** it is an oxide rich in iron in general, as shown in the spectra 3 and 4 in the figure (d). Ni is poorly presented in the outer layer. Therefore, the most possible composition for the outer layer is $(Ni, Fe)Fe_2O_4$ with low Ni content. Based on the spectra 1 and 2, the *second phase* is also extremely rich in Ni. Noting that the Si presented in the spectra comes from the silica deposit during the sample preparation.

Two profile line-scans, indicated by red arrows in Fig.5.25 (a) & (c), have been performed across the oxide layer. It clarifies several points:

- **Double-layer structure** of the oxide film is clearly demonstrated by the compositional profile spectra (Fig.5.25 (b) & (d)):

  1. a layer of $30 \sim 50\%$ iron with $20 \sim 40\%$ oxygen is observed, revealing an outer oxide rich in iron;

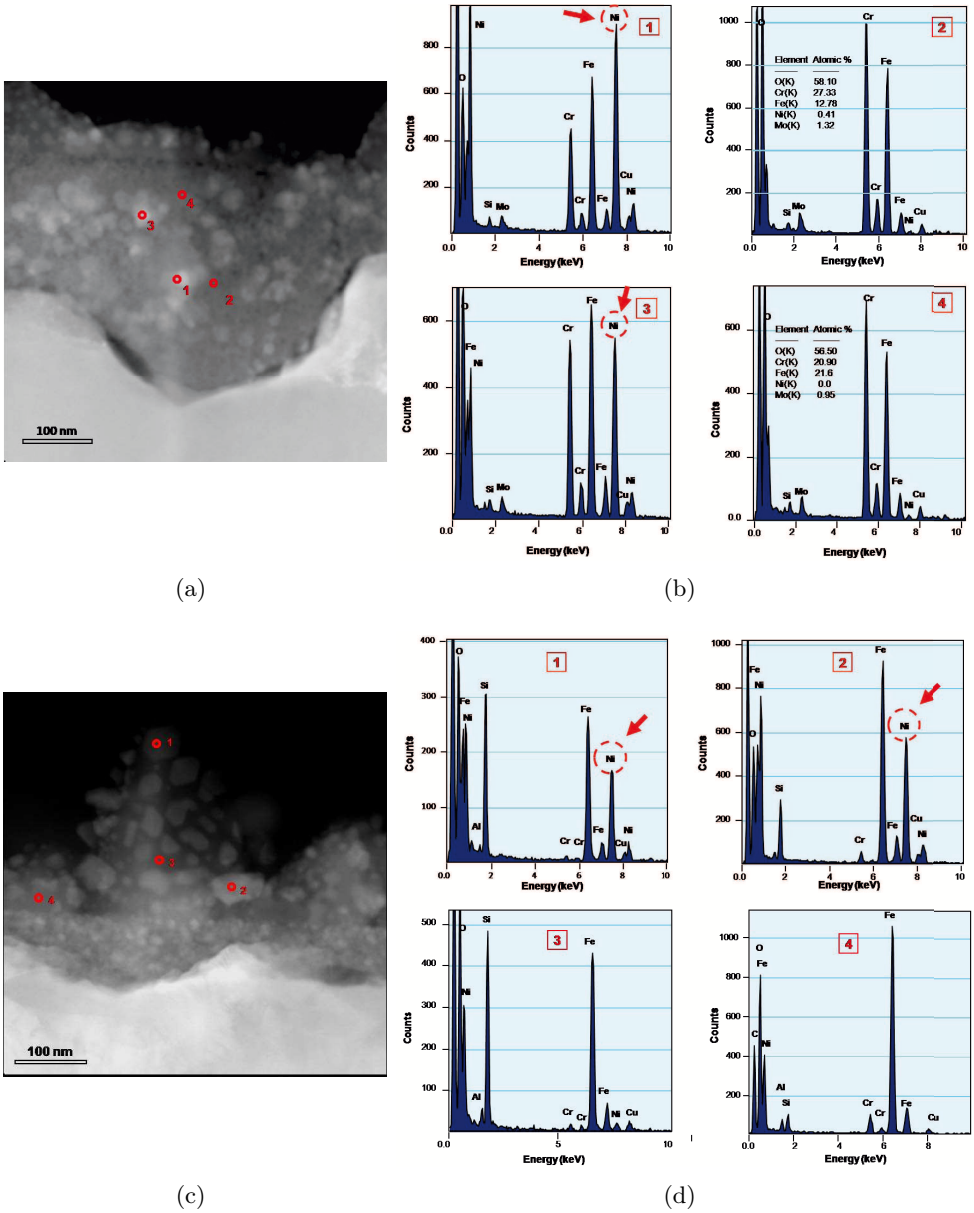

Figure 5.24: TEM-EDX Analysis on LE11-02 ref (72hr, 133$_s$mbar), (a) & (b) for the inner layer, (c) & (d) for the outer layer. (a): STEM-HADDF image of the inner layer; (b): EDX spectra of different spots indicated in (a); (c): STEM-HADDF image of the outer layer; (d): EDX spectra of different spots indicated in (c).

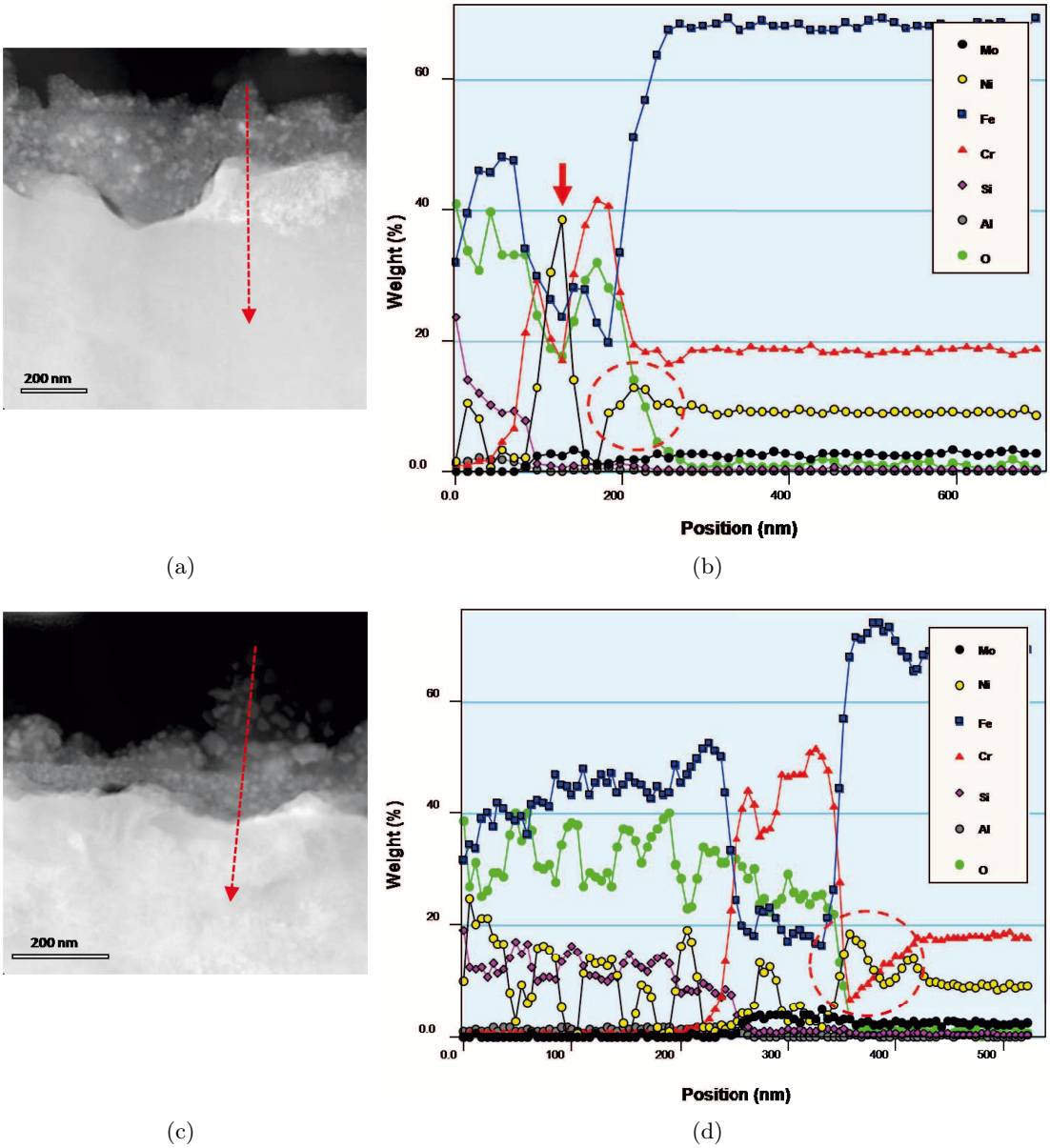

Figure 5.25: STEM-HAADF Analysis on LE11-02 ref (72hr, 133$_s$mbar), (b) & (d) are the EDX compositional profiles obtained across the oxide layer, the paths are indicated in (a) & (c), respectively.

2. afterwards, iron decreases to about 20% while chromium increases sharply to 40 $\sim$ 50% with the same level of oxygen content. This is the inner oxide rich in chromium;
3. finally, it comes to the 316L bulk elements with nearly 70% of iron, when oxygen drops to zero and chromium decreases to a little bit less than 20%.

- **Equivalent thickness** of the oxide films varies a lot, depending on both inner and outer layers. As shown in Fig.5.25 (b) & (d), the thicknesses are about 200 nm and 360 nm, respectively. In general, the inner oxide layer is around 150 nm thick. However, it can be up to 300 nm in several cases. The outer layer is more irregular and it mainly depends on the size of the crystallites.
- **Ni enrichment** in the oxide/metal interface can also be proved. Generally, the nickel enrichment is always with an depletion of chromium, as emphasised by the red circles in Fig.5.25 (b) & (d).
- **Second phase** particles are rich in Ni. Instead of being present continuously in the oxide film, Ni increases discontinuously. Therefore, the presence of Ni in the oxide film seems to be under the form of this *second phase* rather than in the oxide film.
- **Mo** slightly participates in the formation of the inner layer.

Above all, the composition of the oxide film obtained by the TEM investigation is in agreement with the other analyses (SEM-EDX, XPS and Raman). In addition, in the inner layer of the oxide film, a decrease of iron content is observed from the metal interface to the outer layer interface. Though the presence of nickel as a *second phase* in both layers found by TEM investigation has never been observed by the other techniques.

5.2.E.3 Crystal Structure

The crystal structure of both inner and outer layers are shown in Fig.5.26, (a) & (b) for the inner layer, (c) and (d) for the outer layer.

The diffraction pattern illustrated in Fig.5.26 (b) is a series of **rings**, with the atomic distances indicated in blue and the crystal orientations in yellow. It elucidates that the inner layer has a polycrystalline structure of a spinel oxide AB_2O_4. Considering the EDX results, the **A** stands for Fe and **B** means for Fe and Cr, thus it is a spinel oxide $\mathbf{Fe(Fe,\ Cr)_2O_4}$. Surprisingly, other than the ring pattern, some dots under illumination can also be observed, their orientations are indicated in red. It is actually a dispersion of crystals of metallic Ni.

The diffraction pattern showed in Fig.5.26 (d) is a pattern of dots, with the crystal orientations of metallic Ni indicated in red and the ones of spinel oxide indicated in blue. Based on the space group symmetries in the crystal and the crystal orientation, it reveals that a spinel oxide structure for the outer layer. Coupled with EDX analysis, it is probably a spinel oxide (Ni, Fe)Fe_2O_4. However, according to the observation of Fig.5.24 (c) & (d), it may be considered that the presence of Ni in the oxide is extremely little because it is mainly under the form of a *second phase*. It is worth noting that some double diffractions of the spinel oxide and metallic Ni, indicated in green, can also be observed.

Briefly, the crystal structure of the spinel oxide formed on 316L stainless steel under primary PWR conditions is well proved by the TEM investigation. However, the presence of metallic Ni was not

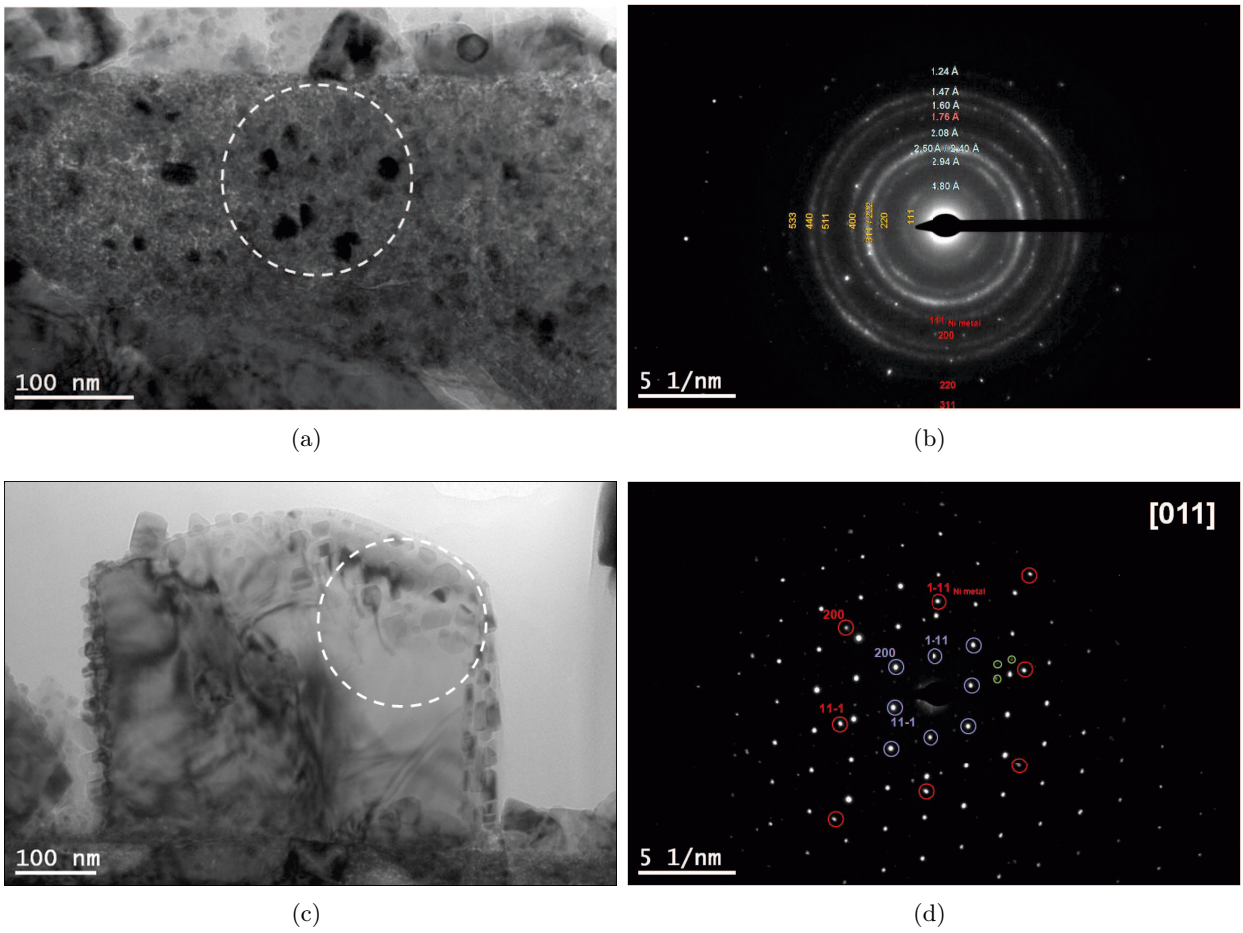

(a) (b)

(c) (d)

Figure 5.26: TEM-SAD analysis on LE11-02 ref (72hr, 133$_s$mbar): (b) & (d) are the electron diffractograms of the selected area on images (a) & (c), respectively. Indicators: blue and yellow for the spinel oxides; red for the metallic Ni and green for the double diffraction.

expected. It implies that there are metallic Ni in the inner and the outer layer of the oxide film formed on LE11-02 ref. The finding was reported previously in the literature for the inner layer [18] but not to the outer layer.

To sum up the TEM investigations as a whole, we conclude that:

- an existence of a *second phase* in both layers is observed in the TEM micrographs;
- the *second phase* is mainly rich in Ni, proven by EDX analyses;
- a presence of metallic Ni in both layers is detected by SAD analyses.

It is not difficult to draw the conclusion that the *second phase* observed is metallic Ni. It may explain that the absence of Ni oxide in the formation of the oxide film, especially for the outer layer. The presence of metallic Ni is probably due to the hydrogen pressure in the HTHP cell during the experiment. Metallic Ni has not been detected by XPS analysis in the first time. A recheck after TEM investigation contrarily demonstrates the existence of metallic Ni. However, the first XPS analysis

was only carried out in two spots while the second one was performed in a line scan. Therefore, the metallic nickel may not be detected from the first analysis, due to its low quantity or to the fact that it is not presented everywhere.

5.2.F GD-OES Analysis

GD-OES, *Glow Discharge Optical Emission Spectrometry*, is an analytical technique used for isotope ratio measurements and trace elements determination in solid samples. It provides a method to analyse elements in depth profiling of oxide films. Indeed, it is a more industrial techniques which may lack precision for the analysis. However, its analysis spot is about 4mm^2, which may bring a confirmation of the chemical composition of the oxide film in a much larger scale.

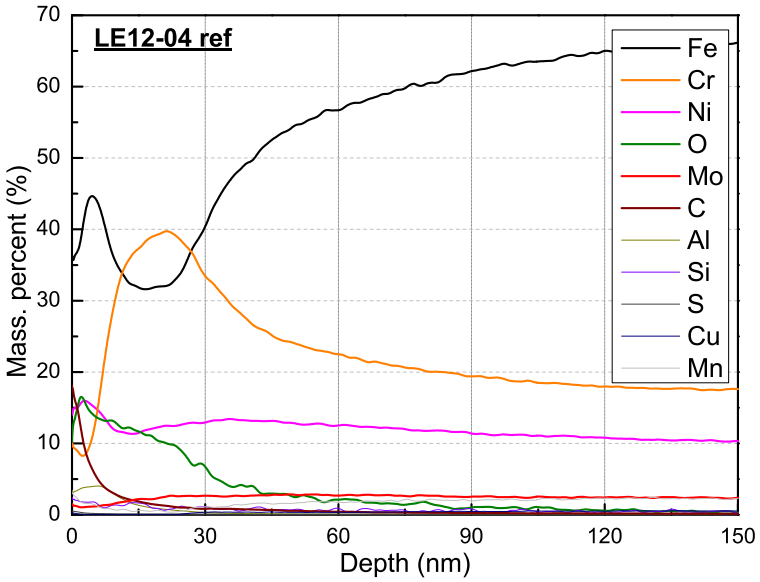

Figure 5.27: GD-OES elemental scan in depth profile for zone 1 (central zone) on LE12-04 ref (120hr, 33$_s$mbar), error bar: ±5%.

Fig.5.27 illustrates that an elemental scan in depth on the zone 1 of LE12-04 ref (120hr, 33$_s$mbar). It needs to be emphasised that it is prepared under normal hydrogen pressure. Based on the spectra, it demonstrates that:

- The first ∼ 12 nm is enriched in Fe, Ni and O, which reveals the major constituents of the outer layer.
- Between 12 and ∼ 30 nm, it indicates the inner oxide layer rich in chromium, together with Fe and Ni. Meanwhile, a slight enrichment in Mo can also be observed.
- From ∼ 30 nm, oxygen and chromium drop while iron increases sharply. It means that they approach to the bulk concentration of the substrate elements of the 316L stainless steel.
- A broad and slight increase of nickel exists in the range of 30 to 60 nm. Afterwards, it decreases to its bulk concentration. It might involve the Ni enrichment at the oxide/metal interface.

- Carbon presented in the extra-surface is a contamination of the surface.
- Since the analysis spot is relatively large, about 4 mm^2, the irregularity of the equivalent thickness of the oxide film is well represented by the straggling of the oxygen line shape.

Overall, the results of GD-OES analysis provide a confirmation on the chemical composition of the oxide film we obtained by the other techniques.

5.2.G CS-AFM Analysis

CS-AFM, *Current Sensing Atomic Force Microscopy*, can be used to study the topography and the local electronic properties of the oxide film.

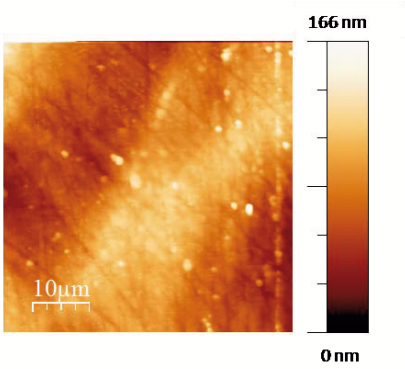

Figure 5.28: CS-AFM analysis in the zone 1 (central zone) of LE11-03 ref (168hr, 33_smbar): Topography AFM image of the **back face** of 316L, which is not in contact with PWR water but with air.

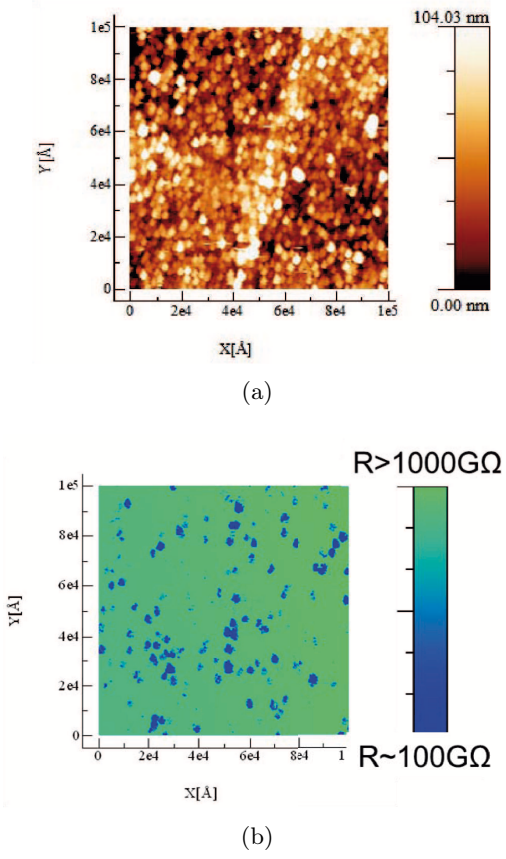

Figure 5.29: CS-AFM analysis in the zone 1 (central zone) of LE11-03 ref (168hr, 33_smbar): (a) topography AFM image and (b) resistance AFM image of the interface in contact with PWR water, respectively.

Fig.5.28 illustrates the topography image obtained by AFM of PWR water free surface, so-called **back face**. It means that the oxide film was formed under air at 300°C. Actually, multiple spots have been analysed, and no current can be detected for the whole surface. Briefly, the **back face** is almost electrically insulated (resistance $>$ 1000 GΩ).

On the other hand, the interface in contact with PWR water is represented in Fig.5.29. The surface is rough (Fig.5.29 (a)), which is linked to the crystallites on the surface. The observation is in accordance with the SEM micrographs (Fig.5.5). However, the comparison between the topography and the resistance images reveals that certain crystallites are more conductive than the others. However, the finding is not systematic for all the crystallites on the surface, (Fig.5.29 (b)). Thus, it implies that different types of crystallites are presented on the surface. The resistance of the interface varies from $\sim$ 100 to 1000 GΩ.

In summary, the CS-AFM analysis of LE11-03 ref (168hr, 33_smbar) gives the following information:

- the interface in contact with PWR water is more rough and less insulated than the interface in contact with air **back face**, which should be related to the different processes of the oxide formation in PWR conditions and in air, respectively;
- more than one type of crystallites are presented on the surface, with large variation of electrical resistances.

5.3 PWR water analysis

PWR water used in the HTHP cell is referred as the liquid interface, which needs to be characterised after the experiments. Tab.5.5 shows the results of the solution analyses, pH and released/ dissolved cations values. However, not all the analyses can be performed due to the lack of solution after ICP-AES analysis. As for the LE11 $-$ 02 ref (72hr, 133_smbar), none of the analyses has been done.

Specimens	pH	Fe	Cr	Ni	Zn	Cu	Mo
				(μg/L)			
PWR water (blank)	6.1 $\sim$ 6.4	0.5	1.8	< 3	< 3	< 3	< 3
LE12-04 ref	4.29	3700	5	324	269	14	9
LE11-03 ref	-	2945	4.3	126	15	-	-

Table 5.5: Concentration of released and dissolved cations and pH of solution: blank PWR water, LE12-04 ref (120hr, 33_smbar), LE11-03 ref (168hr, 33_smbar) after the experiment, error bar: $\pm$3%. - : lack of solution.

The blank PWR water contains 1000 ppm [B] and 2 ppm [Li], the ICP-AES results show that it can be considered as clean before being used in the HTHP cell. Most of the elements are under the detection limit of the techniques, which is 3 μg/L. For iron and chromium, the detection limit is better (less than 3 μg/L). The high concentration of cations detected for LE12-04 ref (120hr, 33_smbar) and LE11-03 ref (168hr, 33_smbar) can be thought as the cations release from the 316L stainless steel discs during the reference experiments.

Comparing the cation release between LE12-04 ref (120hr, 33_smbar) and LE11-03 ref (168hr, 33_smbar), which has the same hydrogen pressure, it reveals that the cation release dose not increase with the duration at 300°C. Oppositely, the cation release (Fe, Cr, Ni, Zn and etc.) of LE11-03 ref (168hr, 33_smbar) are less than the one of LE12-04 ref (120hr, 33_smbar). Indeed, the pH value of

LE12-04 ref (120hr, 33_smbar) is quite low. The increase of acidity may explain the high release of cations from the 316L stainless steel into the solution.

Concerning the release of each cation:

- **Fe:** is the most released element among all. The dissolution of Fe is considered as the first step for the formation of the outer layer [19]. Afterwards, it may deposit on the surface and become the crystallites we have observed by SEM, or it may stay as dissolved in the PWR water. Furthermore, the crystallites formed, which is mainly iron oxide can dissolve again into the PWR water. As a result, the release of Fe is significant as analysed by ICP-AES.
- **Cr:** is the least released element among all due to the fact that it forms the chromium oxide, the inner protective and stable layer against the corrosion. On the other hand, the solubility of Cr in the primary PWR water is relatively low. Consequently, there is nearly no Cr release that can be detected in the PWR water.
- **Ni:** releases less than Fe but more than Cr. As shown by the surface characterisation, Ni is the other element for the crystallites formed on the outer layer.
- **Zn:** is a contamination element observed on the both media: the 316L surface and the PWR water.
- **Others:** minor releases of Cu and Mo are detected, which can be linked to the minor presence on the bulk 316L discs. Moreover, the Cu may also be a contamination from the HTHP cell.

5.4 Summary

In this chapter, the results of the reference experiments have been presented. They can be divided into three parts, the *in-situ* results during the thermal treatment concerning the electrochemistry, and the hydrogen dissolution, the *ex-situ* results after the thermal treatment concerning the characterisations of the oxide film and the analysis of PWR water, respectively.

Both the electrochemical behaviour at the interface between 316L and PWR water and the amount of the dissolved hydrogen in the PWR water are mostly affected by the **thermal ageing**. The oxide film formed on stainless steel can be influenced by external factors such as water chemistry and oxidising-reducing conditions [20, 21]. Therefore, the decrease of potential caused by thermal ageing on one hand demonstrates a change of the electrochemical properties of the interface, and on the other hand implies that an evolution of the oxide film.

Multiple techniques have been used to characterise the oxide film. For all three 316L discs, the results show that it is a double-layer structured spinel oxide, inner rich in chromium ($Fe(Fe,Cr)_2O_4$) and outer rich in iron ($(Ni,Fe)Fe_2O_4$). The inner oxide layer is continuous and compact while the outer one is discontinuous and in the form of crystallites. The equivalent thickness of the layers and the aspect of the surfaces vary with the duration of the thermal treatments and the initial dissolved hydrogen in the solution. The size and the density as well as the composition of the crystallites precipitated on the surface also evolve with the hydrogen dissolved in the solution. For a relatively high concentration of dissolved hydrogen, metallic Ni is detected in the oxide film.

The analysis of the solution after thermal treatment show that the discs release cations such as Fe, Cr, Ni, Zn in the PWR water while the acidity of the solution increases.

The correlation between the changes induced by the thermal treatment in the oxide film, the dissolved solutes in the PWR water and the free potential suggest that the reduction of the hydrogen takes place at the interface during the oxidation of the metallic species.

References

[1] Parisot J. F. *La corrosion et l'altáeration des material du nucléaire*. CEA Group et Group Moniteur, 2010.

[2] Tapping R.L. and Davidson R.D. and McAlpine E. and Lister D. H. The composition and morphology of oxide films formed on type 304 stainless steel in lithiated high temperature water. *Corrosion Science*, 26(8):563 – 576, 1986.

[3] Takeda Y. and Shoji T. and Bojinov M. and Kinnunen P. and Saario T. In situ and ex situ characterisation of oxide films formed on strained stainless steel surfaces in high-temperature water. *Applied Surface Science*, 252(24):8580 – 8588, 2006.

[4] Féron D., Herms E., Tanguy B. Behavior of stainless steel in pressurized water reactor prirmary circuits. *Journal of Nuclear Materials*, 427:364–377, 2012.

[5] Biesinger M. C., Brown C., Mycroft J. R., Davidson R. D., Mclntyre N. S. X-ray photoelectron spectroscopy studies of chromium compounds. *Surf. Interface Anal.*, 36:1550–1563, 2004.

[6] Biesinger M. C., Payne B.P., Grosvenor A. P., Lau L. W. M., Gerson A. R., Smart R. St. C. Resolving surface chemical states in XPS analysis of first row transition metals, oxides and hydroxides: Cr, Mn, Fe, Co and Ni. *Applied Surface Science*, 257:2717–2730, 2011.

[7] Payne B.P., Biesinger M. C., McIntyre N. S. X-ray photoelectron spectroscopy studies of reactions on chromium metal and chromium oxide surfaces. *Journal of Electron Spectroscopy and Related Phenomena*, 184:29–37, 2011.

[8] Loïc Marchetti-Sillans. *Corrosion généralisée des alliages á base nickel en milieu aqueux á haute température: apport á la compréhension des mécanismes*. PhD thesis, Ecole Nationale Supérieure des Mines de Saint-Etienne, 2007.

[9] Marchetti L., Miserque F., Perrin S., Pijolat M. XPS study of Ni-base alloys oxide films formed in primary conditions of pressurised water reactor (internal reference, private communication). Technical report, CEA, 2013.

[10] Grosvenor A. P., Kobe B. A., Biesinger M. C., Mclntyre N. S. Investigation of multiplet splitting of Fe 2p XPS spectra and bonding in iron compounds. *Surf. Interface Anal.*, 36:1564–1574, 2004.

[11] Payne B.P., Biesinger M. C., McIntyre N. S. Use of oxygen/nickel ratios in the XPS characterisation of oxide phases on nickel metal and nickel alloy surfaces. *Journal of Electron Spectroscopy and Related Phenomena*, 185:159–166, 2012.

[12] Biesinger M. C., Payne B.P., Gerson A. R., Smart R. St. C. X-ray photoelectron spectroscopic chemical state quantification of mixed nickel metal, oxide and hydroxide systems. *Surf. Interface Anal.*, 41:324–332, 2009.

[13] Biesinger M. C., Lau L. W. M., Gerson A. R., Smart R. St. C. Resolving surface chemical states in XPS analysis of first row transition metals, oxides and hydroxides: Sc, Ti, Cu and Zn. *Applied Surface Science*, 257:887–898, 2010.

[14] Terachi T. and Yamada T., Miyamoto T., Arioka K., Fukuya K. Corrosion Behavior of Stainless Steels in Simulated PWR Primary Water - Effect of Chromium Content in Alloys and Dissolved Hydrogen -. *Journal of NUCLEAR SCIENCE and TECHNOLOGY*, 45(10):975–984, 2008.

[15] Terachi T. and Fujii K., Arioka K. Microstructural Characterization of SCC Crack tip and Oxide Film for UNSS 316 Stainless Steel in simulated PWR Primary Water at 320°C. *Journal of NUCLEAR SCIENCE and TECHNOLOGY*, 42(2):225–232, 2005.

[16] Perrin S., Marchetti L., Duhamel C., Sennour M., Jomard F. Influence of Irradiation on the Oxide Film Formed on 316L Stainless Steel in PWR Primary Water. *Oxid. Met.*, 2013.

[17] Soulas R., Cheynet M., Rauch E., Neisius T., Legras L., Domain C., Brechet Y. TEM investigations of the oxide layers formed on a 316L alloy in simulated PWR environment. *J Mater Sci*, 48:2861–2871, 2013.

[18] Sergio Lozano-Perez, David W. Saxey, Takuyo Yamada, Takumi Terachi. Atom-probe tomography characterization of the oxidation of stainless steel. *Scripta Materialia*, 62(11):855 – 858, 2010.

[19] D.H. Lister and R.D. Davidson and E. McAlpine. The mechanism and kinetics of corrosion product release from stainless steel in lithiated high temperature water. *Corrosion Science*, 27(2):113 – 140, 1987.

[20] Haupt S., Strehblow. A combined surface analytical and electrochemical study of the formation of passive layers on Fe/Cr alloys in 0.5 M H_2SO_4. *Corrosion Science*, 37(1):43–54, 1995.

[21] Olsson C-O. A., Hamm D., Landolt D. Electrochemical Quartz Crystal Microbalance Studies of the Passive Behavior of Cr in a Sulfuric Acid Solution. *Journal of The Electrochemical Society*, 147(7):2563–2571, 2000.

Chapter 6

Irradiation Experiments

The results of irradiation experiments are divided into two parts, the proton and the electron irradiations. The proton results are only focused on the electrochemistry because all samples are activated after the irradiations. Surface analysis is thus not possible. Meanwhile, the electron irradiation are performed for both the electrochemical behaviour and the interface characterisation.

The results will be presented in the same order as for the reference experiments. It starts with the electrochemistry results, followed by the electron irradiated 316L oxide film characterisation and ends up with the PWR water analyses.

6.1 Hydrogen & Electrochemical Behaviour under Proton Irradiation

The first part of electrochemical behaviour at an interface between 316L and PWR water was investigated under proton irradiation. As stated previously (Ch.4.4.A.2), two sequential irradiation experiments were carried out under different conditions, as indicated in Tab.6.1. It should be emphasised that the 316L stainless steel disc (metal interface) was not changed while the PWR water was renewed between the two sequential irradiations.

Proton Experiments					
Specimens	Energy (MeV)	Flux (nA)	Irradiated Duration (h)	Thickness (mm)	Hydrogen Pressure at 300°C (mbar)
LE11-01 irr (D)	23/12	3×10^{-3} - 30	13.5	~ 1	29(s, L) - 390(s, H)
LE11-01 irr (D)	23/12	3×10^{-3} - 10	13.5	~ 1	29*

Table 6.1: List of proton irradiation experiments with detailed conditions: energy, flux, duration under irradiation, thickness of the 316L disc and hydrogen pressure at 300 °C. D): discontinuous irradiation experiment; (L): low hydrogen pressure; (H): high hydrogen pressure; (s): the initial hydrogen pressure, first measured at 300°C by the sensor; *: estimated value.

Fig.6.1 illustrates the irradiation history of the two sequential experiments. Temperature of the cell is plotted in red and the flux of each irradiation is shown as blue columns.

1^{st} sequential irradiations The irradiations began with low flux, 6.6×10^7 $H^+.m^{-2}.s^{-1}$, (intensity: 3 pA) at high temperature, nearly 300°C and with a 29 mbar hydrogen pressure, measured by the hydrogen sensor. Afterwards, the flux increased gradually with different irradiations, 6.6×10^8 $H^+.m^{-2}.s^{-1}$ (intensity: 30 pA), 6.6×10^9 $H^+.m^{-2}.s^{-1}$ (intensity: 300 pA), 6.6×10^{10} $H^+.m^{-2}.s^{-1}$ (intensity :3 nA) until 6.6×10^{11} $H^+.m^{-2}.s^{-1}$ (intensity: 30 nA), which is the flux used for most irradiations. Then, once the flux was fixed at 6.6×10^{11} $H^+.m^{-2}.s^{-1}$ (30 nA), the temperature was cycled from 150 to 300°C for different irradiations. The first part of the sequential irradiations were carried out at low hydrogen pressure. By adding the hydrogen into the HTHP cell via the hydrogen pressure sensor and let it diffuse at high temperature until it became stable inside the cell (one night). The second part of the sequential irradiations were done at high hydrogen pressure, around 390 mbar. As same as the first part, most irradiations were carried out at 6.6×10^{11} $H^+.m^{-2}.s^{-1}$ (30 nA) at various temperatures ($[150 \sim 300]$°C).

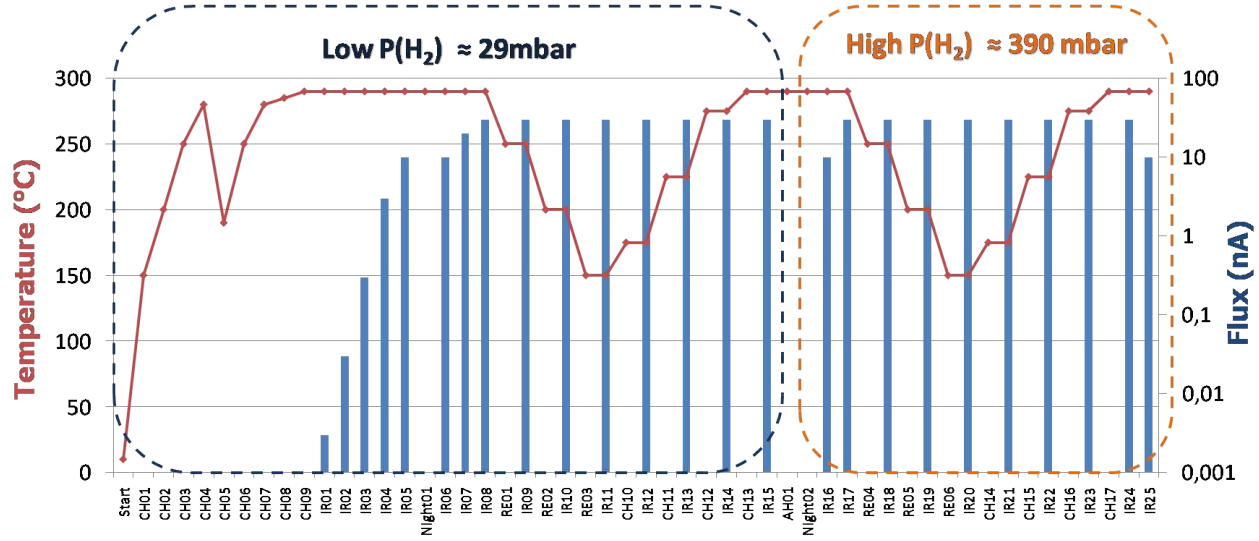

(a) 1^{st} sequential irradiations

(b) 2^{nd} sequential irradiations

Figure 6.1: History diagrams of two sequential irradiation experiments performed on LE11-01 irr (D). Red curve: temperature of the HTHP cell; blue column: flux for each irradiation. (a): 1^{st} sequential irradiations: $[25, 300]$°C, $[3 \times 10^{-3}, 30]$nA; (b): 2^{nd} sequential irradiations with a fixed initial hydrogen pressure 29 mbar: $[25, 300]$°C, $[3 \times 10^{-3}, 10]$nA.

2^{nd} sequential irradiations The irradiations began with low flux, 6.6×10^7 $H^+.m^{-2}.s^{-1}$ (3 pA) at room temperature. Afterwards, both flux and temperature increase gradually with each irradiation. The maximum flux and temperature were 2.2×10^{11} $H^+.m^{-2}.s^{-1}$ (10 nA) and 275°C, respectively. The hydrogen pressure in the cell should be the same with the low pressure of the 1^{st} sequence experiment, as the preparations were done in the same way.

In brief, the effect of radiolysis on electrochemical behaviour of stainless steel 316L under proton irradiation are investigated based on the results of these two sequential irradiation experiments.

6.1.A Flux Influence

Muzeau *et al.* [1] have announced a preliminary result on the flux effect under proton irradiation with the HTHP cell. However, a further study on the flux effect at 300°C has been carried out, as shown in Fig.6.2, after some improvements were done on both cell and the beam energy after his work.

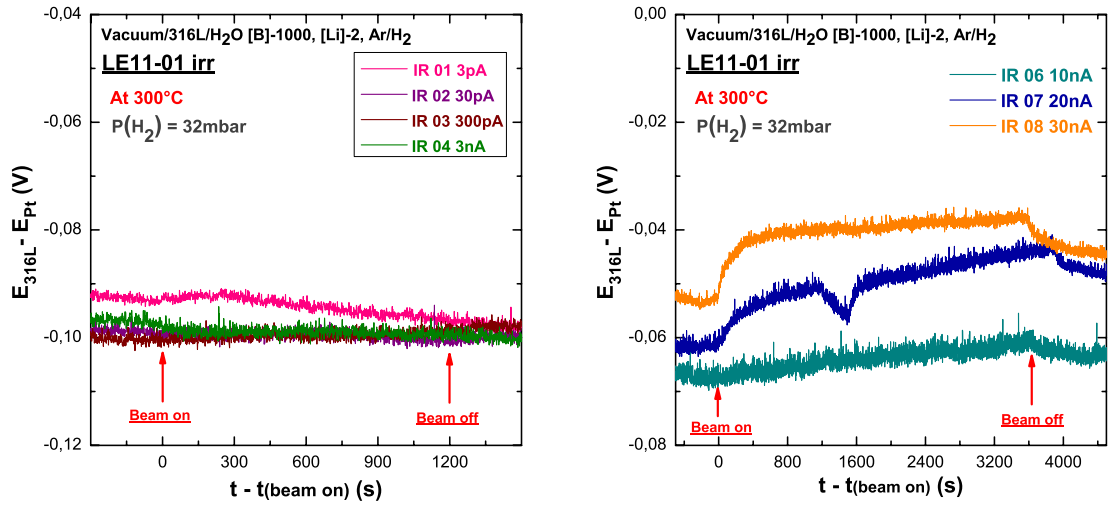

(a) (b)

Figure 6.2: 1^{st} sequential irradiations experiments of LE11-01 irr (D), potential between 316L and Pt as a function of time at 300°C and P(H_2) 32 mbar: (a) flux intensity for IR01 - IR04 are listed in proper order: 3pA, 30pA, 300pA, and 30nA; (b) flux intensity for IR06 - IR08 are listed sequentially: 10nA, 20nA and 30nA.

In Fig.6.2 (a), no obvious change of the free potential between the 316L and the platinum can be noticed in the presence of proton beam for IR01 - IR04, which flux varies from 3 pA (6.6×10^7 $H^+.m^{-2}.s^{-1}$) to 3 nA (6.6×10^{10} $H^+.m^{-2}.s^{-1}$). Contrarily, response of the potential under proton beam can be seen in Fig.6.2 (b), for IR06 - IR08. Their flux were 10 nA (2.2×10^{11} $H^+.m^{-2}.s^{-1}$), 20 nA (4.4×10^{11} $H^+.m^{-2}.s^{-1}$) and 30 nA (6.6×10^{11} $H^+.m^{-2}.s^{-1}$), respectively. More precisely, based on the results shown in Fig.6.2 (b), it is clear that:

- The potential response between 316L and platinum under a proton beam is an **oxidative** response. It increases when the beam is switched-on while it decreases when the beam is cut-off. Since the platinum wire is situated at the position out of irradiation zone, this oxidative response

observed should come from the interface. It implies that the irradiation/ radiolysis at the interface leads to an increase of free potential. In other words, the effect of radiolysis, creating the radiolysis species in the media (PWR water), can be observed on the corrosion potential.

- The potential response under proton irradiation increases with the flux. The higher the flux, the stronger the potential response. Furthermore, it seems that the kinetics of the potential evolution is also correlated with the flux. With a higher flux, the potential response reaches a stationary value faster under irradiation. In the same way, the potential decreases faster with a higher flux after the beam is cut-off.

- The free potential between 316L and platinum after irradiation seems to be higher than the one before irradiation.

Comparing the two figures (Fig.6.2), a **threshold** is observed for the radiolysis effect being observed on the electrochemical potential. If the local chemistry changes at the interface are important, it will certainly lead to a change on the electrochemical potential of the interface. It means that the irradiations with the lower flux, as illustrated in Fig.6.2 (a), did not lead to enough interfacial chemistry change. Thus, the water decomposition is not intense enough to be exhibited by the electrochemistry measurement. The flux, also noted as the *dose rate*, reflects the intensity of radiation. As stated in Chapter 2, with the increase of flux, higher concentrations of radicals are produced by the irradiation. Briefly, the water decomposition is promoted with the flux. In consequence, it explains the electrochemical potential variation at the interface under irradiation. Besides, compared the potential after and before irradiation, it seems to be slightly enhanced. This may also be related to the stable oxidising species, such as H_2O_2, produced by the water radiolysis and remain in the solution afterwards.

Furthermore, the kinetics of the potential evolution can also be explained by the flux influence. The reactions at the interface become faster with a higher concentration of radicals, and hence more quickly they can be reflected on the electrochemical potential. Likewise, when the beam is cut-off, the potential evolution react faster with the higher flux irradiation.

Temperature (°C)	$g(e^-_{aq})$	$g(H_2)$	$g(H^\bullet)$	$g(OH^\bullet)$	$g(H_2O_2)$
25	2.75	0.44	0.60	2.81	0.71
50	2.87	0.45	0.64	3.07	0.67
100	3.10	0.47	0.71	3.57	0.59
150	3.31	0.49	0.80	4.07	0.51
200	3.46	0.51	0.94	4.57	0.43
250	3.51	0.56	1.18	5.12	0.35
300	3.43	0.64	1.56	5.74	0.27
350	3.19	0.76	2.11	6.45	0.19

Table 6.2: Table of the g-values for low LET radiation deposited in light water at temperature between 25°C and 350°C [2].

On the other hand, proton beam can be considered as a low LET radiation, (see Chapter 2, Tab.2.2). Based on the g-value proposed by Elliot *et al.* [2], Tab.6.2, it reveals that the radiolytic

yields of oxidising products ($OH^\bullet$ and H_2O_2) are superior the ones of reducing radicals (e^-_{aq}, $H^\bullet$ and H_2) at 300°C. It may be the reason that the potential response under proton irradiation at 300°C is **oxidative**. Moreover, according to this table, the reducing radicals overcome the oxidising species below 150°C. And just over 150°C, the oxidising products defeat the reducing radicals and become more dominant with the increase of temperature.

The hypothesis of *oxidative response* under proton irradiation is established without considering the diffusion of the radiolysis species. They may diffuse out of the irradiation zone, towards the platinum wire and eventually influence the potential. However, the presence of radicals in the solution is extremely short, they are more likely react with each other rather than diffuse in the solution. Therefore, the diffusion issue can only be addressed to the stable species, meaning H_2O_2, H_2, H^+ (H_3O^+) and OH^-. Based on the reference [2], the diffusion coefficient of H^+ and OH^- are close at high temperature (300 $\sim$ 350°C). For H_2O_2 and H_2, there is no specific data about their diffusion coefficient.

Few comments can be made on the thermal decomposition of H_2O_2 at high temperature, such as Eqs.6.1. It seems that there are two regimes where an activation energy near 65 kJ/mole is observed up to 200°C and then a lower value near 43 kJ/mole is found above 200°C. This apparent change leads to the thermal decomposition of H_2O_2 becoming mass transport limited for the transfer of H_2O_2 from the bulk solution to the surface. In other words, the H_2O_2 decomposition at high temperature is considered to occur principally on the wall surface of the container [2].

$$H_2O_2 \rightarrow \frac{1}{2}O_2 + H_2O \qquad H_2O_2 \rightarrow 2OH^\bullet \tag{6.1}$$

From another perspective, instead of considering the diffusion of H_2O_2, H_2O_2 is going to eventually decompose at high temperature. Thus the reaction mostly takes place at the wall surface of the tank, including the interface 316L/ PWR water [2]. During and even after irradiation, the oxidising species, O_2 and/ or $OH^\bullet$, can always be produced at the interface through Eqs.6.1. These species, especially O_2, are the *poison* of the reducing chain reactions because they can react much more quickly with $H^\bullet$ and thus inhibit the formation H_2. The local chemistry becomes more and more oxidative, and thus an oxidative response of free potential between 316L and platinum is observed under irradiation.

Concerning H_2, there is dissolved hydrogen added to the PWR water, the one produced by water radiolysis and the one produced by corrosion. By knowing the radiolysis reactions of H_2 the potential evolution can be understood. In the very beginning of irradiation, H_2 should be in excess because it is already contained in the PWR water. Thus, it reacts quickly with the oxidising species while its formation is less efficient. It seems that the formation of oxidising products overcomes the reducing ones which leads to an increase of potential. Afterwards, the potential reaches a stationary value under irradiation when a balance is achieved. As soon as the beam is cut-off, no more oxidising radicals can react with H_2 and then the balance is broken. As a result, the potential decreases immediately.

Above all, based on the flux influence, all the following irradiations for the 1^{st} sequential irradiations were carried out with 30 nA (6.6×10^{11} $H^+.m^{-2}.s^{-1}$). By interpreting the results shown in Figs.6.3 & 6.4, further studies on the other parameters can be obtained.

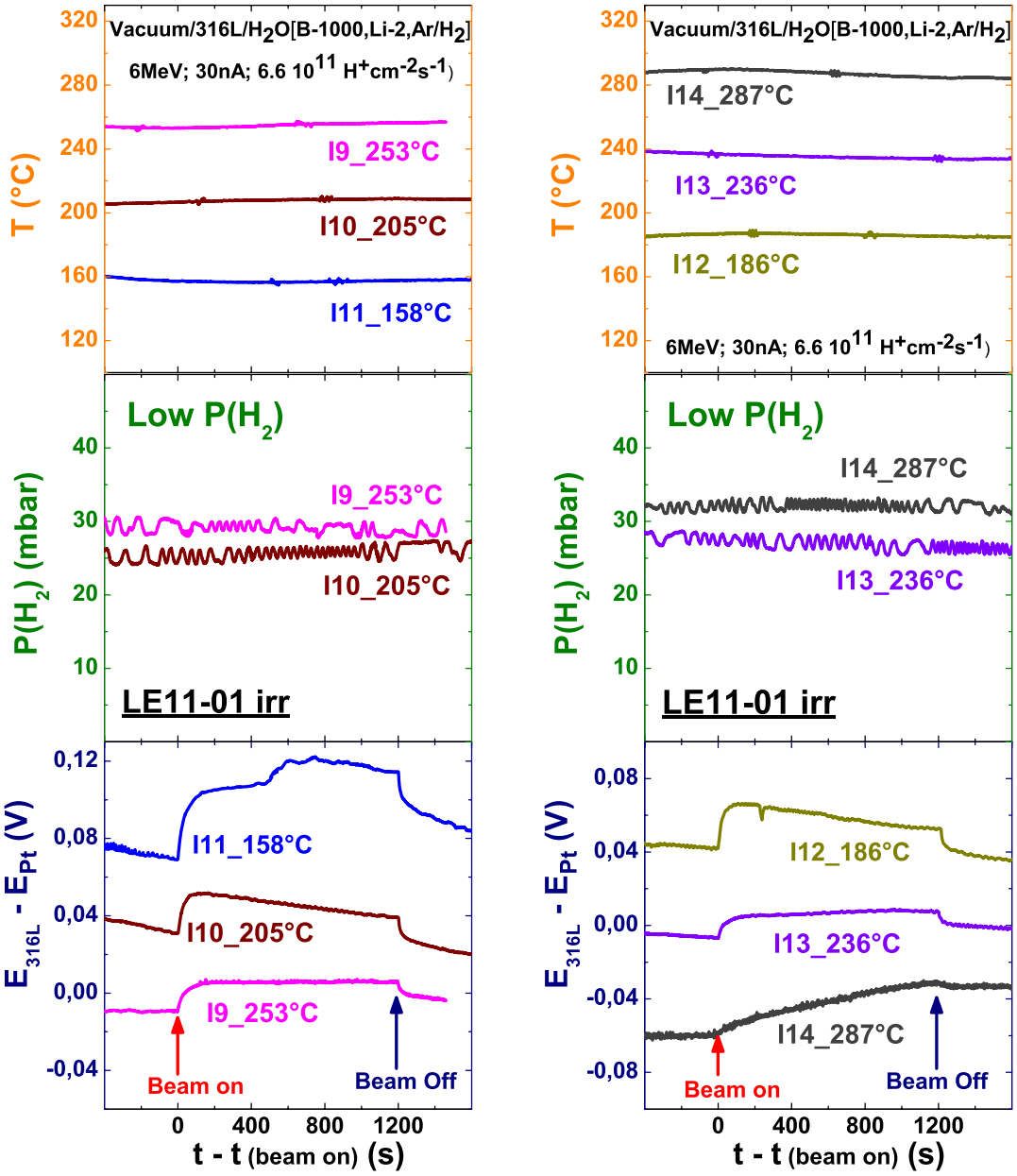

(a) (b)

Figure 6.3: 1^{st} sequential irradiations experiments of LE11-01 irr (D), temperature (uppermost), hydrogen pressure (middle), potential difference between 316L and Pt (bottom) versus time, beam starts at *on* (0 s) and stops at *off*. At **low $P(H_2)$**: (a) IR09 - IR11; (b) IR12 - IR14.

6.1.B Irradiation Temperature Influence

Figs.6.3 & 6.4 illustrate the irradiations experiments performed at low hydrogen pressure, and high hydrogen pressure, respectively. It reveals that the *oxidative response* under irradiation is a function of temperature. In order to get a better idea on this, a calculation of ΔE, defined by Eq.6.2 has been done for all the irradiations, including the ones at 300°C shown in Fig.6.8.

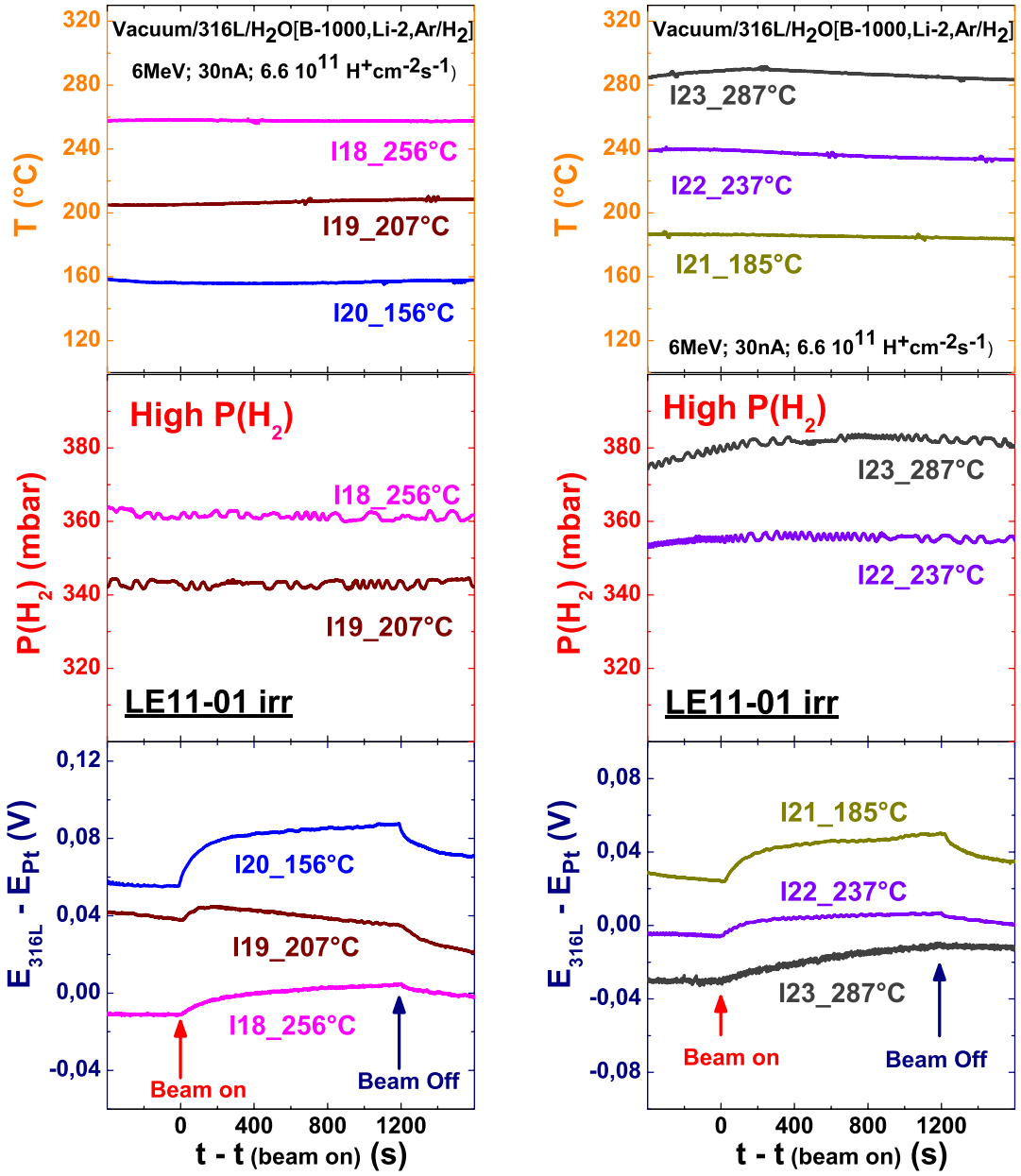

(a) (b)

Figure 6.4: 1^{st} sequential irradiations experiments of LE11-01 irr (D), temperature (uppermost), hydrogen pressure (middle), potential difference between 316L and Pt (bottom) versus time, beam starts at *on* (0 s) and stops at *off*. At **high $P(H_2)$**: (a) IR18 - IR20; (b): IR21 - IR23.

$$\Delta E_{400s} = E_{400s} - E_{0s} \tag{6.2}$$

Generally, the duration for each proton irradiation is 20 minutes. The value of ΔE at 400 seconds corresponds to an *oxidative response* at one third of irradiation duration. In most cases, at this time, the potential has already reached the stationary value under irradiation. Although, as shown in Fig.6.5, either increasing or decreasing tendency of the potential with or without beam should be

related to the small evolution of temperature, few Celsius degrees. An increasing tendency is observed for a little drop of temperature (Fig.6.5 (a)). Oppositely, when the temperature goes up, the potential slightly decreases (Fig.6.5 (b)).

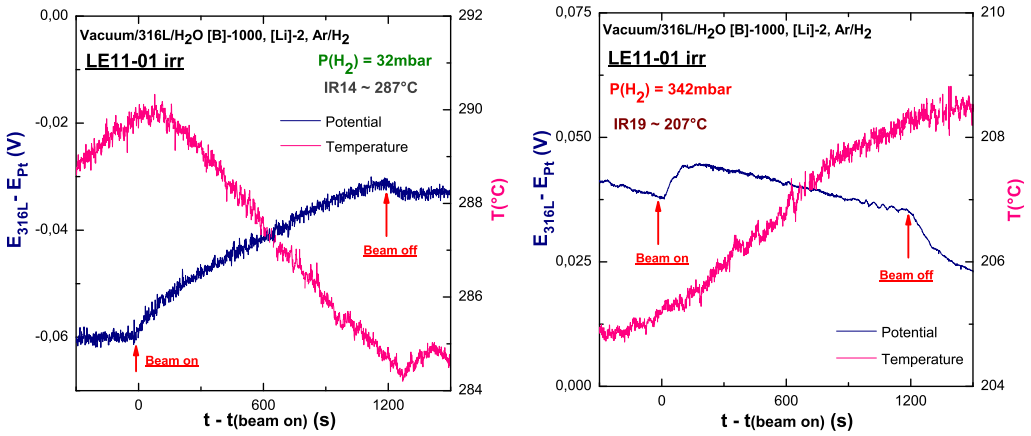

(a) (b)

Figure 6.5: 1^{st} sequential irradiations experiments of LE11-01 irr (D), potential between 316L and Pt (*on the left*) and temperature (*on the right*) in function of time. (a): I14 at 287°C and P(H_2) 32 mbar; (b): I19 at 207°C and P(H_2) 342 mbar.

The ΔE at 400 s under beam versus irradiation temperature is plotted in Fig.6.6 (a), for both low and high hydrogen pressures:

- **First temperature range:** ΔE_{400s} decreases with temperature, though the regimes are different for the pressures. For low hydrogen pressure, it is from 150 to 240°C, while for high hydrogen pressure, it is from 150 to 200°C.
- **Second temperature range:** ΔE_{400s} slightly increases afterwards and gives a weak maximum at the temperature around 270 $\sim$ 280°C.

As known, one of the strongest influence for g-value is the temperature, (see Chap.2). The diffusion coefficient and the constant reaction rate varies significantly with temperature. Based on the Tab.6.2, the oxidising species exceed the reducing ones when the temperature is over 150°C. However, other than the primary yields, there are still a lot of secondary reactions which can take place and play a role in the process. Moreover, the temperature effect is still debatable, and other parameters may be involved in the process like hydrogen.

Nevertheless, with the increase of temperature, all the species increases except for H_2O_2 [2]. It may be considered as one explanation for the decrease of the *oxidative response* in the **first temperature range**. For the weak maximum around 270 $\sim$ 280°C at the **second temperature range**, the explanation is not clear. But, it needs to be pointed out that the ΔE_{400s} at the **second temperature range** is actually very minor, only about 10 mV. Thus, a tiny change on local chemistry at the interface may result in this observation.

On the other hand, in Fig.6.6 (b), the hydrogen pressure appears to grow quasi-linearly with the

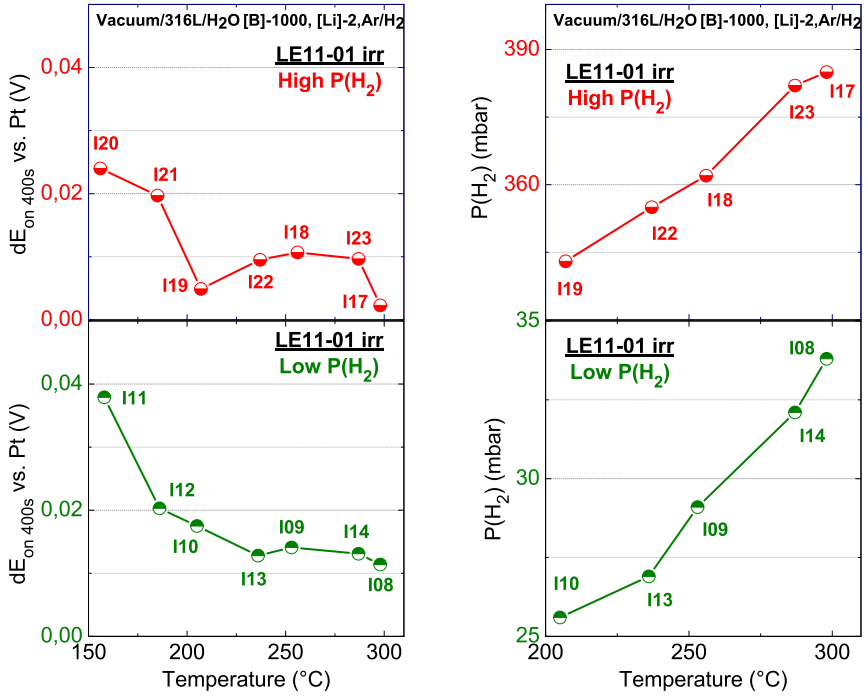

(a) (b)

Figure 6.6: 1^{st} sequential irradiations experiments of LE11-01 irr (D), irradiation temperature influence: (a) ΔE_{400s} versus temperature, irradiations under low hydrogen pressure on the *bottom* and the ones at high hydrogen pressure on the *top*; (b) hydrogen pressure of each irradiation versus temperature, low hydrogen part on the *bottom* and high hydrogen part on the *top*. Duration of each irradiation: $\sim$ 20 min.

temperature. In order to understand the phenomenon observed, one needs to take into account two factors:

- **Henry's law**, the solubility of H_2 in the PWR water is directly proportional to the $P(H_2)$ at a constant temperature. However, the Henry's law constant (k_H) depends on the temperature. In general, the solubility of H_2 increase with temperature. The more it dissolves in the PWR water, less pressure of H_2 gas can be detected by the sensor.
- **Ideal gas law**, the $P(H_2)$ is inversely proportional to the volume of H_2 gas. With the increase of temperature, the volume of PWR water dilates (because of thermal expansion), and the volume of H_2 gas is decreased subsequently. Therefore, $P(H_2)$ is going to be increased under the circumstance.

In brief, one needs to combine Henry's law and Ideal gas law to obtain the evolution of the $P(H_2)$ with temperature. Fig.6.7 illustrates the $P(H_2)$ ratio ($P(H_2)/P(H_2)_{205°C}$) as a function of temperature:

1. *Experimental data (Ex. data)*, the values come from Fig.6.6 (b), and $P(H_2)$ ratios are calculated by using the $P(H_2)$ around 200°C as the datum point.
2. *Theoretically data (Th. data)*, based on Henry's law and ideal gas law, are calculated using the $P(H_2)$ around 200°C as the datum point (see Appendix C for the calculation).

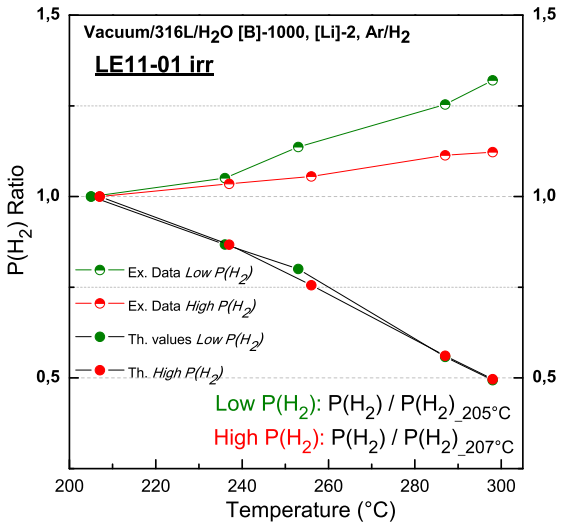

Figure 6.7: Hydrogen Pressure Ratio versus temperature, $P(H_2)/P(H_2)_{205°C}$ for low $P(H_2)$ and $P(H_2)/P(H_2)_{207°C}$ for High $P(H_2)$. Ex. data are calculated on the basis of Fig.6.6 (b), and Th. data are calculated in Appendix C.

Theoretically, under the experimental conditions of LE11-01 irr (D), Henry's law is predominating and thus the $P(H_2)$ decreases with the temperature. In other words, with the increase of temperature, the volume of PWR water increases and the Henry's law constant increase, and thus more H_2 dissolves in the PWR water, Th. data in Fig.6.7.

However, the experimental data shows an increase of $P(H_2)$ as a function of temperature. It elucidates clearly that H_2 are produced by the radiolysis of water. Furthermore, the production inclines to be more significant at low $P(H_2)$. In general, a higher concentration of H_2 maintains and reinforces the reducing environment, and thus decelerating the water radiolysis. Consequently, the production of H_2 may also be slow down. Therefore, it is interesting to study the influence of hydrogen.

6.1.C Hydrogen Influence

Fig. 6.8 clearly shows that at 300°C, the *oxidative response* is much more visible at low hydrogen pressure than at high. Moreover, by comparing the upper and bottom figures in Fig.6.6 (a), it shows that at no matter what temperature (from 150 - 300°C), the ΔE_{400s} at low hydrogen pressure are always higher than the ones at high. In brief, the *oxidative response* under irradiation is **reduced** under a higher hydrogen pressure at the same temperature.

Hydrogen is considered as an *inhibitor* of water radiolysis, that is why it is added to the nuclear reactors. In the presence of more hydrogen, the *oxidative response* of the free potential becomes smaller in accordance with the aim of adding it. Because it accelerates the reducing chain reactions and slows down the process of water decomposition.

Considering the sequence of the irradiations, the observed influence here is actually a set of **hydrogen** plus **ageing** effect by taking into account the irradiation order. This is the reason for looking into the ageing influence.

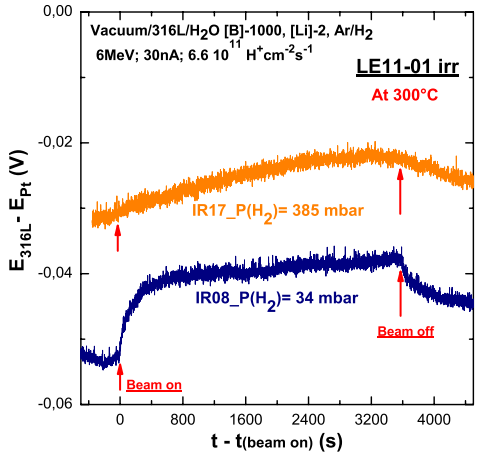

Figure 6.8: 1^{st} sequential irradiations experiments of LE11-01 irr (D), 300°C: IR08 low hydrogen pressure; IR17 high hydrogen pressure.

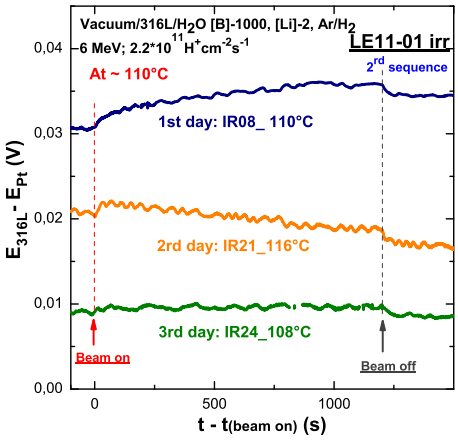

Figure 6.9: 2^{nd} sequential irradiations experiments of LE11-01 irr (D): IR08, IR21 and IR24, irradiation at close temperature ($\sim$ 110°C) and same initial hydrogen pressure in different days.

6.1.D Ageing Influence

The ageing influence is studied by using the data from the 2^{nd} sequential irradiation experiments on LE11-01 irr. Because it has been fairly irradiated by the first round, the ageing effect should be more visible.

Fig.6.9 illustrates three experiments (IR08, IR21 and IR24) of the 2^{nd} sequential irradiation, which were irradiated at quite close temperatures but different durations (days). Two remarks can be made:

1. a decrease of free corrosion potential between 316L and platinum before irradiation, from day 1 to day 3 gradually;

2. a reduction of oxidative potential response under irradiation: an evident response for day 1, visible for day 2 and nearly no response for day 3.

The ageing influence can be divided into two parts: **thermal ageing** and **fluence cumulation**. They can be addressed to the two phenomena observed on Fig.6.9.

The decrease of free corrosion potential caused by **thermal ageing** has already been demonstrated in the reference experiment, (see Chap.5, Fig.5.1). The reduction of the oxidative response accounts for an evolution of both oxide film and PWR water under irradiation, which can be reflected directly on the electrochemical potential. It means that the interface with a higher fluence there is less respondse for the irradiation.

Briefly, under proton irradiation, we may conclude the following influences that may play a role on the electrochemical potential under irradiation:

- **flux** of the beam directly affects on the electrochemical potential, and leads to an *oxidative response*;

- **irradiation temperature** decreases the oxidative response at first, then a weak increase at the second temperature range and eventually results in a maximum around 280°C;
- **hydrogen pressure** reduces the oxidative response under irradiation;
- **ageing**, combining thermal ageing with cumulated fluence, the electrochemical potential under or out of irradiation:
  1. decreases the free potential without the presence of beam;
  2. lowers the oxidative response under irradiation.

As stated previously, the samples were activated by proton irradiation, and hence *ex-situ* characterisation for the interface (316L stainless steel and PWR water) is impossible in this study. Meanwhile, as a second irradiation source, electron beams, do not activate the samples, which provides a way to study the electrochemical behaviour *in-situ* as well as characterise the interface *ex-situ*.

Therefore, it is important to identify and investigate the influences of electron irradiation versus proton irradiation. If these two irradiation methods show the same electrochemical behaviour, it can be assumed that their surface characterisation is comparable. In return, this may give a general idea on the interface of proton irradiated samples.

6.2 Hydrogen & Electrochemical Behaviour under Electron Irradiation

As listed in Tab.6.3, three irradiation experiments were performed under electron beam, among which LE11-04 irr and LE12-07 irr are mainly concerned for the study of electrochemical behaviour under irradiation. The history of irradiation diagram is illustrated in Fig.6.10.

Electron Experiments					
Specimens	Energy (MeV)	Flux (nA)	Irradiated Duration (h)	Thickness (mm)	Hydrogen Pressure at 300°C (mbar)
LE11-04 irr (D)	1.5/0.6	168 & 465	177	0.62	190(s)
LE12-05 irr (C)	1.8/0.6	920 $\sim$ 600	65	0.95	29(s)- 53(e)
LE12-07 irr (D)	1.75/0.6	1100	107	0.88	32(s, L) -187 (s, H)

Table 6.3: List of electron irradiation experiments with detailed conditions: energy, flux, duration under irradiation, thickness of the 316L discs and hydrogen pressure at 300 °C. (D): discontinuous irradiation experiment; (C): continuous irradiation experiment, (L): low hydrogen pressure; (H): high hydrogen pressure; (s): the initial hydrogen pressure, first measured at 300°C by the sensor; (e): the hydrogen pressure measured at 300°C in the end of the thermal treatment.

6.2.A Flux Influence

The flux influence shown in Fig.6.11, is based on the study of the interface LE11-04 irr. It is the first experiment carried out with the electron beam. Thus, a thorough study on the flux influence is performed in order to make sure of the presence of the electrochemical response under irradiation.

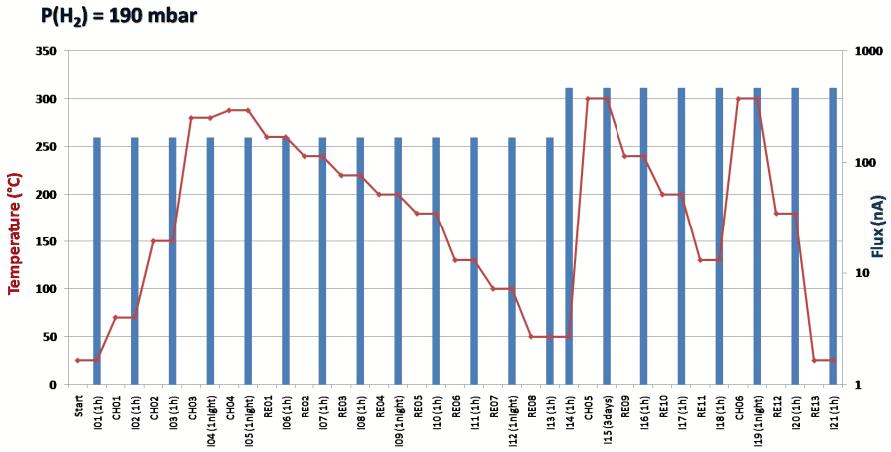

(a) LE11-04 irr (D)

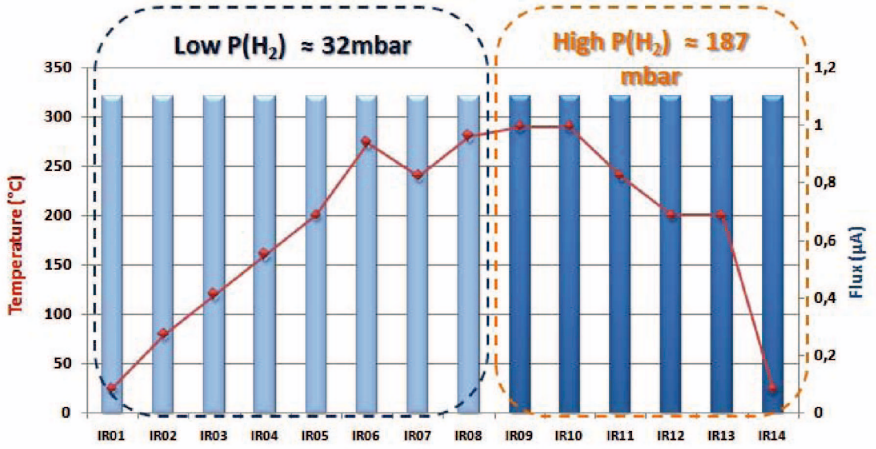

(b) LE12-07 irr (D)

Figure 6.10: History diagrams of sequential irradiations experiments performed on LE11-04 irr (D) and LE12-07 irr (D), respectively. Red curve: temperature of the HTHP cell; Blue column: flux for each irradiation. (a): LE11-04 irr (D): $[25, 300]$°C, $[168, 465]$ nA, fixed initial P(H_2), 190 mbar; (b): LE12-07 irr (D): $[25, 300]$°C, 1.1 ± 0.2 μA, $[32, 195]$ mbar of P(H_2).

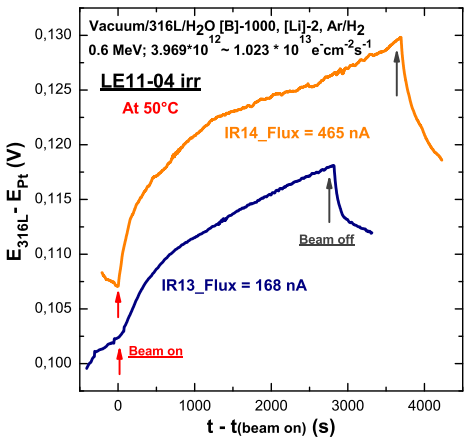

Figure 6.11: Sequential irradiations experiments of LE11-04 irr (D): IR13 (168 nA) and IR14 (465 nA) at the same temperature 50°C with the same initial hydrogen pressure.

Fig.6.11 illustrates two irradiations (IR13 and IR14) with different flux at the same temperature, 50°C. It shows an immediate *oxidative response* to the electron beam. Moreover, with the increase of the flux, from 3.969×10^{12} $e^-.m^{-2}.s^{-1}$ (intensity: 168 nA) to 1.023×10^{13} $e^-.m^{-2}.s^{-1}$ (intensity: 465 nA), the *oxidative response* becomes higher.

On the other hand, it also reveals that the *oxidative response* to the electron beam is much less than the one to the proton beam. However, it is not comparable because many parameters are different: the beam is different, the energy at the interface is different, the flux, etc. Still, it demonstrates that the electrochemical potential response to the electron irradiation is very minor. Furthermore, the reason for showing the irradiations at 50°C instead of at 300°C is because the *oxidative response* is no longer visible at relatively high temperature.

For this reason, the following electron irradiation experiments, LE12-05 irr (C) and LE12-07 irr (D) were carried out at higher flux. Fig.6.12 illustrates the sequential irradiation experiment of LE12-07 irr (D), which was irradiated with a higher flux 2.42×10^{13} $e^-.m^{-2}.s^{-1}$ (intensity: 1.1 μA). It is almost the highest stable flux at the specific energy (0.6 MeV at the interface) that can be provided by the accelerator SIRIUS.

6.2.B Temperature Influence

As illustrated in Fig.6.12, the *oxidative response* is not quite visible when the temperature is over $\sim$ 200°C. The plot between the *oxidative response* and the temperature is shown in Fig.6.13 (a). However, considering the duration of electron irradiation is longer than the proton ones, it is better to redefine a ΔE, which is written in Eq.6.3. As for proton irradiation, it is the *oxidative response* at one third of the irradiation duration.

$$\Delta E_{1200s} = E_{1200s} - E_{0s} \tag{6.3}$$

Under low hydrogen pressure, Fig.6.13 (a) *bottom*, ΔE_{1200s} first decreases with the temperature until $\sim$ 200°C, afterwards it increases and results in a weak maximum around 270°C. Under high hydrogen pressure, Fig.6.13 (a) *top*, a weak maximum around 270°C can also be found. Due to the fact that no experiment was carried out at lower temperature, the first temperature range is lacking in the figure.

A high similarity to the **two temperature range** phenomenon found in the proton irradiations, can also be observed on the electron irradiation, at least for the low $P(H_2)$. At high $P(H_2)$, only the **second temperature range** is shown.

Hydrogen Influence The reduction of ΔE caused by hydrogen pressure cannot be seen on the electron irradiation. Comparing the two figures of Fig.6.13 (a) (*upper* and *bottom*), the ΔE are almost in the same range. However, several remarks can be made on the hydrogen influence:

- All the ΔE under electron irradiation are less than 20 mV, thus the comparison is less significative than the proton irradiation.
- It is worth mentioning that the high $P(H_2)$ of LE12-07 irr (D) is about 187 mbar, which is much less the one for proton irradiation (LE11-01 irr, 390 mbar). It may explained the reason why

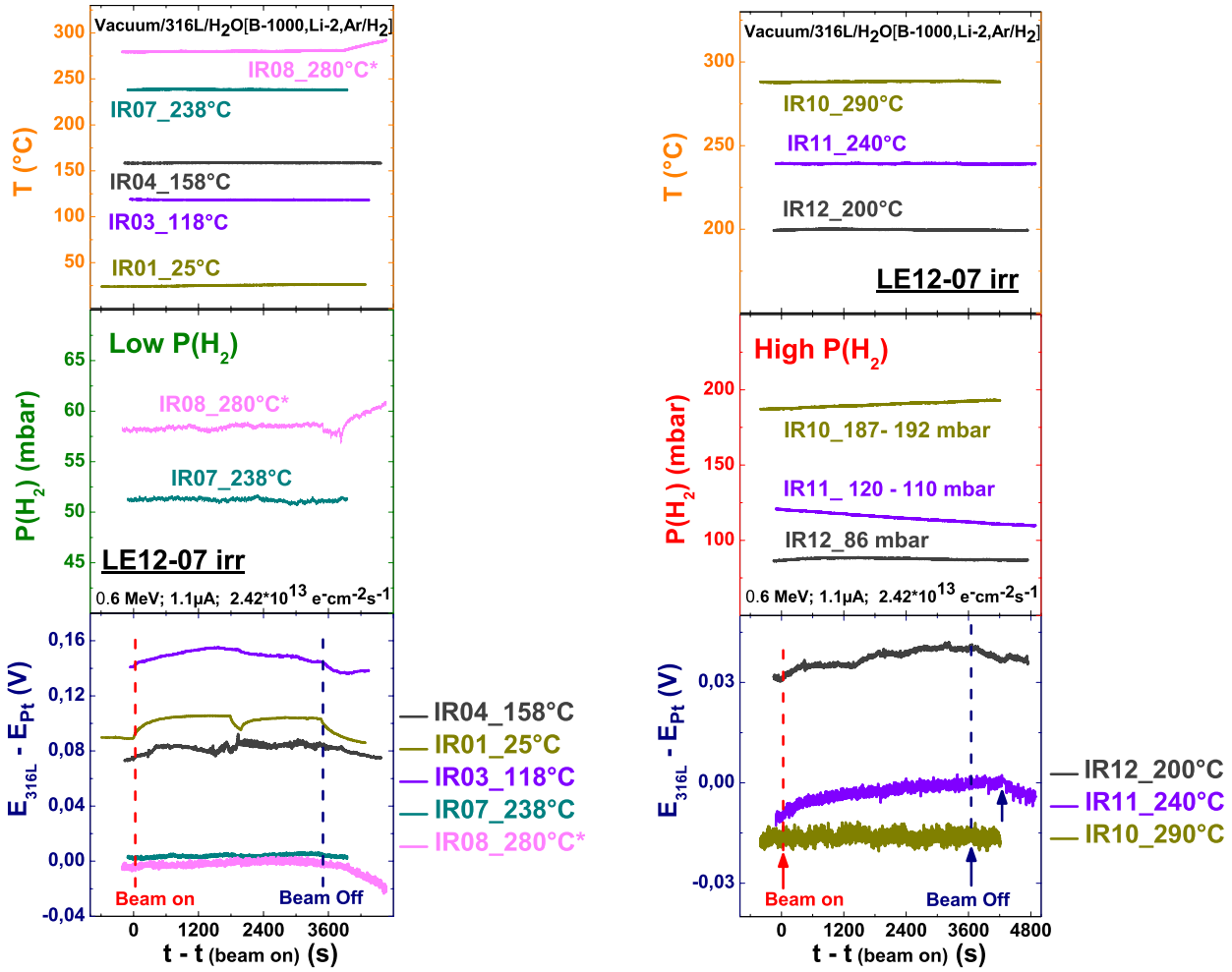

(a) (b)

Figure 6.12: Sequential irradiations experiments of LE12-07 irr (D), temperature (uppermost), hydrogen pressure (middle), potential difference between 316L and Pt (bottom) versus time, beam starts at *on* (0 s) and stops at *off*: (a) IR01, IR03 - IR04 and IR07 - IR08 at low $P(H_2)$; (b) IR10 - IR12 at high $P(H_2)$.

the hydrogen influence is not observed for the electron irradiation.

- Besides, there is no data for the ΔE from room temperature to 200°C (Fig.6.13 (a), *upper*), thus the comparison/ conclusion is incomplete.

On the other hand, the relationship between $P(H_2)$ and temperature is illustrated in Fig.6.13 (b). As with proton irradiation, it increases quasi-linearly with the temperature. It is worth mentioning that a drop (10 mbar) of $P(H_2)$ during the IR11 at 240°C while a jump of $P(H_2)$ (5 mbar) during the IR12 can be noticed at 300°C (Fig.6.13 (b) *upper*).

Fig.6.14 shows the $P(H_2)$ ratio as a function of temperature, with the same calculation method of proton irradiation (Fig.6.7). The increase of H_2 means that water radiolysis produces H_2. It appears that the ratio slope of high $P(H_2)$ is more inclined than the low one here. However, it needs to be emphasised that the high $P(H_2)$ is around 200 mbar and the one for proton is about 390 mbar. They

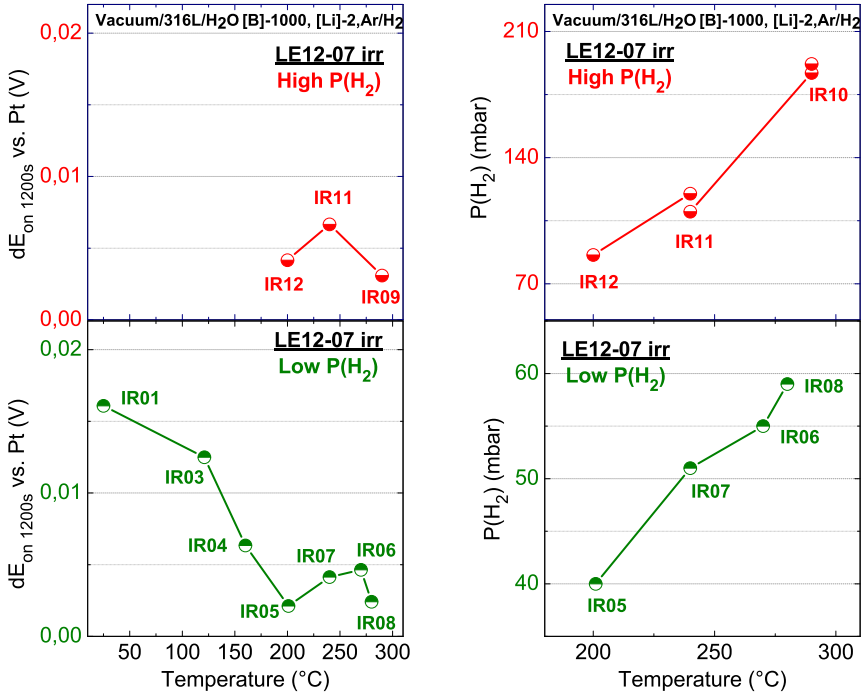

(a) (b)

Figure 6.13: Sequential irradiations experiments of LE12-07 irr (D): (a) ΔE_{1200s} versus temperature, irradiations under low hydrogen pressure on the *bottom* and the ones at high hydrogen pressure on the *top*; (b) hydrogen pressure of each irradiation versus temperature, low hydrogen part on the *bottom* and high hydrogen part on the *top*.

are not of the same magnitude. More probably, the H_2 here is not yet enough to decelerate the water radiolysis yet.

6.2.C Ageing Influence

Fig.6.15 illustrates two irradiation process, IR06 at low $P(H_2)$ in (a) and IR13 at high $P(H_2)$ in (b). They are ageing under a heat treatment together with a fluence cumulation. It is quite obvious that these two figures recall the reference experiments. They exhibit, especially for Fig.6.15 (a), a high similarity of **thermal ageing** process on the reference LE11-03 irr at 300°C (see Chap.5, Fig.5.1 (c)). Without any doubt, not only the **thermal ageing** but also the **fluence cumulation** can play an important role in the process. However, based on the high similarity to the reference figure, it implies that the thermal ageing is the predominating influence.

In summary, the electrochemical behaviour of an interface between 316L stainless steel and PWR water under electron irradiation is similar to the one under proton irradiation. Basically, the flux and the temperature influences have the same evolution under both beams. The hydrogen influence is not as obvious as proton irradiation. The ageing influence is a **synergetic effect** of the thermal ageing and fluence cumulation. For both proton and electron irradiations, the ageing influence can play an important role on the electrochemical potential. Moreover, it seems that thermal ageing takes the dominant position in the whole effect.

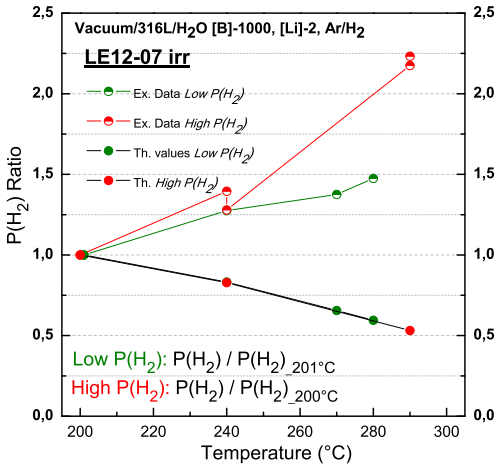

Figure 6.14: Hydrogen Pressure Ratio versus temperature, $P(H_2)/P(H_2)_{201°C}$ for low $P(H_2)$ and $P(H_2)/P(H_2)_{200°C}$ for High $P(H_2)$. Ex. data are calculated on the basis of Fig.6.6 (b), and Th. data are calculated in Appendix C.

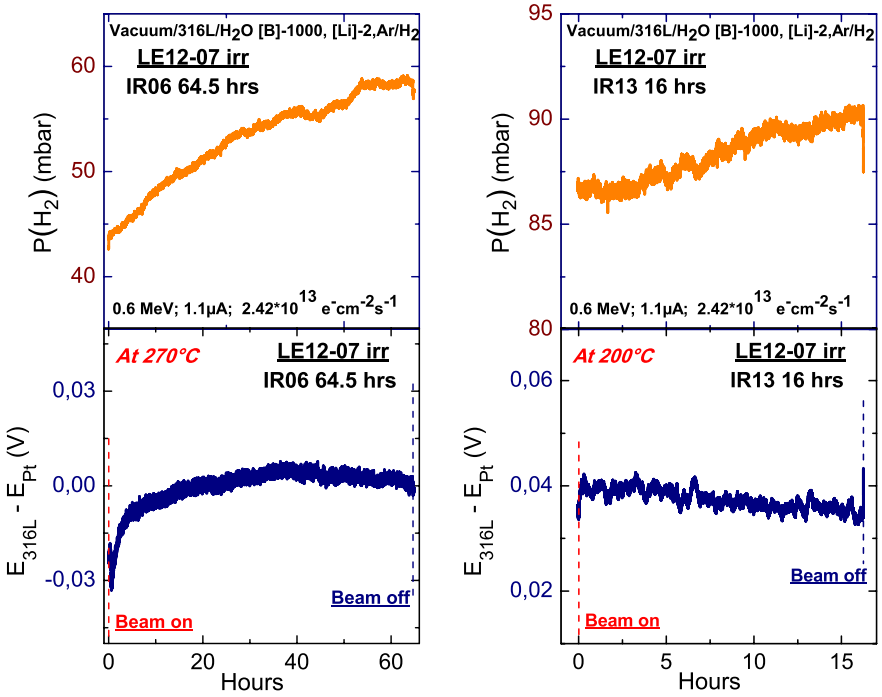

(a) Low $P(H_2)$ (b) High $P(H_2)$

Figure 6.15: Sequential irradiations experiments of LE12-07 irr (D), ageing influence: (a) IR06: 64.5 hours under electron irradiation at 270°C; (b) IR13: 16 hours under electron irradiation at 200°C.

6.3 Characterisation of Electron Irradiated 316L Oxide Films

The characterisation of irradiated 316L oxide films is only carried out for the electron irradiation, due to the fact that the proton irradiated 316L stainless steels were and still are activated by the proton beam. However, based on the high similarity of electrochemical behaviour between proton and electron irradiation, the evolution of oxide film may also exhibit the same properties.

Same methods and techniques, mentioned in the previous chapter for the reference experiments, have been used for the characterisation of the irradiated 316L oxide films. The interpretations are aimed at recognising and identifying the electron irradiation effects on the oxide films, and thus the comparison between the irradiation and reference experiments can be done in the next chapter.

Tabs.6.4 & 6.5 list the corresponding duration under irradiation and fluence at different temperatures, respectively. Together with the hydrogen pressure (indicated in Tab.6.3), they are the three important parameters for the interpretation of the oxide films. LE11-04 irr (D) had the highest $P(H_2)$ and lowest fluence, LE12-05 irr (C) was continuously irradiated at the highest temperature (300°C) and LE12-07 irr (D) was irradiated with a highest flux and fluence.

Specimens	Durations under Irradiation (hrs)		
	$<$ 200°C	200 - 250 °C	250 - 300 °C
LE11-04 irr (D)	37	25	115
LE12-05 irr (C)	/	/	65 (at 300°C)
LE12-07 irr (D)	20	20	67

Table 6.4: Table of the duration under electron irradiation at different temperature. (D): discontinuous irradiation experiment; (C): continuous irradiation experiment.

Specimens	Fluence ($\times 10^{18}$ $e^+.cm^{-2}$)			
	$<$ 250 °C	250 - 300 °C	Total	$\frac{250-300°C}{total}$
LE11-04 irr (D)	0.789	3.412	4.2	0.81
LE12-05 irr (C)	/	$3.089(_{min}) \sim 4.736(_{max})$	$3.089(_{min}) \sim 4.736(_{max})$	1
LE12-07 irr (D)	3.485	5.837	9.322	0.63

Table 6.5: Table of the cumulated fluence for each electron irradiation (LE11-04 irr, LE12-05 irr, and LE12-07 irr) at different temperature. (D): discontinuous irradiation experiment; (C): continuous irradiation experiment.

6.3.A Surface Morphology - SEM Analysis

The irradiated 316L stainless steel interfaces look like the reference ones at the macroscopic scale. Though the LE11-04 irr (D) has a little different pattern in the central of the disc, see in Fig.6.16. It seems like a *question mark* and slightly larger than 6 mm in the centre. Considering the feature of electron irradiation and the possible shifting of the beam (caused by the accelerator), we assume that the *question mark* zone may also have been contacted by/ irradiated by the electron beam. Therefore, this zone is referred to "**mixed zone**" from this context. It is difficult to indicate the exact location for the mixed zone, although it can be considered as the region outer than the zone 1 (central 6 mm) and much inner than the board of the zone 2 (identified by the sealed mark).

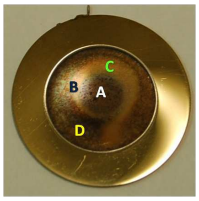

Figure 6.16: Photo of LE11-04 irr (D), showing the different spots for the SEM analysis. (A): zone 1, irradiated zone, (B) and (C) mixed zone, between zone 1 and 2, (D) zone 2, unirradiated zone.

Consequently, for the results of SEM characterisations, three zones have been shown, zone 1 (irradiated), zone 2 (unirradiated) and an additional mixed zone.

6.3.A.1 LE11-04 irr (D)

The SEM micrographs of the zone 1 for irradiated 316L stainless steel interface LE11-04 irr (D) are shown in Fig.6.17. There are four figures with different magnifications for describing the different observations in the zone 1.

It exhibits a *new* interface morphology mainly characterised by:

- Some big crystallites are partly dissolved while new small crystallites grow on the big ones, as shown in Fig.6.17 (a) & (b). In other words, it seems like that the big crystallites are dissolved and followed by the formation of the extremely small ones.
- Small **round** spots can be found, either adhering to the big crystals like a droplet, or just presenting on the surface, isolated with others, as shown in Fig.6.17 (c) & (d).

Fig.6.18 portrays the SEM micrographs of the mixed zone and zone 2 for LE11-04 irr. In the mixed zone, Fig.6.18 (a) & (b), the big and extremely small crystallites co-exist with each other. It appears that the big crystallites are less covered by small ones. And the existence of the small **round** spots can still be proven. They are no longer glued to the big crystals, only shown on the surface. In addition, **long-shaped** crystallites are found in the mixed zone, shown in Fig.6.18 (a). It is difficult to conclude whether they are contamination on the surface or a new form of crystallites.

For zone 2, Fig.6.18 (c) & (d), *normal* crystallites with different sizes were observed all over the surface with no evidence shown for the extremely small crystallites.

In order to get a better idea on the *new* surface morphology, a further EDX analysis has been preformed on the **long-shaped** crystallites and the **round** spots.

Fig.6.19 shows:

- The long-shaped crystallites look like a reunion of small crystallites;
- No element difference is found amongst all the analysed points;
- The spectrum of *big crystals* has higher intensities on O, Fe, Ni elements, constituent elements of the crystallites. The spectrum of *matrix with crystallites* has a higher intensity of Cr because that the smaller size of crystallites. More inner oxide rich in chromium can be analysed. The spectra of *long-shaped crystallite* are in the middle of these two cases. Briefly, the intensity is

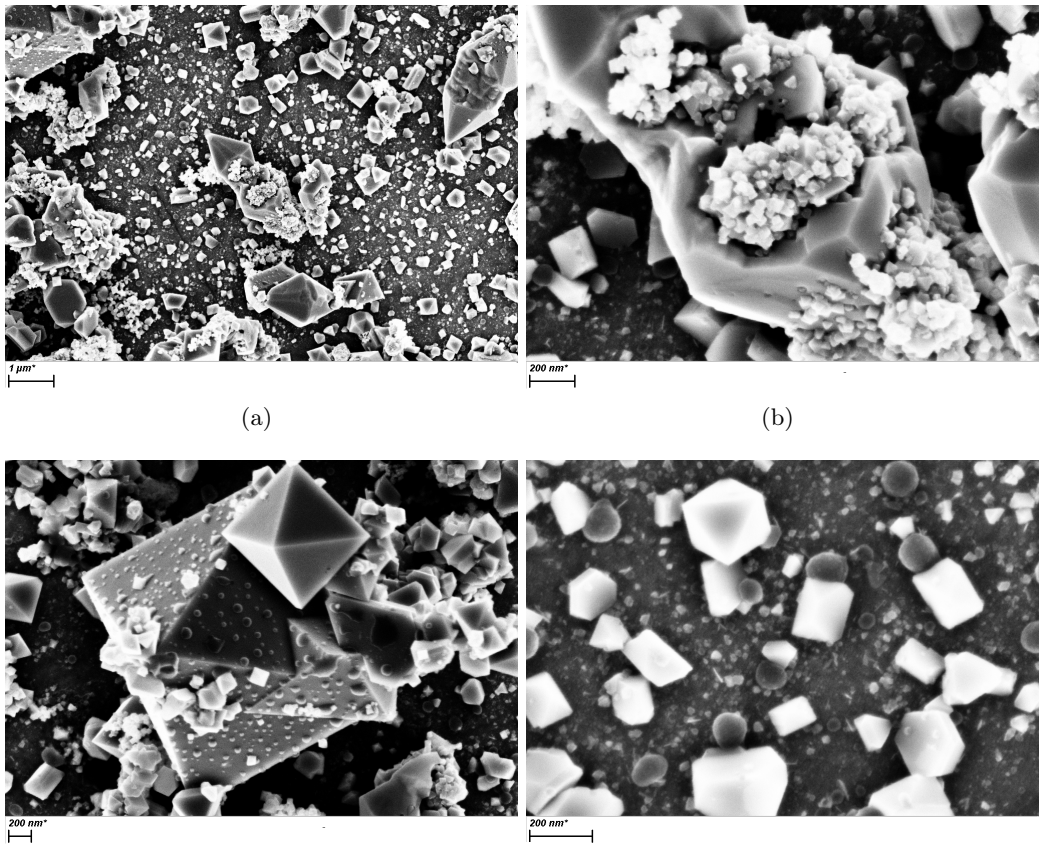

Figure 6.17: SEM micrographs of LE11-04 irr (D) of different spots in the **zone** 1 (region **A** in Fig.6.16), SEM under the conditions: EHT = 5kV, WD = 6.1 mm: (a) Mag = 10 kX; (b) Mag = 25 kX; (c) Mag = 50 kX; (d) Mag = 70 kX.

actually based on the size of the crystallites which may strongly influence the volume of the analysing zones.

The superimposed spectra of an EDX analysis on a **round** spots on the matrix is shown in Fig.6.20 (a) & (c). Comparing the round spot with the matrix, an enrichment of carbon was found. The relative quantification results for the spectra demonstrated that the enrichment can be up to more than 10%. Therefore, carbon is selected with reasonable suspicion for the constituent of the round spot. However, it is not clear of the form of carbon on the surface.

An EDX profile scan, crossing a round spot and two crystallites, has been shown in Fig.6.20 (d). Actually, this profile scan is aimed at confirming and concluding all the observation obtained before. Among all the elements detected, indicated in Fig.6.20 (b), the most concerned elements are chosen for quantification: C, O, Cr, Fe and Ni. For the big crystallites, an obvious enrichment of Fe and a slight increase of O are found, while the evolution of Ni stays relatively constant. The volume of analysing zone is strongly influenced by the presence of the crystallites, and thus led to the decrease of chromium. Lastly, it seems that a slight increase of carbon can be recognised for the round spot.

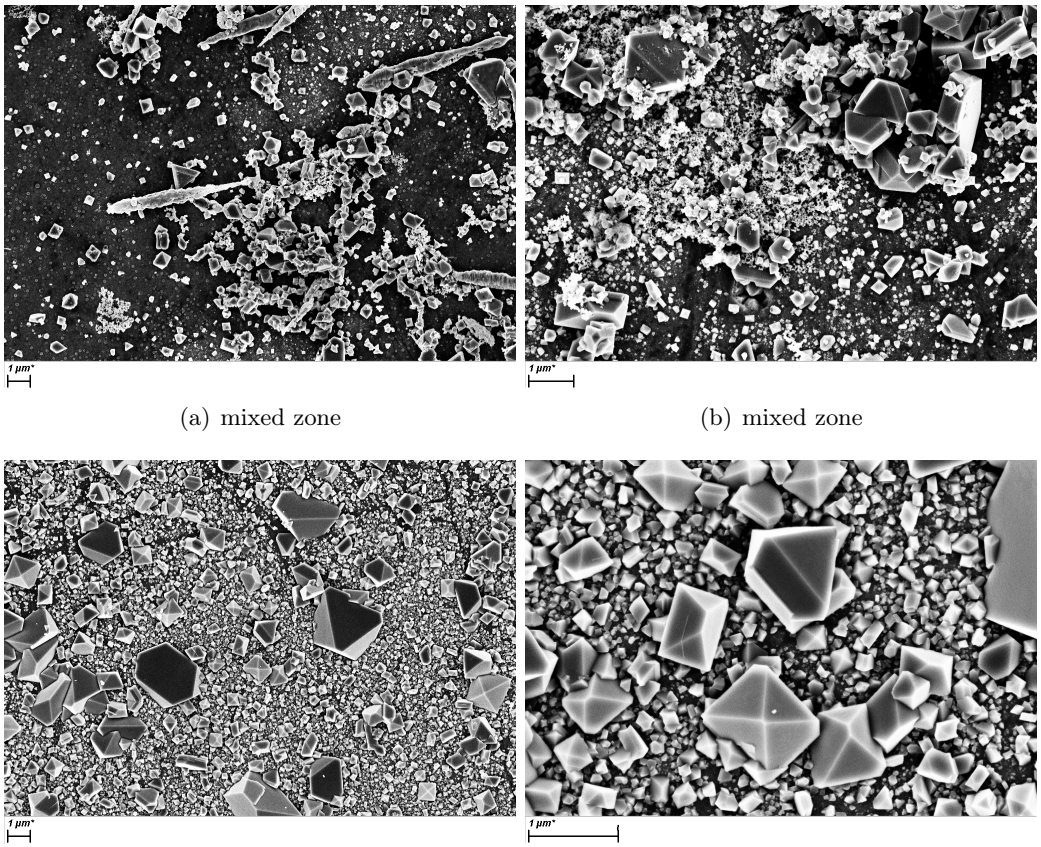

(a) mixed zone (b) mixed zone

(c) zone 2 (d) zone 2

Figure 6.18: SEM micrographs of LE11-04 irr (D) of different spots in the **mixed zone** (a) (region **B** in Fig.6.16) and (b) (region **C** in Fig.6.16), and in the **zone** 2 (c) and (d) (region **D** in Fig.6.16), SEM under the conditions: EHT = 5kV, WD = 6.1 mm: (a) Mag = 5 kX; (b) Mag = 10 kX; (c) Mag = 5 kX; (d) Mag = 20 kX.

6.3.A.2 LE12-05 irr (C)

For LE12-05 irr, the surface morphology of the zone 1, the mixed zone and the zone 2 are shown in Fig.6.21, Fig.6.22 (a) & (b) and Fig.6.22 (c) & (d), respectively.

In the zone 1 (irradiated), as shown in Fig.6.21:

- There is no sign of large crystallites on the surface, only the tiny crystallites are presented. They seem to be precipitated with a preference on the pattern, **circular pattern**, as shown in Fig.6.21 (a). Moreover, the tiny crystallites are too small to exhibit their crystallites geometry form.
- **Cavities** are found on the surface. They are presented in a large amount, especially in the circular pattern. Most of them have a large dimension in area. For instance, the one shown in Fig.6.21 (c), the area is about 6.5×2.5 μm^2. Furthermore, inside of some cavities, crystallites can also be found. On the border the cavities, cracks may also be observed (Fig.6.21 (d)).

The surface morphology of the mixed zone, Fig.6.22 (a) & (b), exhibits a highly similarity to the zone 1: lack of big crystallites; only tiny ones can be observed. The **cavities** are observed and most

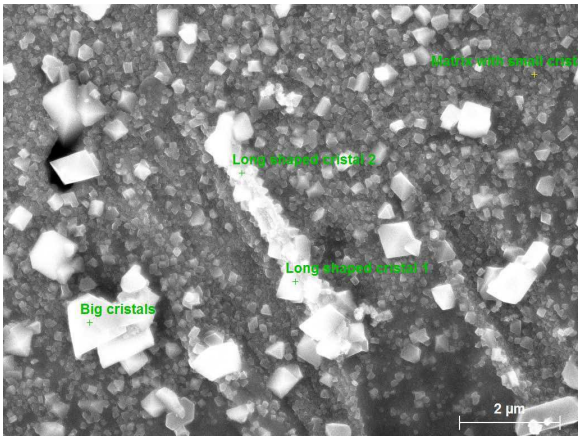

(a)

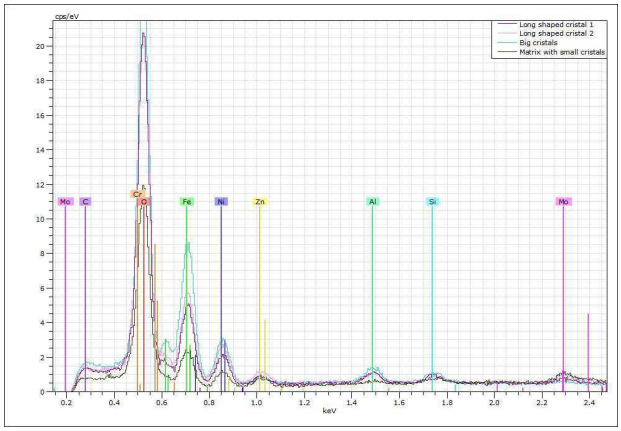

(b)

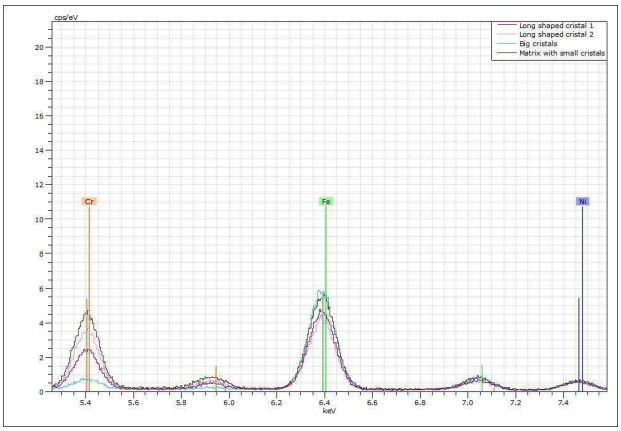

(c)

Figure 6.19: EDX analysis for different spots of LE11-04 irr (D) in the **mixed zone**, with SEM under the conditions: EHT = 15 kV, WD = 6 mm, Mag = 10 kX. (a), (b) and (c): photos and EDX spectra for the point analyses: long-shaped crystallites (dark violet and light violet lines), crystals (light blue line), and matrix covered with small crystallites (black line).

of them are also located in the circular pattern. Large crystallites can only be found in the zone 2, as shown in Fig.6.22 (c) & (d).

6.3.A.3 LE12-07 irr (D)

Figs.6.23 & 6.24 illustrate the surface morphology of LE12-07 irr. As for LE12-05 irr, in the zone 1, extremely small crystallites are seen on the surface. They are precipitated under a preference of the **circular pattern**. Cavities and crystallites inside cavities can also be observed. The mixed zone also exhibits a high similarity to the zone 1. For zone 2, it shows the common observation for the unirradiated zone, crystallites cover the surface.

Above all, the SEM results bring information about surface morphology of the 316L oxide formed in PWR water under electron irradiation. In general, three observation can be underlined from the results :

1. tiny crystallites precipitate on big crystallites;

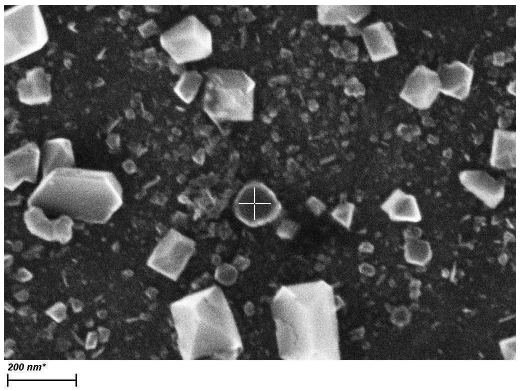

(a)

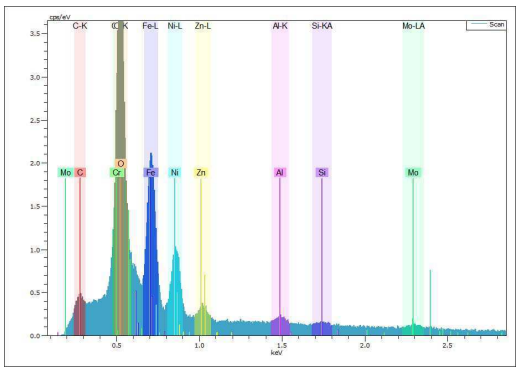

(b)

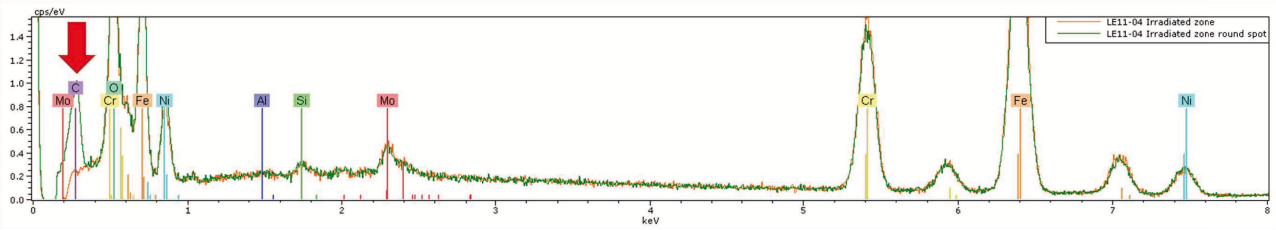

(c)

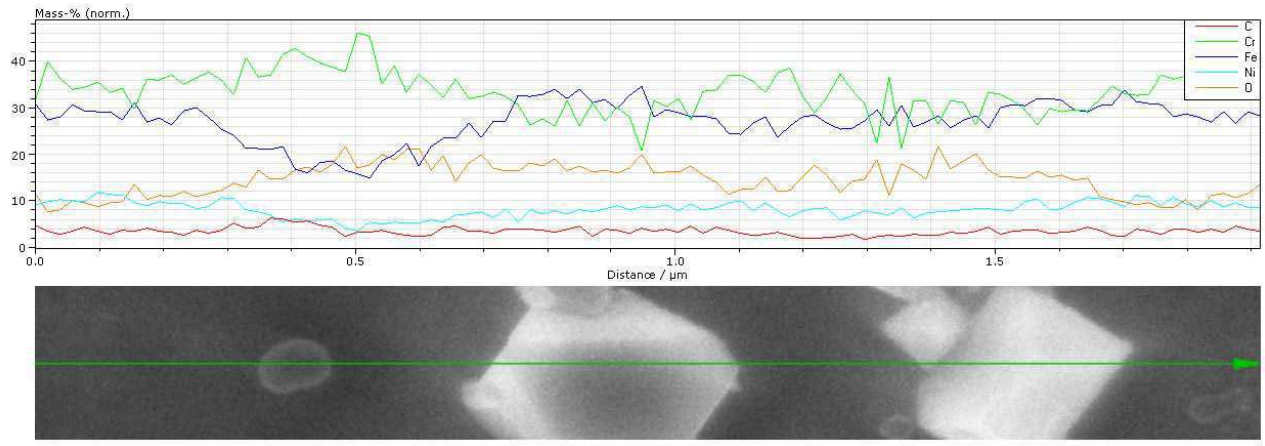

(d)

Figure 6.20: EDX analysis of LE11-04 irr (D) in the **zone** 1: (c) two superimposed EDX spectra of matrix with small crystallites (orange line), and the round spot (green line) which is indicated in (a), with SEM under the conditions: EHT = 15 kV, WD = 6 mm, Mag = 76.7 kX; (d) a quantification (% mass.) profile scan (profile path, insert image) with its spectrum showing in (b), with SEM under the conditions: EHT = 5 kV, WD = 5.8 mm, Mag = 40 kX.

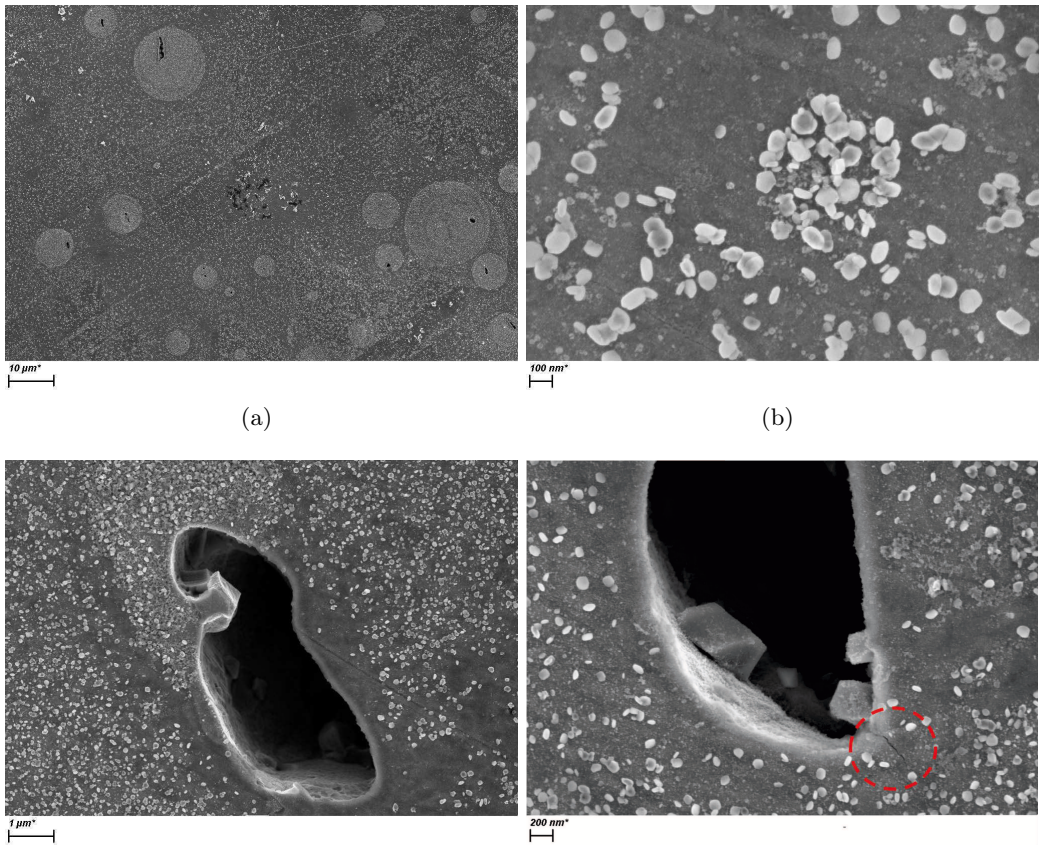

Figure 6.21: SEM micrographs for different spots of LE12-05 irr (C) in the **zone** 1 (irradiated). SEM under the conditions: EHT = 5kV, WD = 3.9 mm, (a) Mag = 1 kX; (b) Mag = 50 kX; (c) Mag = 10 kX; (d) Mag = 25 kX;

2. creation of **cavities**;

3. evolution of the geometrical form of the crystallites.

The three samples (LE11-04 irr (D), LE12-05 irr (C) and LE12-07 irr (D)) have different exposure conditions during the irradiation experiments, as indicated in Tabs.6.3, 6.4 & 6.5.

LE11-04 irr (D), is the one with the highest $P(H_2)$ and the lowest fluence. It is also the only one with three cyclic thermal treatments, as shown in Fig.6.10 (a). Therefore, the phenomenon of extremely tiny crystallites precipitated on big ones seems to be linked with the multiple cyclic thermal treatments. Big crystallites dissolve or partly dissolve when temperature decreases, while the small ones precipitate (reprecipitate) when temperature increases. The size and density of the crystallites are related to the thermal treatment and hydrogen pressure. However, the presence of carbon is probably related to a pollution on the surface after the experiment.

It needs to be emphasised that the observation of **cavities** can be found on LE12-05 irr (C) and LE12-07 irr (D) but not on LE11-04 irr (D). Likewise, the evolution of geometrical form on the crystallites are only observed on LE12-05 irr (C) and LE12-07 irr (D). Actually, they are irradiated with a relatively strong flux for a long period at high temperature. It implies that the **cavities** on the

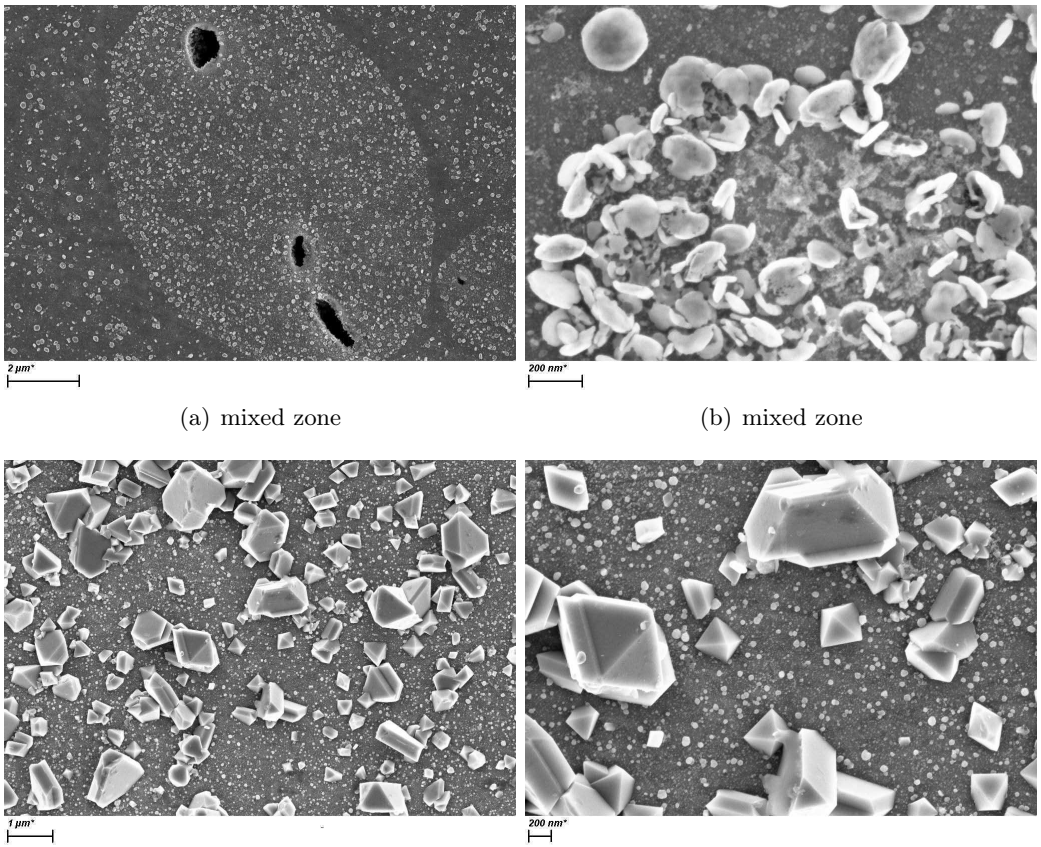

(a) mixed zone (b) mixed zone

(c) zone 2 (d) zone 2

Figure 6.22: SEM micrographs for different spots of LE12-05 irr (C): (a) and (b) in the **mixed zone**; (c) and (d) in the **zone** 2 (unirradiated). SEM under the conditions: EHT = 5kV, WD = 6.0 mm, (a) WD = 3.7 mm, Mag = 8 kX; (b) WD = 3.9 mm, Mag = 60 kX; (c) WD = 3.5 mm, Mag = 10 kX; (d) WD = 3.5 mm, Mag = 25 kX;

oxide film and the evolution of the geometry on the crystallites are related to irradiation conditions. They depend on **flux** and **fluence** of the irradiation, since the interfaces were all irradiated at the same energy. Although, it is hard to tell if the predominating parameter is the flux or the fluence.

In short, cavity creation and geometry evolution are the irradiation-induced defects which can be observed on the surface.

Actually, a recent study of radiation induced corrosion of copper [3] shows that circular shaped corrosion features spread out all over the surface. These features are pretty much alike to the cavities we observed but less deep. However, the irradiation was carried out with γ radiation in their case. In order to get a better idea on the depth of the cavities, an additional measurement of interferometer (in CEA Saclay) was performed on the LE12-07 irr (D).

A 3D image of a selected area on LE12-07 irr (D) is illustrated in Fig.6.25, it exhibits the presence of cavities. Based on the measurements of the cavities, as shown in Fig.6.26, it can be considered that most cavities are approximately $1 \sim 1.5$ μm in depth. It also shows that the radiation induced cavities are quite homogenous in dimension (magnitude: μm.)

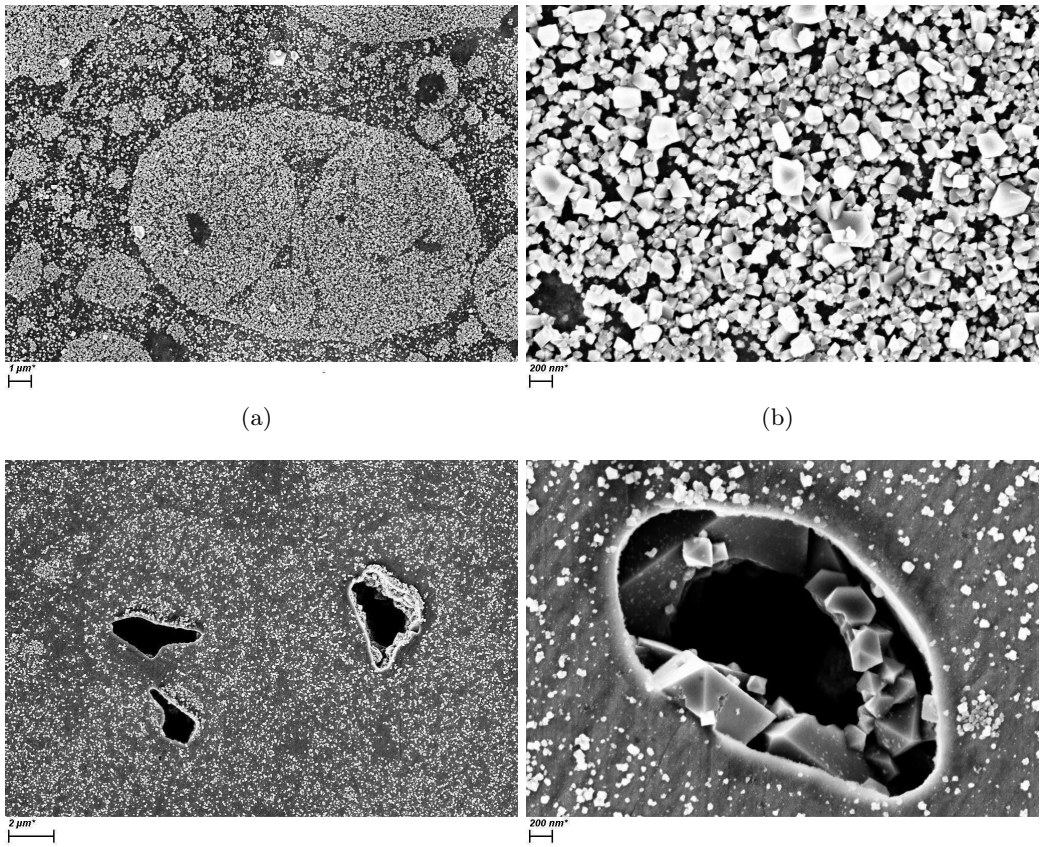

(a) (b)

(c) (d)

Figure 6.23: SEM micrographs for different sports of LE12-07 irr (D) in **zone** 1 (irradiated). SEM under the conditions: EHT = 5kV, WD = 6.0 mm.

6.3.B Compositions - XPS Analysis

According to survey scans, the oxide films formed on the irradiated 316L surface under electron irradiation are mainly formed by Cr, Fe, Ni, Zn and Mo, which is not different from the reference ones.

Based on the high resolution spectra of XPS analysis, illustrated in Figs.6.27 & 6.28, the atomic percentage of each element has been determined form side to side of the whole PWR water contacted zone (position 0 to position 14, see Chap.5, Fig.5.7).

Therefore, Figs.6.27 & 6.28 reveal that:

- A high concentration of chromium oxide is shown by the XPS results. In other words, more chromium oxide is detected in the irradiated zone where small crystallites are observed. The **confined effect** is only exhibited on LE11-04 irr, in Fig.6.27 (a): an increase of chromium oxide in the central zone (position 4 $\sim$ position 10) while a drop in the confined zone (position 0 $\sim$ 4 and position 10 $\sim$ 14). However, for both LE12-05 irr (C) and LE12-07 irr (D), the **confined effect** is less evident.

- The sudden drop of chromium oxide shown in Fig.6.28 (a), is zoomed in Fig.6.28 (b) with a smaller scale in distance. Actually, the chromium content decreases gradually. The explanation

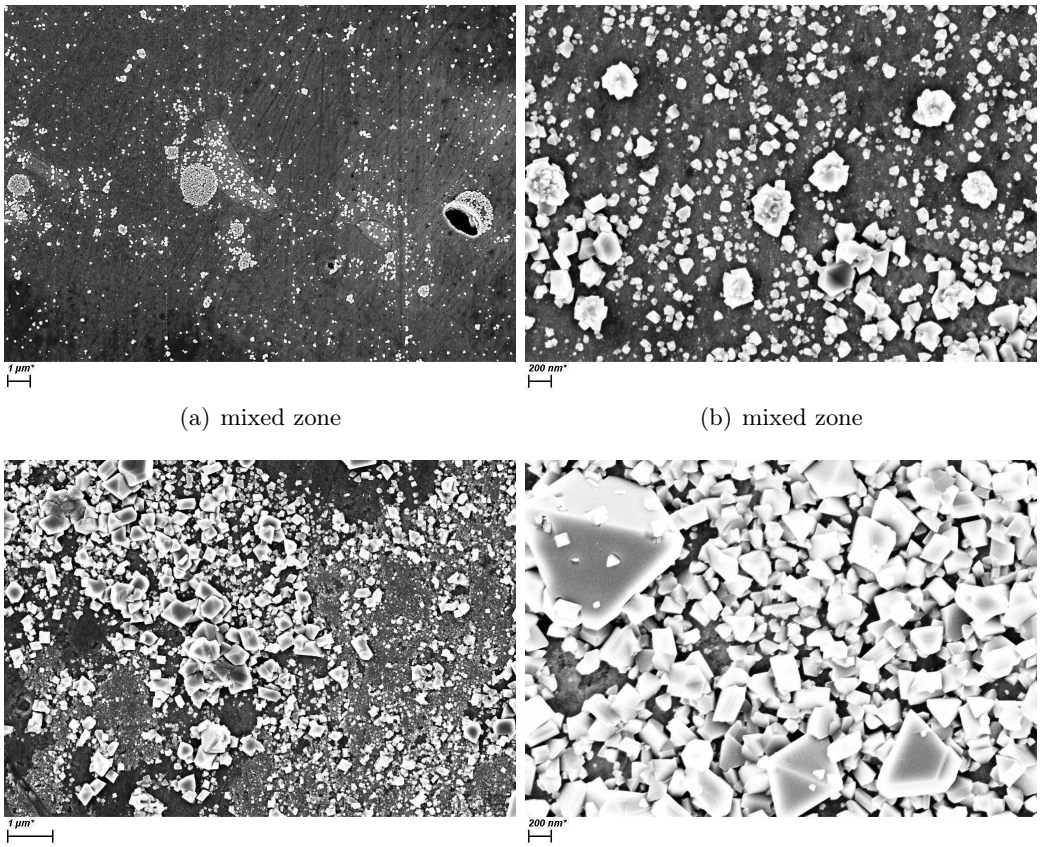

(a) mixed zone (b) mixed zone

(c) zone 2 (d) zone 2

Figure 6.24: SEM micrographs of LE12-07 irr (D): (a) and (b) in the **mixed** zone; (c) and (d) in the **zone** 2 (unirradiated). SEM under the conditions: EHT = 5kV, WD = 6.0 mm.

should trace back to the presence of the crystallites. They happen to be largely deposited there, and thus an increase of iron oxide (with little nickel) leads to the drop the chromium oxide.

Briefly, the XPS quantification results are in accordance with the SEM observation. More chromium oxide is detected because the decrease of crystallites in both size and density. The **confined effect** is less evident in both LE12-05 irr (C) and LE12-07 irr (D), which seems to be linked with their irradiation conditions (high flux and high flunece).

6.3.C Structures - Raman Spectroscopy Analysis

Raman analyses were performed on both LE11-04 irr (D) (Fig.6.29 (a), (b) and (c)) and LE12-05 irr (C) (Fig.6.29 (d)). As for the reference experiments, the Raman image can be identified into two colours, dark red and green/ grey (see Chap.5, Fig.5.17). However, no difference between these colours can be observed except for the intensity of the peaks.

For LE11-04 irr (D) (Fig.6.29 (a), (b) and (c)), the spectra are quite different for each zone. In the irradiated zone (zone 1, Fig.6.29 (a)), the main peak is no longer the one at 700 cm^{-1}. Two peaks at higher wavenumbers ($\sim$ 1330 cm^{-1} and $\sim$ 1607 cm^{-1}, respectively) take over. In the unirradiated

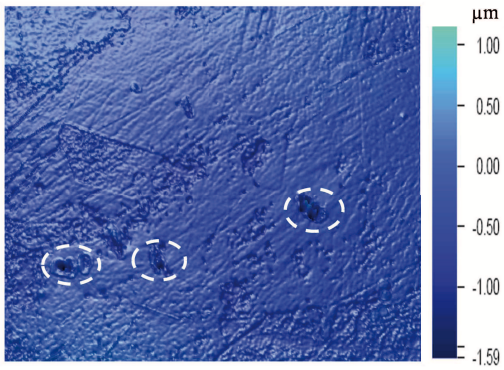

Figure 6.25: 3D image of interferometer on a selected area of LE12-07 irr (D).

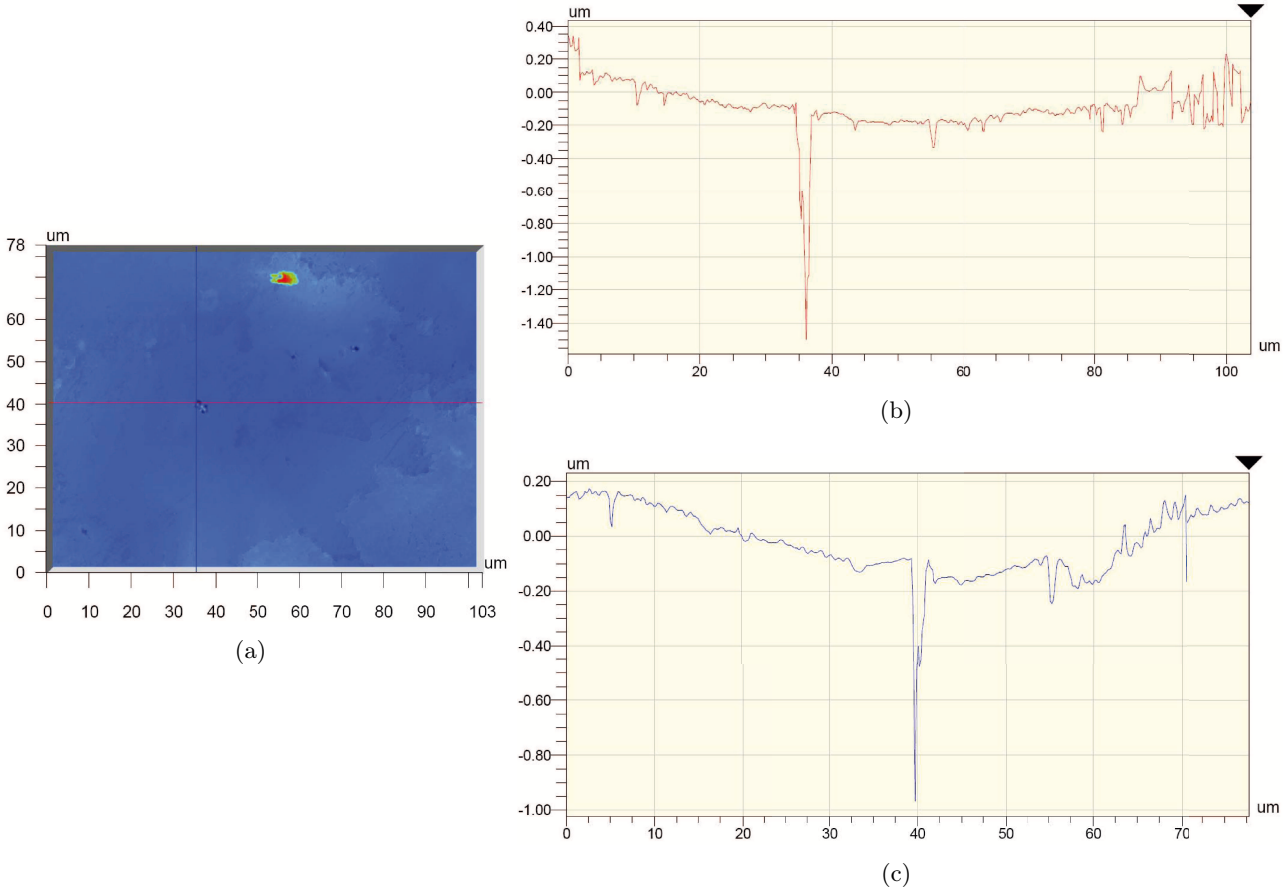

Figure 6.26: Interferometer profile measurements on a cavity, error bar: ±5%. (a) location of the cavity: X-axis in red curve and Y-axis in blue; (b) X-axis profile scan: (c) Y-axis profile scan.

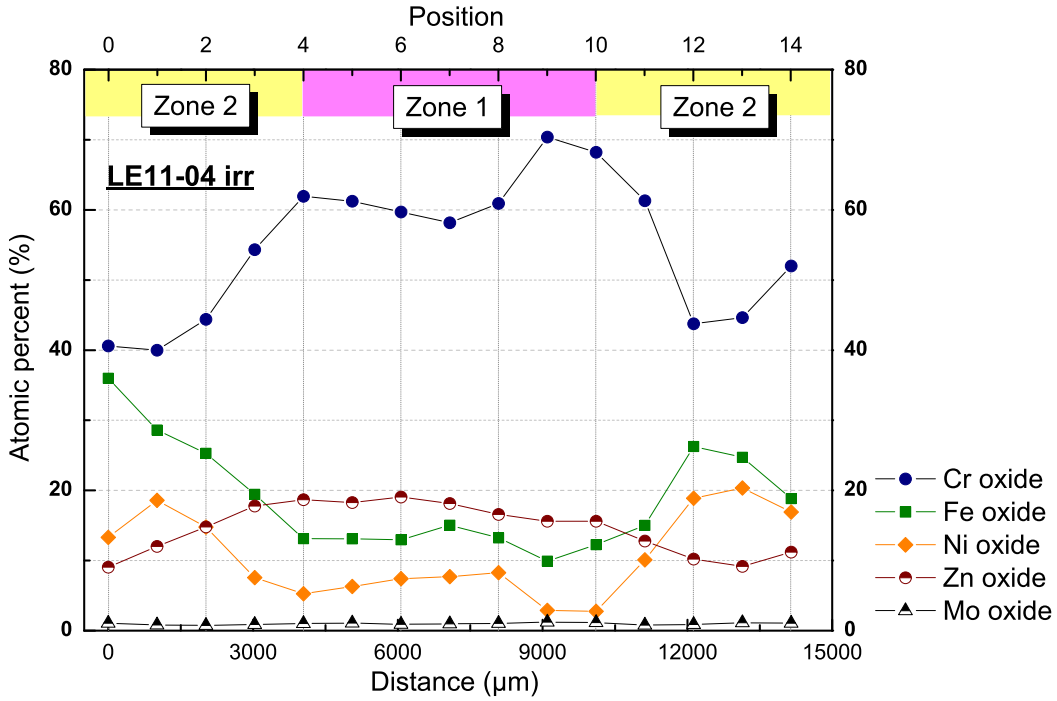

(a) LE11-04 irr (D)

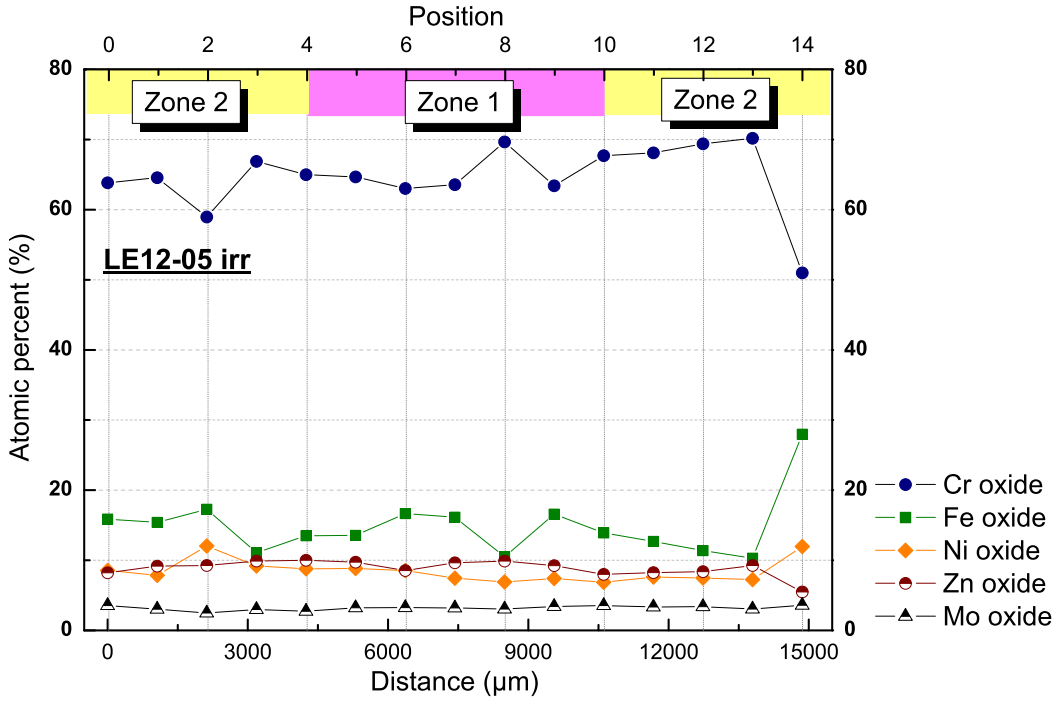

(b) LE12-05 irr (C)

Figure 6.27: The XPS quantification results of (a) LE11-04 irr (D) and (b) LE12-05irr (C), error bar: ±5%.

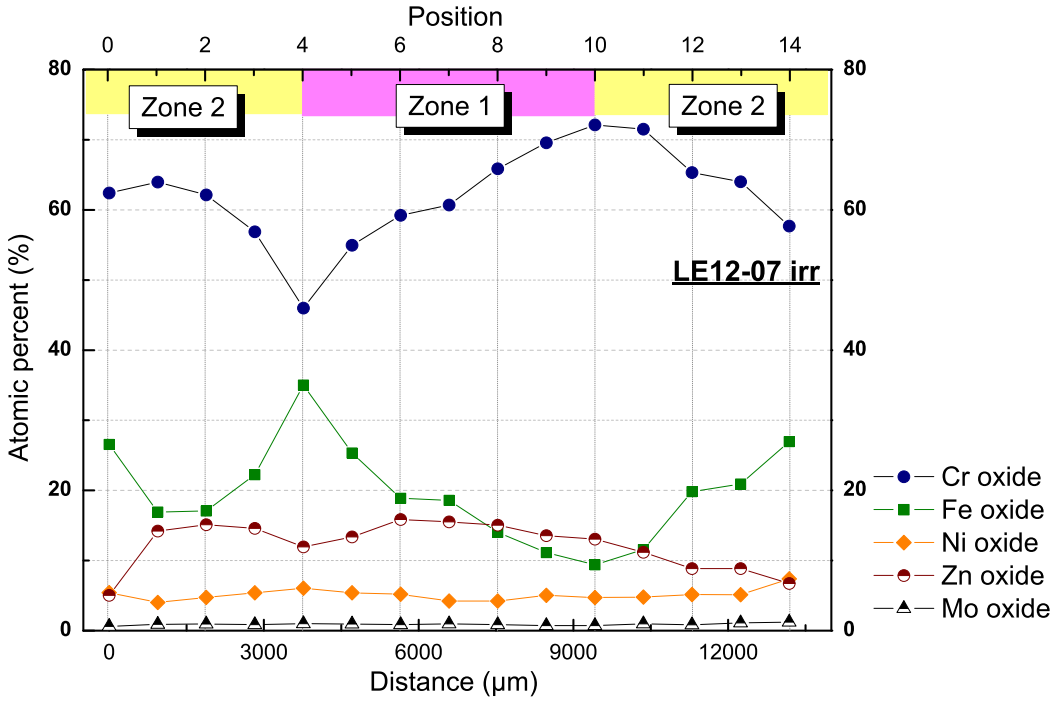

(a) LE12-07 irr (D)

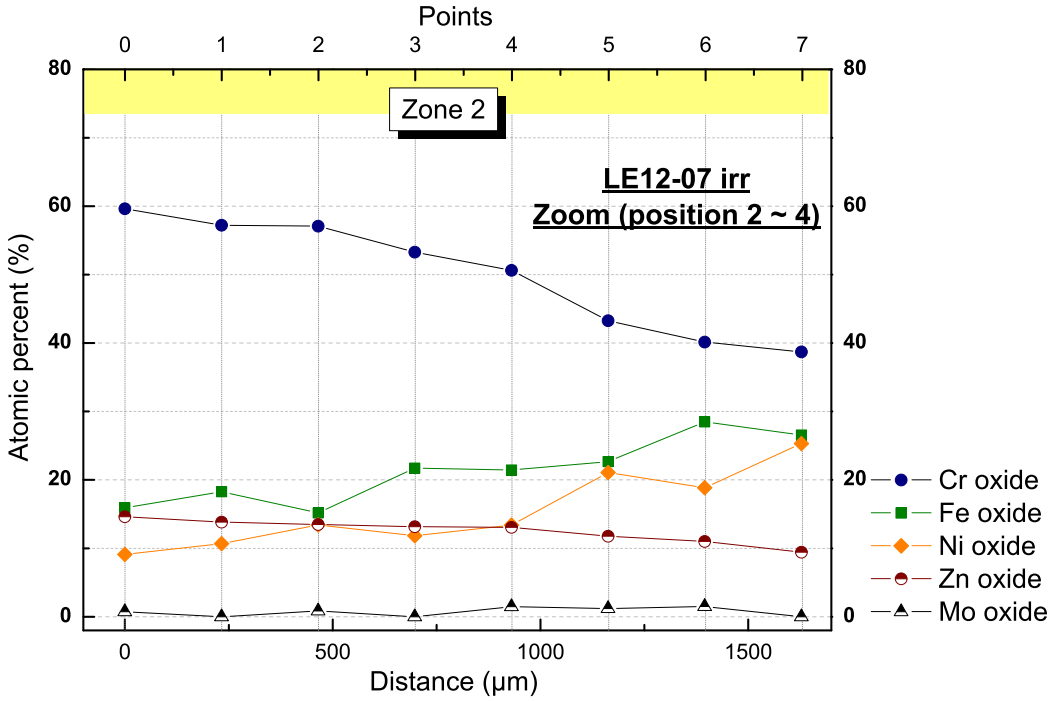

(b) LE12-07 (D) zoom

Figure 6.28: The XPS quantification results of LE12-07 irr (D): (a) the whole spectra from position 0 to position 14; (b) a zoom of the spectrum from position 2 to 4 in the (a), error bar: ±5%.

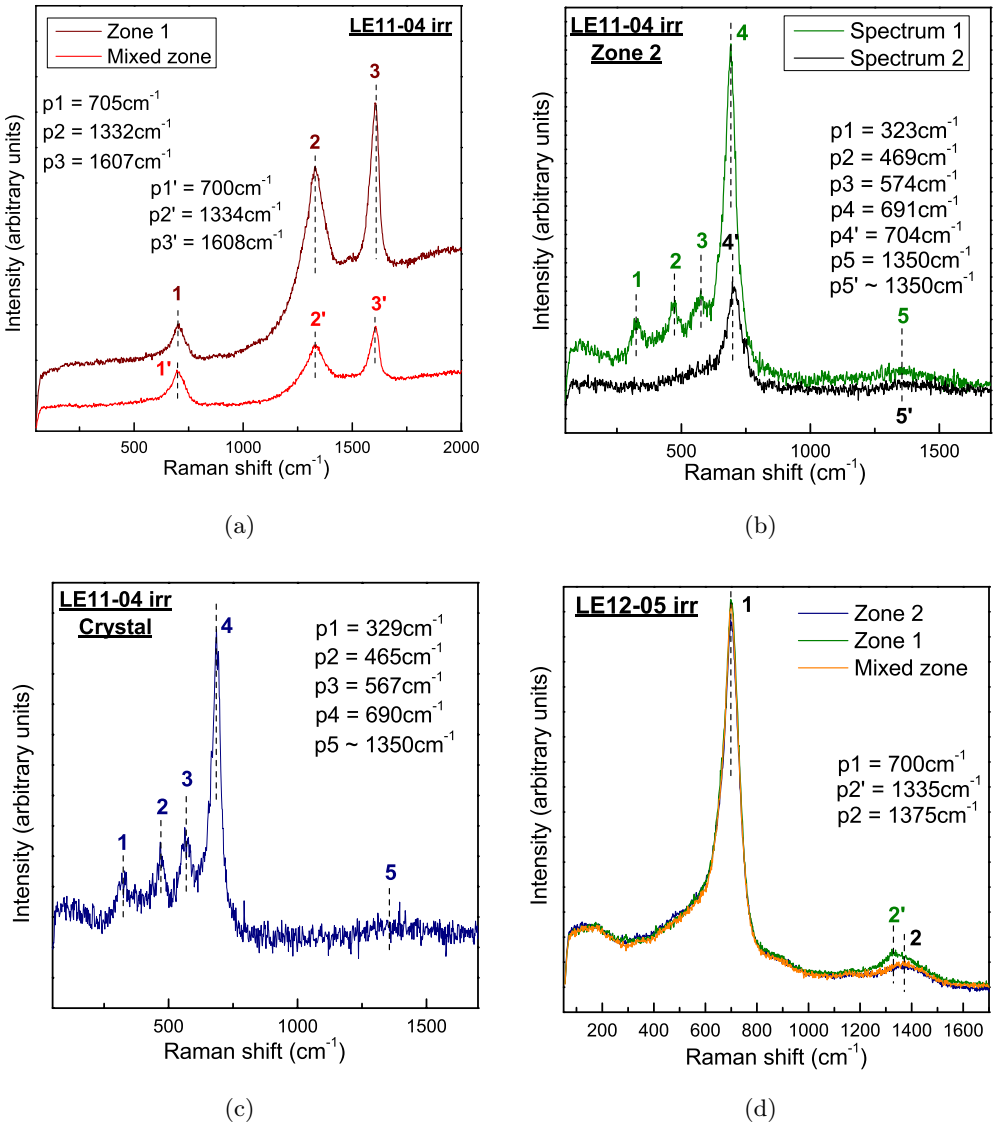

Figure 6.29: Raman spectra in different zones: (a) zone 1 (irradiated) and mixed zone, (b) zone 2 (unirradiated), (c) a crystallite of LE11-04 irr (D); (d) LE12-05 irr (C), zone 1 (irradiated), mixed zone and zone 2 (unirradiated).

zone (zone 2, Fig.6.29 (b)), there exist two different features, one has five peaks and only the peak at at 700 cm^{-1} remains on the other one. As demonstrated in Fig.6.29 (c), the feature with five peaks is corresponded to a crystallite spectrum.

Therefore, it shows that:

- The two features in zone 2 means either a spinel oxide close to a crystallite (green curve) or a spinel oxide close to $FeCr_2O_4$ (black curve) [4].
- The two peaks at higher wavenumbers (p2 and p3 in Fig.6.29 (a)) are probably showing the carbon, which is in accordance with the SEM-EDX analysis on LE11-04 irr (D). Based on the SEM results, small **round** spots, most possibly carbon (shown in Fig.6.20), are all over the irradiated and mixed zone of LE11-04 irr (D).

For LE12-05 irr (C) (Fig.6.29 (d)), the spectra show a high similarity among each zone. There are a main peak is at 700 cm^{-1} and a broad feature around 1350 cm^{-1}. According to the reference [4, 5], the oxide formed is close to $FeCr_2O_4$.

In short, on the surface where the small crystallites are presented, the oxide formed is a spinel oxide close to the $FeCr_2O_4$. However, in the case of large crystallites, the spinel oxide is still close to $NiFe_xCr_{2-x}O_4$.

6.3.D Quantification of Oxygen - NRA Analysis

The quantity of oxygen atoms of each electron irradiated 316L oxide film has been determined by NRA. As pictured in Fig.6.30, several spots analyses were done for each discs. And the results are given in the Tab.6.6.

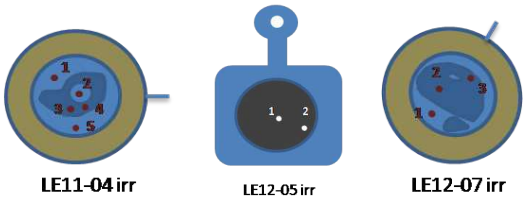

(a) (b) (c)

Figure 6.30: Sketches of LE11-04 irr (D), LE12-05 irr (C) and LE12-07 irr (D), indicating the analysed spots in the zone1 (irradiated) and the zone 2 (unirradiated), respectively. Duration and fluence of each specimen are indicated in Tabs.6.4 and 6.5, respectively.

Specimens	N oxygen atom (10^{15} at/cm^2)				
	spot1	spot2	spot 3	spot 4	spot 5
LE11-04 irr (D)	993	463	365	461	1151
LE12-05 irr (C)	997	1085			
LE12-07 irr (D)	665	401	401		

Table 6.6: NRA estimated quantity of oxygen atoms (atoms per cm^2) of LE11-04 irr (D), LE12-05 irr (C) and LE12-07 irr (D), error bar ±10 %.

Based on the values in Tab.6.6, the results show that:

- The quantity of the oxygen atoms varies two or three times among different spots in the same disc. By roughly converting the quantity into an equivalent thickness of the oxide film in order to be more visualised, it varies from $\sim$ 70 to $\sim$ 200 nm.

- The **irregularity** of the oxide film is well exhibited, especially for the LE11-04 irr (D). Depending on the different zones, the thickness varies significantly, which can be explained by the distribution of the crystallites on the surface.

6.3.E TEM Analysis

The TEM analysis was performed on LE12-05 irr (C), which was irradiated at 300°C for 65 hours continuously in the HTHP cell.

6.3.E.1 Morphology

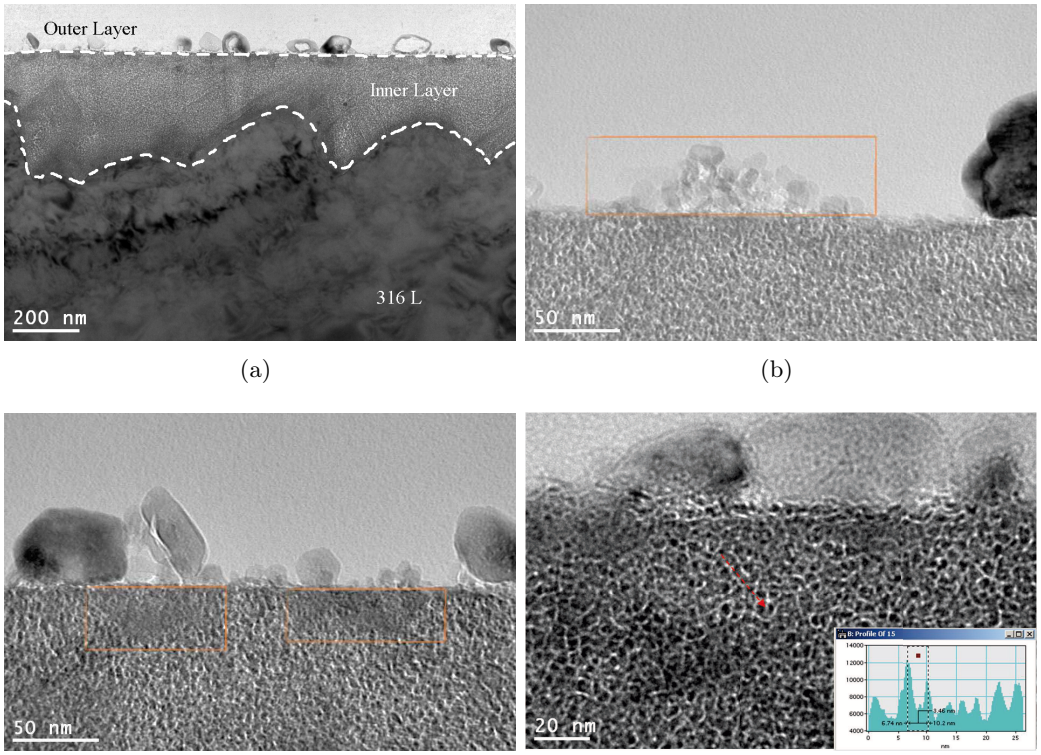

(a) (b)

(c) (d)

Figure 6.31: TEM micrographs in the zone 1 (irradaited) of LE12-05 irr (C): (a), (b), (c) and (d) different spots in the oxide film.

As illustrated in Fig.6.31, it reveals that:

- figure (a): the inner layer is continuous while the outer layer is discontinuous. Because of the roughness at the interface of metal/ oxide, the thickness of the inner layer varies from 100 to 400 nm.
- figure (b): the size of the crystallites on the outer layer is relatively small (less than 100 nm). Moreover, an evolution of geometry form on the crystallite can be observed.
- figure (c): the inner layer is not homogenous. Some places (close to the extreme surface) present a less granular appearance, as shown in the orange blocks.
- figure (d): the inner layer is composed with nano-grains with an average size about 3 nm.

Due to the fact that the crystallites are too small, they are easy detached during the preparation, and thus the *dark materials* surrounding the crystallites are the C-rich layers.

6.3.E.2 Compositions

The inner oxide layer is mainly composed of Cr, Fe, Ni with the trace of Mo and Zn, as demonstrated in Fig.6.32. The composition is close to (Ni,Fe)Cr_2O_4. Comparing the spot 1 and 2 (less granular), it shows that a slight increase of chromium content in spot 1.

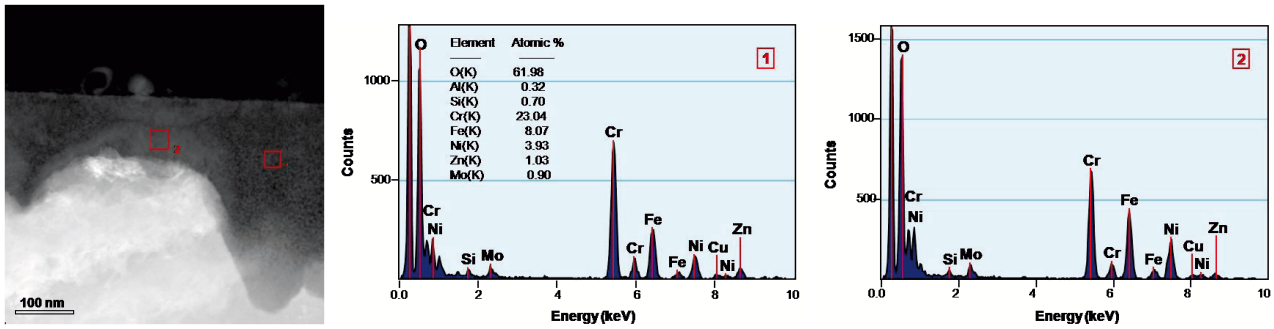

(a) (b) (c)

Figure 6.32: TEM-EDX Analysis in the zone 1 (irradiated) of LE12-05 irr (C), (a): STEM-HADDF image indicated the analysed spots 1 and 2; (b) and (c): EDX spectra of different spots indicated in (a).

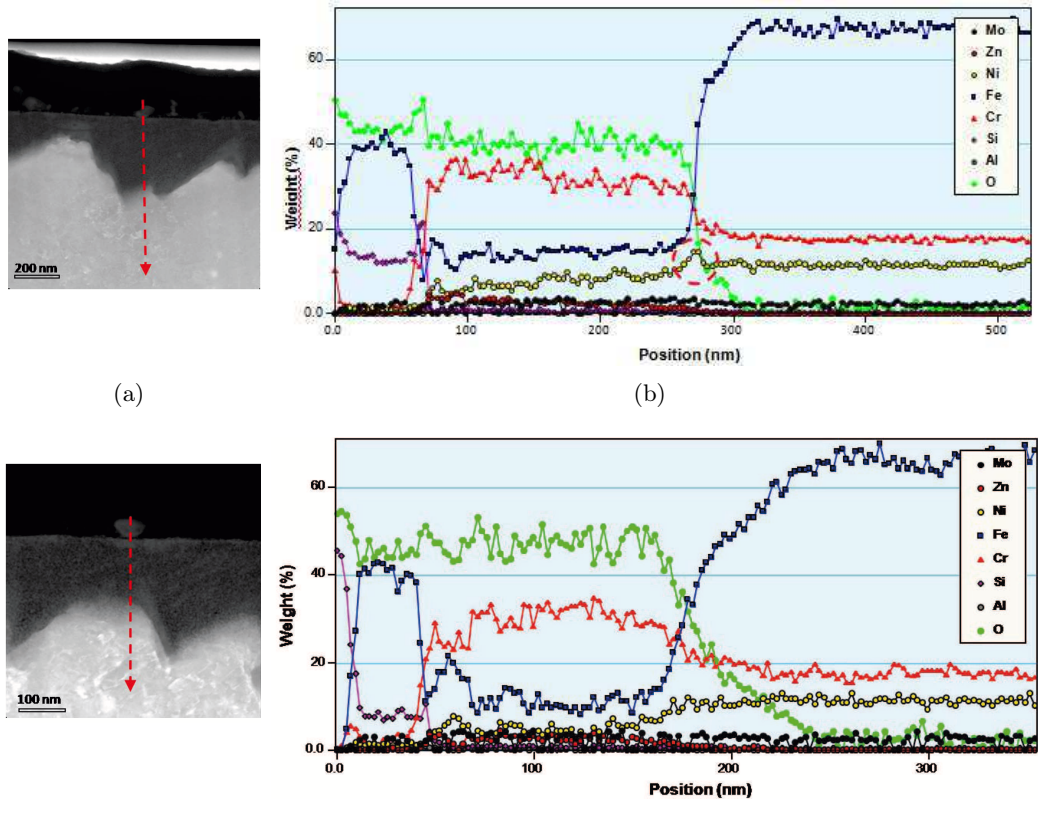

(a) (b)

(c) (d)

Figure 6.33: TEM-EDX Analysis in the zone 1 (irradiated) of LE12-05 irr (C), (b) and (d): the EDX compositional profiles obtained across the oxide layer, the paths are indicated in the STEM-HADDF images (a) and (c).

Two profile line-scans, indicated by red arrows in Fig.6.33, have been performed across the oxide layer. They show that:

- **Outer layer** is composed by Fe and O, nearly no Ni has participated in its formation. Furthermore, the iron content is only up to 40%, while a high concentration of O about 50%. However, the overdose of the O should be explained by the deposit of SiO_2 during the sample preparation for the TEM investigation.
- **Ni enrichment** is not so obvious under the oxide film, only a faint increase can be observed, emphasised by the red circle in Fig.6.33 (b).

6.3.E.3 Structure

The crystal structure of the inner layer is shown in Fig.6.34 and the outer layer is illustrated in Fig.6.35:

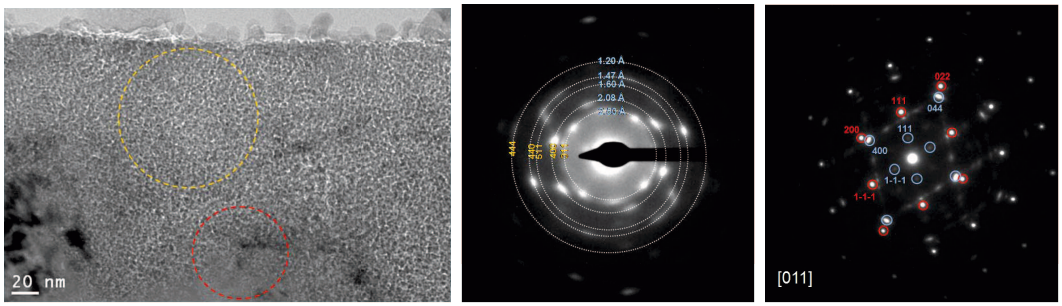

(a) (b) yellow (c) red

Figure 6.34: TEM-SAD Analysis on the inner layer oxide in the zone 1 (irradiated) of LE12-05 irr (C), (a): TEM image indicated two selected analysed spots (yellow and red); (b) and (c): are the electron diffractograms of the selected area on the TEM images (a).

- The **inner layer:** the diffraction pattern exhibited in Fig.6.34 (b) (for the yellow circle in figure (a)) is a series of **rings**. However, several spots under high illumination can also be noticed. It reveals that the inner layer has a polycrystalline structure of a spinel oxide $(Ni,Fe)Cr_2O_4$ with a strong texture. In Fig.6.34 (c) (for the red circle in figure (a)), the orientations of the 316L substrate are indicated in red while the orientations of the oxide are shown in blue. It seems that the inner layer is grown epitaxially with the 316L substrate.
- The **outer layer:** the diffraction patterns shown in Fig.6.35 (b) & (d) are patterns of **dots** with the crystal orientations indicated in red. The atomic distance measurements on the diffraction patterns reveal that the oxide formed on the outer layer is consistent with a hematite structure, α-Fe_2O_3. Therefore, the oxide no longer has a spinel structure but a corundum one. Furthermore, the presence of α-Fe_2O_3 means that the environment is more oxidative than expected, because all the Fe is oxidised into Fe(III). It is not the case for Fe_3O_4, which contains Fe(III) and Fe(II).

In addition, a precision should be made for the outer layer of the oxide. Some crystallites are well crystallised while others are looked like empty **hollow** spheres. In the same way, an extremely

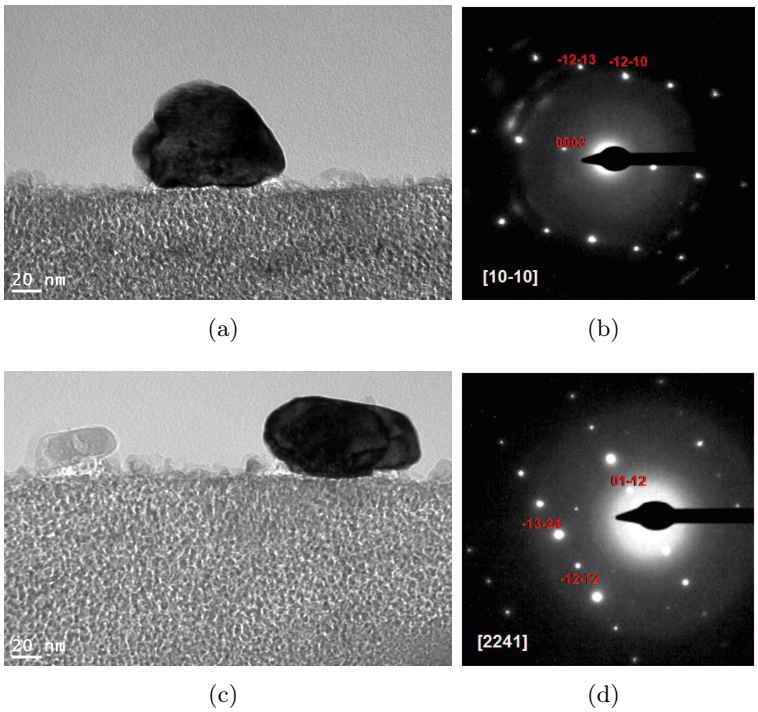

Figure 6.35: TEM-SAD Analysis on the outer layer oxide in the zone 1 (irradiated) of LE12-05 irr (C), (b) and (d): the electron diffractograms of the crystallite shown in the TEM images (a) and (c), respectively.

slight increase of chromium concentration on the periphery of external oxides (crystallites) can be noticed by the EDX profiles, Fig.6.33 (d). Therefore, a further probing was performed on the outer layer.

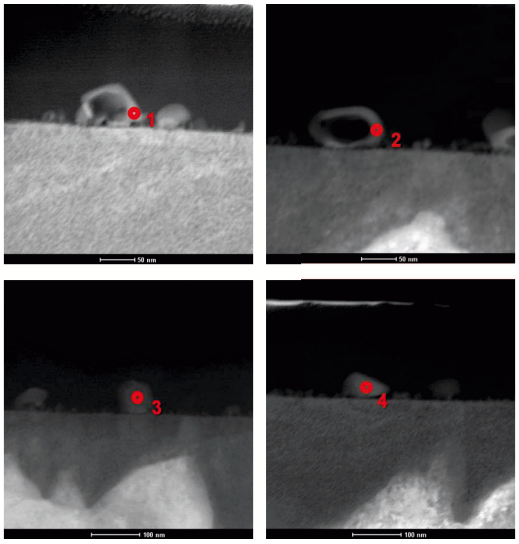

Figure 6.36: TEM-EDX analysis on LE12-05 irr (C): STEM-HADDF image indicated the analysed spots 1 - 4.

Positions	Cr	Fe	Ni	Mo
	%Weight.			
Spot 1	27.42	65.61	4.17	2.79
Spot 2	11.54	81.34	5.75	1.35
Spot 3	3.36	90.45	3.28	2.89
Spot 4	4.19	87.84	3.73	4.21

Table 6.7: TEM-EDX analysis in the zone 1 (irradiated) of LE12-05 irr (C): EDX analysis on four spots in different positions indicated in 6.36.

Fig.6.36 illustrates the EDX analysis on the spots located in the different places of the crystallites. Spots 1 and 2 are for the external region of crystallites which look like the *crowns* of the **hollow** crystallites. Meanwhile, spots 3 and 4 are for the internal region of the **solid** crystallites. Tab.6.7 clearly indicates that there is an enrichment of chromium for the *crowns* of the **hollow** crystallites while the **solid** crystallites are still rich in iron. It elucidates that the crystallites are covered by a Cr-rich layer, especially for the **hollow** ones. Moreover, a further structural analysis on the periphery of crystallites can confirm this observation, shown in Fig.6.37.

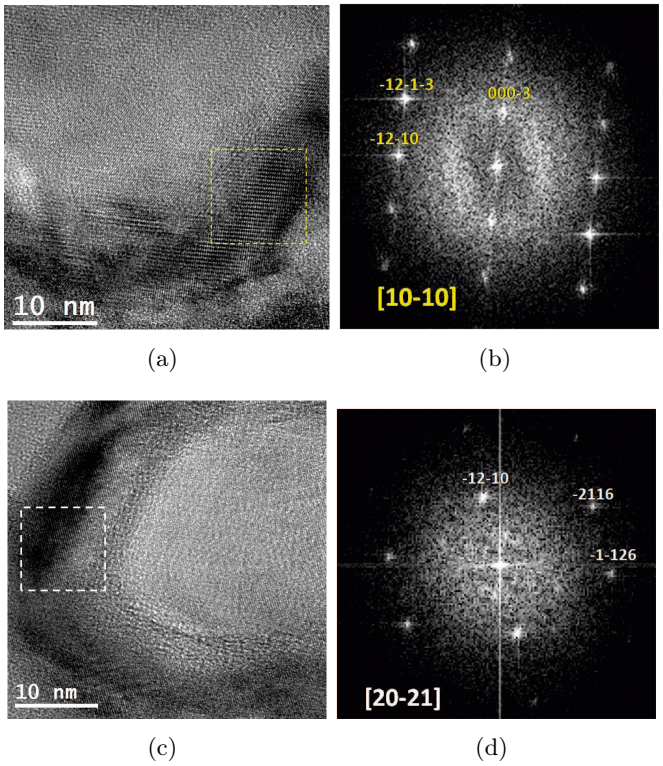

Figure 6.37: HRTEM Analysis on the outer layer of LE12-05 irr (C), (a) and (c): HRTEM images on the the crystallites; (b) and (d): Fournier transformation diffractograms on the border of the crystallite, the selected zones shown in (a) and (c), respectively.

The two Fourier Transform diffractrograms, Fig.6.37 (b) & (d), demonstrates a corundum structure of hematites (R-3c), for the selected zone indicated in the yellow or white boxes in Fig.6.37 (a) & (c), respectively. Taking into account the composition, it reveals that the crystallite is actually $(Fe, Cr)_2O_3$ instead of pure α-Fe_2O_3.

6.3.F GD-OES Analysis

A GD-OES depth profile scan in the central zone of LE12-07 irr (D) is shown in Fig.6.38. In general, the composition of the oxide film measured in a larger scale (4 mm^2) is in accordance with XPS results. However, Zn does not shown up in the GDMS spectrum because it has not been analysed.

Furthermore, it shows that:

- The first part is rich in Fe, Ni and O, which is the outer layer. Afterwards, it is the inner layer,

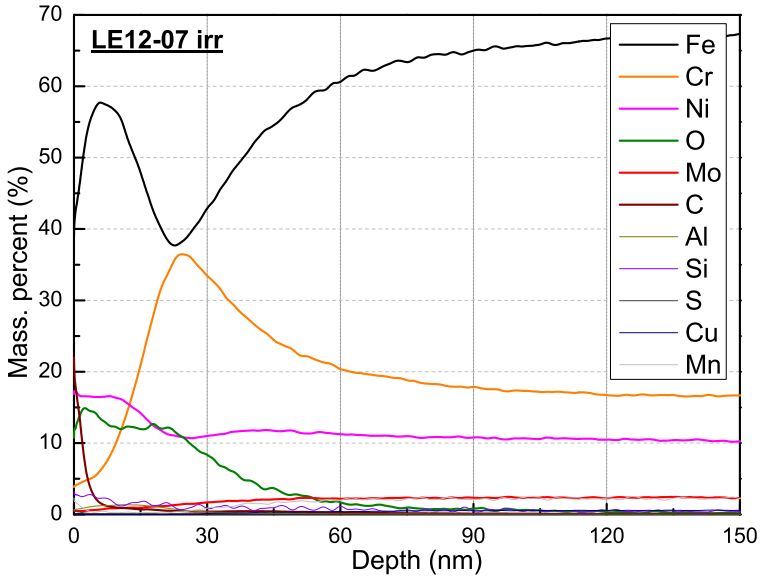

Figure 6.38: GD-OES elemental scan in depth profile on LE12-07 irr (D) (zone 1, irradiated), error bar: ±5%.

which is composed of Fe, Cr, Ni and little presence of Mo.

- An extremely high concentration iron content can be noticed. It is up to nearly 60% for the outer layer, and even for the inner layer, the iron concentration is always higher than chromium.

Actually, it needs to emphasis that GD-OES is an analysis on a spot of about 4 mm^2. Based on the inhomogeneity of the oxide thickness, the results may combine the oxide with the substrate together. Consequently, a high concentration of iron in the oxide film is shown by GE-OES, which is significantly affected by the bulk concentration of iron in the 316L stainless steel.

6.3.G CS-AFM Analysis

A CS-AFM analysis was carried out on LE12-07 irr (D), on zone 1 (irradiated), mixed zone and zone 2 (unirradiated).

Figs.6.39, 6.40 and 6.41, it shows that:

1. **zone** 1: the roughness is relatively homogenous, and the surface is quite insulated;
2. **mixed zone**: the surface is more rough and less insulated compared to the other zones, meanwhile two big crystallites (white spots) are observed;
3. **zone** 2: the surface is rough and inhomogeneous, partly it is quite insulated and partly not.

In all the cartographies, a smooth area shown in dark colour on the topography image is in correlation with an insulated zone on the current image.

The results obtained by CS-AFM are relative measurements of the surface. Concerning the roughness of the surface (topography images), they are in agreement with SEM images. In the rough, the electrical resistance of the irradiated interface is around 80 MΩ to 1000GΩ.

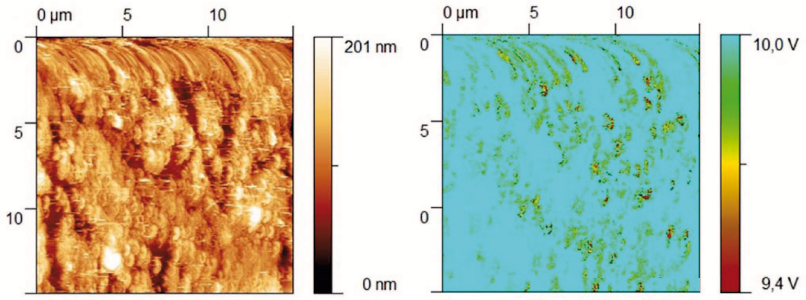

(a) (b)

Figure 6.39: Cartography images of LE12-07 irr (D), **zone** 1 (irradiated), analysed area: $15 \times 15 \mu m^2$. (a) topography images and (b) current image.

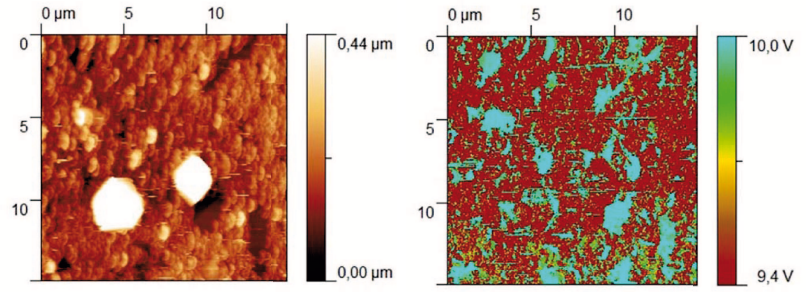

(a) (b)

Figure 6.40: Cartography images of LE12-07 irr (D), **mixed zone**, analysed area: $15 \times 15 \mu m^2$. (a) topography images and (b) current image.

Based on the observation, the difference of conductivity may be caused by the crystallites:

- **General case**, Fig.6.42 (a), the big crystallites have a close composition with the small ones. Considering the conduction is not limit by the thickness of the oxide film, the big and small crystallites exhibit the same conductivity.

- **Conductive case**, Fig.6.42 (b), the big crystallites have a different composition from the small ones, which are more conductive than the small ones. Consequently, a higher conductivity can be measured on the position of the big crystallites.

- **Resistive case**, Fig.6.42 (c), on the contrary of conductive case, the big crystallites can be more insulating than the small ones, and leads to a lower conductivity.

In short, the CM-AFM results confirm that the surface is quite inhomogeneous and different types of crystallites are presented on the outer layer of the oxide film.

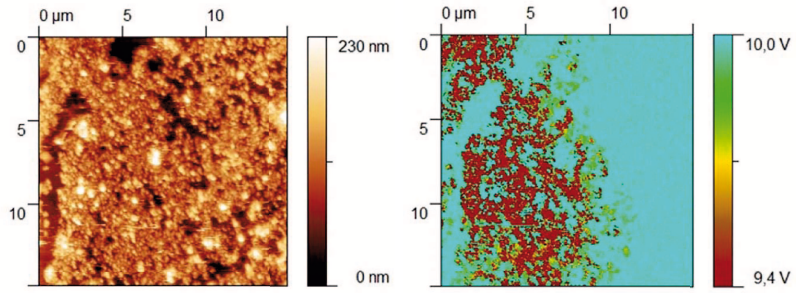

(a) (b)

Figure 6.41: Cartography images of LE12-07 irr (D), **zone** 2 (unirradiated), analysed area: $15 \times 15 \mu m^2$. (a) topography images and (b) current image.

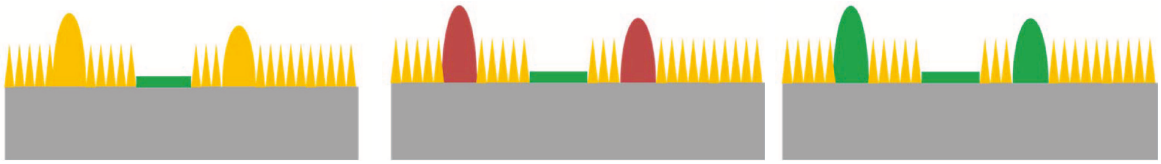

(a) (b) (c)

Figure 6.42: Schematic layout of the oxide film formed on LE12-07 irr (D), observed by CS-AFM, (a) general case; (b) conductive case and (c) resistive case. Small and big yellow triangle: small and big general crystallites; big red triangle: conductive crystallites; big green triangle: resistive crystallites; green substrate: smooth and insulated area.

6.4 Irradiated PWR water analysis

As same as the 316L surface characterisation, due to the activation after irradiation, only the electron irradiated PWR water has been analysed, and the results are indicated in Tab.6.8.

Specimens	$pH_{25°C}$	Fe	Cr	Ni	Zn	Cu
				(μg/L)		
PWR water (blank)	6.1 $\sim$ 6.4	0.5	1.8	< 3	< 3	< 3
LE11-04 irr (D)	-	230	2.2	66	16	-
LE12-05 irr (C)	4.25	60550	**44**	5100	20170	1835
LE12-07 irr (D)	6.06	232	**74**	597	128	51

Table 6.8: The pH and concentrations of released and dissolved cations of solution: blank PWR water, LE11-04 irr (D), LE12-05 irr (C) and LE12-07 irr (D); - : lack of solution, error bar: $\pm 3\%$.

The blank PWR water corresponds to the analysis of the PWR water after preparation and before experiment. Concerning the irradiated PWR water, the analyses show:

- **pH:** it becomes more acid when cation release is important. The pH evolution and cation release are linked as the reason or the consequence to each other.
- **Cation release:** it depends on the conditions of each experiment: the temperature, hydrogen

concentration, the duration at high temperature and whether it is continuous or not. Except for LE12-05 irr (C), cation release of the other two seems to be reasonable according to the reference experiments.

1. **LE**11-04 **irr (D):** the release of cations is minor in this case. Considering the initial concentration of hydrogen is relatively high, it may be responsible for this minimum release.
2. **LE**12-05 **irr (C):** has the most significant release of cations. Even though it was irradiated at 300°C continuously for 65 hours, the release of cations should not be as much as observed. The important increase happens to each cation, especially for Fe and Zn. The release of Zn comes from the HTHP cell itself while the Fe is certainly from the 316L stainless steel. Other than these, the release of Cr also needs to be noticed. The chromium element in 316L stainless steel is actually difficult to release as the oxide film (inner layer, more precisely) stays protective. In other words, it implies that the oxide film is no longer or less passive. Indeed, based on the characterisation of the oxide film formed on LE12-05 irr (C) in the previous section, it has been shown: the presence of *cavities* on the surface, the size reduce of crystallites and the outer layer of the oxide is α-Fe_2O_3 which should be formed in a oxidative environment. Therefore, it shows an agreement between the characterisation of oxide film and the analysis of the PWR water.
3. **LE**12-07 **irr (D):** it is the one in the middle of the three cases. It is noticed that the release of Fe is relatively low comparing with the other elements while the release of Cr is essentially important, even over the one of LE12-05 irr (C). Such a high release of Cr means for sure that the oxide film (inner layer) is well affected.
4. **Chromium release:** both LE12-05 irr and LE12-07 irr (D) had an important release of chromium, which can be ten (or even twenty) times higher than usual. On the other hand, the specific corrosion feature in common between LE12-07 irr (D) and LE12-05 irr (C) is the presence of *cavities* on the surface. Evidently, the high release of Cr is caused by *cavity* creation on the surface of the oxide film. In other words, the protective passive film, rich in chromium, is somehow brokendown.
5. **Iron release:** other than the specific case (LE12-05 irr (C)), the release of iron is not significant, around 200 μg/L.

Overall, the analysis on the irradiated PWR water brings out the effect of radiolysis on pH and the release of cations. Due to the irradiation at the interface, the 316L releases more chromium into the solution. It means that the radiolysis affects and further reduces locally the protective oxide film which is rich in chromium. Consequently, a correlation with the observation of **cavities** can also be made.

6.5 Summary

In this chapter, the effect of radiolysis on an interface 316/ PWR water in three directions has been studied:

- evolution of electrochemical potential under irradiation;
- changes in the characteristic of oxide film formed 316L;
- influence on the release of cations in the irradiated PWR water.

First of all, an irradiation-induced variation of free potential is demonstrated for both proton and electron beams. In most cases, it is an oxidative response to the beam. The intensity of this response varies with different parameters: irradiation temperature, hydrogen concentration, thermal treatment, and fluence cumulation.

The oxide film formed on the irradiated 316L stainless steel disc is a double-layer oxide, inner layer rich in chromium while outer layer rich in iron. Other than the small crystallites of the outer layer, more defects on the oxide can be observed. Among them, the most impressive are the presence of *cavities* and the formation of the α-Fe_2O_3. It is proposed in this work, the creation of *cavities* is related to the breakdown of the passive oxide film and to the high release of chromium cations. Because as long as there are *cavities* on the surface, the release of chromium is ten (or even twenty) times higher than usual. The formation of the α-Fe_2O_3 requires a relatively oxidative environment which is not the case in this work. Single thermal treatment with dissolved hydrogen in the PWR water is not able to create such an oxidative environment and leads to these consequences. However, it is considered to be an evolution of the environment induced by the radiolysis. The radiolysis affect the oxide film and may also break down the oxide film. Meanwhile, it is clear that a correlation can be build between the damage of the oxide film and the release of cations in the PWR water.

More important, the *oxidative response* induced by irradiation shown on the electrochemical potential can be considered as an indicator to tell the environment is becoming more and more oxidant. Therefore, more oxidant oxide species may be formed due to the environment changes.

Finally, in order to get a better and whole image of the radiolysis effect at high temperature and high pressure, it is worth considering the reference experiment. The discussion will be done in the next chapter.

References

[1] Muzeau B., Perrin S., Corbel C., Simon D. and Fron D. Electrochemical behaviour of stainless steel in PWR primary coolant conditions: Effects of radiolysis. *Journal of Nuclear Materials*, 419(1–3):241 – 247, 2011.

[2] A.J. Elliot, D.M. Bartels. The Reaction set, rate sonstants and g-Values for the Simulation of the Radiolysis of Light Water over the Range 20°C to 350°C Based on Information Available in 2008. Technical report, Atomic energy of Canada Limited, 2009.

[3] Björkbacka A., Hosseinpour S., Leygraf C., Jonsson M. Radiation Induced Corrosion of Copper in Anoxic Aqueous Solution. *Electrochemical and Solid-State Letters*, 15(5).

[4] McCarty K. F., Boehme D. R. A Raman Study of the Systems $Fe_{3-x}Cr_xO_4$ and $Fe_{2-x}Cr_xO_3$. *Journal of Solid State Chemistry*, 79:19–27, 1989.

[5] Hosterman Brain D. *Raman Spectroscopic Study of Solid Solution Spinel Oxides*. PhD thesis, University of Nevada, Las Vegas, 2011.

Chapter 7

Discussions for HTHP Irradiations

The two previous chapters have shown the entire results of the experiments performed on the HTHP cell, including the reference and irradiation ones. Based on these observations, a further discussion can be dragged out in this chapter. Tabs.G.2 & 7.2 summarise the results and indicate an overview for the discussions. The proton irradiated specimen is not listed inside the tables. Because both 316L stainless steel and PWR water are activated after the irradiation, no interface characterisations have been performed.

Specimens	Irradiation	Duration (h) at 250 - 300°C	$P(H_2)$ ($mbar_{300°C}$) start	end	Fluence ($\times 10^{18}.e^{-}.cm^{-2}$) at 250 - 300°C
LE11-02 ref	*no*	72	133	166	*no*
LE12-04 ref	*no*	120	33	-	*no*
LE11-03 ref	*no*	168	33	80	*no*
LE11-04 irr	*yes*	115	190	-	3.412
LE12-05 irr	*yes*	65	29	53	$3.809 \sim 4.736$
LE12-07 irr	*yes*	67	32(L)/ 187(H)	-	5.837

Table 7.1: Overview of the experimental conditions of the specimens, reference and irradiated. (L): low hydrogen pressure; (H): high hydrogen pressure.

Specimens	Oxide Film			PWR Solution		
	Inner layer	Outer Layer	Cavities	Fe	Cr	$pH_{25°C}$
LE11-02 ref	$Fe(Fe,Cr)_2O_4$ with metallic Ni	$(Ni,Fe)Fe_2O_4$ with metallic Ni	*no*	/	/	/
LE12-04 ref	$(Ni,Fe)(Fe,Cr)_2O_4$ with Zn oxide	$(Ni,Fe)(Fe,Cr)_2O_4$ with Zn oxide	*no*	++	+	< 5
LE11-03 ref	$(Ni,Fe)(Fe,Cr)_2O_4$ with Zn oxide	$(Ni,Fe)(Fe,Cr)_2O_4$ with Zn oxide	*no*	++	+	/
LE11-04 irr	$(Ni,Fe)(Fe,Cr)_2O_4$ with Zn oxide	$(Ni,Fe)(Fe,Cr)_2O_4$ with Zn oxide & carbon	*no*	+	+	/
LE12-05 irr	$(Ni,Fe)(Fe,Cr)_2O_4$ with Zn oxide	α-Fe_2O_3 with Cr oxide	*yes*	++++	+++	< 5
LE12-07 irr	$(Ni,Fe)(Fe,Cr)_2O_4$ with Zn oxide	α-Fe_2O_3 (probably) with Zn oxide	*yes*	+	+++	~ 6

Table 7.2: Overview of the major characterisation results on the specimens, reference and irradiated.

7.1 Model of Reference Oxide Films

A simplified sketch for the oxide film formed on the 316L stainless steel under primary PWR conditions without irradiations can be portrayed in Fig.7.1 based on the observations (Chap.5.2). It illustrates the bi-layer oxide film, the inner one is rich in chromium while the outer one is rich in iron. Thanks to the different characterisation techniques, more details can be concluded:

- the most possible hypothesis of the composition for the outer layer is a inverse spinel oxide $(Ni,Fe)Fe_2O_4$ while the inner layer can be a mixed spinel oxide $(Ni,Fe)(Fe,Cr)_2O_4$, (Chaps.5.2.B & 5.2.C);

- the crystallites precipitated on the outer layer have a well defined geometry form, and the inner oxide is relatively compact with a nano-grain structure (Chaps.5.2.A & 5.2.E);
- the thickness of the oxide film varies significantly not only due to the size of the crystallites, but also because of the inner layer is inhomogeneous in thickness (Chaps.5.2.E & 5.2.D);
- Ni enrichment (or Cr depletion) is observed at the oxide/ metal interface (Chaps.5.2.E & 5.2.D);
- the inhomogeneity of the oxide film is also exhibited on the outer layer, which presents more than one type of crystallites (Chap.5.2.G).

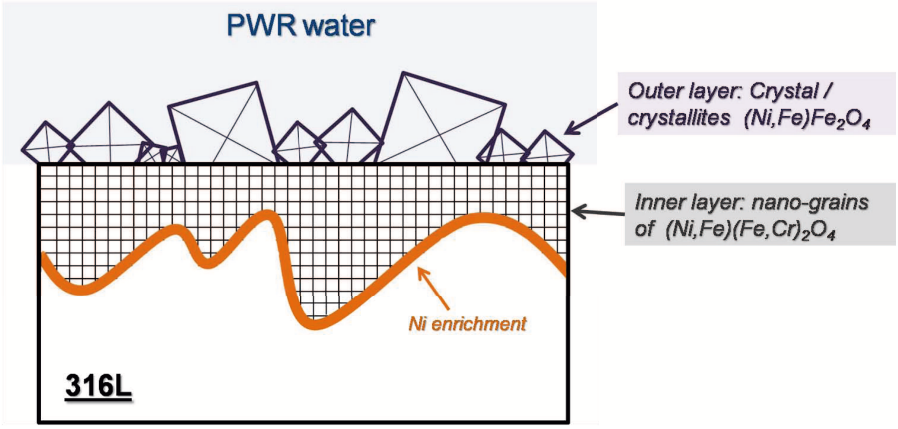

Figure 7.1: Schematic sketch for the **reference** oxide film formed on 316L stainless steel exposed to primary PWR water at 300°C in the HTHP cell for a duration around 70 - 170 hours.

Furthermore, from the literature review in Chapter 3, [1–4], and the observation and conclusion obtained, the process of the oxide formation can be determined, and is shown in Fig.7.2.

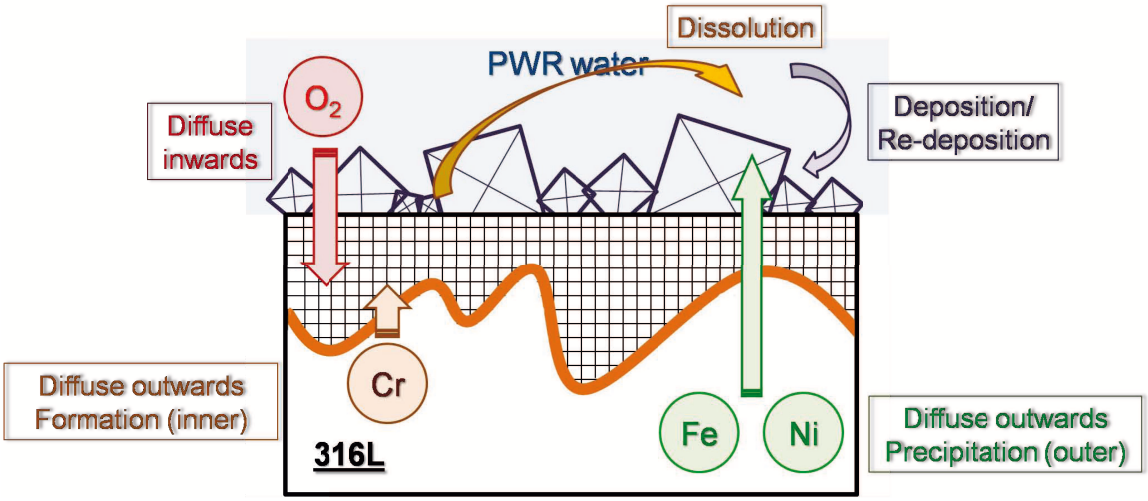

Figure 7.2: Schematic layout for the process of the **reference** oxide film formation of a 316L stainless steel exposed to primary PWR water at 300°C in the HTHP cell for a duration around 70 - 170 hours.

Basically, it can be considered:

- At the early stage, the oxygen diffuses inwards [4] and leads to a selective oxidation of chromium over the other cations in order to form the inner layer. Meanwhile, the iron and nickel cations diffuses outwards, either dissolve in the PWR water or precipitate on the surface to form the outer layer [1];
- The nickel enrichment (or chromium depletion) at the oxide/ metal interface may be due to:
  1. the depletion of chromium which is consumed by the formation of the inner layer;
  2. the inner layer enriches in chromium gradually and pushes nickel to the oxide/ metal interface according to some authors [2, 3];
- Finally, the inner layer continues to grow inwards, more or less homogeneously depending on the diffusion though the grain boundaries, while the outer layer enters into a cycle of dissolution and redeposition.

7.2 Model of Irradiated Oxide Films

Fig.7.3 illustrates a sketch for the irradiated oxide film, mostly based on the observation made on LE12-05 irr and LE12-07 irr (Chap.6.3). As stated previously, the case of LE11-04 irr is quite different from the other two. It is irradiated with a relatively low flux and fluence, under high P(H_2) with several cyclic thermal treatments. According to the characterisation, the dissolution and reprecipitation of the crystallites are probably related to the cyclic thermal treatment. Moreover, under such a high P(H_2), the environment normally remain reductive, and hence the radiolysis effect is low on the interface. In a word, LE11-04 irr is not taken into account for the following discussion.

The model has been considered all the details on the oxide after electron irradiation, including:

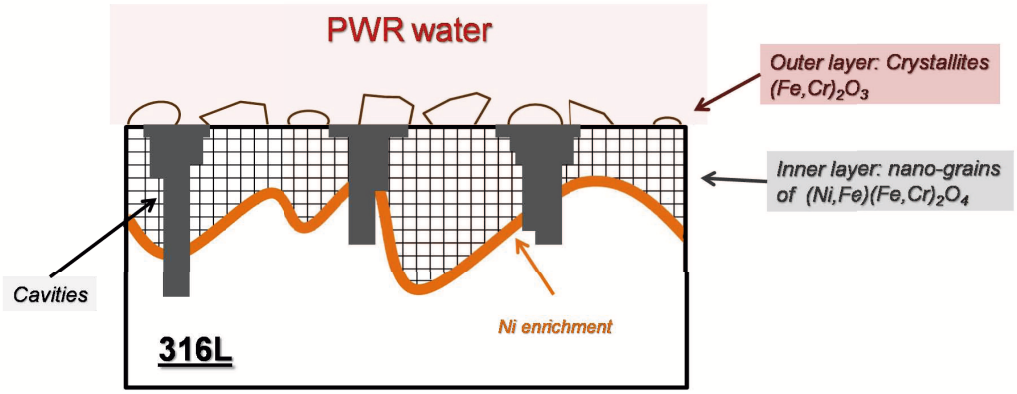

Figure 7.3: Schematic sketch for the **irradiated** oxide film formed on a 316L stainless steel, LE12-05 irr, exposed to primary PWR water at 300°C under electron irradiation in the HTHP cell for a duration around 60 - 200 hours.

- the most possible hypothesis of the composition for the outer layer is an oxide with a corundum structure, αFe_2O_3 with a little presence of Cr, while the inner layer is still a mixed spinel oxide (Ni,Fe)(Fe,Cr)$_2$O$_4$ (Chaps.6.3.B, 6.3.C & 6.3.E);

- the crystallites precipitated on the outer layer are smaller and probably less crystallised than the ones formed without irradiation, and cavities are formed on the surface of the inner layer which is still relatively compact with a nano-grain structure (Chaps.6.3.A & 6.3.E);
- the inhomogeneity of the oxide film is not only represented in thickness but also on the surface (Chaps.6.3.D & 6.3.G).

The process of the irradiated oxide formation can be roughly divided into four stages, as described in Fig.7.4:

- **Stage** 1 *start of irradiation:* the beam starts to irradiate directly on a reference oxide type due to the pre-heating treatment.
- **Stage** 2 *early period under irradiation:* the radiolytic species in the form of bubbles are created at the oxide/ solution interface, and a part of crystallites on the outer layer oxide, (Ni,Fe)Fe_2O_4, are dissolved into solution at the same time. In result, the media (PWR water) is changed at least at the oxide/ water interface.
- **Stage** 3 *later period under irradiation:* the continuous creation of radiolytic species reaches a certain quantity, and then changes the *reductive* PWR water into an *oxidative* PWR water at the oxide/ water interface. Because of this, the dissolved cations can be oxidised. For instance, the oxidation of dissolved divalent Fe(II) into Fe(III) and deposited on the surface afterwards. Meanwhile, the inner oxide layer is dissolved in different tiny zones all over the irradiated surface, probably due to locally high potentials. Consequently, the chromium cations from the inner layer begin to be dissolved into PWR water.
- **Stage** 4 *end of irradiation:* as soon as the beam stops, the production of radiolytic species stops. However, the stable radiolytic products, H_2 and H_2O_2(the precursor of O_2) still stay in the PWR water. In parallel, iron and chromium cations are deposited on the surface to form the outer layer oxide, Fe_2O_3, with a little presence of Cr on the crown of the crystallites.

The change of media at least near the metal/oxide interface is a hypothesis based on the presence of hematite type oxide, α-Fe_2O_3 on the oxide film of the irradiated 316L discs. Otherwise, α-Fe_2O_3 cannot be formed without an oxidative environment, (Fig.7.11). The media is reductive before irradiation because of the dissolved hydrogen, thus the only reason for the change is via irradiation. In addition, the pH drop and the release of cations in the PWR water can verify this point of view. Considering the reference and irradiation experiments together, the release of iron seems to be linked to the thermal ageing while the release of chromium should be traced back to the irradiation effect (high oxidant power, breakdown of the passive layer, release of chromium). The pH drop is due to cation dissolution [5], it decreases with the increase of dissolved cations.

The idea of the radiolytic species in form of bubbles is based on the observation of surface morphology. After electron beam stops, it seems that the crystallites incline to precipitate on the locations of bubbles during the irradiation. More precisely, it is used to explain the *circular feature* of the precipitation preference observed on the irradiated surface. Furthermore, it seems to be related to the presence of cavities. Indeed, the cavities can be found all over the irradiated surface. However,

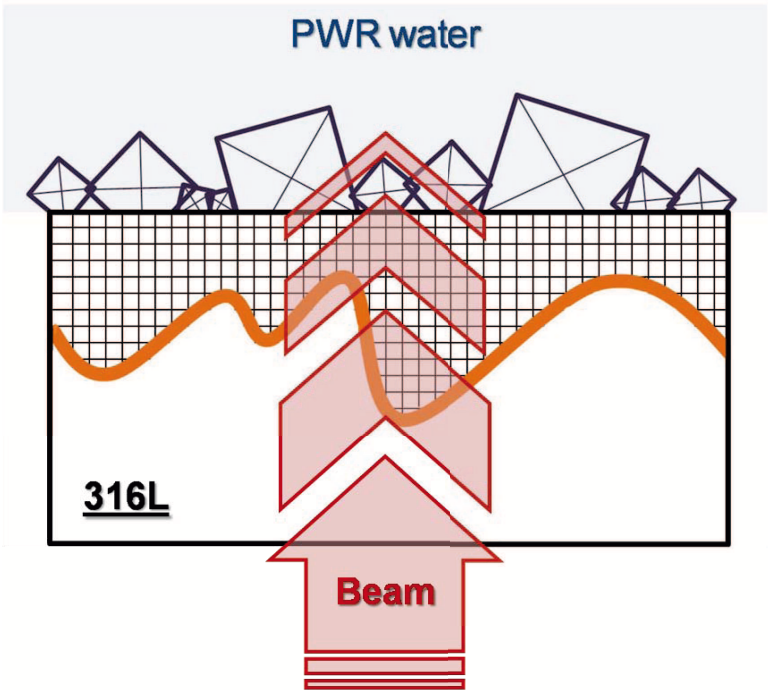

(a) Stage 1: start of irradiation

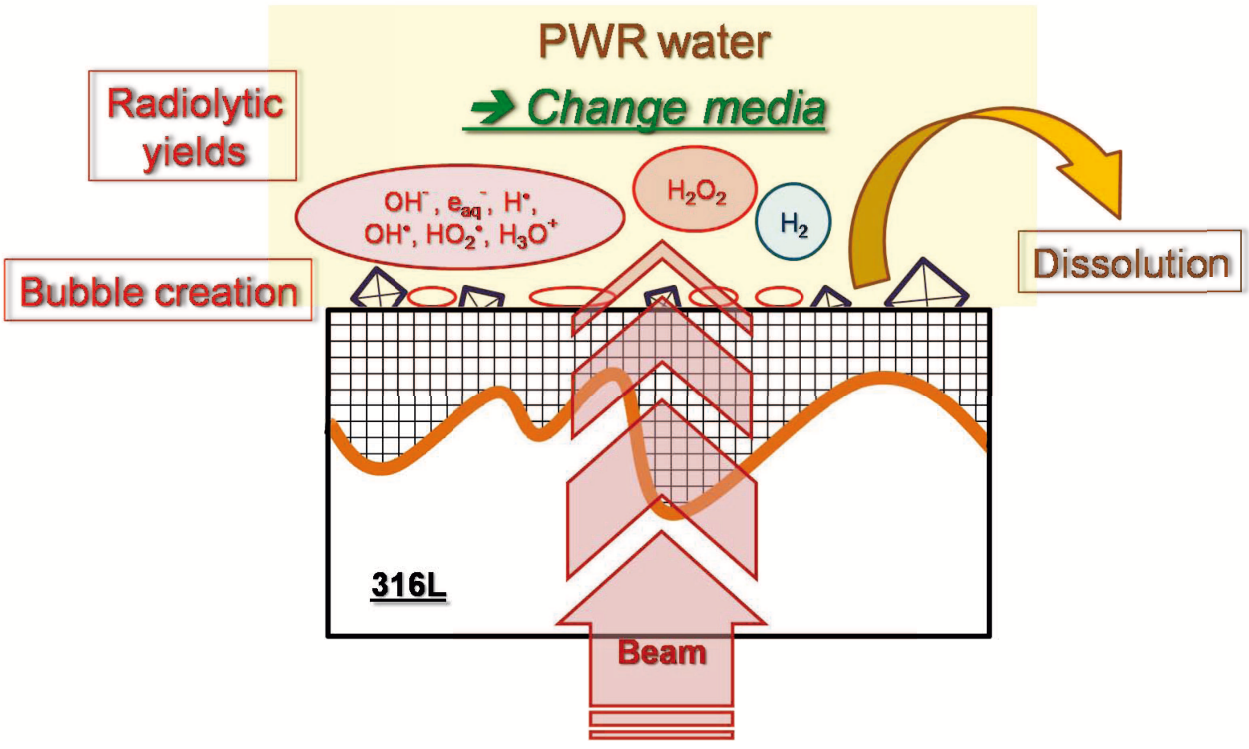

(b) Stage 2: early period under irradiation

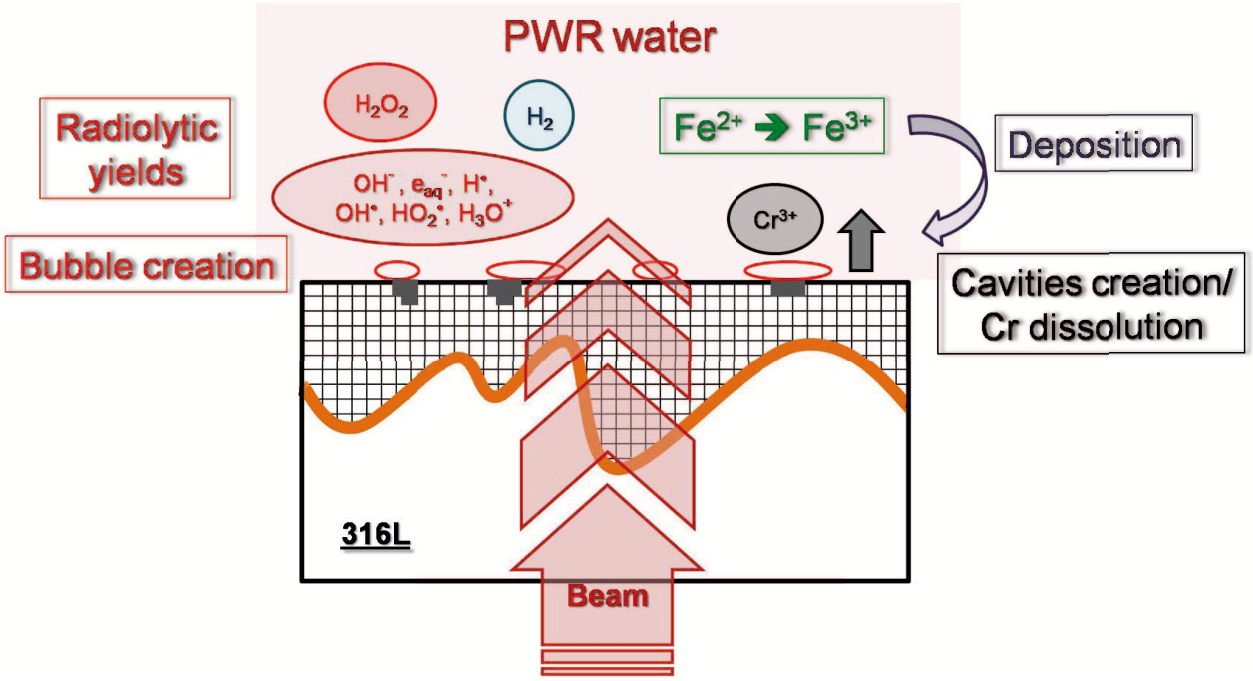

(c) Stage 3: later period under irradaiton

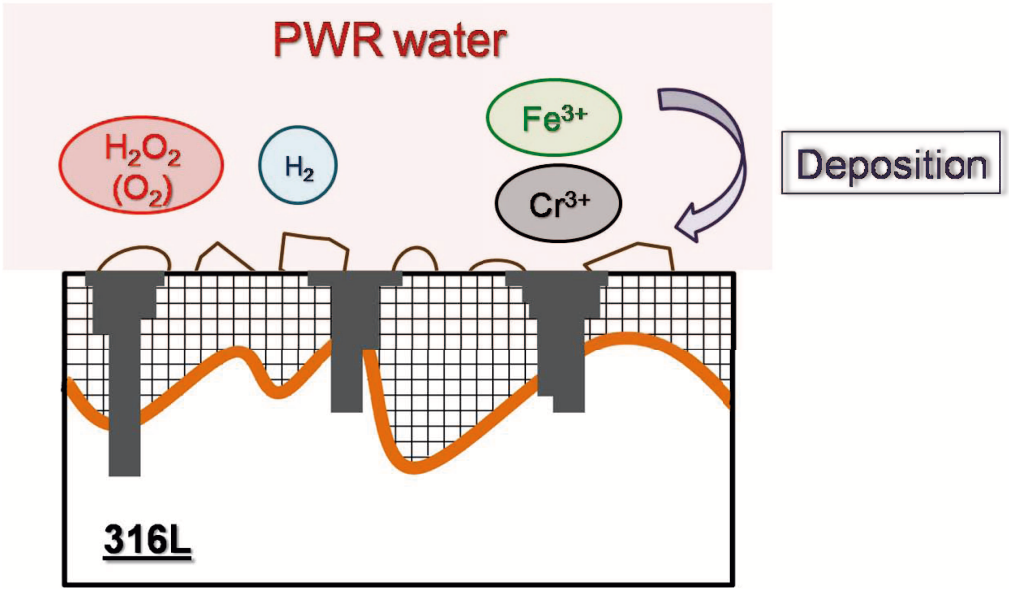

(d) Stage 4: end of irradiation

Figure 7.4: Schematic layout for the process of the **irradiated** oxide film formation of a 316L stainless steel exposed to primary PWR water at 300°C under electron irradiation in the HTHP cell for a duration around 60 - 200 hours.

the probability of their presences is much higher in these *circular features*. Almost in each *circular feature*, at least one cavity can be found. In other words, it verifies that the presence of the cavities is a consequence of the radiolysis effect.

Finally, the crystallites found inside the cavities elucidates that a repassivation process occurs after the oxide film breakdown.

Two models of oxide formation have been proposed for the reference and the irradiated oxide films formed on 316L stainless steel exposed to the primary PWR water in the HTHP cell. In order to validate the models, further developments should be made in parallel:

1. The dissolution of the oxide film: *Which parameters influence the dissolution?*
2. The relationship between the potential and the oxide film: *Do these oxides sustain under the electrochemical conditions?*
3. Modelling of radiolysis: radiolytic species production and their effects on electrochemical potentials.

7.3 Dissolution of The Oxide Films

Speaking of the dissolution of the oxide, it implies for the outer layer, Fe_3O_4 and $NiFe_2O_4$, because the solubility of chromium oxide (protective oxide) is very minor in general. The solubility of the magnetite and nickel ferrite is influenced by temperature [5], pH [5–7] and hydrogen concentration (or partial pressure of dissolved hydrogen $P(H_2)$) [6–9].

As demonstrated in Fig.7.5 and Fig.7.6, a media with a pH value about 7 at 300°C can result in a minimum solubility of nickel ferrite and magnetite [6], which is exactly the case for the PWR water prepared [10], as calculated in Fig.7.7. The high purity (Milli-Q) water contains 1000 ppm boron and 2 ppm lithium degassed by Ar/H_2 gas mixture, has a pH of 7 at 300°C.

Therefore, the PWR water ensures a minimum dissolution of nickel ferrite and magnetite at 300°C in the HTHP cell. However, the circumstance becomes complicated when the third parameter, dissolved hydrogen is taken into account. The dissolution reaction in the presence of hydrogen can be assumed to be a reduction reaction [7, 11]. To simplify the complexing reaction with OH^- ions for either iron or nickel, it can be written as Eq.7.1. In other words, the more cations dissolve, the more OH^- ions are needed, and thus more H^+ will be formed by hydrolyse in H_2O. Subsequently, the acidity of the solution can be increased (pH drop), which may lead to more cations dissolution.

$$M^{2+} + n(OH)^- \rightleftharpoons M(OH)_n^{(2-n)+} \tag{7.1}$$

Furthermore, Sandler *et al.* [7] and Sweeton *et al.* [11], have demonstrated that the solubility dependence of nickel ferrite and magnetite are proportional to $[H_2]^{\frac{1}{3}}$, as plotted in Fig.7.8 and written in Eq.7.2. It can be applied to the hydrogen concentration range ordinarily used in PWRs.

$$S = \sum^{n} [M(OH)_2^{(2-n)+}] \propto [H_2]^{\frac{1}{3}} \tag{7.2}$$

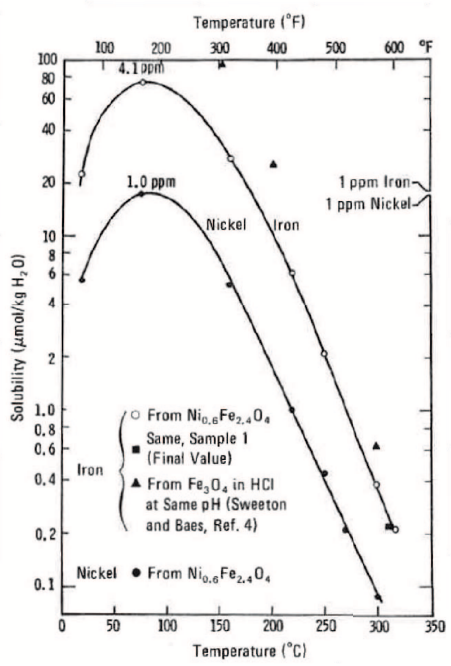

Figure 7.5: Solubility of iron and nickel from nickel ferrite ($Ni_{0.6}Fe_{2.4}O_4$) as a function of temperature, comparing with solubility of Fe_3O_4 at same pH [5].

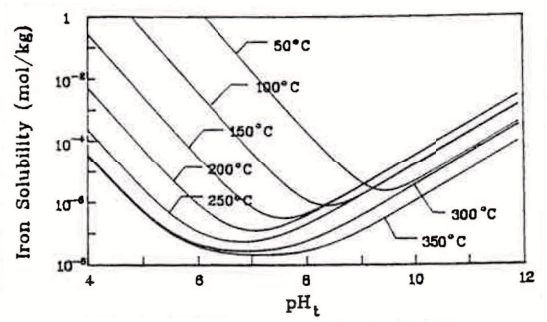

(a)

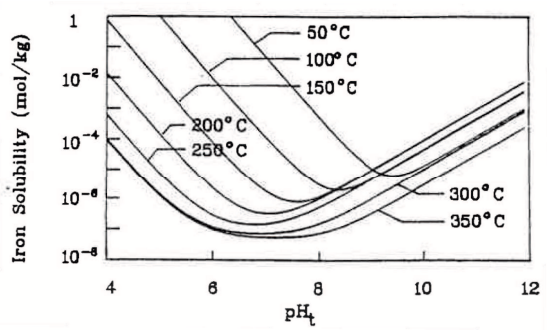

(b)

Figure 7.6: Influence of pH_t and temperature on iron solubility of nickel ferrite ($NiFe_2O_4$) under two hydrogen concentration: (a) 15 cc/kg; (b) 40 cc/kg [6].

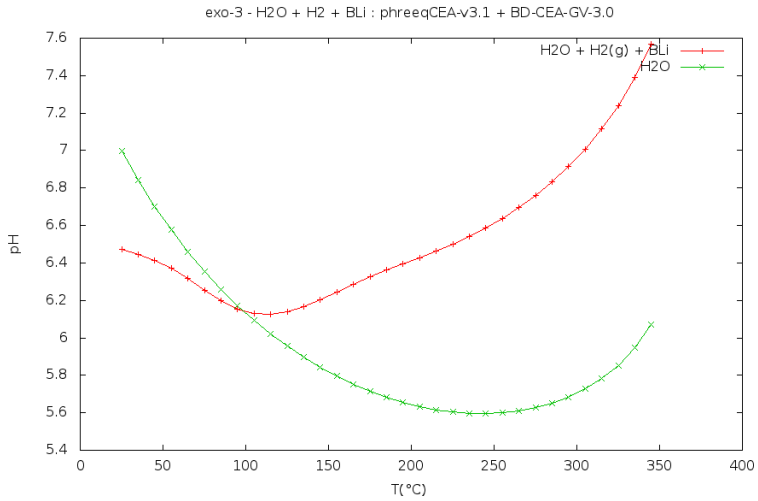

Figure 7.7: The evolution of pH value versus temperature of a PWR water (red curve), 1000 ppm [B] and 2 ppm [Li] in presence of H_2, and a pure water (green curve), modelling by the code PHREEQ-CEA-v3.1 [10].

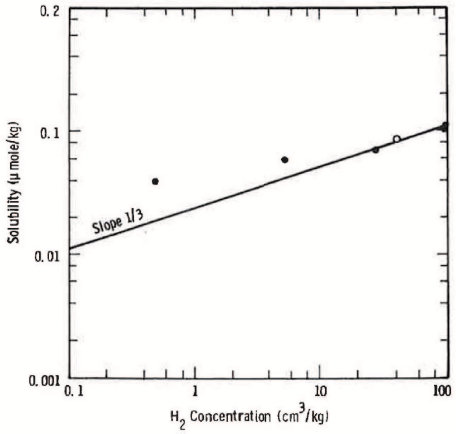

Figure 7.8: Log-log plot of average solubility values of iron from nickel ferrite ($Ni_{0.6}Fe_{2.4}O_4$, 300°C, $pH_{25°C}$ = 6.3) versus hydrogen pressure, • and ∘ are experimental and interpolated values; straight line indicates a slope of 1/3 [7].

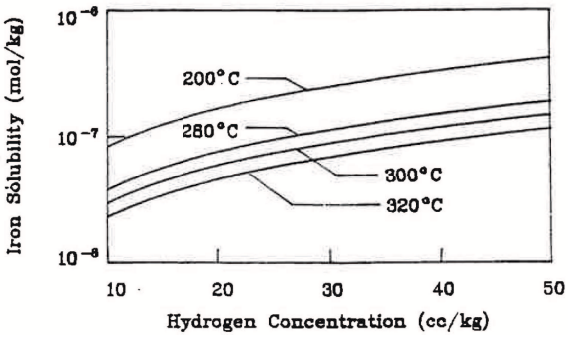

Figure 7.9: Influence of hydrogen concentration on the iron solubility of nickel ferrite (3000 ppm $B(OH)_3$ and 7 ppm Li) [6].

In addition, Chung *et al.* [6] have explained that the ionic activities from the dissolution of magnetite and nickel ferrite increase with partial hydrogen pressure. They considered that the dissolution of magnetite and nickel ferrite involve changes in oxidation number of iron atoms present in the solid phase and thus the individual ionic activities play an important role. Briefly, under a normal PWR hydrogen concentration (25-50 cc/kg (STP)), the iron solubility increases with the hydrogen concentration, illustrated in Fig.7.9.

However, different arguments have also been announced. Soustelle *et al.* [8, 9] have studied the influence of partial hydrogen pressure on the PWSCC of nickel base alloy (Alloy 600 and Alloy 690) at high temperature (360°C). It says that the partial hydrogen pressure can affect the crack initiation and even the propagation which corresponds to the highest metal dissolution. Meanwhile, they find that the presence of crystallites on the outer layer of nickel base alloys depends significantly on the hydrogen pressure. At low (10 mbar) and at high (20 bar) partial pressure of hydrogen, there is no sign of crystallites on the surface while at an intermediate level (300 mbar), an obvious presence of crystallites can be observed. Moreover, the total amount of oxidised metal (oxide + dissolved cations) as well as the oxide thickness are maximum for a hydrogen partial pressure 30 kPa. In other words, the oxide film is less protective at an intermediate level (300 mbar) of partial hydrogen pressure than the ones at low (10 mbar) and high (20 bar).

In our case, the presence of crystallites on LE11-02 ref (133 mbar, 72 hrs) is more significant than on the other two reference discs, LE12-04 ref (33 mbar, 120 hrs) and LE11-03 ref (33 mbar, 168 hrs). Other than tracing back to the duration of the experiments, it can also be considered that more crystallites have been produced due to this intermediate range of partial hydrogen pressure. For the other two cases, the hydrogen pressure stayed at the low range of hydrogen pressure and thus less crystallites on the surface.

Furthermore, Soustelle *et al.* [8, 9] also think that with the increase of hydrogen partial pressure, the oxide film of nickel base alloys become more and more rich in chromium and eventually will be

nickel free. It shows a stronger selective oxidation of chromium over nickel at a high hydrogen pressure.

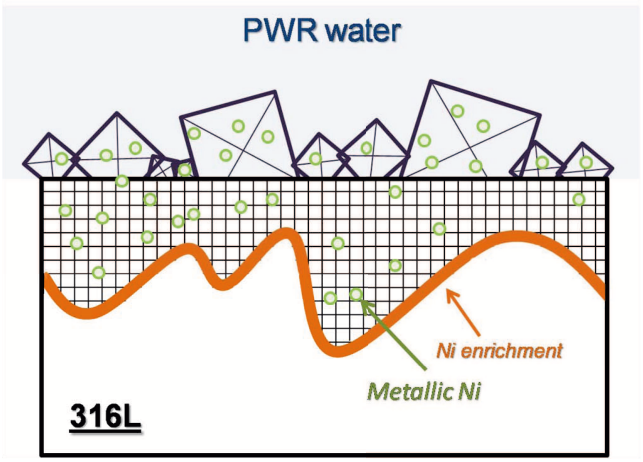

Figure 7.10: Schematic sketch for the **reference** oxide film formed on LE11-02 ref (133 mbar, 72 hrs) exposed to primary PWR water at 300°C in the HTHP cell.

In the case of LE11-02 ref (133 mbar, 72 hrs), Ni exists in a second phase of metallic nickel instead of nickel oxide in the oxide film, as portrayed in Fig.7.10. It may be explained:

- Based on the observation of Soustelle *et al.* [8, 9], the presence of the metallic nickel can be considered to be an intermediate stage of depletion of nickel in the oxide film. The hydrogen pressure here is high enough to avoid the formation of nickel oxide. It is possible that nickel has been oxidised previously and reduced later. According to the Nickel Pourbaix diagram, Fig.7.11 (f), at a reductive environment, metallic Ni is the more stable species.

- As stated, due to the selective oxidation, a preference of chromium and iron over nickel can be noticed. For the inner layer, oxygen grows inwards and more chromium (than bulk concentration) diffuse outwards, combining to be the protective layer rich in chromium. Meanwhile, it isolates the nickel in the oxide layer. This phenomenon has already been observed by Sergio *et al.* [2]. Afterward, it may push the nickel to the oxide/ metal interface which results in the nickel enrichment at this interface. For the outer layer, more magnetite replaces the nickel ferrite on the surface because of the selective oxidation. The content of nickel in the nickel ferrite ($Ni_xFe_{3-x}O_4$), x, is decreasing during the oxidation process at high H_2. On the other hand, due to the high H_2, the crystallites may be reduced. It may be one explanation why the metallic nickel are inside of the crystallites. The another explanation is that the electrochemical potential is too low for the oxidation of nickel.

7.4 Relationship between Potential and Oxide Film

7.4.A Pourbaix Diagram for Fe-Cr-Ni at 300°C

Pourbaix diagram (potential - pH diagram) enables us to give the stability of an oxide at a specific pH and the corresponding potential. Beverskog *et* Puigdomenech [12–15] have done a series of studies on the Pourbaix diagrams of iron, chromium and nickel. Fig.7.11 illustrates the Pourbaix diagrams for

the ternary system of Fe-Cr-Ni at 300°C. The concentration of dissolved cations used in the Pourbaix diagrams is 10^{-6} molal instead of 10^{-8} mole. Because it is closer to the values obtained from the cation analyses of both reference and irradiation experiments.

Beverskog *et* Puigdomenech [12] conclude that bimetallic oxides had a stability area on top of those for the corresponding monometallic oxide. On the other hand, the dissolved hydrogen added reacts with oxidising species H_2O_2 and O_2 produced by water radiolysis, and then decreases the corrosion potential. A potential less than -230 mV_{SHE} ensures a low crack growth rate of IGSCC in the BWRs. No reference potential values were reported in PWRs because of the presence of H_2. The conversion of the platinum wire to the standard hydrogen electrode (SHE) is -730 mV at a $pH_{300°C} = 7$ [16, 17]. Therefore, the concerning zone in the Pourbaix diagram for us is actually near the hydrogen line (lower dashed line) at 300°C.

Based on these conditions, it shows that:

- **Iron diagram**, Figs.7.11 (a) & (b): $NiFe_2O_4$ has the largest stability area of the spinels at 300°C. It covers the entire potential range of the stability of water at intermediated pH. $FeCr_2O_4$ has a stability area located around the hydrogen line (H_2/H_2O). Fe_3O_4 does not appear in the diagram because $FeCr_2O_4$ and $NiFe_2O_4$ are more stable under these conditions. The stability of these mixed oxides actually reflect a complicated interplay of reactions, which may involve several metal oxides. Like $FeCr_2O_4$, Eqs.7.3 & 7.4 give the lowest pH limit between $FeCr_2O_4$(cr) and Cr_2O_3(cr), which are limited by the stability of Fe(cr) at low potential and the stability of hematite (α-Fe_2O_3) at higher potentials, respectively.

$$FeCr_2O_4(cr) + 2H^+ \rightarrow Fe^{2+} + Cr_2O_3(cr) + H_2O \tag{7.3}$$

$$FeCr_2O_4(cr) + \frac{1}{2}H_2O \rightarrow \frac{1}{2}Fe_2O_3(cr) + Cr_2O_3(cr) + H^+ + e^- \tag{7.4}$$

- **Chromium diagram**, Figs.7.11 (c) & (d): $FeCr_2O_4$ is the most stable spinel oxide in the figure while $NiFe_2O_4$ does not appear at 300°C. However, it appears at a higher concentration (10^{-6} molal) diagram. It seems that it is more concentration dependent than for other bimetallic spinels.

- **Nickel diagram**, Figs.7.11 (e) & (f); $NiFe_2O_4$ appears on top of nickel oxide in the figure at the intermediate potential-pH range at 300°C. Ni^{2+} and $Ni[OH]_3^-$ dissolved from $Ni(OH)_2$ at either low or high pH may also exist. Though, until a pH $\approx$ 7.9, $NiFe_2O_4$ and $FeCr_2O_4$ are still stable, a reaction between them is written in Eq.7.5.

$$2FeCr_2O_4(cr) + \beta - Ni(OH)_2 \rightarrow 2Cr_2O_3(cr) + NiFe_2O_4(cr) + 2H^+ + 2e^- \tag{7.5}$$

In brief, the existence of spinel oxides results in a rigid and fully occupied crystal structure. They have relatively high surface energies and result in high crystal stability. In other words, their solubilities are low. **That is the reason why the release of cations in the reference experiments are relatively low.** It is worth mentioning that Fe_3O_4 does not appear on the Pourbaix diagram, Fig.7.11. It is eliminated by the authors because Fe_3O_4 is considered to be less stable. However, without any

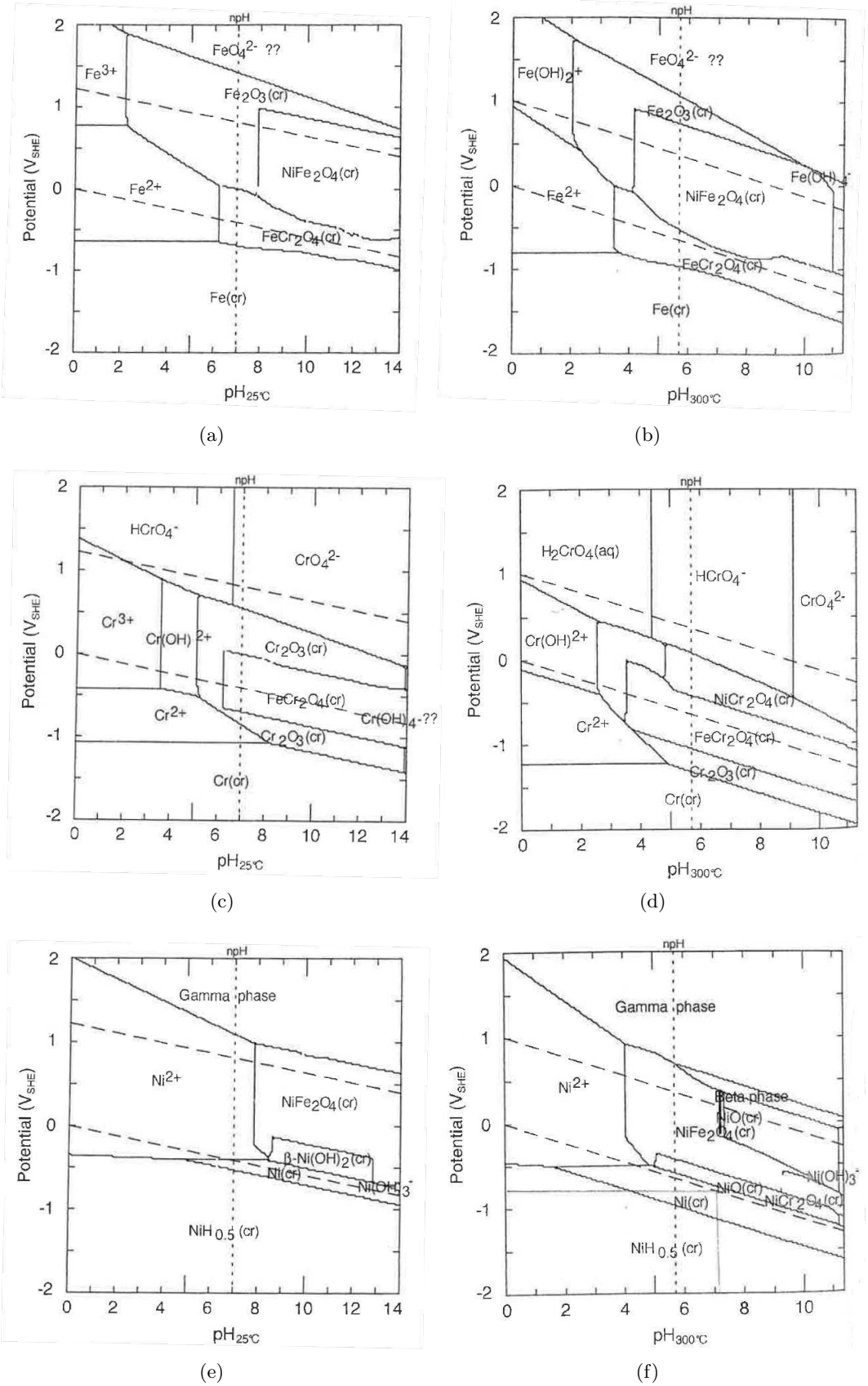

(a) (b)

(c) (d)

(e) (f)

Figure 7.11: Pourbaix diagrams for the ternary system of iron-chromium-nickel at 25°C and 300°C and $[\text{Fe(aq)}]_{tot} = [\text{Cr(aq)}]_{tot} = [\text{Ni(aq)}]_{tot} = 10^{-6}$ molal: (a) and (b) iron species; (c) and (d) chromium species; (e) and (f) nickel species, (cr): crystallised [12].

doubt, the existence of Fe_3O_4 on the 316L stainless steel can be confirmed by the characterisation results. Since Fe_3O_4 is an inverse spinel oxide, the conclusion concerning the solubilities should be applicable as well.

According to Beverskog *et* Puigdomenech, $NiFe_2O_4$ is the predominating solid phase at the operation temperature (around 300°C) and at the corrosion potential (-230 mV_{SHE}). Meanwhile, $FeCr_2O_4$ formed at a lower potential <-400 mV_{SHE} at 285°C which is not as prevailing as $NiFe_2O_4$. However, based on the studies of Cubicciotti *et al.* [18–20], they consider the $FeCr_2O_4$ as the predominating phase for the media contains enough H_2, such as PWRs and BWRs with hydrogen water chemistry (HWC). **No matter which oxide is dominant, it confirms the inner oxide (Ni,Fe)$(Fe,Cr)_2O_4$ and the outer oxide (Ni,Fe)Fe_2O_4, formed on 316L exposed to a PWR environment at 300°C during the reference experiments.**

Furthermore, when the environment contains a certain quantity of O_2 (or even the precursor, H_2O_2), hematite, α-Fe_2O_3 is claimed to be the predominating phase [18–20]. In addition, calculation showed formation of α-Fe_2O_3 at excess of dissolved iron in the media. **It may explain the formation of $(Fe,Cr)_2O_3$ on the irradiated 316L stainless steel, LE12-05 irr, which is in accordance with its great release of iron and chromium.**

7.4.B Electrochemical Behaviour

Vankeerberghen *et al.* [17, 21–24] have done a series of researches about electrochemistry and SCC on 316SS crevices exposed to PWR-relevant conditions. More precisely, they studied the effect of water radiolysis on the local crevice conditions, like electrode potential, oxidising species concentration and pH. They think that SCC (IASCC) occurs more likely in occluded (combined) regions due to the local electrochemical changes. A reduced mass transport caused by limited convection can certainly influence the local chemistry conditions. In the presence of irradiation, the circumstance becomes more complicated.

They found that the corrosion potential increased and the polarisation resistance decreased with the flux level [21]. Furthermore, the electrochemical behaviour of the electrodes is dominated by the electrokinetics of water and hydrogen [22]. Afterwards, by using their own codes, such as the electrochemistry code ECHEM [17, 24] and the crack propagation rate code CGR316BLi [23], they managed to do some predictions on the electrochemical behaviour of 316SS exposed to PWR-relevant conditions.

Concerning the ECHEM code, it assembles the homogenous reaction (Eqs.7.6) within coolant and the heterogeneous reactions (Eqs.7.7) on the metal surface on one hand, and many transport factors (fluid flow, electro-migration and diffusion) on the other hand. Tab.7.3 lists the corresponding expression of current density for the main electrode reactions, hydrogen, oxygen and water [24], which are important for the modelling.

$$\begin{gathered} B(OH)_3 + OH^- \rightleftharpoons B(OH)_4^- \\ B(OH)_4^- + B(OH)_3 \rightleftharpoons B_2(OH)_7^- \\ B(OH)_7^- + B(OH)_3 \rightleftharpoons B_3(OH)_{10}^- \\ Li^+ + OH^- \rightleftharpoons Li(OH) \\ Li^+ + B(OH)_4^- \rightleftharpoons LiB(OH)_4 \\ H_2O \rightleftharpoons H^+ + OH^- \end{gathered} \tag{7.6}$$

$$\begin{gathered} M^{2+} + H_2O \rightarrow M(OH)^+ + H^+ \\ M(OH)^- + H_2O \rightarrow M(OH)_2 \downarrow + H^+ \end{gathered} \tag{7.7}$$

Reaction (Eq n°)		Current density (A/m^2)
$2H^+ + 2e^- \rightleftharpoons H_2$	(7.8)	$i = 1.682[H_2]exp(\frac{2\times0.099F}{RT}E) - 7.89\times10^{-4}[H^+]exp(\frac{-2\times0.45F}{RT}E)$
$O_2 + 4e^- + 2H_2O \rightleftharpoons 4OH^-$	(7.9)	$i = -0.18[O_2]^{0.66}exp(\frac{4\times0.17F}{RT}E)$
$2H_2O + 2e^- \rightleftharpoons 2OH^- + H_2$	(7.10)	$i = -7.5\times10^{-8}exp(\frac{2\times0.57F}{RT}E)$

Table 7.3: Table of electrode reactions and their associated current density, (concentrations are expressed in mol/m^3 and local electrode potential in V_{SHE}) [24].

It predicts that:

- a concentration of 20 cc/kg(STP) dissolved hydrogen is sufficient for the electrode potential being sustained below -230 mV_{SHE} which is the guideline value with respect to SCC in BWRs;
- a pH drop (1−2 units) inside the crevice cannot be avoided until a concentration of 50 cc/kg(STP) dissolved hydrogen;

According to this calculation, the concentrations of dissolved hydrogen for the electron irradiation experiments are less than 20 cc/kg(STP), (see Appendix C). **Indeed, an increase of potential during the irradiation was observed and a pH drop has been found after the irradiation, respectively.** Meanwhile, it appears that hydrolysis can reduce radiolysis effects, depending on the corrosion rate inside crevices, as expressed in Eqs.7.7. Though, it is not the case for our experiments, and hence the presence of hydroxide is observed.

7.4.C Cavities - Potential

It has been proven that the presence of the cavities on the irradiated surface of 316L stainless steel is due to radiolysis effect while the mechanism of this process is not clear. We can speculate that a local depletion of chromium oxide at the oxide (inner layer)/ solution interface. However, several possible processes can be considered:

1. inward process, pitting from outside;
2. outward process, diffusing from inside.

7.4.C.1 Inward Process - Pitting

According to Frankel [25], "*pitting corrosion is localised accelerate dissolution of metal that occurs as a result of a breakdown of the otherwise protective passive film on the metal surface.*" The phenomenon of pitting occurs in the presence of aggressive anionic species, usually chloride ions. It is an environmental effects on the oxide and results in a local chemistry development and a high potential locally. Even without chloride ions in the environment, the radiolytic yields can also be considered to be the aggressive oxidising species under the circumstance.

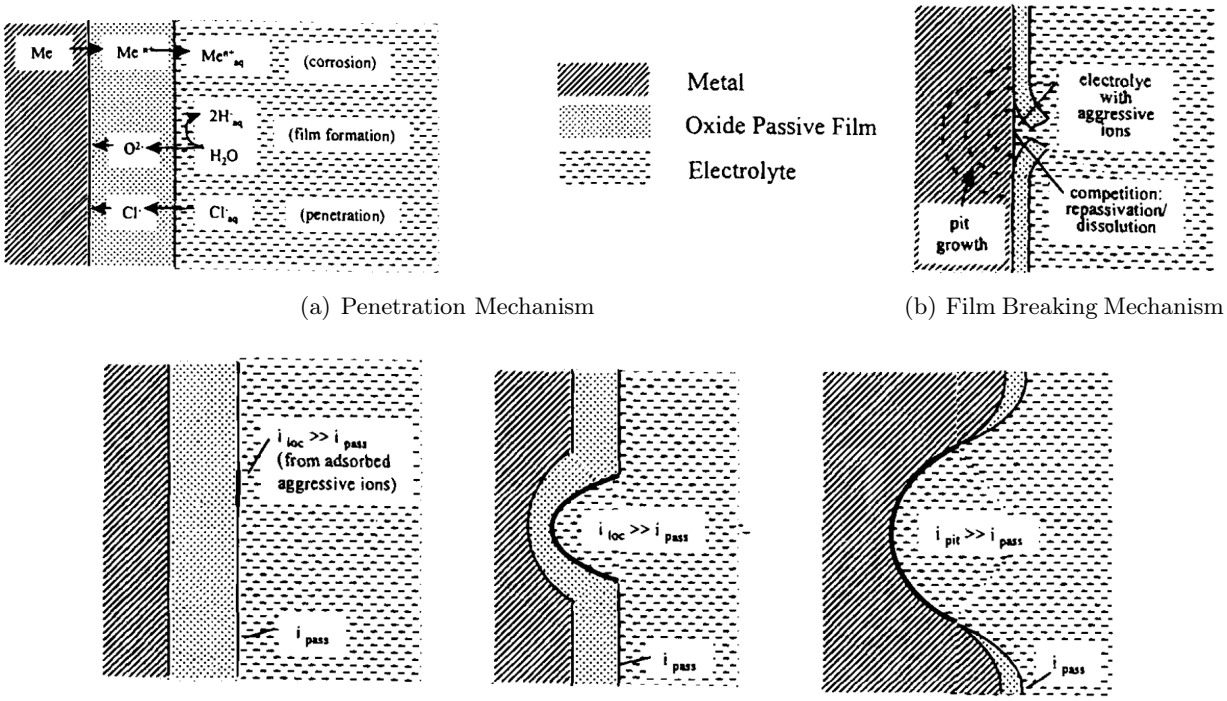

(a) Penetration Mechanism

(b) Film Breaking Mechanism

(c) Adsorption and Thinning Mechanism

Figure 7.12: Schematic diagrams representing pit initiation by (a) penetration, (b) film breaking and (c) adsorption and thinning [25].

Fig.7.12 shows the main mechanisms for the passive film breakdown and pit initiation due to the high potentials:

- **Penetration mechanism:** involves the transport of the aggressive anions, such as chloride ions, through the passive film to the metal/ oxide interface where aggressive dissolution is promoted.
- **Film breaking mechanism:** considers the thin passive film is cyclically breakdown and repaired.
- **Adsorption and thinning mechanism:** occurs locally due to some local adsorbed species. The local electric field strength will increase, then lead to complete breakdown and eventually the formation of a pit.

Among them, the penetration mechanism can be excluded because it is mainly related to the presence of chloride ions. The film breaking mechanism is possible, though it needs a mechanical

stress in a specific environment where pit growth can occur. The adsorption and thinning mechanism can take place with or without the presence of chloride ions [26]. Consequently, it is the most possible mechanism for the cavities caused by radiolysis of water.

Ulteriorly, during our irradiation experiments, the radiolytic yields, the oxidised species, H_2O_2 (O_2), can be adsorbed locally on the surface of the oxide. In return, the local current is highly increased because of these aggressive species and thus thinning the inner chromium-rich oxide film. Therefore, a significant dissolution of chromium shown up in the PWR water together with the observation of cavities on the surface.

In the aspect of potential, the pitting potential, E_P, is higher than the repassivation potential, E_R, for a material. It backs up the theory that the cavities are created during the irradiation (higher potential due to the oxidative respsonse), and the repassivation occurs after the irradiation (lower potential).

However, the potentiodynamically determined pitting potential of most materials exhibits a wide experimental scatter, of the order of hundreds of millivolts can be observed generally. From what we observed, the scatter is much smaller, only tens of millivolts. It should be explained by the electro-migration/ potential gradient of the measurement, as pictured in Fig.7.13. The **oxidative response** under irradiation, $\Delta E = b - a$ (tens of millivolts), is an average value obtained over the whole interface. For this reason, electro-migration (a potential gradient due to the transportation of charged species) should be taking into account. Besides, based on the measurements, the potential after irradiation is a little bit higher than the one before irradiation, $c > a$. It is believed that the radiolysis of water affect the PWR water and an evolution on the passive film, which results in a little bit higher potential c. Also, it is considered that the potential will eventually approach to its original position a, as long as there is enough time for the effect of water radiolysis being receded.

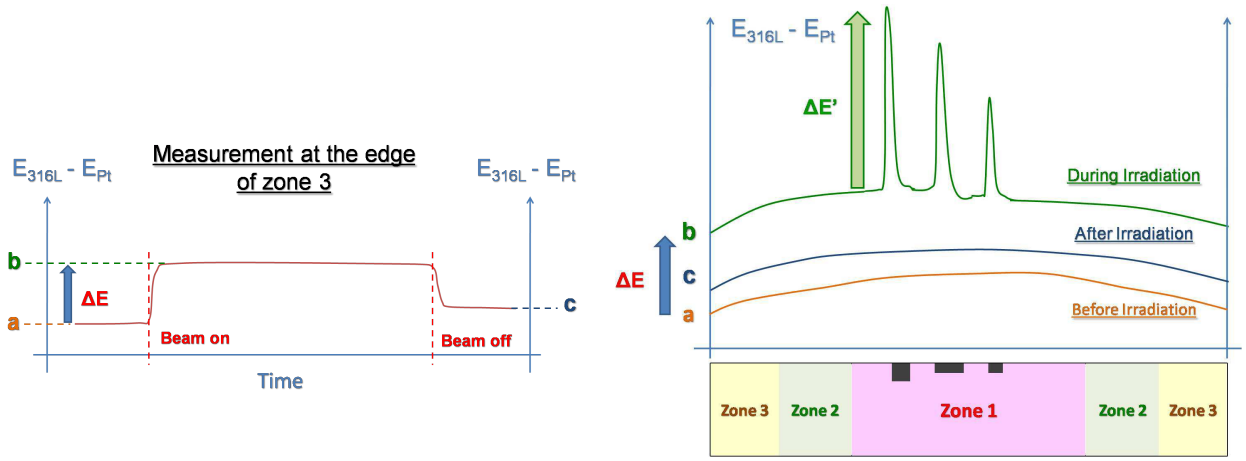

(a) (b)

Figure 7.13: Schematic diagrams representing the electrochemical behaviour: (a) measurement obtained at the edge of zone 3; (b) hypothesis of local electrochemical behaviour: before, during and after irradiation.

Moreover, due to the local chemistry change during the irradiation, very high ΔE' may be possible in some specific zones, such as the location of cavities. Even the ΔE measured is only tens of millivolts,

the local potentiodynamic, ΔE + ΔE', may be extremely high, like hundreds of millivolts. It may be the explanation for the presence of cavities (pittings) on the surface, as illustrates in Fig.7.13 (b).

7.4.C.2 Outward Process - Diffusion of Voids

The migration of vacancies can combine into voids at the oxide/ metal interface and eventually diffuse outwards by breaking down the oxide film. This is the basis of the outward process.

Indeed, a detachment at the oxide/metal interface has been observed on the reference 316L stainless steel, LE11-02 ref (133 mbar, 72 hrs) by TEM image (Chap.5.2.E, Fig.5.22 (c)). In other words, the defects like holes, metal and oxide vacancies may also exist and be enhanced on the irradiated one (LE12-05 irr) just without being observed.

Assuming that detachments of the oxide and metal are existed in the irradiation specimens, then the diffusion of voids may be accelerate by the assistance of irradiation. Because the migration of voids, vacancies is considered very low at the temperature (300°C) in general. Once the oxide film is ruptured, more cations will dissolve into the PWR water. In the mean time, the repassivation can also take place. For instance, some crystallites are precipitated inside the cavities.

However, this is a preliminary idea without considering the limits, such as the concentration of vacancy, the role of electrode potential, and the migration of vacancy, etc.

7.5 Modelling of Water Radiolysis at 300°C

A simulation of water radiolysis at 300°C has been calculated by an homogeneous calculation program of chemical kinetics [27]. It is performed with the specific conditions of our electron irradiation experiments. Fig.7.14 illustrates the production of radiolysis species in function of time at different flux, 30, 300 and 3000 nA.

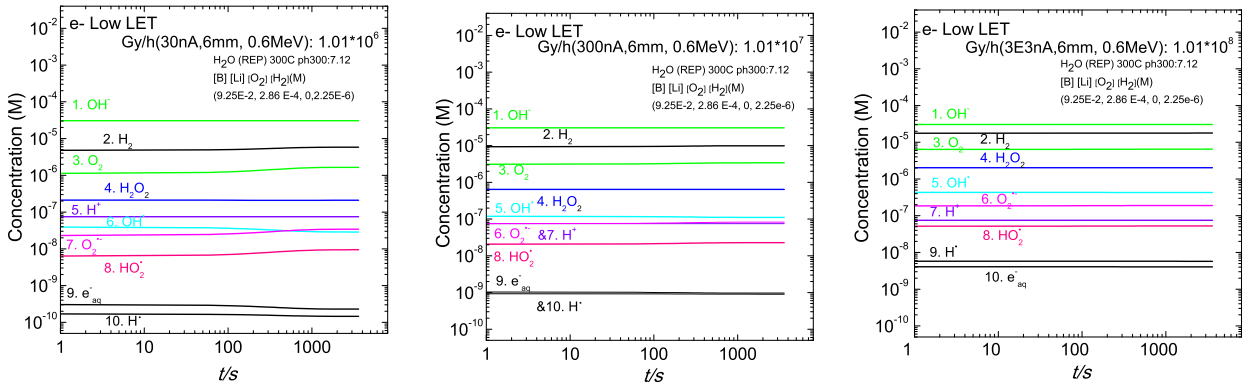

(a) (b) (c)

Figure 7.14: Modelling of radiolysis species produced at 300°C, PWR water (1000 ppm [B] and 2ppm [Li]) aerated by Ar/H_2 5%, by using homogeneous calculation of chemical kinetics, Data Set ($g_{300°C}$, $k_{300°C}$) [27] for an electron beam of: (a) 30 nA; (b) 300 nA; (c) 3000 nA.

According to these individual simulations, Fig.7.14, it shows that:

- For a lower flux irradiation, Fig.7.14 (a), the concentration of several radiolytic species evolve with time. After 100 s of irradiation, the oxidising species (O_2, $O_2^{\bullet -}$ and $HO_2^{\bullet}$) slightly increases while the reducing species (e^-_{aq} and $H^{\bullet}$) gently decreases.
- For higher flux, Fig.7.14 (b) & (c), the concentrations are constant during the whole irradiation process.
- The concentration order of radiolytic species is the same for high flux ones while a sight difference can be noticed for the lower. The orders are actually indicated in the figures. It shows that the oxidising species is dominant at 300°C radiolysis.
- In general, the concentrations of radiolytic species increase with the flux. Among all, OH^- is the most produced species, about 2×10^{-5} M, and it is also the only one which is indifferent with flux. On the other hand, the reducing species (e^-_{aq} and $H^{\bullet}$) increase most with the flux. Between 30 to 3000 nA, they jump up by two magnitude, form 10^{-10} to 10^{-8} M. Though, the oxidising species have a much higher concentration, particularly O_2 (10^{-6} to 10^{-5} M) and H_2O_2 (10^{-7} to 10^{-6} M).

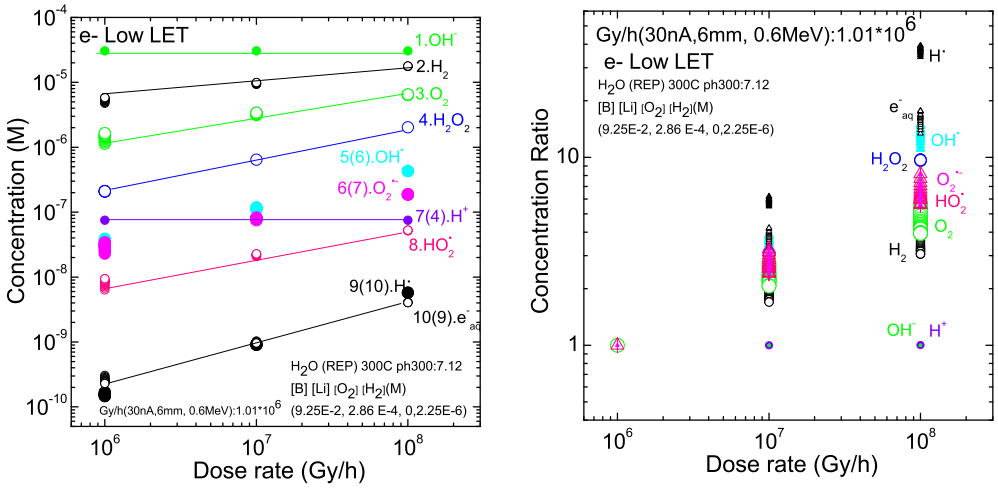

(a) (b)

Figure 7.15: Modeling of radiolysis species at 300°C PWR water (1000 ppm [B] and 2ppm [Li]) aerated by Ar/H_2 5%, by using homogeneous calculation of chemical kinetics, Data Set ($g_{300°C}$, $k_{300°C}$) [27]: (a) concentration of radiolytic species in function of dose; (b) concentration ratio $[C]/[C]_{30nA}$, by using 30 nA as the datum.

Fig.7.15 illustrates the evolution of radiolytic species with flux. It is quite obvious that with the increase of flux, the most four produced species are always the same, OH^-, H_2, O_2 and H_2O_2. It seems that the environment is still predominating by the four specie, which may be quite oxidative. However, the most increased species with flux are the reducing species, OH^- and $H^{\bullet}$.

Based on modelling our own experiments, it clarifies several points. On one hand, it explains for the **oxidative response** of electrochemical potential under irradiation, because the environment is actually oxidative at 300°C. On the other hand, it is also understandable that the augmentation of

the **oxidative response** with the flux. Furthermore, the concentration of the OH^- is about 10^{-5}, which seems to be in the same magnitude as the cation release in our experiment, especially for iron. In other words, it is in accordance with the cation dissolution reactions, Eq.7.1. And the formation of cation hydroxides in the solution explains the increase of acidity after irradiation.

7.6 Summary

In this chapter, two models for reference (unirradiated) and irradiated oxide films have been proposed, respectively. They are established on the oxide characterisation presented in Chapters 5 and 6. For the oxide films formed on the reference discs at high temperature and high pressure with the PWR water, the results are in agreement with literature. The process of the reference oxide formation is consequently concluded based on the literature. The process of the irradiated oxide formation is an original hypothesis based on the specific features observed on the irradiated oxide film. In order to support this hypothesis, further investigations have been made.

The first ones concern the irradiation induced release from the oxide. In general, the chromium oxide does not dissolve because of the excellent passive character, and thus it is focused on the iron oxide, magnetite and nickel ferrite. The influences of temperature and pH are quite clear while the role of dissolved hydrogen seems to be confusing. Even though, it can be sured that the concentration of dissolved hydrogen affects significantly on the dissolution in our experiments.

Secondly, the oxide film and the electrochemical behaviour are related to each other: the corrosion potential influences the oxide film formation; at high potentials, the degradation of the oxide film occurs. The characterisation (surface analysis) of the oxide formed is in accordance with the Pourbaix diagram. And the creation of cavities, or depletion of chromium oxide on the surface, can be thought either as a process which is similar to adsorption and thinning mechanism from pitting corrosion or an outward diffusion of voids.

Finally, a preliminary modelling correlate the electrochemical behaviours to the radiolysis of water. The dominant oxidising species produced by water radiolysis may lead to an oxidative response of potential under irradiation.

In summary, the difference between the models, reference and irradiated, is caused by the radiolysis of water. It can be recognised not only in the electrochemical behaviour but also in the formation of the oxide film.

References

[1] D.H. Lister and R.D. Davidson and E. McAlpine. The mechanism and kinetics of corrosion product release from stainless steel in lithiated high temperature water. *Corrosion Science*, 27(2):113 – 140, 1987.

[2] Sergio Lozano-Perez, David W. Saxey, Takuyo Yamada, Takumi Terachi. Atom-probe tomography characterization of the oxidation of stainless steel. *Scripta Materialia*, 62(11):855 – 858, 2010.

[3] Terachi T. and Fujii K., Arioka K. Microstructural Characterization of SCC Crack tip and Oxide Film for UNSS 316 Stainless Steel in simulated PWR Primary Water at 320°C. *Journal of NUCLEAR SCIENCE and TECHNOLOGY*, 42(2):225–232, 2005.

[4] Perrin S., Marchetti L., Duhamel C., Sennour M., Jomard F. Influence of Irradiation on the Oxide Film Formed on 316L Stainless Steel in PWR Primary Water. *Oxid. Met.*, 2013.

[5] Sandler Y. L., Kunig R. H. The Solubility of Nickel Ferrite in Aqueous Boric Acid Solution. *Nuclear Science and Engineering*, 77:211–218, 1981.

[6] Chung J. Y., Lee K. J. The Solubility of Magnetite and Nickel Ferrite in High Temperature Aqueous Solutions. *High Temperature Science*, 30:51–66, 1990.

[7] Sandler Y. L., Kunig R. H. The Solubility of Nonstoichiometric Nickel Ferrite in High-Temperature Aqueous Solution. *Nuclear Science and Engineering*, 64:866–874, 1977.

[8] Soustelle C., Foucault M., Combrade P. PWSCC of Alloy 600: A Parametric Study of Surface Film Effects. In Ford F. P., Bruemmer S. M. and Was G., editor, *Proceedings of the Ninth International Symposium on Environmental Degradation of Materials in Nuclear Power Systems - Water Reactors*, pages 105 – 113. The Minerals Metal and Materials Society (TMS), 1999.

[9] Soustelle C., Combrade P., Foucault M. A parametric study of PWSCC of alloy 600. In *Proceedings of the EUROCORR'98*, 1998.

[10] You D. Code: phreeqcea-v.3.1 + bd-cea-gv-3.0, private communication. Technical report, CEA, 2013.

[11] Sweeton F. H., Baes C. F. Jr. The Solubility of magnetite and hydrolysis of ferrous ion in aqueous solutions at elevated temperature. *J. Chem. Thermodyn.*, 2:479–500, 1970.

[12] Beverskog B., Puigdomenech I. Pourbaix Diagrams for the Ternary System of Iron-Chromium-Nickel. *Corrosion*, 55(11):1077–1087, 1999.

[13] Beverskog G. and Puigdomenech I. Revised pourbaix diagrams for chromium at 25-300°C. *Corrosion Science*, 39(1):43–57, 1996.

[14] Beverskog G. and Puigdomenech I. Revised pourbaix diagrams for iron at 25-300°C. *Corrosion Science*, 38(12):2121–2135, 1996.

[15] Beverskog G. and Puigdomenech I. Revised pourbaix diagams for nickel at 25-300°C. *Corrosion Science*, 39(5):969–980, 1997.

[16] Parisot J. F. *La corrosion et l'altáeration des material du nucléaire*. CEA Group et Group Moniteur, 2010.

[17] Vankeerberghen M., Gavrilov S. Experimental measurements and numerical simulations to evaluate the elect ode kinetics for 316 stainless steel under PWR-relevant conditions. *Journal of Nuclear Materials*, 377:331–339, 2008.

[18] Cubicciotti D. Potential-pH Diagrams for Alloy-Water Systems Under LWR Conditions. *J. Nucl. Mater*, 201:176, 1993.

[19] Cubicciotti D., Ljungberg L. Pourbaix Diagrams for Cr with Fe and the Stress Corrosion Cracking of Stainless Steel. *J. Electrochem. Soc.*, 132:987, 1985.

[20] Cubicciotti D. *Water Chemistry in Nuclear Reactor Systems 6, vol. 1, Potential-pH Diagrams for Alloy-Water Systems Under LWR Conditions.* British Nuclear Energy Society (BNES), London, U.K., 1992.

[21] Vankeerberghen M., Bosch R. W., Nieuwenhoven R. V. In-pile electrochemical measurements on AISI 316 (L)N IG and EUROFER 97 - I: experimental results. *Journal of Nuclear Materials*, 312:191–198, 2003.

[22] Bosch R. W., Wéher M., Vankeerberghen M. In-pile electrochemical measurements on AISI 304 and AISI 306 in PWR conditions - Experimental results. *Journal of Nuclear Materials*, 360:304–314, 2007.

[23] Vankeerberghen M., Weynes G., Gavrilov S., Martens B., Deconinck J. Crack propagation rate modelling for 316SS exposed to PWR-relevant conditions. *Journal of Nuclear Materials*, 384:274–285, 2009.

[24] Vankeerberghen M., Weynes G., Gavrilov S., Henshaw J., Deconinck J. The electrochemistry in 316SS crevices exposed to PWR-relevant conditions. *Journal of Nuclear Materials*, 385:517–526, 2009.

[25] Frankel G. S. Pitting Corrosion of Metals: A Review of the Critical Factors. *J. Electrochem. Soc.*, 145(6):2186–2198, 1998.

[26] Bardwell J. A., MacDougall B., Sproule G. I. Use of SIMS to Investigate the Induction Stage in the Pitting of Iron. *J. Electrochem. Soc.*, 136(5):1331–1336, 1989.

[27] Sims H., Cobel C. Modelling of radiolysis species at 300°C, private communication. Technical report, 2013.

Part IV

Results at Room Temperature and Discussion

Chapter 8

Proton Irradiation Experiments at room Temperature

The low temperature proton irradiation experiments were carried out with Teflon® cells in an aerated environment. Cyclotron at the laboratory CEMHTI (CNRS-Orléans, France) was used as the proton source. Two types of 316L disc preparation procedures were used which have been described in Chapter 4. The first one is prepared at room temperature, and the other has sustained a heat treatment in an autoclave at 300°C in PWR primary water during 7 days.

The results can be divided into two parts:

- ***In-situ* electrochemical behaviour**: it is investigated by measuring and then recording the free corrosion potential as a function of time under proton irradiation at room temperature and atmospheric pressure. The evolution of the free corrosion potential induced by irradiation is studied as a function of different parameters, such as the flux, fluence cumulation, etc.
- ***Ex-situ* solution analysis**: the chemical evolution of the solution has been investigated as a function of the cumulated fluence on 316L stainless steel disc during sequential irradiations. The investigated solutes include:
  1. the released cations, such as Fe, Ni, Cr, etc;
  2. the hydronium ions;
  3. the radiolytic H_2O_2.

Impedance measurement before or during irradiation have been also performed. However, it is quite preliminary results, thus it will only be represented in Appendix E. Tab.8.1 lists the detail information of irradiation experiments that will be presented in this chapter.

Sample	Preparation Procedure	Energy (MeV)	Flux (nA)	Duration$_{irr}$ (min)
X10-01	cleaned at 25°C	12/6	3×10^{-3} - 3	480
X10-06	cleaned at 25°C	12/6	10	240
X10-10	cleaned at 25°C	12/6	30	220
X11-01	cleaned at 25°C	12/6	30	220
X11-10	cleaned at 25°C	12/6	30	220
X11-11	cleaned at 25°C	12/6	30	220
X12-300-01	passivated at 300°C (7 days)	12/6	30	$\geqslant$ 220
X12-300-04	passivated at 300°C (7 days)	12/6	30	$\geqslant$ 220

Table 8.1: List of irradiation experiments on different 316L stainless steel with detailed conditions: preparation procedure, energy and flux.

As mentioned, two different reference electrodes (SCE and Hg/Hg_2SO_4) were used, though the values presented in the figures were all adjusted to the standard hydrogen electrode (SHE) [1, 2]. The adjustment values are +0.245 mV and +0.658 mV, for the specific SCE and Hg/Hg_2SO_2 electrodes used in the experiments, respectively.

8.1 Investigation of Electrochemical Behaviour under Irradiation

The major difference between the preparation procedures is the oxide film on the surface of the stainless steel. The oxide for the one cleaned at room temperature (25°C) is mainly chromium oxide, probably

Cr_2O_3 and/ or $FeCr_2O_4$. The passive film is relatively thin, few nanometers. Oppositely, the oxide for the one passivated under primary PWR media at 300°C in an autoclave is a bi-layer oxide. The outer layer is rich in iron while the inner layer enriches in chromium. The oxide film has a tens or hundreds of nanometer in thickness, mostly depending on the duration at high temperature exposed to PWR water [3]. Therefore, the following study is distinguished into two parts: **Ox**25°**C** for the 316L stainless steel discs cleaned at 25°C and **Ox**300°**C** for the ones passivated at 300°C.

8.1.A Non Oxidised Sample (Ox25°C)

Fig.8.1 illustrates the irradiation history of the sample X10-01, which has been submitted to two sequential irradiations with a gradually increasing flux from 3 pA to 3 nA. During the sequential irradiations, the PWR water was not removed. It was the same water during the whole experiment (IR01 to IR08).

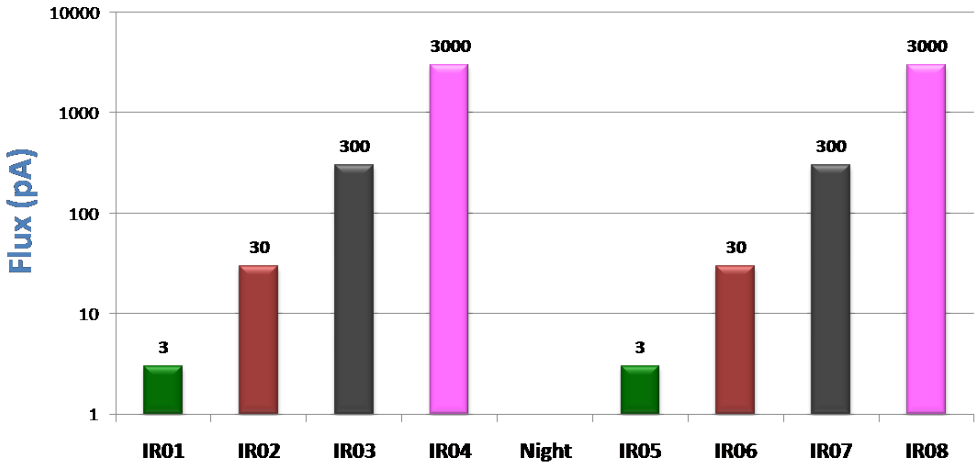

Figure 8.1: History diagrams of two sequential irradiations experiments performed on X10-01 at room temperature (25°C), 1^{st} sequential irradiations with increasing flux: IR01 - IR04, 2^{nd} sequential irradiations with increasing flux: IR05 - IR08.

Fig.8.2 & 8.3 show the free corrosion potential of the sample X10-01 during each irradiation for the 1^{st} (IR01 - IR04) and the 2^{nd} (IR05 - IR08) sequential experiments. The experiments were performed in an aerated environment, and thus it may have oxygen dissolved in PWR water.

For the 1^{st} sequential irradiations, Fig.8.2:

- from IR01 (3 pA, 6.6×10^{7} $H^{+}.cm^{-2}.s^{-1}$) to IR03 (300 pA, 6.6×10^{9} $H^{+}.cm^{-2}.s^{-1}$), the potential decreases immediately when the beam starts and increases when the beam stops. It reveals an immediate and **reductive** response to proton beams. During the irradiation, a slight increase of the potential can be seen, though it still remains **reductive** under the whole irradiation. The potential after irradiation becomes higher than the one before irradiation.
- for IR04 (3 nA, 6.6×10^{10} $H^{+}.cm^{-2}.s^{-1}$), an immediate drop of the potential can be seen when the beam starts. No longer than 100 s, the potential increases significantly. Afterwards, around $600\sim700$ s, it has already exceeded the potential before irradiation. However, when the beam

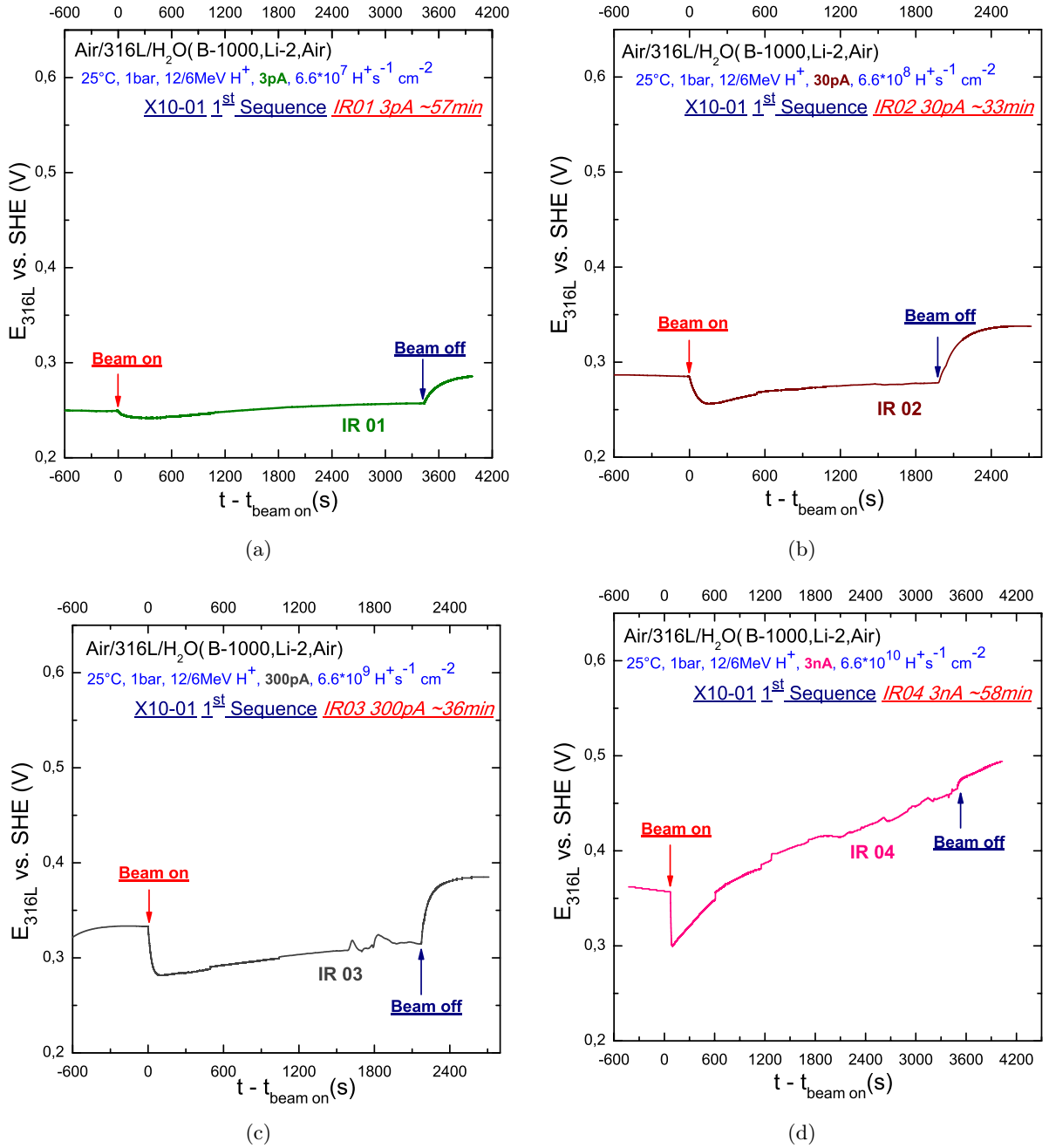

Figure 8.2: Evolution of the free corrosion potential of stainless steel 316L in PWR water under proton irradiation at room temperature. 1^{st} sequential irradiations: IR01 - IR04, free corrosion potential versus time. (a): IR01, 3 pA; (b): IR02, 30 pA; (c): IR03, 300 pA; (d): IR04, 3 nA. (e): free corrosion potential of IR01 - IR04 versus cumulated fluence.

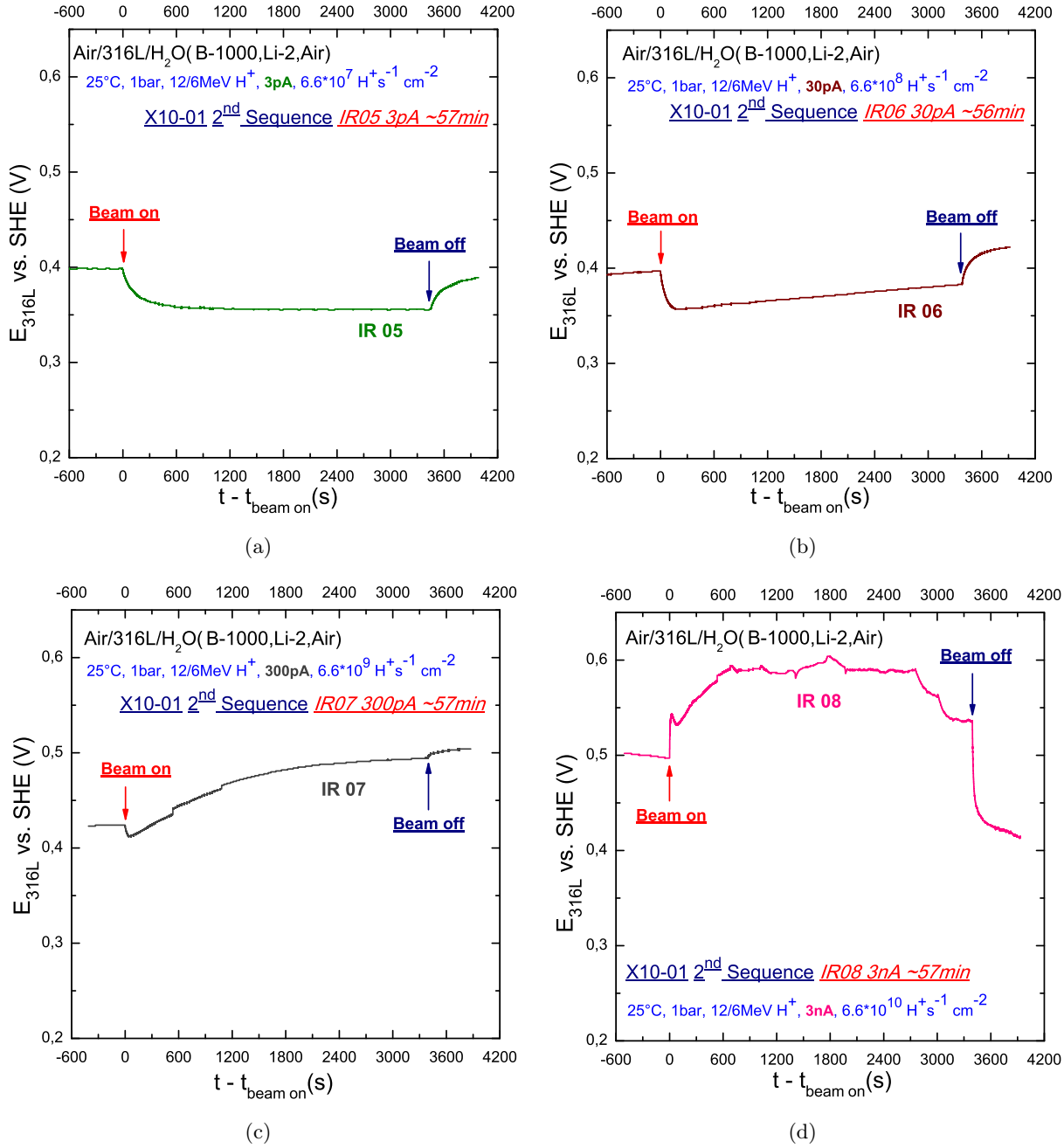

Figure 8.3: Evolution of the free corrosion potential of stainless steel 316L in PWR water under proton irradiation at room temperature. 2^{nd} sequential irradiations: IR05 - IR08, free corrosion potential versus time. (a): IR05, 3 pA; (b): IR06, 30 pA; (c): IR07, 300 pA; (d): IR08, 3 nA.

stops, as for the first three irradiations, it also increases. Thus, the potential after irradiation is much higher than the one before irradiation.

- the potential range for the first four irradiations is from 0.23 V($_{SHE}$) to 0.5 V($_{SHE}$), it increases progressively with the irradiations.

For the 2^{nd} sequential irradiations, Fig.8.3:

- for IR05 (3 pA, 6.6×10^7 $H^+.cm^{-2}.s^{-1}$) and IR06 (30 pA, 6.6×10^8 $H^+.cm^{-2}.s^{-1}$), the evolution of the potential is quite similar to the ones at same flux of the 1^{st} sequence, an immediate and **reductive** response of potential to proton beams can be observed.
- for IR07 (300 pA, 6.6×10^9 $H^+.cm^{-2}.s^{-1}$), the evolution of the potential is similar to IR04 (3 nA) of the $1st$ sequence, with a less intense response of the potential. The evolution of the potential before and after irradiation is within 0.1 V while it is 0.2 V for the IR04.
- for IR08 (3 nA, 6.6×10^{10} $H^+.cm^{-2}.s^{-1}$), the electrochemical behaviour is totally different. It is an **oxidative** response to proton beams. It has a sudden jump when the beam starts. During the irradiation, it increases for the early and decreases for the late stages, respectively. As soon as the beam stops, an important drop of potential can be observed.
- the potential range for the second sequential irradiations is from 0.35 V_{SHE} to 0.6 V_{SHE}. It is higher than the potential range of the first one (0.25V_{SHE} to 0.5 V_{SHE}). It also increases progressively with the irradiations until the middle of IR08, and afterwards a decrease is finally observed.

Based on the results of these two sequential experiments, flux, ageing, fluence influences have been studied.

8.1.A.1 Flux Influence

It is obvious that the flux affects the intensity of the potential response to irradiation. For either the 1^{st} and the 2^{nd} sequence, the potential response is always increased with the increasing flux. It shows that more local chemistry changes occur at the interface when the it is irradiated by a higher flux.

On the other hand, it seems that with the increase of flux, the **reductive** response is changed to an **oxidative** one. At room temperature and a neutral pH, the reducing radiolytic yields is higher than the oxidising species [4, 5], and thus it results in a lower potential under irradiation. However, with the increasing of flux, water decomposition is promoted by favouring the radical-radical recombination reactions [6–8]. That is the reason for a **reductive** response of potential becoming an **oxidative** one.

Although, the flux influence can be represented more directly. Fig.8.4 illustrates the first irradiation of a sequential experiments on the sample X10-10 with a fixed flux, 30 nA (6.6×10^{11} $H^+.cm^{-2}.s^{-1}$). It shows the flux influence thoroughly. For a new interface, no fluence history, when it is irradiated by a much higher flux, it had an immediate drop of potential at the very beginning. Afterwards, it increased and surpassed the potential before irradiation. It dropped instantly as soon as the beam is cut-off. The immediate drop of potential should be related to the dominant reducing radiolytic produced by water

radiolysis at room temperature and neutral pH in an aerated environment. However, it is overcame quickly because more oxidising products are produced during the high flux irradiation. In general, higher flux leads to an **oxidative** response (Fig.8.4) while a lower flux results in a **reductive** one (Fig.8.2 (a) & Fig.8.3 (b)).

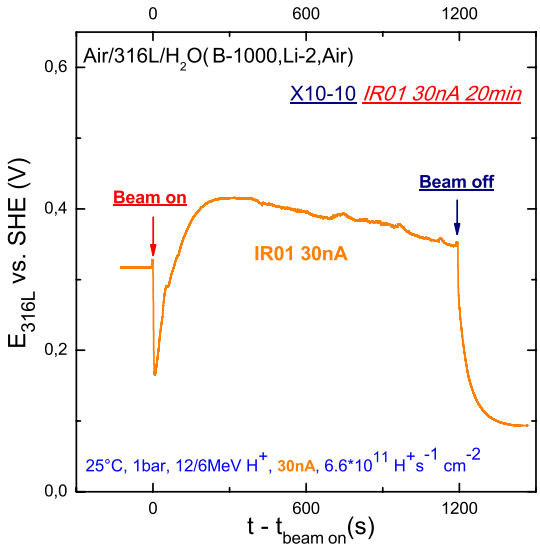

Figure 8.4: Free corrosion potential of 316L as a function of time for the sample X10-10, irradiated with a flux of 30 nA at room temperature.

8.1.A.2 Ageing influence - fluence cumulation

At room temperature, the fluence is the main factor for the ageing effect. Comparing the 1^{st} and the 2^{nd} sequence of X10-01 (Fig.8.2 & 8.3), the different electrochemical behaviour of IR07 and IR08 should be considered as an effect of fluence cumulation.

IR03, Fig.8.2 (c), had a **reductive** response while IR07, Fig.8.3 (c), had an **oxidative** one under irradiation with the same flux, 300 pA. At this moment, the flux influence has been overstepped by the fluence cumulation. Actually, it seems that a threshold of fluence exists. When the local chemistry is changed to a certain level, the environment becomes more and more oxidative. Like for IR08, instead of a drop of potential at the beginning of the irradiation, a sudden jump can be found. Moreover, it is a total **oxidative** response of potential during the irradiation. It even decreases at the late stage of the irradiation. The potential under irradiation is higher than the ones before and after irradiation.

Fig.8.5 illustrates the relationship between the free corrosion potential and the fluence cumulation. Briefly, the potential increases with the fluence cumulated on the interface. From another point of view, this increase of the potential should be considered as an influence of irradiation.

In summary, flux and fluence have clear and significant effects on the electrochemical behaviour of 316L stainless steel in PWR water at room temperature. Globally, the electrochemical potential increases with the irradiation through different manners, depending on the specific conditions. It needs to be pointed out that a large variety of the electrochemical behaviours has been observed. Nevertheless, the figures represented above are very reproducible.

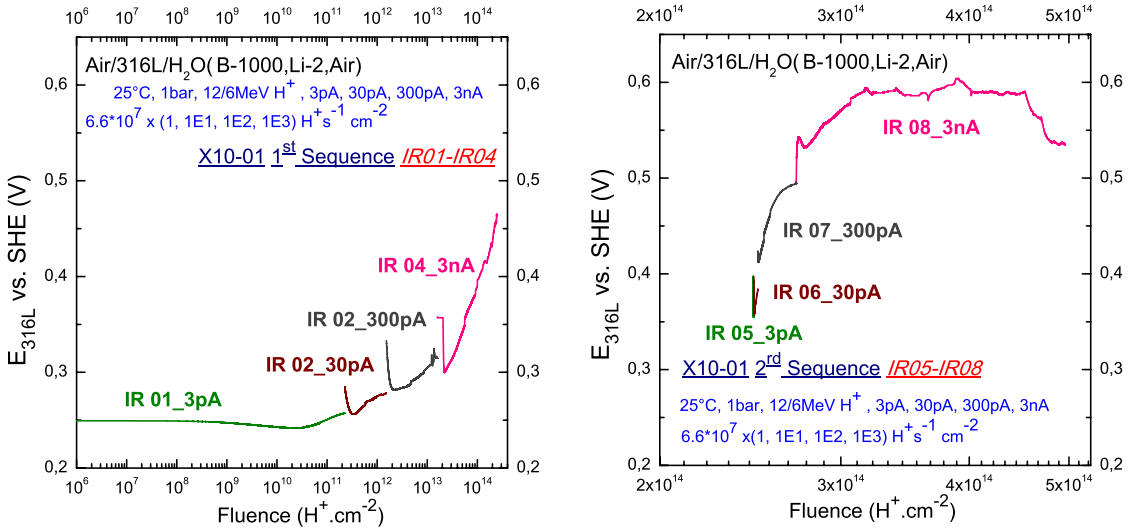

(a) (b)

Figure 8.5: Free corrosion potential versus fluence cumulated on X10-01: (a) 1^{st} sequential irradiation experiment, IR01 - IR04; (b) 2^{nd} sequential irradiation experiments, IR05 - IR08.

8.1.B Oxidised Sample (Ox300°C)

The proton irradiation experiments at 25°C with an oxide film passivated at 300°C have been performed to investigate the influence of the passive film on the electrochemical behaviour under irradiation. The electrochemical measurement is an additional information for understanding the process. However, some comments should be pointed out:

- most irradiations were done with a 30 nA flux for investigating the release of cations as well as for comparing with the proton irradiations experiments on the HTHP cell which were performed with a flux at 30 nA;
- after each irradiation, the PWR water in the cell was renewed, which means that the interface 316L stainless steel remained the same while the PWR water is a new one (never irradiated before) for each irradiation.

Fig.8.6 illustrates a sequential irradiation experiments with a fixed flux, 30 nA, on the sample X12-300-01. Actually, the duration for IR01 - IR04 is 40 minutes each, and 60 minutes for IR05.

It is clear that:

- for IR01, the evolution of the free corrosion potential is quite different from the one at same flux of X10-10, Fig.8.4. The potential under irradiation did not surpass the one before irradiation. It jumped significantly as soon as the beam was cut-off. It seems that this difference should be related to the nature of the oxide film, which is the only important difference between IR01 of X10-10 and the IR01 of X12-300-01.
- for the following irradiations, IR02 - IR05, they all had an **oxidative** potential response to the beam. It appears that the response was getting intenser with the cumulating irradiation.

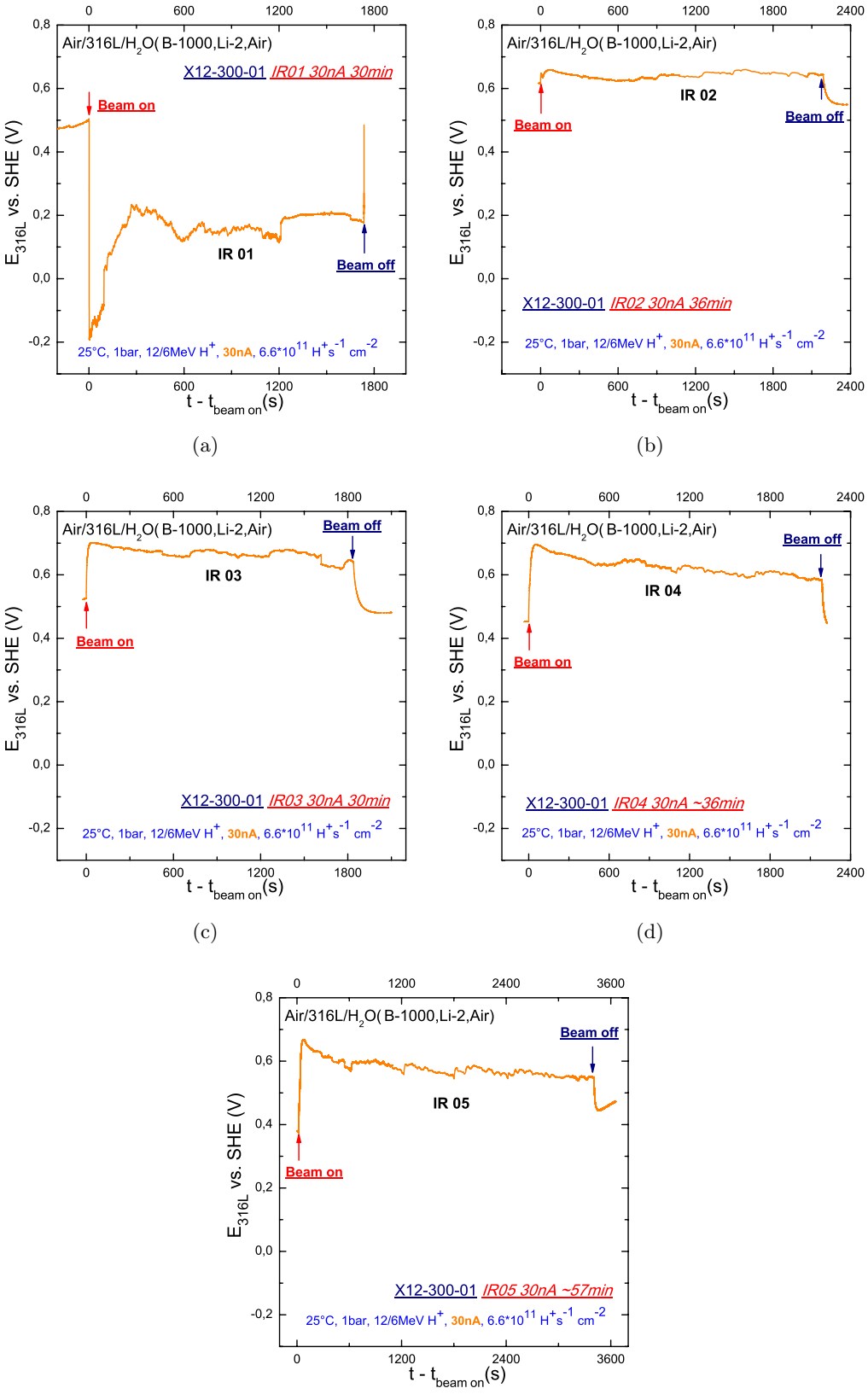

Figure 8.6: Evolution of the free corrosion potential of stainless steel 316L in PWR water under proton irradiation at room temperature. Five sequential irradiations (IR01 - IR05) with 30 nA flux (6.6×10^{11} $H^+.cm^{-2}.s^{-1}$) on the interface X12-300-01.

The high flux leads to an **oxidative** potential response to the beam in general. And with the cumulation of fluence (the duration of irradiation) on the 316L, the potential evolution is more important and leads to a higher response. The electrochemical behaviour of Ox300°C is in accordance with the conclusion of the flux and the fluence influences dragged out from the Ox25°C.

In brief, water radiolysis at room temperature in an aerated environment on the interface between 316L stainless steel and PWR water can enhance the electrochemical potential. Generally speaking, the more it is irradiated, the higher the potential will be.

Other than the presenting results, more experiments have been carried out to study the reproducibility. It seems that the reproducibility of the electrochemical behaviour of Ox300°C is higher than the one of Ox25°C. It can be explained by the fact that the oxide film formed at 300°C is more stable and reproducible than at 25°C. Besides, the renewing PWR water for each irradiation and the nature of oxide film certainly influence the reproducibility.

As far as known, the nature of the oxide films formed at room temperature (Ox25°C) and at 300°C (Ox300°C) are completely different, such as the composition, the morphology, the thickness, the structure, etc. According to the results, it appears that the electrochemical behaviour of both passive films (Ox25°C and Ox300°C) under proton irradiation is quite similar. Depending on the flux and/ or fluence, it gives either reductive or oxidative potential response to proton irradiation.

8.2 Solution Analysis

The chemical analysis of the solution is important for understanding the effect of water radiolysis. The evolution of the electrochemical potential induced by irradiation is not only affected by the oxide film evolution of the 316L stainless steel, but also influenced by the PWR water chemistry. Depending on different factors, the release of cations and anions, the evolution of protons and the production of hydrogen peroxide (H_2O_2) in the solution are also dependant of irradiation.

The solution analysis is performed after each irradiation (See Appendix F), in order to detect the concentration of cations (Fe, Cr, Ni, etc.), H_2O_2 and the H_3O^+. The different oxide film, Ox25°C and Ox300°C, may also play a role under the circumstance. The irradiation experiment were preformed in an aerated environment, and thus the dissolved N_2 and O_2 may also be irradiated to NO_3^- and etc. Besides, the cell is made by Teflon®, thus anions like F^- or even Cl^- may also appear in the solution.

8.2.A Prerequisite Conditions

Tab.8.2 shows the solution analysis for several experiments. The PWR water of X10-01, SX10-01, has been irradiated by two sequential irradiations for 8 hours with a maximum flux 3 nA. SX10-10 n°1 is the PWR water from the first irradiation of X10-10, 30 nA flux for 20 minutes. X10-06 has been irradiated twice with 10 nA flux for 1 and 3 hours, respectively; and hence there are two irradiated PWR waters, SX10-06 n°1 and sX10-06 n°2.

Tab.8.2 shows that:

- the release of cations is relatively low, or even under the detection limits, for irradiation with a relatively low flux (SX10-01 and SX10-06 n°1);

Solution N°	Flux (nA)	$Duration_{irr}$ (min)	Fluence $\times 10^{15} H^+.cm^{-2}$	Fe	Cr (μg/L)	Ni	pH
PWR water (blank)	without irradiation			0.5	1.8	< 3	$6.1 \sim 6.4$
SX10-01	3×10^{-3} - 3	240	4.95	6±1	< 1	< 2	-
SX10-10 n°1	30	20	0.792	2	0.3	< 3	4.96
SX10-06 n°1	10	60	0.792	< 3	< 3	< 3	6.41
SX10-06 n°2	10	180	2.376	170	32	8±1	4.96

Table 8.2: Analysis of four irradiated PWR waters: X10-01 (1 solution), X10-06 (2 solutions), X10-10 (1 solution), with the specific irradiation conditions (flux and duration under irradiation). - : analysis impossible (lack of solution); **S:** solution (PWR water); n°: is the order for several solutions come form the same metal (316L) interface.

- the release of cations is difficult to be detected when the 316L stainless steel has a low fluence (SX10-10 n°1 and SX10-06 n°1).

These results reveal that the release of cations under irradiation depends on both flux and fluence. If the flux or the fluence is low, the release will also be relatively low (usually under few μg/L). That is the reason why almost all the experiments for solution analysis were done with a 30 nA flux for a relatively long duration, which can be considered as the leaching time.

8.2.B Solution Analysis of Non Oxidised Sample (Ox25°C)

As stated before, the release of cations, production of H_2O_2 and H_3O^+ are the most important parameters to be analysed, because it may offer more information of the evolution of the water radiolysis. Tab.8.3 gives the details for a series of irradiated PWR waters collected from the experiments on an Ox25°C interface, X11-11. It was irradiated under proton beam five times with the same energy and the same flux. After each irradiation, the PWR water is changed, and a new one is introduced for the next irradiation. Therefore, there are five irradiated PWR waters for the solution analysis.

Solution n°	Energy (MeV)	Flux (nA)	$Duration_{irr}$ (min)
SX11-11 n°1	12/6	30	40
SX11-11 n°2	12/6	30	40
SX11-11 n°3	12/6	30	40
SX11-11 n°4	12/6	30	40
SX11-11 n°5	12/6	30	60

Table 8.3: List of the irradiated PWR water form the interface X11-11 with the specific conditions for each irradiation. **S:** solution (PWR water).

Fig.8.7 (a) illustrates the concentrations of $[H_3O^+]$, cations ([Fe], [Cr], [Ni], [Zn]) and $[H_2O_2]$ of each irradiated solution form the interface X11-11. One point on the figure is actually meant for one irradiated PWR water. It needs to be recalled that the 316L stainless steel discs were sustained the sequential irradiations of each interface without renewed. Thereby, the fluence was only cumulated on the discs. In addition, the blank PWR water has already contained a certain quantity of H_3O^+, of which pH is around $6.1 \sim 6.4$. That is why the first point of $[H_3O^+]$ is at 0 cumulated fluence in the figure.

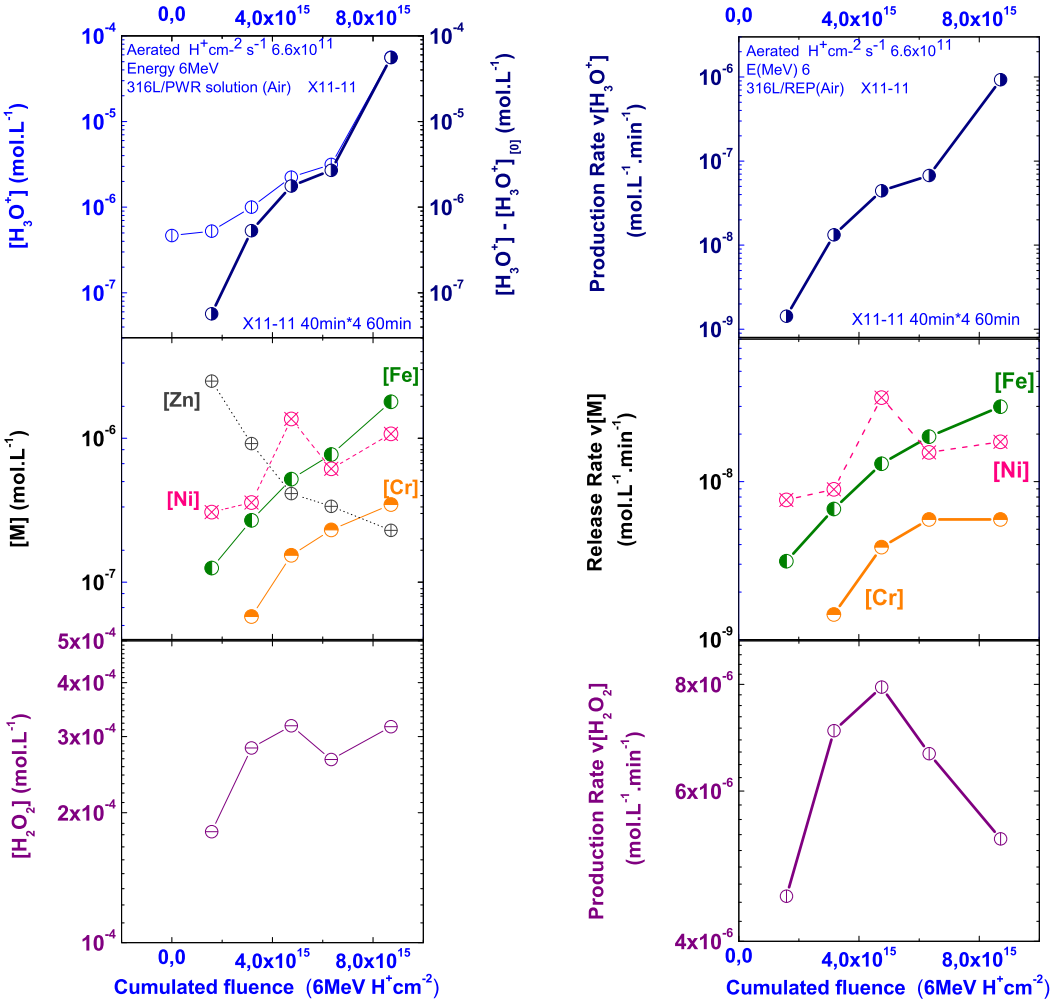

(a) (b)

Figure 8.7: Solution analysis of different parameters versus cumulated fluence on the 316L stainless steel X11-11: (a) concentration of $[H_3O^+]$ (left) and $[H_3O^+]$ - $[H_3O^+]_0$ (right) (*on the top*), cations (*in the middle*) and $[H_2O_2]$ (*at the bottom*) versus cumulated fluence on 316L stainless steel X11-11; (b) production rate of $[H_3O^+]$ (*on the top*), release rate of cations (*in the middle*) and production rate of $[H_2O_2]$ (*at the bottom*).

According to these concentration values, it allows us to calculate the kinetic of the release/ production for each irradiation, as written in Eq.8.1 and plotted in Fig.8.7 (b).

$$v[conc] = \frac{[conc]}{Duration_{irr}} \tag{8.1}$$

Globally, H_3O^+ and the release of cations (alloying elements, Fe, Cr and Ni) increase with the cumulated fluence on the 316L. Especially for H_3O^+, it increases sharply from $\sim 10^{-7}$ to $\sim 10^{-4}$ mol.L^{-1}. H_2O_2 is detectable in every irradiated PWR water sample, which has a maximum production rate at the fluence about 4.5×10^{15} H^+cm^{-2}. The presence of Zn is otherwise not expected. It should be considered to be a contamination somewhere during the experiment, which will be well explained

later.

8.2.C Tendency of Different Parameters - Ox25°C

The following discussions are based on three different discs, X11-11, X11-01 and X11-10. They may be treated as a whole, because they shared the same irradiation conditions:

1. disc preparation: cleaning process at room temperature (25°C);
2. temperature & pressure: room temperature (25°C) and atmospheric pressure (1 bar);
3. energy & flux: 6 MeV proton beam at the interface with a 30 nA flux;
4. sequential irradiation: 5 times irradiations, leaving 5 irradiated PWR water behind;
5. duration under irradiation: four times 40 minutes, followed by a 60 minutes irradiation in the end (4×40 min + 60 min).

Fig.8.8 illustrates the release rate of cations (figure (a)) and the production rate of H_3O^+ (figure (b)) and H_2O_2 (figure (c)) with the fluence cumulated on the corresponding 316L stainless steel. Indeed, since the flux and the duration under irradiation were the same, the three interfaces shared the same cumulated fluence. The rate figures are chosen for the comparison.

8.2.C.1 The Release of Cations

Generally, the release of cations for a stainless steel is very weak, which has been proved by our *blank test*. A similar sequential experiments have been done for the 316L stainless steel discs in a beaker without irradiation. The results are presented in Appendix F. However, at room temperature and atmospheric pressure, there is no sign for the release of cations, which can be detected by the ICP-AES analysis. However, in the presence of either thermal treatment or irradiation, the story can change totally.

According to Fig.8.8 (a):

- **Fe release:** among all the elements, the release rate of iron depends most on the fluence. It increases sharply, from 10^{-9} to 10^{-7} $mol^{-1}.L^{-1}.min^{-1}$, with the cumulated fluence on the 316L disc. As the base element in 316L stainless steel and the most soluble cations in PWR water, it seems reasonable that the release of iron is the most important.
- **Cr release:** the release of chromium is the less important among the three cations. It is not always detectable at low cumulated fluence. It explains the missing points in the figure. Normally, it slightly increases with the cumulated fluence, from 10^{-9} to 10^{-8} $mol^{-1}.L^{-1}.min^{-1}$. Most of the chromium participates in the formation of the passive film which is extremely protective, instead of being released in the PWR water. As a result, the release of chromium is relatively low.

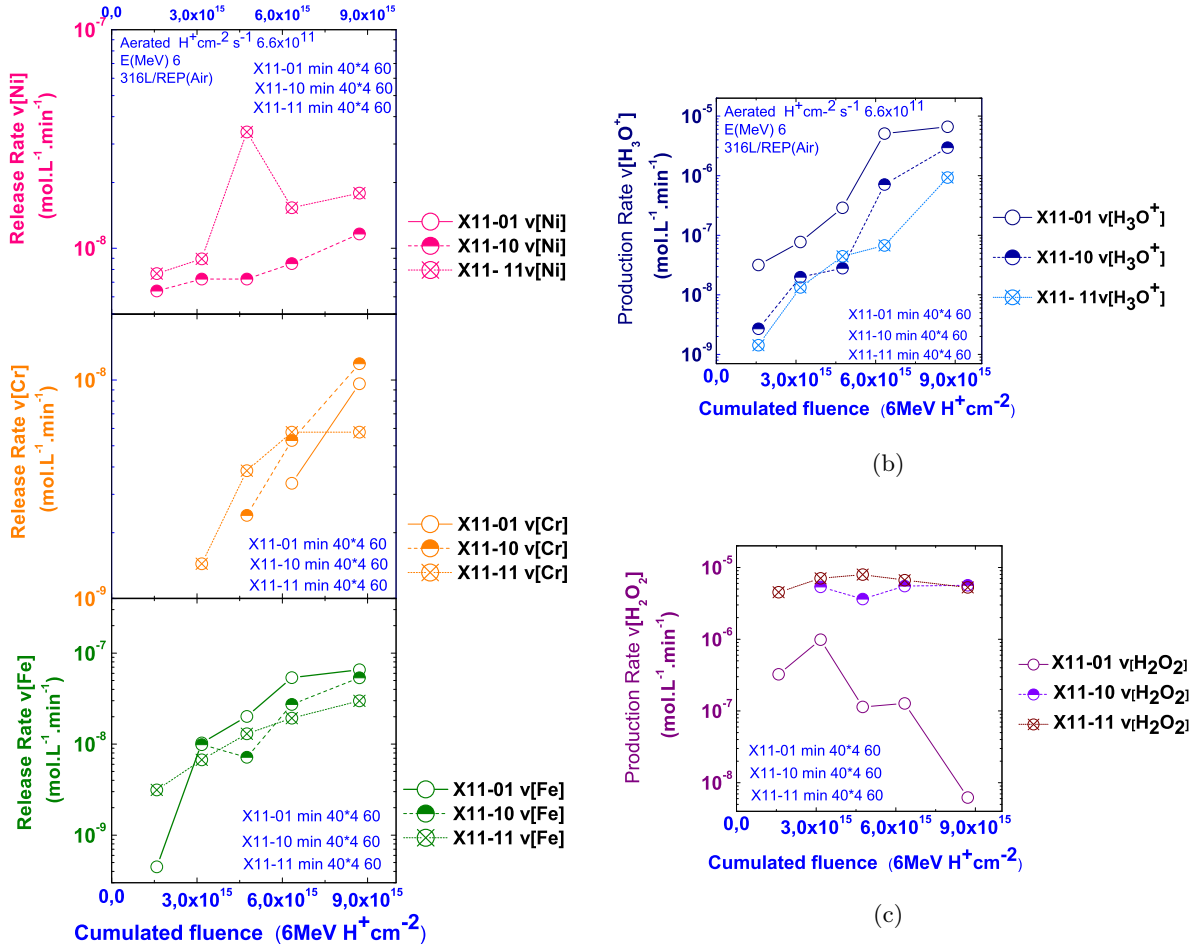

Figure 8.8: Solution analysis on different parameters of different interfaces, X11-01, X11-10 and X11-11, versus cumulated fluence on the 316L stainless steels: (a) release rate of cations: Ni (*on the top*), Cr (*in the middle*) and Fe (*at the bottom*); (b) production rate of H_3O^+; (c) production rate of H_2O_2.

- **Ni release:** the release of nickel is the most difficult to interpret. It appears to be released more than chromium while less than iron. However, it may also be under the detection limit sometimes, such as the case of X11-01. That is the reason for its absence in the figure. In the rough, the release of nickel increases with irradiation, from 10^{-8} to 10^{-7} $mol^{-1}.L^{-1}.min^{-1}$. However, the evolution with cumulated fluence is not as clear as the others cations. On one hand, the slope of nickel release is even less than the one of chromium. On the other hand, nickel release is even more significantly than iron at the beginning of irradiation.

In short, Fig.8.8 (a) exhibits the release of cations induced by irradiation from a 316L stainless steel. Without any thermal treatment, the description of the radiolysis effect is more evident and direct. Indeed, the irradiation can somehow influence the diffusion properties of cations in the substrate and the oxide film, and thus results in the release of cations.

8.2.C.2 Proton and Hydrogen Peroxide

The evolution of proton H_3O^+ and hydrogen peroxide H_2O_2 with the cumulated fluence are plotted in Fig.8.8 (b) and Fig.8.8 (c), respectively.

- **H_3O^+:** it represents the acidity of the solution, which increases sharply with cumulated fluence on the disc, from 10^{-9} to 10^{-5} $mol^{-1}.L^{-1}.min^{-1}$. There are three different sources for the presence of proton in the solution:
  1. it comes from the radiolysis of water which leaves H_3O^+ (H^+) as a radiolytic species, which can be varied due to the evolution of the chemical system induced by irradiation;
  2. it comes directly form the proton beam (H^+), it should be the same for each irradiation;
  3. it comes from the hydrolysis of metallic cations.
- **H_2O_2:** it is a "*stable*" molecular product, produced by the water radiolysis directly. The range of the production rate is from 10^{-8} to 10^{-5} $mol^{-1}.L^{-1}.min^{-1}$. Indeed, the evolution of the H_2O_2 is not obvious. On one hand, it is continuously produced by the water radiolysis. On the other hand, it can also be consumed by the cathodic corrosion reaction or by the oxidation of metallic cations (Fe^{2+} to Fe^{3+}, for instance). Therefore, the tendency of the H_2O_2 production is not shown directly.

In summary, with the fluence cumulated on the 316L stainless steel disc, the irradiated PWR water becomes more acidic and release more cations.

8.2.D Influence of Leaching Time

The leaching time of the 316L stainless steel in each PWR water is actually the duration of each irradiation. Fig.8.9 shows a comparison of a leaching time between 20 min (X10-10) and 40 min (X11-11). Tabs.8.3 & 8.4 indicates the leaching time for each irradiated solution.

Solution n°	Energy (MeV)	Flux (nA)	$Duration_{irr}$ (min)
SX10-10 n°1	12/6	30	20
SX10-10 n°2	12/6	30	20
SX10-10 n°3	12/6	30	20
SX10-10 n°4	12/6	30	20
SX10-10 n°5	12/6	30	20
SX10-10 n°6	12/6	30	20
SX10-10 n°7	12/6	30	20
SX10-10 n°8	12/6	30	20
SX10-10 n°9	12/6	30	60

Table 8.4: List of the irradiated PWR water form the interface X10-10 with the specific conditions for each irradiation. **S:** solution (PWR water).

For the release of cations, except for nickel, X10-10 has a higher release than X11-11, which in accordance with the acidity evolution. Each irradiated PWR water of X10-10 is more acid. Concerning H_2O_2, as usual, the evolution is not predictable. For the 20 minutes leaching time, it is only detectable

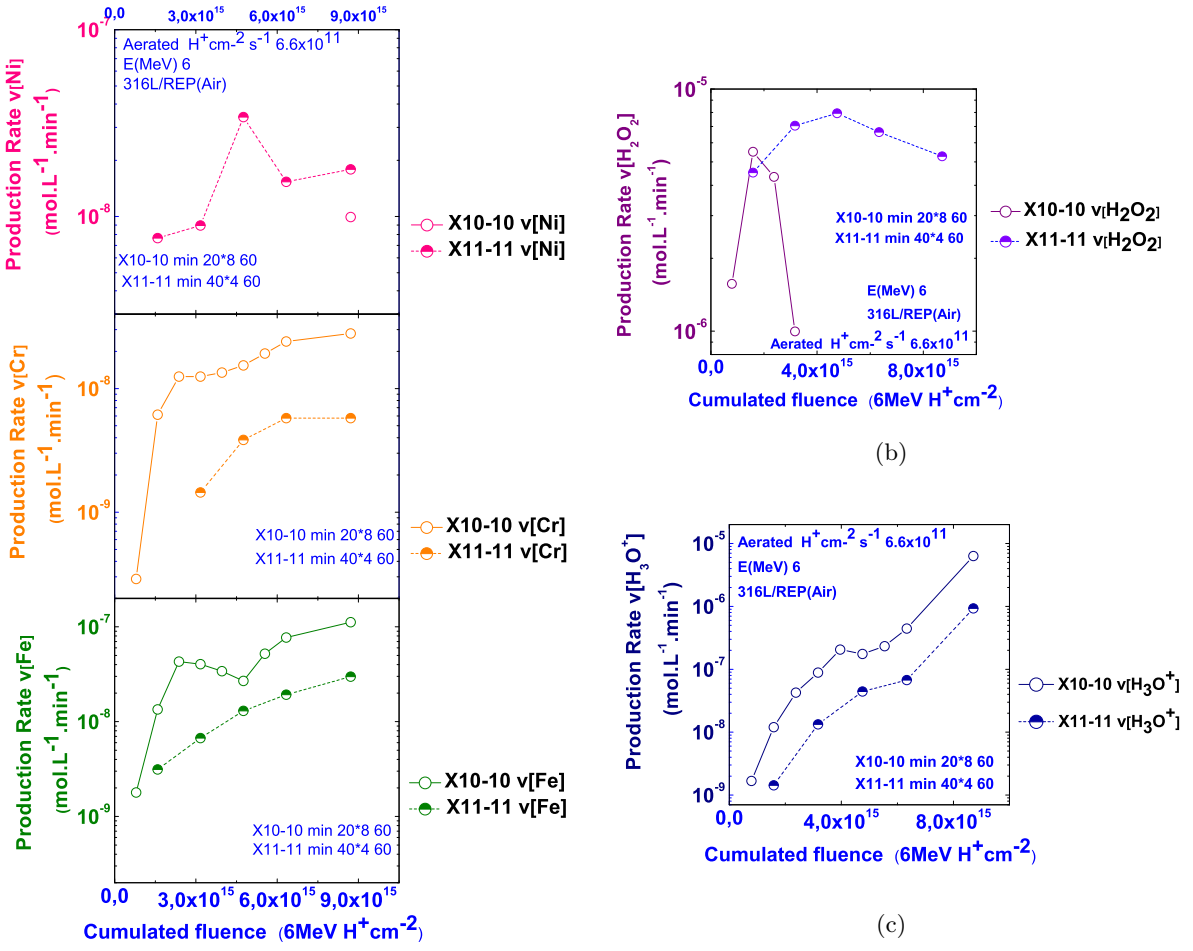

Figure 8.9: Solution analysis on different parameters of X10-10 and X11-11 versus cumulated fluence on the 316L stainless steels: (a) release rate of cations: Ni (*on the top*), Cr (*in the middle*) and Fe (*at the bottom*); production rate of (b) H_3O^+ and (c) H_2O_2.

for the first four solutions, which seems to have a maximum around 2×10^{15} H^+cm^{-2}. For the 40 minutes leaching time, H_2O_2 is always detectable. Globally, the production of H_2O_2 is higher than X10-10 and it also appears to have a maximum at fluence around 5×10^{15} H^+cm^{-2}. A longer duration of water radiolysis leads to more H_2O_2 production. As already concluded, the release of nickel is quite difficult to interpret. And in the case of X10-10, it is not detectable until the last solution.

Generally speaking, the correlation between the cation release and acidity is verified. More important, this correlation is not affected by the leaching time. Comparing the leaching time between 20 minutes and the 40 minutes, it is obvious that the release of cations is more efficient when the solution is renewed more often. Two explanation may be applied here:

- **Efficiency**: the release of cations responds to the irradiation more efficiently at the beginning, afterwards it stabilises and reaches a regime more or less constant. With renewing the solution more often, the efficiency of the release is well exhibited.
- **Concentration**: The cation (iron, chromium and nickel) dissolution reaches a saturation during

the irradiation. In other words, renewing the PWR water increases the cation release. Therefore, for the same cumulated fluence on 316L stainless steel, the release is higher when the solution is renewed more often.

8.2.E Analysis of Ox300°C- X12-300-01

As same as for Ox25°C, Fig.8.10 illustrates a complete solution analysis on an Ox300°C interface, X12-300-01, of which the specific irradiation conditions are indicated in Tab.8.5.

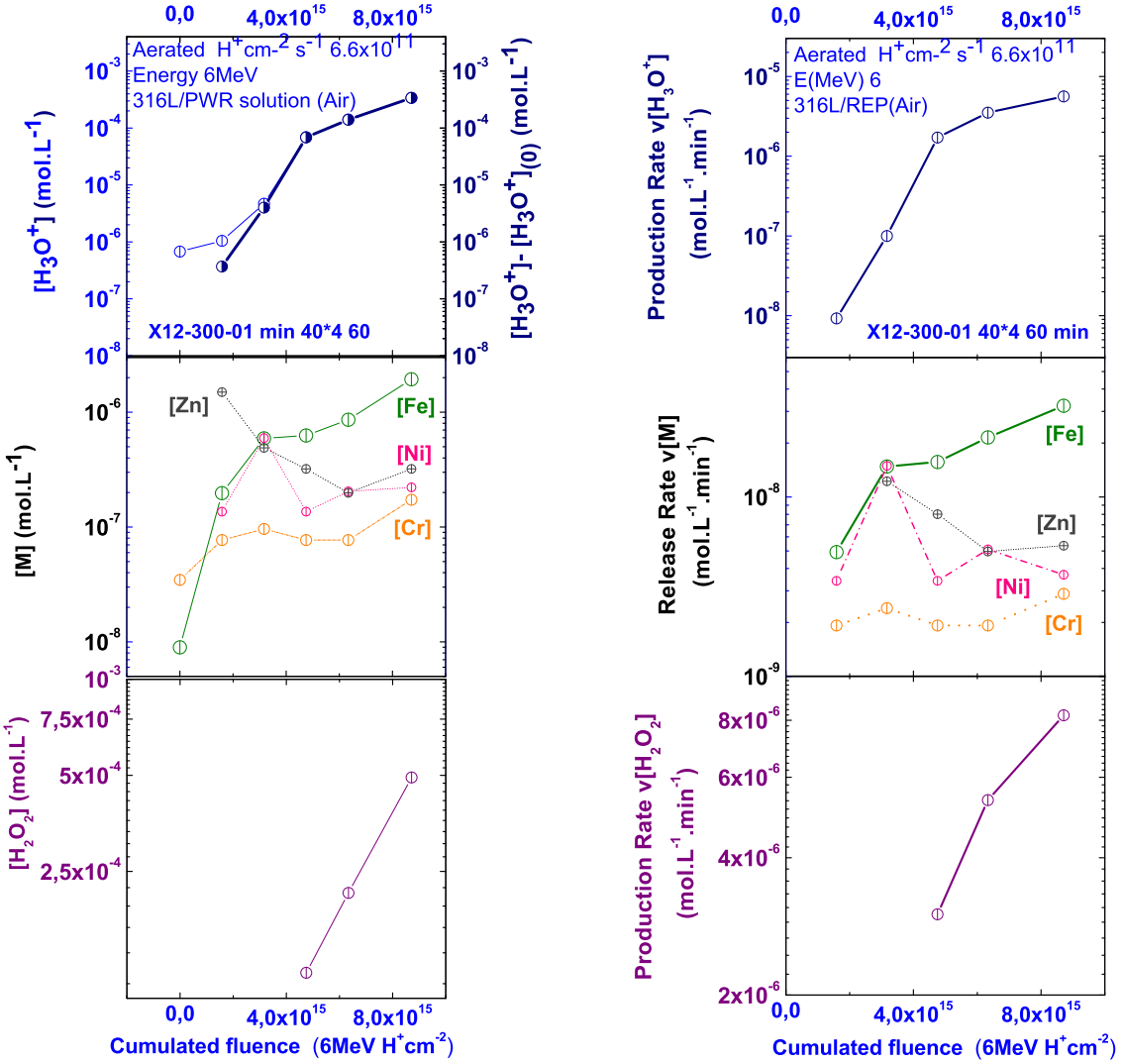

(a) (b)

Figure 8.10: Solution analysis on different parameters of different interfaces, X12-300-01, versus cumulated fluence on the 316L stainless steels: (a) concentration of $[H_3O^+]$ (left) and $[H_3O^+]$ - $[H_3O^+]_0$ (right) (*on the top*), cations (*in the middle*) and $[H_2O_2]$ (*at the bottom*) versus cumulated fluence on 316L stainless steel X11-11; (b) production rate of $[H_3O^+]$ (*on the top*), release rate of cations (*in the middle*) and production rate of $[H_2O_2]$ (*at the bottom*).

As shown in Fig.8.10, the increase of iron release and proton irradiation with the cumulated fluence

Solution n°	Energy (MeV)	Flux (nA)	Duration$_{irr}$ (min)
SX12-300-01 n°1	12/6	30	40
SX12-300-01 n°2	12/6	30	40
SX12-300-01 n°3	12/6	30	40
SX12-300-01 n°4	12/6	30	40
SX12-300-01 n°5	12/6	30	60

Table 8.5: List of the irradiated PWR water form the interface X12-300-01 with the specific conditions for each irradiation. **S:** solution (PWR water).

is quiet obvious in both concentration and rate. The release of chromium seems to be monotonous with irradiation. And the release of nickel appears to be a little bit random. The H_2O_2, which is not detectable until the third solution, increases with the cumulated fluence on the 316L.

As a matter of fact, a series of experiments have been performed under the same irradiation conditions. Some of 316L discs were passivated at 300°C for 3 days, some of them were irradiated by using different water (like demineralised water, etc.). Among them, the most representative one is the X12-300-01. However, it appears that the reproducibility of the solutions analysis is lower for the Ox300°C than for the Ox25°C. Especially for the production of H_2O_2, because it is not always detectable in the solution. As stated previously, the evolution of H_2O_2 under irradiation is produced by water raidolysis while consumed by cathodic corrosion reaction and/or metallic cation oxidation.

Combining the other results, it is clear that the duration of the passivation process at 300°C directly affects the quality of the oxide film, which leads to a different behaviour for the cation release. Other than an evident tendency (increase, decrease or constant), the release of cations is more random, even for iron and chromium. Though it still leaves an impression that the release of cations increase with cumulated fluence. Actually, the only parameter which has shown a high similarity in the production behaviour, is the proton (H_3O^+). It always increases sharply with cumulated fluence, by a factor of $10^3 \sim 10^4$.

To sum up, with an oxide film developed at 300°C, the PWR water is becoming more and more acidic with irradiation at 25°C. However, the correlation between acidity and cation release seems to be weaken for the Ox300°C. In order to get a better understanding, a comparison of solution analysis between Ox25°C and Ox300°C will be presented below.

8.2.F Comparison between Ox25°C and Ox300°C

Fig.8.11 illustrates the solution analysis results of two interfaces X11-11 for the Ox25°C and X12-300 -01 for the Ox300°C. It shows that:

- **Cations:** the release of iron and chromium evolves similarly between Ox25°C and Ox300°C. Moreover, the values are in the same range. It appears that the release of iron is always superior than of chromium. For the release of nickel, the release of Ox25°C and Ox300°C show the same tendency with a maximum somewhere. Globally, slight increase tendency of the cation release is showed with irradiation.

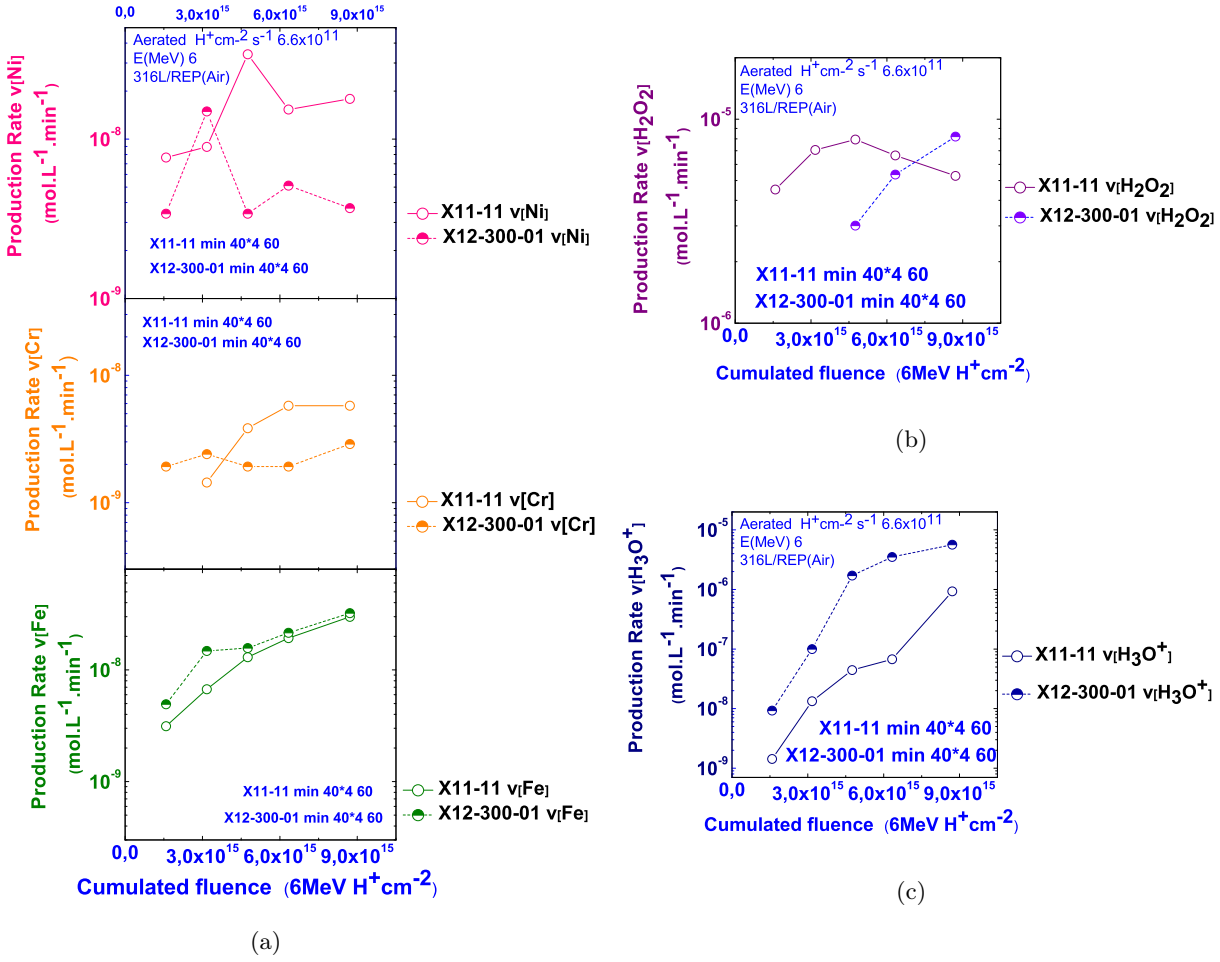

Figure 8.11: Solution analysis on different parameters of X11-11, X12-300-01 versus cumulated fluence on the 316L stainless steels: (a) release rate of cations: Ni (*on the top*), Cr (*in the middle*) and Fe (*at the bottom*); production rate of (b) H_3O^+ and (c) H_2O_2.

- **Acidity:** the increase of acidity is actually more significant for Ox300°C than Ox25°C.

- **Hydrogen peroxide:** H_2O_2 is produced during the water radiolysis and detected at the concentration around $10^{-6} \sim 10^{-5}$ $mol^{-1}.L^{-1}.min^{-1}$, except for few particular cases. It appears that the quantity of H_2O_2 for both Ox300°C and Ox25°C are in the same magnitude.

As stated at the beginning of this chapter, the oxide film of Ox25°C is totally different from the ones of Ox300°C. When they were irradiated under the same conditions, the nature of oxide film plays an important role on the release behaviour. However, some common observation can be figured out based on these results, which may also be thought as the conclusion:

- Irradiation induces the solution becoming more acidic, and more cation release in the solution consequently. However, the acidity of the Ox300°C is much higher than the Ox25°C while the release of cations are in the same magnitude. It may reveal that the Ox300°C is more protective than Ox25°C, which results in less cation release under irradiation.

- A certain quantity of H_2O_2 is produced by the radiolysis of water while a certain quantity of H_2O_2 is consumed by cathodic corrosion reaction and/or metallic cation oxidation. Therefore, the evolution is not quite clear.

8.2.G Anion Release

The technique of *Ion Chromatography* is first used for verifying the concentration of lithium in the blank PWR water. Afterwards, it is adapted to analyse the irradiated PWR water for the contamination of anions occasionally. Therefore, the following results conclude the release of anion and the concentration of lithium.

	Li^+	NH_4^-	K^-	Cl^-	$\mathbf{F^-}$	NO_3^-	PO_4^-	SO_4^{2-}
[Conc] (μg/L)	$1.7 \sim 2.5$	< 1	$0 \sim 100$	$0 \sim 80$	$\mathbf{0 \sim 30}$	< 1	< 1	$0 \sim 50$

Table 8.6: The ranges of different anions concentration in the irradiated PWR water analysed by Ion Chromatography, combining all the results of different analyses (see Appendix F).

According to the analyses, Tab.8.6, several observations and remarks can be made:

- Most upper limits of [K^-], [Cl^-], [SO_4^{2-}] was observed after the first irradiation. It implies that after *cleaning* by the first solution, the cell becomes cleaner. In other words, parts of the anions comes from the contamination of the Teflon® cell.
- The concentration of NO_3^- is not as high (<1 ppm) as predicted. Considering the irradiation experiments were performed in the presence of air, the nitrogen (N_2) in the air may be dissolved in the PWR water, then irradiated and detected in the form of NO_3^-. However, based on the results, this hypothesis can be excluded.
- The only anion release, which can linked to the irradiation, is the F^-, because it increases gradually with the cumulated fluence in most cases. However, it increases slightly, and thus the concentration is low ($< 30\mu$g/L) in the solution. Indeed, the Teflon® cell contains fluorine. However, the cell is not directly irradiated by the beam. The possible explanation is that the acidity of the PWR water increases with irradiation, and thus it may dissolve more and more F^- in the solution.

In short, most anions analysed in the irradiated PWR water come form a contamination of the Teflon® cell. Thanks to this conclusion, it helps to elucidate the origin of the zinc contamination.

8.2.H Zinc Contamination

Zn has been detected for almost all the irradiated PWR water in a relatively important concentration. Contrary to the alloying elements (iron, chromium, nickel), it decreases gradually with the cumulated fluence on 316L stainless steel, see Figs.8.7 (a) & 8.10 (a). Since zinc is neither alloying nor additional element in 316L stainless steel, its systematic presence in the irradiated PWR water has to be explained by a contamination.

Combining a series of *blank tests* (same leaching time, same quantity of PWR water, but without irradiation) in the beakers and Teflon® cells with the irradiation experiments, it demonstrates that:

- Zinc contamination does not come from the blank PWR water preparation. In other words, the water supply is actually fine.
- **Ox25°C Experiments:** after cleaning process, the 316L stainless steel discs are clean with no trace of zinc, confirmed by XPS analysis. However, as well as most anions, the first PWR water (unirradiated or irradiated) contains a large quantity of zinc. It implies that the origin of zinc should be related to a contamination of the Teflon® cell. After the first PWR water, for the unirradiated experiments, the following PWR waters are zinc free. Though for the irradiated ones, zinc decreases with cumulated fluence as stated above.
- **OX300°C Experiments:** partly of the zinc comes from the contamination of the Teflon® cell as same as Ox25°C. The other source of zinc can be traced back the passivation in the autoclave during the preparation. The zinc contamination in the autoclave can be transferred to the oxide film (surface) formed on the 316L stainless steel discs, which has been proved by XPS analysis.

In general, the release of zinc should be more significant for the Ox300°C. Though, it also depends on the specific Teflon® cell used in the experiment. Therefore, it complicates the conclusion by adding the random variable. Briefly, the contamination, mainly comes from the experimental device (Teflon® cell) rather than the samples (316L stainless steel and PWR water). Finally, it is worth recalling that the presence of zinc impurities appears to be harmless to the water radiolysis [9–12]. Actually, zinc is added in some PWR primary water in order to decrease SCC susceptibility and nickel release.

8.3 Discussion

8.3.A Evolution of Electrochemical Behaviours

The electrochemical behaviour of 316L stainless steel in PWR water under proton irradiation at room temperature is influenced by flux and fluence.

The evolution with flux depends on the balance between the production of radiolytic yields and the recombination of the radicals. Under the circumstance, the reducing radiolytic products is predominating. When the production rate is relatively low, the recombination rate will stay lower due to the lack of radicals, then results in a reducing environment. Therefore, it gives a **reductive** potential response to the beam. Contrarily, if the production rate becomes higher, the recombination rate is raised consequently. Eventually, the concentration of molecular products will overcome the reducing species, and leads to an oxidative media. As a result, an **oxidative** potential response can be observed under irradiation.

On the other hand, the electrochemical potential increases gradually with fluence. Generally, when the oxide film stays at the passive stage, the corrosion potential can be increased with the cathodic reaction (oxidative species) which can be considered as a consequence of water radiolysis [13], as illustrated in Fig.8.12.

8.3.B Correlation between Cation Release and Acidity

As known, the solubility of the iron and nickel increases with the decreasing pH [14–16]. In other words, the increase of cation release may be caused by the increase of the acidity. Reciprocally, the acidity

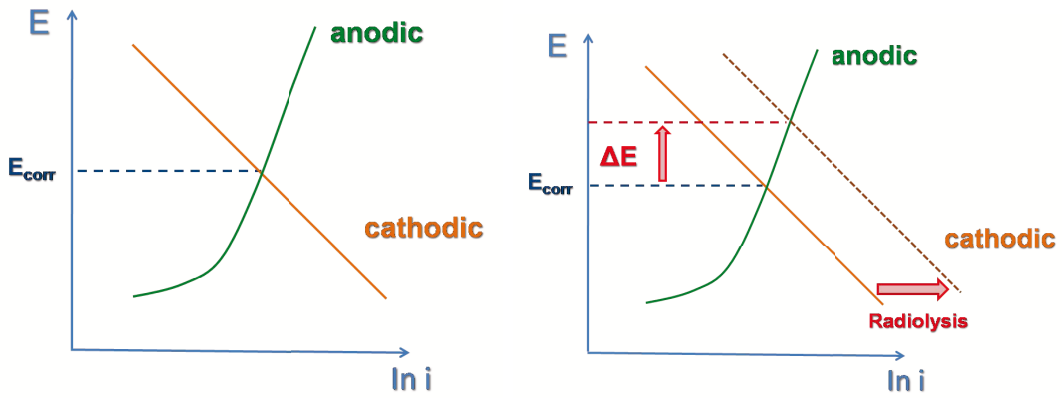

(a) (b)

Figure 8.12: Schematic layout of Evans diagrams explaining the possible evolution in electrochemical corrosion potential evolutions due to the water radiolysis: (a) initial conditions; (b) when radiolytic oxidising species are produced.

is also affected by the cations dissolved in the solution, such as the reactions, Eqs.8.2 for instance. Briefly, it reveals that the evolution of both cation release and acidity with cumulated fluence are actually correlated to each other.

$$\begin{aligned} 2Fe^{2+} + 2H^{+} + \tfrac{1}{2}O_2 &\rightarrow 2Fe^{3+}_{aq} + H_2O \\ Fe^{2+} + HO^{\bullet} &\rightarrow Fe^{3+} + OH^{-} \\ Fe^{3+} + H^{\bullet} &\rightarrow Fe^{2+} + H^{+} \end{aligned} \tag{8.2}$$

Furthermore, for the dissolution of the oxides and the release of cations, it takes OH^- for the reaction, as written in Eq.8.3. Briefly, it frees H^+ from the water molecule. As consequence, more release of cations in the solution gives a higher acidity.

$$M^{2+} + nOH^{-} \rightarrow M(OH)_n^{(2-n)+} \tag{8.3}$$

8.3.C Correlation between H_2O_2 and Acidity

It seems that the one who has the highest production rate of H_3O^+ also owns the lowest of H_2O_2, X11-01 in Fig.8.8 (c). Actually, there is an equilibrium equation between hydrogen peroxide and proton, as indicated in Eq.8.4. It may explain the inverse proportion between H_3O^+ and H_2O_2.

$$H_2O_2 \rightleftharpoons H^{+} + OH_2^{-} \qquad pK_a(20°C) = 11.84 \tag{8.4}$$

According to reference [4, 17], when a solution becomes more acidic, more H_2O_2 will be produced during the radiolysis. However, it is the case for a pH less than 4. As far as the figure (Fig.8.8 (b)) shown, the pH is coming up to 4, but not yet reaches this value.

8.3.D Correlation between H_2O_2 and Cation Release

Also, the iron release also influences the production of H_2O_2 and H_3O^+ [9, 18], as indicated in Eqs.8.5. The presence of iron impurities (ferric ions) promotes water radiolysis in producing more H_2O_2, especially at high boron concentration. Based on our results, the increase of iron release is well demonstrated though the increase of H_2O_2 is not.

$$\begin{aligned} 2Fe^{2+} + 2H^+ + \tfrac{1}{2}O_2 &\rightarrow 2Fe^{3+}_{aq} + H_2O \\ Fe^{2+} + O_2^- &\rightarrow Fe^{3+} + H_2O_2 + 2OH^- \\ 2Fe^{2+} + H_2O_2 &\rightarrow 2Fe^{3+} + OH_2^- \end{aligned} \tag{8.5}$$

8.4 Summary

Proton irradiation experiments on Teflon® cell have been presented in this chapter. Along with the electrochemistry results, several solution analyses have also been shown.

Concerning the electrochemical behaviours, a strong dependence on both flux and fluence have been observed. The dominating effects of water radiolysis has been exhibited for constant temperature and pressure values. With increasing proton flux and fluence, the free potential of 316L stainless steel in PWR water changes under irradiation. An evolution from a *reductive* response to an *oxidative* one under irradiation has been noticed. Flux and fluence both play important roles on this evolution. However, it is hard to tell whether the flux and/ or the fluence effect can be attributed to a change of the nature and/ or the rate of the chemical reactions at the irradiated interface.

The solution analysis after irradiation shows that the acidity of the solution is increased together with the cations concentration of the main 316L alloying elements (iron, chromium and nickel), although the PWR water is renewed for each irradiation. The correlation between the two parameters is clear, though it cannot be certain that whether it is the irradiation or the acidity takes more responsibility for the cation release. Irradiation provokes the release of cations and the increase of acidity in the PWR water. However, the continuous increase of the cation release can be caused by the cumulated fluence on one hand. On the other hand, the increasing acidity can also enhance the solubility of cations, which leads to dissolve more cations in the solution.

H_2O_2, a stable oxidising species produced by water radiolysis, is detected for the irradiation performed at room temperature depending on the interface under investigation. The evolution of the H_2O_2 is linked not only to its production by water radiolysis but also to its consumption in the oxidation reactions with either interface or dissolved solutes. The production of H_2O_2 does not seem to be affected by the dissolved cations and acidity induced by irradiation in the PWR water at the 316L/ PWR water interface. Therefore, it is the reason that further experiments are needed to elucidate the evolution variability of the H_2O_2.

The characterisation of the oxide film formed on the 316L stainless steel discs after irradiation is not feasible due to the radioactivity induced by the proton beam. However, the changes in the release of cations and acidity during the sequential irradiations where the irradiations were performed at the same conditions with a fresh PWR water for each irradiation reflects rather an evolution of the 316L disc than of the PWR water. In other words, the release of cations and the chemical reactions at the 316L/ PWR water interface implies either a change in the oxide composition or the production of the

chemically active defects on the 316L under irradiation.

References

[1] Ramette R. W. Outmoded terminology: The normal hydrogen electrode. *Journal of Chemical Education*, 64(10).

[2] Pavlishchuk V. V., Addison A. W. Conversion constants for redox potentials measured versus different reference electrodes in acetonitrile solutions at 25°C. *Inorganica Chimica Acta*, 298:97–102, 2000.

[3] Féron D., Herms E., Tanguy B. Behavior of stainless steel in pressurized water reactor prirmary circuits. *Journal of Nuclear Materials*, 427:364–377, 2012.

[4] B.G. Ershov, A.V. Gordeev. A model for radiolysis of water and aqueous solutions of H_2, H_2O_2 and O_2. *Radiation Physics and Chemistry*, 77(8):928 – 935, 2008.

[5] A.J. Elliot, D.M. Bartels. The Reaction set, rate sonstants and g-Values for the Simulation of the Radiolysis of Light Water over the Range 20°C to 350°C Based on Information Available in 2008. Technical report, Atomic energy of Canada Limited, 2009.

[6] TRUPIN-WASSELIN Virginie. *Processus primaries en chimie sous rayonnement. Influence du Transfert d'Energie Linéique sur la radiolyse de l'eau.* PhD thesis, Universite de Paris-SUD U.F.R. Scientifique d'Orsay, 2000.

[7] Ned E. Bibler. Dose Rate Effects in the Steady and pulse Radiolysis of Liquid Chloroform. *The Journal of Chemical Physics*, 75(16):2436– 2442, 1971.

[8] Schwarz H. A. A Determination of Some Rate Constants for the Radical Process in the Radiation Chemistry of Water. *J. Phys. Chem.*, 66:255–262, 1962.

[9] B. Pastina, J. Isabey, B. Hickel. The influence of water chemistry on the radiolysis of the primary coolant water in pressurized water reactors. *Journal of Nuclear Materials*, 264:309–318, 1998.

[10] PASTINA Barbara. *Etude sur la radiolyse de l'eau en relation avec le circuit primaire de refroidissement des réacteurs nucléaires á eau sous pression.* PhD thesis, Universite de Paris-SUD U.F.R. Scientifique d'Orsay, 1997.

[11] Domae M., Chitose N., Zuo Z., Katasumura Y. Pulse radiolysis study on redox reactions of zinc (II). *Radiation Physics and Chemistry*, 56:315–322, 1999.

[12] Buxton G.V., Sellers R. M. and McCracken D. R. Pulse Radiolysis Study of Monovalent Cadmium, Cobalt, Nickel and Zinc in Aqueous Soltuion. *J. Chem. Soc., Faraday Trans. 1*, 76:1464–1476, 1972.

[13] Bosch R. W., Wéher M., Vankeerberghen M. In-pile electrochemical measurements on AISI 304 and AISI 306 in PWR conditions - Experimental results. *Journal of Nuclear Materials*, 360:304–314, 2007.

[14] Sandler Y. L., Kunig R. H. The Solubility of Nickel Ferrite in Aqueous Boric Acid Solution. *Nuclear Science and Engineering*, 77:211–218, 1981.

[15] Chung J. Y., Lee K. J. The Solubility of Magnetite and Nickel Ferrite in High Temperature Aqueous Solutions. *High Temperature Science*, 30:51–66, 1990.

[16] Sandler Y. L., Kunig R. H. The Solubility of Nonstoichiometric Nickel Ferrite in High-Temperature Aqueous Solution. *Nuclear Science and Engineering*, 64:866–874, 1977.

[17] Kabakchi S. A., Shubin V. N., Dolin P.I. Effect of pH on the stationary concentration of radiolysis products of aqueous solution of oxygen. *High Energ. Chem.*, 1(2):148–153, 1967.

[18] Allen A. O., Rothschild W. G. Studies in the Radiolysis of Ferrous Sulfate Solutions. Effect of Oxygen Concentration in 0.8 N Sulfuric Acid. *Radiation Research*, 7:591–602, 1957.

Conclusion and Outlooks

This thesis focused on the electrochemical behaviour of stainless steel under irradiation and exposed to primary PWR conditions. The electrochemical potential of austenitic 316L stainless steel has been measured at high temperature (HT) and high pressure (HP) in primary PWR conditions under irradiation, using a unique experimental working cell (HTHP cell). The free potential between a 316L stainless steel and a Platinum pseudo-reference electrode, has been measured continuously *in-situ* under irradiation while monitoring the environmental changes (hydrogen pressure, temperature and total pressure). The obtained results allow the evolution of both electrochemical potential and environmental parameters under irradiation to be further understood.

Two sources of irradiation, proton and electron beams, have been employed in the study. A high similarity of electrochemical behaviour under both types of irradiations has been observed:

1. an oxidative potential response under irradiation, which is slight but measurable (tens of mV);
2. an increasing temperature decreases the oxidative potential response at a first temperature range ($\lessapprox 200°C$), but results in a weak maximum at the second range ($\approxeq 200 - 300°C$);
3. an increasing hydrogen concentration reduces the oxidative potential response;
4. a synergetic effect of thermal ageing and fluence cumulation has been observed, leading to a decrease in the electrochemical potential without irradiation, and a decrease in the oxidative response under irradiation.

In general, the evolution of the electrochemical behaviour is more significant under proton irradiation rather than electron irradiation. Proton beam radiation can be considered as representative of neutron irradiation induced effects in primary coolant circuit of PWRs whereas electron beam irradiation is more representative of γ radiation induced effects. Due to the activation of 316L stainless steel for the energy range of proton irradiation used in this work, it is impossible to characterise a proton irradiated oxide film for a long period; based on the high similarity of the electrochemical behaviour of proton and electron irradiations, it is assumed that their surface characterisations are comparable.

Based on the characterisation of the oxide film, μm scale *cavities* (small pittings) have been observed in the strongly electron irradiated oxide film formed on 316L stainless steel. By comparison to reference discs with oxide films prepared in similar conditions than those submitted to irradiation, it can be concluded that these *cavities* are induced by the effect of irradiation and water radiolysis. Water radiolysis also influences the PWR water chemistry by transforming it into a stronger oxidant at the interface. As a result, α-Fe_2O_3 hematite has been observed on the irradiated oxide film where

cavities have been shown. Moreover, the release of chromium in the PWR water has been analysed after irradiation, proving high when the protective oxide film rich in chromium is locally broken (presence of *cavities*). In addition, other than inhibiting the water radiolysis, it has been found that the presence of hydrogen in PWR water has a strong effect on the composition of the oxide film. Without irradiation, metallic nickel in the oxide films (inner and outer layers) has been observed under a high hydrogen concentration. However, in the presence of irradiation, no metallic nickel is ever detected in the oxide film.

In a complementary study, proton irradiation experiments on Teflon® cell at room temperature in an aerated environment have been performed, showing that the electrochemical behaviour of 316L stainless steel with a passive film formed at 25°C (Ox25°C) or formed at 300°C under primary PWR conditions (Ox300°C) are quite similar. Depending on flux and fluence, either a reductive or an oxidative potential response is measured under irradiation. Regarding the effect of water radiolysis on water chemistry, with the fluence cumulated on 316L, the PWR water becomes continuously more acidic and releases more cations, in correlation with each other. The properties of the oxide film are certainly evolving during the irradiation, however no characterisation has been performed due to the sample activation. Nevertheless, it seems that the oxide film formed at 300°C is more protective and stable than the film formed at 25°C mainly based on the release data.

The overall results describe the evolution of the electrochemical behaviour of stainless steel in a simulated PWR conditions. Clearly, in the presence of hydrogen, the global evolution of the electrochemical potential is quite small at high temperature (300°C), however the surface characterisation proves the existence of *cavities* (pittings) in the strongly electron irradiated oxide films. This can be considered a signal for localised high potentials, which may be expected to have little effect on the global free corrosion potential recorded in this work. Furthermore, the increase of acidity and cation release can be trigged by disc irradiation as well as by water radiolysis, and then enhanced by each other. Therefore, it proves that the combination of irradiation on the disc and water radiolysis increase the corrosivity of PWR water.

Few industrial inputs can be drawn from these results regarding the behaviour of stainless steel in the core vessel of PWRs:

- The overall increase of corrosion potentials under irradiation on the order of tens of millivolts, attributed to the effect of water radiolysis, is far from the hundreds of millivolts which are needed to induce stress corrosion cracking of these materials (-230mV_{SHE}).

- Local breakdown (*cavities*) in the passive film of stainless steel has been observed and attributed to localised high electrochemical potentials. The effect of localised regions of high electrochemical potential is probably linked to the design of the HTHP cell (no flow rate, static conditions). As the flow rate is quite important in PWR conditions, this effect has not been found on the surfaces of reactor components. Nevertheless, the local decohesion of the passive film and the initiation of a crack observed after irradiation may be interpreted as an ageing effect of the passive film under irradiation at high temperature (300°C). More studies are needed to investigate the effect of cumulated fluence (dose).

- The monitoring of the electrochemical corrosion potential (ECP), which is performed in Boiling

Water Reactors (BWRs), is certainly not necessary in the primary circuit of PWRs. As shown by this study, very little changes of ECP (few tens of millivolts) under irradiation have been observed.

- During the shutdown of the nuclear power plants (NPPs), the residual radiation is probably very low. The free corrosion potential of the stainless steel will not be increased by low irradiation, though it has to be verified by radiation calculations.
- Our results show that a standard hydrogen concentration ($\sim$ 20 cc/kg) of primary PWR water, may lead to the formation of an oxide film with metallic nickel inside without irradiation, while no metallic nickel is detected under irradiation. In the debate regarding the low optimum hydrogen concentration in primary circuit of PWRs, more investigation regarding radiolysis effect on the passive film is needed to determine this value. As shown, for a low hydrogen concentration of 30mbar, 3 cc/kg (STP), no evolution of ECP is found under electron irradiation at 300°C while a slight increase of ECP is observed with proton irradiation at the same temperature.

At the end of this work, several developments are proposed:

1. For the HTHP cell, instead of a Platinum pseudo-reference electrode, a real electrochemical reference electrode could bring more accurate information about the evolution of the electrochemical behaviour under irradiation.
2. A high reproducibility of electrochemical data is always needed, this will help estimate and explain the variability of the irradiation effects.
3. A preliminary modelling work of radiolytic species for the electron irradiation has been presented in the dissertation. It has to be improved and further developed with the objective to better interpret our experimental results and to apply them to NPPs operations.

Part

Appendix

Appendix A

H_2 Production in the Cathodic Reaction

A.1 Theoretical Calculation

The cathodic reaction of corrosion, Eq.A.1, can produce hydrogen in water without the presence of oxidising species, like oxygen due to the reduction of water itself.

$$H_2O + e^- \rightleftharpoons \frac{1}{2}H_2 + OH^- \tag{A.1}$$

The quantity of hydrogen produced can be calculated directly from the corrosion rate of the materials.

The corrosion rate of 316L stainless steel (specimen) and the Zirconium (constructed material for the tank in the HTHP cell) under primary PWR conditions are needed.

According to literature [1], the corrosion rate of 316L stainless steel at 300°C in PWR water (containing B and Li in different concentration), is around 5.37×10^{-14} cm/s. The surface of 316L stainless steel inside the tank is about 1.65 cm^{-2}. One possible corrosion reaction of 316L stainless steel is written in Eq.A.2, and thus the production of hydrogen can be calculated by Eq.A.3, where r is the corrosion rate, ρ and M are the density and the molar mass of Fe_3O_4, t is the duration at 300°C and s is the surface of the stainless steel.

$$Fe + 4H_2O \rightarrow Fe_3O_4 + 4H_2 \tag{A.2}$$

$$moleH_2 = 4 \times \frac{r \times \rho}{M} \times s \times t \tag{A.3}$$

In the case of LE11-03 ref (168 hr, 33 mbar), the duration at 300°C is 168 hours, thus, the mole of hydrogen produced is:

$$moleH_2 = 4 \times \frac{5.37 \times 10^{-14} \times 5.17}{231.533} \times 1.65 \times 168 \times 3600 = 4.8 \times 10^{-9}$$

The corrosion of Zirconium is written in Eq.A.4, and the production of hydrogen can be calculated by Eq.A.5, where r is the corrosion rate, ρ and M are the density and the molar mass of ZrO_2, t is the duration at 300°C and s is the surface of the Zirconium.

$$Zr + 2H_2O \rightarrow Zr_2O + 2H_2 \tag{A.4}$$

$$moleH_2 = 2 \times \frac{r \times \rho}{M} \times s \times t \tag{A.5}$$

The tank is made by Zirconium with a surface area of 35 cm^2. The corrosion rate is about 7μm/year [2], which equals to 2.2×10^{-11} cm/s at 360°C. And thus the hydrogen produced is:

$$moleH_2 = 2 \times \frac{2.2 \times 10^{-11} \times 5.68}{123.218} \times 1.65 \times 168 \times 3600 = 4.33 \times 10^{-5}$$

In total, the cathodic reaction can produce 4.33×10^{-5} mole of hydrogen during 168 hours at 300°C, which corresponds to an increase of hydrogen concentration at 300°C about 45 cc/kg (STP).

A.2 Experimental H_2 Production

Based on the interpretation of the measurement. P(H_2) of LE11-03 ref has increased from 33 to 80 mbar at 300°C during 168 hours. Therefore, the measured increase of hydrogen concentration is 4.9 cc/kg [3].

There is a difference between the theoretical value and the experimental measurement. One explanation is the following: during the experiments at 300°C, the corrosion rates of stainless steel and Zirconium are lower than the values used in the calculation. Another explanation is that some oxidising species are in the solution, and are consumed by the cathodic reaction. Therefore, the cathodic reaction does not lead to hydrogen production.

References

[1] Perrin S., Marchetti L. Oxide growth mechanism of 316L stainless steel in PWR primary coolant conditions: influence of irradiation. In *PERFORM* 60 *SP*2*: Internals WP*2 − 3*: Corrosion behaviour*, 2013.

[2] Parisot J. F. *La corrosion et l'altáeration des material du nucléaire*. CEA Group et Group Moniteur, 2010.

[3] Laboratoire de l'étude de la Corrosion Aqueuse. Relation p(H_2) and concentration, private communication. Technical report, CEA, 2013.

Appendix B

Raman Spectroscopy Results - Interpretation

This appendix describes the interpretation of the Raman spectroscopy results.

B.1 Experimental Results

Raman spectroscopy is used to analyse the crystal structure of the oxide film. All the spectra were obtained by using a 532 nm laser. Using the objective lens of Raman, it exhibits the whole PWR water contacted surface with two different colours, as pictured in Fig.B.1. Two individual scans have been done for each colour in zones 1 (central zone) and 2 (confined zone), respectively, shown in Figs.B.2 (a) & (b).

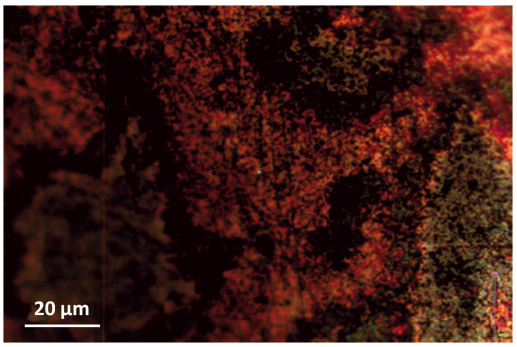

Figure B.1: Optical image taken by the Raman objective lens for LE11-02 ref (72hr, 133_smbar), showing two areas with either dark red or green/ grey colour.

All the obtained Raman spectra are alike, five peaks can be found in each spectrum, with the main peak around 700 cm^{-1} which is relatively sharp and symmetric. One main difference should be noticed: the signals of peaks 1, 2 and 3 for the dark red area are less intensive than the green/ grey one. Oppositely, peak 5 is more visible for the dark red area.

Fig.B.3 illustrates a spectrum of a precipitate found in zone 1 with the values of the Raman wavenumbers. It is obvious that the intensity of the precipitate spectrum is the strongest among all. An extremely slight peak 0 at 203 cm^{-1} can be detected.

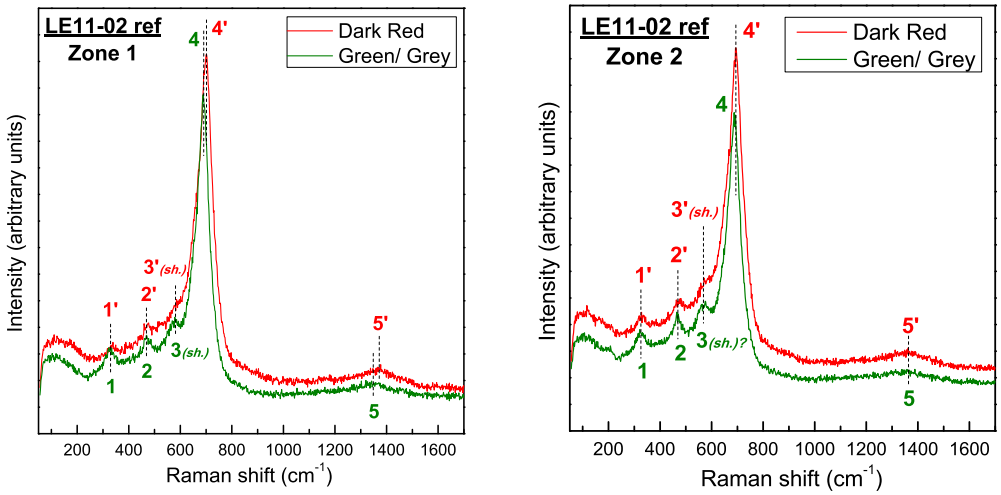

(a) (b)

Figure B.2: Raman spectra of LE11-02 ref (72hr, 133$_s$mbar), zone 1 (central zone) in (a) and zone 2 (confined zone) in (b).

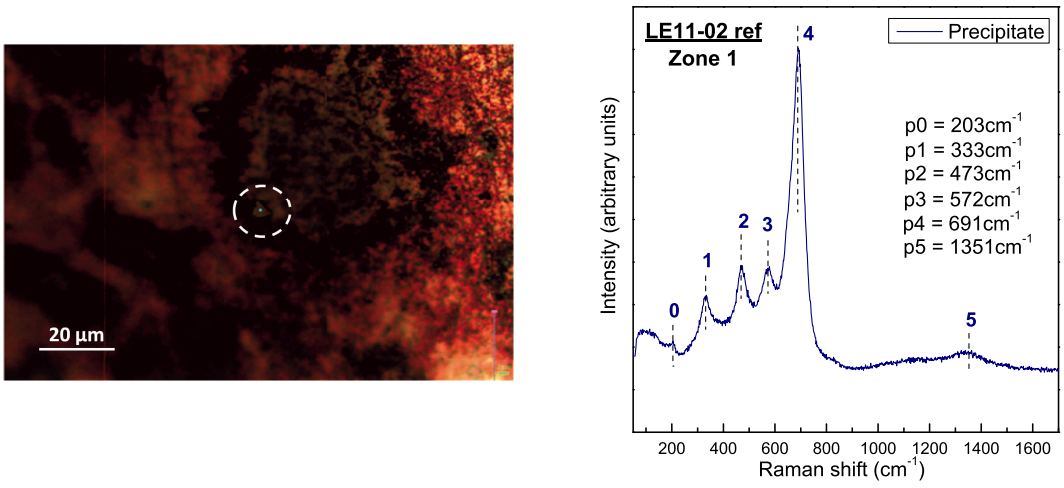

(a) (b)

Figure B.3: Raman analysis on a precipitate in zone 1 (central zone): (a) the objective photo on the analysed precipitate; (b) Raman spectrum of the precipitate.

B.2 Raman Spectra - 316L Oxide film

There are no reference wavenumbers of spectra that can be found for the oxide film formed on 316L stainless steel under primary PWR conditions. However, it appears that similar spectra, Fig.B.4, have been observed by other researchers [1]. The spectra obtained after 5 and 24 hours in PWR conditions are pretty much like the ones we obtained for LE11-02 ref (72hr, 133_smbar). The main peak and the three peaks at lower wavenumbers are nearly at the same position as LE11-02 ref (72hr, 133_smbar).

A small shift of the main peak ($\sim$ 690 cm^{-1}) is observed the spectra of 1 min to the one of 24 hours. This shift is due to the change in the chemistry and can be explained by an iron and chromium redistribution in the layers as oxidation progresses. In addition, it seems that the intensity of the peaks at 5 hours are stronger than the one at 24 hours. The most probable explanation is that the competition between deposition and dissolution of the precipitates on the surface depends on the saturation of the environment by metallic cations. It is as a function of the oxidation time [2].

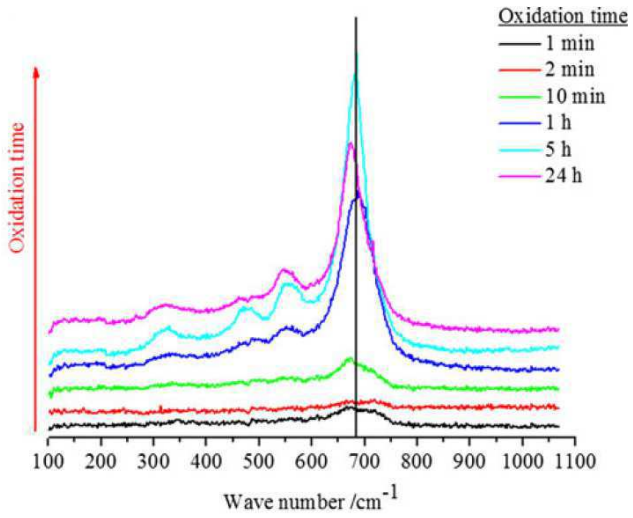

Figure B.4: Raman spectra of 316L stainless steels oxidised from 1 min to 24 hours under primary PWR conditions (325°C, 155 bar, 1000 ppm [B] and 2 ppm [Li], pH 7.2 and dissolve hydrogen = 30 cc/kg H_2O) [1].

In a word, it reveals a possible variation of the peak positions due to the heating process. Peak positions can vary with a small change in the composition. Therefore, it complicates the interpretation of the spectra. Furthermore, it is impossible to conclude the exact type and structure of oxide film without further digging in the literature. Before that, it is necessary to recall the basis of a spinel oxide structure.

B.3 Spinel Oxide Structure

As mentioned in the literature [3–6], the oxide film formed on 316L stainless steel under primary PWR conditions has a spinel structure. A spinel oxide, AB_2O_4, A and B represent for different cations and O is oxygen as illustrated in Fig.B.5. It is a cubic lattice consisting of 8 molecules within the unit cell, for a total of 56 atoms. A normal spinel means that the A^{2+} cations occupy the tetrahedral

positions while the B^{3+} cations occupy the octahedral positions. An inverse spinel is defined that the B^{3+} cations are divided into two halves, one half for the tetrahedral positions and the other half for the octahedral sites, whilst the A^{2+} cations fill up the remaining half of the octahedral positions. Also there exists a mixed spinel structure which is a state between normal and inverse.

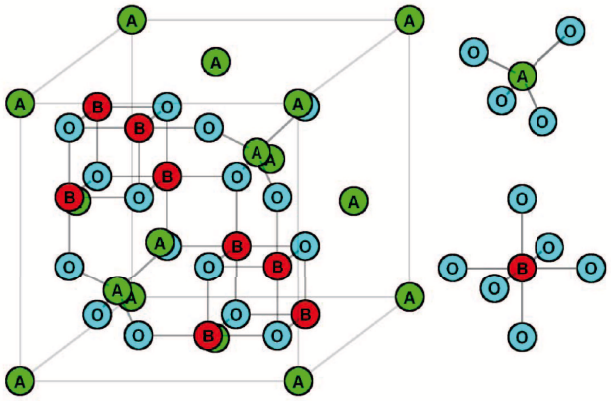

Figure B.5: The unit cell of a normal spinel oxide, AB_2O_4, contains 8 molecules. The A^{2+} and B^{3+} cations occupy the tetrahedral and octahedral sites, respectively. The tetrahedral cations are bonded to four oxygen atoms, whereas the octahedral cations are bonded to six oxygen atoms, as shown to the right of the unit cell [7].

Most chromites (spinel oxide contains chromium) are normal spinel oxide, because Cr^{3+} has a stronger preference for the octahedral site than the other cations [8]. Pure Cr_2O_3 has actually a corundum structure which is a hexagonal close-packed array of oxide ions with two-thirds of the octahedral sites being filled with the Cr^{3+} cations. The most common ferrites (spinel oxide contains iron), Fe_3O_4 and $NiFe_2O_4$ are inverse spinel oxide [9–11]. However, when the grain size is reduced to nanometer range, the $NiFe_2O_4$ is reported to exhibit a mixed spinel structure [12].

B.4 Reference - Raman Peak Table

For a spinel structure oxide, five Raman-active modes can usually be identified, $A_{1g} + E_g + 3F_{2g}$. In general, the highest frequency amongst all belongs to A_{1g} mode, the E_g and F_{2g} modes are doubly and triply degenerate, respectively. F_{2g} can be divided into three Raman-active modes, $F_{2g}(1)$ for the lowest-frequency, $F_{2g}(2)$ mode and $F_{2g}(3)$ for the highest-frequency mode of this vibrational species. Many arguments have been made for the assignment of the Raman-active vibrations of spinel [7]. However, the major concern here is to identify the complex oxide and its structure, formed on the 316L stainless steel under primary PWR conditions. Therefore, the values of the wavenumbers for the five Raman-active modes are more important for the interpretation of our Raman spectra. The wavenumbers of some spinel oxide and Cr_2O_3 from the literature are indicated in Tab.B.1.

According to this table, the highest-frequency mode A_{1g} close to 700 cm^{-1} can found for all the spinel oxide listed in the Tab.B.1. Together with the values of other bands, we assume that the most possible oxide on the LE11-02 ref (72hr, 133_smbar) analysed by Raman spectroscopy is $NiFe_2O_4$. More precisely, it is an oxide close to $NiFe_2O_4$ because there are still a slight difference between the reference wavenumbers and the observed ones (indicated in Fig.B.3 (b)). Moreover, for all the

Spinel	type	$F_{2g}(1)$	E_g	$F_{2g}(2)$	$F_{2g}(3)$	A_{1g}
LE11-02 ref	316L oxide	**203**	**333**	**473**	**572**	**691**
$FeCr_2O_4$ [13]	normal					686
$NiCr_2O_4$ [7]	normal	191	429	508		676
$NiCr_2O_4$ [14]	normal	181	425	511	580	686
$ZnCr_2O_4$ [15, 16]	normal	180	430, 457	511	605	687
$ZnFe_2O_4$ [17]	normal	221	246	355	451	647
Fe_3O_4 [13]					542	671
Fe_3O_4 [18, 19]	inverse	193	306		538	668
Fe_3O_4 [20]			301.6	513.0	533.6	662.7
$NiFe_2O_4$ [7]		189(*sh.*), 211	333	456(*sh.*), 487	568(*sh.*), 590	663(*sh.*), 704
$NiFe_2O_4$ [21]	inverse			460(*sh.*), 492	574(*sh.*), 595	654(*sh.*), 702
$NiFe_2O_4$ [22]			339	490	579(*sh.*)	666(*sh.*), 700

Oxides	Raman Wavenumber (cm^{-1})				
Cr_3O_4 [23]	296.3	350.4	528.5	554.2	615.0

Table B.1: Raman data (wavenumbers cm^{-1}) of some spinel oxides (AB_2O_4) from the literature in comparing with LE11-02 ref (72hr, 133_smbar), *sh.* = shoulder.

pronounced reference wavenumbers of $NiFe_2O_4$, shoulders are observed for $F_{2g}(2)$, $F_{2g}(3)$ modes, and especially for A_{1g} mode. However, on the spectra of LE11-02 ref, no obvious shoulders were observed. Only the red curves is meant for the dark red features in Fig.B.2, peak 3', may be referred as a shoulder, for a corresponding wavenumber of $568 \sim 579 sh.$ cm^{-1}. If so, the disappearance of $F_{2g}(3)$ mode can not be explained. Another possibility may be assigned to $NiCr_2O_4$ due to the wavenumber of the $F_{2g}(3)$ (580 cm^{-1}), which is the closest to the one on the spectra of LE11-02 ref, 572 cm^{-1}. But, this mode at 580 cm^{-1} is very board when it becomes identifiable [14]. Thus, it may be different from what we observed.

Although, the wavenumbers and the intensity for the five Raman-active modes are influenced by many parameters, such as the laser power [18, 20], the excitation laser [21, 24], and the pressure [14, 15, 17]. For instance, the laser power and the excitation laser may cause an alternative shifts on the wavenumbers or even disappearance, depending on the different oxide. Also, it is reported that the wavenumbers increases with the pressure of the experiment. Therefore, not only the values of the wavenumbers, but also the reference spectra of the spinel oxides should be studied in order to compare the line shapes.

B.5 Reference - Pure Oxides Spectra

Fig.B.6 presents the reference spectra of the pure spinel oxides individually: $NiFe_2O_4$, Fe_3O_4, Cr_2O_3, $FeCr_2O_4$ and $NiCr_2O_4$, observed by Hosterman [7].

Clearly, it is confirmed that the oxide film formed on 316L can not simply be recognised by one pure spinel oxide based on the difference from the spectra. Shoulders are apparent for $NiFe_2O_4$ but

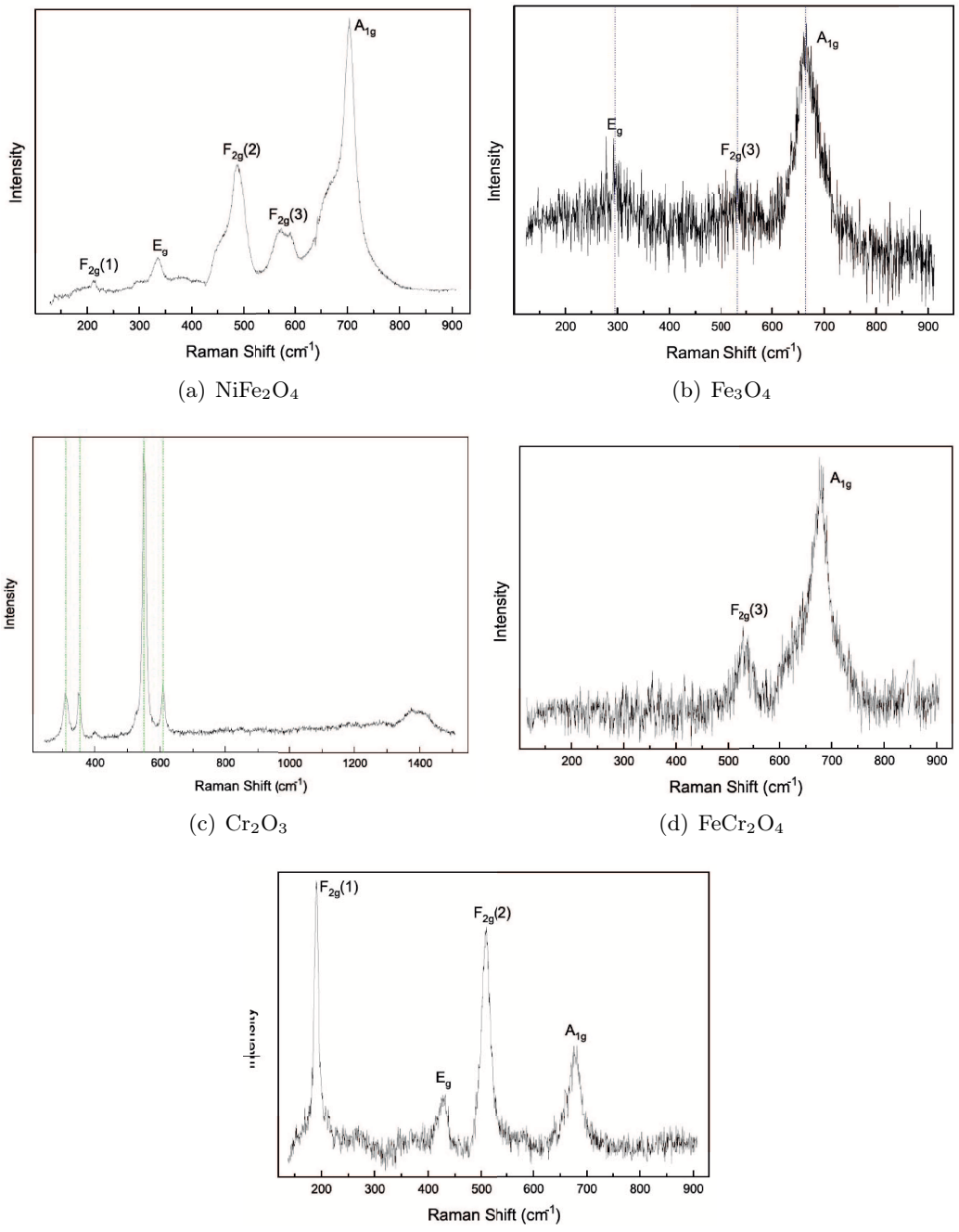

(a) $NiFe_2O_4$

(b) Fe_3O_4

(c) Cr_2O_3

(d) $FeCr_2O_4$

(e) $NiCr_2O_4$

Figure B.6: Reference spectra of different spinel oxides with conditions: laser excited in 647.1nm, except for the spectrum of Cr_2O_3, using a 514.5 nm laser; output power 5 mW. (a) $NiFe_2O_4$; (b) Fe_3O_4; (c) Cr_2O_3; (d) $FeCr_2O_4$; (e): $NiCr_2O_4$ [7].

not for Fe_3O_4 in the spectra (Fig.B.6 (a) & (b)), which may light up the version for the iron oxide. Indeed, the presence of the iron rich oxide on the outer layer of the 316L oxide film is for sure. But as detailed in the Chapter 3, the exact composition of 316L oxide is still under debate, in which Fe_3O_4 and $NiFe_2O_4$ are the most discussed ones. Based on the fact that no shoulders have been observed on the spectra of LE11-02 ref (72hr, 133_smbar), indicates Fe_3O_4 oxide. However, if it is a pure Fe_3O_4 oxide, it cannot explain the presence of the other modes in the spectra of LE11-02 ref (72hr, 133_smbar).

In addition, we may eliminated the pure Cr_2O_3 as the potential candidate for the oxide film, due to the absence of the most intense A_{1g} mode around 700 cm^{-1} in the spectrum, B.6 (c). But, the presence of chromium oxide as the inner layer of the oxide film formed on 316L is a common sense from the literature. Therefore, it may imply that the chromium oxide is present with *impurity* elements, either Fe, or Ni, or both in a small quantity.

In short, based on the Raman results, no pure oxide ($NiFe_2O_4$, $NiCr_2O_4$, Fe_3O_4 and $FeCr_2O_4$) is found on the 316L stainless steel under primary PWR conditions. However, it seems to be an impure spinel oxide.

B.6 Reference - Mixed Oxide Spectra

As known, the oxide is constituted with Ni, Fe, and Cr with specific content of each element. Figs.B.7 & B.8 describe two series of spinel oxides $NiFe_xCr_{2-x}O_4$ and $Fe_{3-x}Cr_xO_4$.

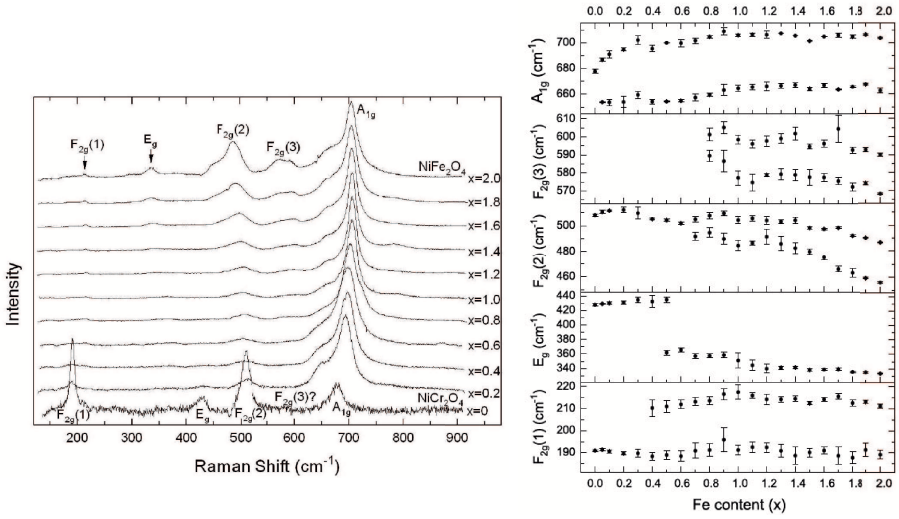

(a) (b)

Figure B.7: Spinel oxides $NiFe_xCr_{2-x}O_4$: (a) reference spectra; (b) Raman peak positions [7].

Hosterman [7] has studied the $NiFe_xCr_{2-x}O_4$ in his thesis, the reference spectra and the peak positions are exhibited in Fig.B.7 (a) & (b). It is a continuous transition from $NiCr_2O_4$ to $NiFe_2O_4$, a normal spinel oxide to an inverse one. The cation inversion, between the octahedral and tetrahedral sites, occurs at $0 \leqslant x \leqslant 1$. At the initial substitution of iron, Ni^{2+} cations occupy the octahedral sites while Fe^{3+} cations take the tetrahedral sites. Afterwards, when $x \geqslant 1$, all tetrahedral sites are filled with Fe^{3+} cations, thus they have to take over the octahedral ones from the Cr^{3+} cations [25].

Furthermore, the results show that:

- **$\mathbf{A}_{1g}$:** With the increase of Fe content in the lattice, the wavenumbers increase, especially in the range $0 \leqslant x \leqslant 1$. Actually, the wavenumber is $\leqslant 690$ cm^{-1} for a x above 0.1. The shoulder is developed with only a little iron substituted into the system, though the wavenumber and the intensity are indifferent with the Fe content.
- **$\mathbf{F}_{2g}(3)$:** It can only be detected when $x \geqslant 0.9$. With the introduction of Fe in the lattice, the wavenumber decreases together with a shoulder develops.
- **$\mathbf{F}_{2g}(2)$:** The wavenumber decreases linearly over the entire iron content range, a lower-frequency shoulder is detected for a $x \geqslant 0.7$.
- **$\mathbf{E}_g$:** It decreases a lot with the increase of Fe content in the system. There is an important drop of the wavenumber at $x = 0.5$, from $\gtrapprox 420$ cm^{-1} to $\lessapprox 360$ cm^{-1}, and the intensity decreases all alone.
- **$\mathbf{F}_{2g}(1)$:** It develops a shoulder on the high-wavenumber side of this mode, and the intensity decreases with the substitution of Fe.

Briefly, without considering the shoulder, the oxide has a $x > 0.9$ at least for the appearance of the $F_{2g}(3)$ mode (p3 in the spectra of LE11-02 ref (72hr, 133_smbar)). However, the development of shoulders for most modes are inevitable for a Fe substitution in the system.

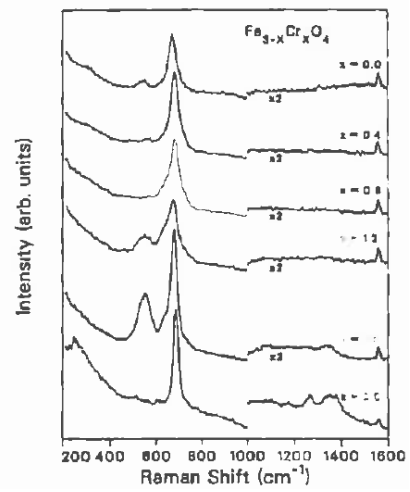

Figure B.8: Reference spectra of spinel oxide $Fe_{3-x}Cr_xO_4$, with x = 0.0, 0.4, 0.8, 1.2, 1.6 and 2.0, using a 514.5 nm laser [13].

$Fe_{3-x}Cr_xO_4$	Raman Bands (cm^{-1})				
Fe_3O_4	542		671		
$Fe_{2.6}Cr_{0.4}O_4$	562		682		
$Fe_{2.2}Cr_{0.8}O_4$			681		
$Fe_{1.8}Cr_{1.2}O_4$	548	636*sh*	674		
$Fe_{1.4}Cr_{1.6}O_4$	550	636*sh*	679		1335
$FeCr_2O_4$			686	1265	1357

Table B.2: Raman wavenumbers (cm^{-1}) of spinel oxide, $Fe_{3-x}Cr_xO_4$, with x = 0.0, 0.4, 0.8, 1.2, 1.6 and 2.0, *sh* = shoulder [13].

On the other hand, McCarty *et al.* [13] have done the Raman study of $Fe_{3-x}Cr_xO_4$ (Fig.B.8), and the wavenumbers for each oxide with different x values are indicated in Tab.B.2. As a matter of fact, $Fe_{3-x}Cr_xO_4$ is often proposed in literature for the inner oxide film formed on the 316L stainless steel under primary PWR conditions.

The transition between $FeCr_2O_4$ and Fe_3O_4 is another process for a normal spinel oxide to become an inverse one. The cation inversion occurs in the iron content range $1.7 \leqslant x \leqslant 2.4$, when Fe^{3+} cations take over the tetrahedral sits and push the Fe^{2+} ones to the octahedral sites. Below this range, Fe^{3+} cations only replaces Cr^{3+} at the octahedral sites.

According to McCarty *et al.* [13], with the introduction of more Cr, from $Fe_{1.4}Cr_{1.6}O_4$ to $FeCr_2O_4$, a weak and broad feature appears at ~ 1335 and ~ 1357 cm^{-1}, respectively. It is the only corresponding band for p5 (about 1351 cm^{-1}) we observed on the spectra of LE11-02 ref. In addition, the A_{1g} mode does not vary a lot among all the range. Meanwhile the $F_{2g}(3)$ mode, around $530 \sim 550$ cm^{-1}, was not consistently detected over all the range, it may be reduced until not discernible by the substitution of Cr for Fe in the structure. Depending on the proportion of Cr and Fe, it may reappear as indicated in the Tab.B.2. Therefore, a $x \gtrapprox 1.4$ may be preferred based on the presence of the broad feature around ~ 1350 cm^{-1}.

B.7 Summary

In conclusion, the Raman spectroscopy results elucidate that the oxide film formed on 316L stainless steel under primary PWR conditions is a mixed spinel oxide with a co-existence of $NiFe_xCr_{2-x}O_4$ with a $x > 0.9$, and $Fe_{3-x}Cr_xO_4$ with a $x \gtrapprox 1.4$. More probably, $NiFe_xCr_{2-x}O_4$ for the green/ grey feature while $Fe_{3-x}Cr_xO_4$ for the dark red one, and the precipitates are close to a $NiFe_xCr_{2-x}O_4$.

References

[1] Soulas R., Cheynet M., Rauch E., Neisius T., Legras L., Domain C., Brechet Y. TEM investigations of the oxide layers formed on a 316L alloy in simulated PWR environment. *J Mater Sci*, 48:2861–2871, 2013.

[2] D.H. Lister and R.D. Davidson and E. McAlpine. The mechanism and kinetics of corrosion product release from stainless steel in lithiated high temperature water. *Corrosion Science*, 27(2):113 – 140, 1987.

[3] S.E. Ziemniak and M. Hanson. Corrosion behavior of 304 stainless steel in high temperature, hydrogenated water. *Corrosion Science*, 44(10):2209 – 2230, 2002.

[4] Da Cunha Belo M. and Walls M. and Hakiki N. E. and Corset J. and Picquenard E. and Sagon G. and Noël D. Composition, structure and properties of the oxide films formed on the stainless steel 316L in a primary type PWR environment. *Corrosion Science*, 40(2–3):447 – 463, 1998.

[5] Kim Y. J. Characterisation of the Oxide Film Formed on Type 316 Stainless Steel in 288°C Water in Cyclic Normal and Hydrogen Water Chemistries. *CORROSION*, 51(11):849–860, 1995.

[6] Féron D., Herms E., Tanguy B. Behavior of stainless steel in pressurized water reactor prirmary circuits. *Journal of Nuclear Materials*, 427:364–377, 2012.

[7] Hosterman Brain D. *Raman Spectroscopic Study of Solid Solution Spinel Oxides*. PhD thesis, University of Nevada, Las Vegas, 2011.

[8] Dunitz J. D., Orgel L. E. Electronic properties of transition-metal oxides - II cations distribution amongst octahedral and tetrahedral sites. *Journal of Physics and Chemistry*, 3:318–323, 1957.

[9] Lazarevic Z. Z., Jovalekic C., Milutinovic A., Romcevic M. J., Romcevic N. Z. Preparation and Characterization of Nano Ferrites. *ACTA PHYSICA POLONICA A*, 121(No. 3):682–686, 2012.

[10] Perron H., Mellier T., Domain C., Roques J., Simon E., Drot R., Catalette H. Structural investigation and electronic properties of the nickel ferrite $NiFe_2O_4$: a periodic density functional theory approach. *Journal of Physics: Condensed Matter*, 19:346219, 2007.

[11] Singhal S., Chandra K. Cation distribution and magnetic properties in chromium-substituted nickel ferrets prepared using aerosol route. *Journal of Solid State Chemistry*, 180:296–300, 2007.

[12] Jacob J., Khadar M. A. Investigation of mixed spinel structure of nanostructured nickel ferrite. *J. Appl. Phys.*, 107:114310(1–10), 2010.

[13] McCarty K. F., Boehme D. R. A Raman Study of the Systems $Fe_{3-x}Cr_xO_4$ and $Fe_{2-x}Cr_xO_3$. *Journal of Solid State Chemistry*, 79:19–27, 1989.

[14] Wang Z. W., Saxena S. K., Lazor P., O'Neil H. S. C. An in situ Raman Spectroscopy study of the pressure induced dissociation of spinel $NiCr_2O_4$. *Journal of Physics and Chemistry of Solids*, 64:425–431, 2003.

[15] Wang Z. W., Lazor P., Saxena S. K., and Artioli G. High pressure Raman Spectroscopic study of spinel $ZnCr_2O_4$. *Journal of Solid State Chemistry*.

[16] Kant C. *et al.* Optical phonons, spin correlations, and spin-phonon coupling in the frustrated pyrochlore magnets $CdCr_2O_4$ and $ZnCr_2O_4$. *Physical Review B*, 80:214417, 2009.

[17] Wang Z. W., Schiferl D., Zhao Y. S., O'Neil H. S. C. High pressure Raman Spectroscopic of spinel-type $ZnFe_2O_4$. *Journal of Solid State Chemistry*, 64:2517–2523, 2003.

[18] Shebanova O. N., Lazor P. Raman study of magnetite (Fe_3O_4): laser-induced thermal effects and oxidation. *Journal of Raman Spectroscopy*, 34:845–852, 2003.

[19] Shebanova O. N., Lazor P. Raman spectroscopy study of magnetite ($FeFe_2O_4$): A new assignment for the vibration spectrum. *Journal of Solid State Chemistry*, 174:424–430, 2003.

[20] De Faria D. L. A., Venancio Silva S., De Oliveria M. T. Raman Microspectroscopy of Some Iron Oxides and Oxyhydroxides. *Journal of Raman Spectroscopy*, 28:873–878, 1997.

[21] Kim H. J., Hwang I. S. Development of an in situ Raman spectroscopic system for system for surface oxide films on metals and alloys in high temperature water. *Nuclear Engineering and Design*, 235:1029–1040, 2005.

[22] Graves P. R., Johnston C., Campaniello J. J. Raman scattering in spinel structured ferrites. *Materials Research Bulletin*, 23:1651–1660, 1988.

[23] Mougin J., Le Bihan T., Lucazeau G. High-pressure study of Cr_2O_3 obtained by high-temperature oxidation by x-ray diffraction and Raman spectroscopy. *Journal of Physics and Chemistry of Solids*, 62:553–563, 2001.

[24] Sousa M. H., Tourinho F. A., Rubim J. C. Use of Raman micro-spectroscopy in the characterisation of $M^{II}Fe_2O_4$ (M = Fe, Zn) electric double layer ferrofluids. *Journal of Raman Spectroscopy*, 31:185–191, 2000.

[25] Rais A., Gismelseed A. M., Al-Omari I. A. Cation distribution and magnetic properties of nickel-chromium ferrets $NiCr_xFe_{2-x}O_4$ ($0 \leqslant x \leqslant 1.4$). *Physica Status Solidi B*, 242(7):1497–1503, 2005.

Appendix C

Conversion of Hydrogen

This appendix gives a conversion of hydrogen between pressure and concentration.

C.1 Conversion Table between P(H_2) and [H_2] at 300°C

The hydrogen is measured and expressed in pressure in the study. In order to make the comparison clearer, a conversion table based on the calculation of the Henry's law is indicated below, Tab.C.1.

$P(H_2)_{300°C}$ (mbar)	$[H_2]$ (cc/kg) (STP)
29	3
32	3.3
33	3.4
53	5.5
133	13.7
166	17.1
187	19.3
190	19.6
390	40.2

Table C.1: Conversion of hydrogen pressure P(H_2) (mbar) with the concentration (cc/kg) (STP) at 300°C.

C.2 Calculation of P(H_2) Ration versus Temperature

In order to calculate the P(H_2) in function of temperature theoretically, understand the phenomenon observed, it needs to take into account two factors:

- **Henry's law**, the solubility of H_2 in the PWR water is directly proportional to the P(H_2) at a constant temperature. However, the Henry's law constant (k_H) depends on the temperature. In general, the solubility of H_2 increase with temperature. The more it dissolves in the PWR water, less pressure of H_2 gas can be detected by the sensor.

- **Ideal gas law**, the P(H_2) is inversely proportional to the volume of H_2 gas. With the increase of temperature, the volume of PWR water dilates (because of thermal expansion), and the volume of H_2 gas is decreased subsequently. Therefore, P(H_2) is going to be increased under the circumstance.

One version of Henry's law is written in Eq.C.1, where c is the concentration of the solute, p is the partial pressure of the solute in the gas above the solution and k_H is a constant with the dimension of concentration divided by pressure. The equation can also be written inversely with an inverse k_H. The k_H, known as the Henry's law constant, depends on the solute, the solvent and the temperature.

$$c = k_H(T) \times p \tag{C.1}$$

Based on the NIST data base [1], the Henry's law constant can be calculated by Eq.C.2, where k_H° the Henry's law constant for solubility in water at 298.15K and $d(\ln(k_H))/d(\frac{1}{T})$ the temperature dependence. According to the most recent reference [2], k_H° equals to 0.00078 mol.kg^{-1}*bar and $d(\ln(k_H))/d(\frac{1}{T})$ is 500 K.

$$k_H(T) = k_H^\circ exp\left((d(ln(k_H))/d(\frac{1}{T})\right)\left(\frac{1}{T} - \frac{1}{298.15K}\right) \tag{C.2}$$

According to this equation, it is enabled to calculate the Henry's law constant at a specific temperature, and thus the solubility of H_2 can also be reckoned.

On the other hand, the ideal gas law is written in Eq.C.3, where P is the pressure, V is the volume, n is the amount of substance of the gas (in moles), R is the gas constant, T is the absolute temperature.

$$PV = nRT \tag{C.3}$$

The conservation of H_2 amount can be expressed in Eq.C.4, the amount of H_2 at T_1 should equals to the one at T_2. It needs to combine Henry's law and Ideal gas law to obtain the total amount of H_2: the H_2 gas (in mole) and the H_2 dissolved (in mole).

$$[P_{T_1} \times \frac{V_g(T_1)}{R \times T_1}] + [\frac{P_{T_1}}{k_H(T_1)^{-1}} \times \frac{V_l(T_1) \times d_{T_1}}{0.018}] = [P_{T_2} \times \frac{(V_g(T_2)}{R \times T_2}] + [\frac{P_{T_2}}{k_H(T_2)^{-1}} \times \frac{V_l(T_2) \times d_{T_2}}{0.018}] \tag{C.4}$$

In Eq.C.4: P is the pressure (Pa), V_g (m^3) is the volume of gas, R is the gas constant (8.314 m^3.Pa.K^{-1}.mol^{-1}), T_1 and T_2 are the absolute temperature (K), k_H^{-1} is the inverse Henry's law constant, V_l is the volume of PWR water (m^3), d is the density of water (m^{3}kg^{-1}) and $\frac{1}{0.018}$ mol H_2O equals to 1 kg H_2O. Other than the gas constant R, all the factors are temperature related, which means the values is depending on the temperature.

On supposing that the amount of the H_2 (in mole) at $\sim$ 200°C is the datum, it enables us to calculate on the P(H_2) theoretically at the temperatures which we performed our experiments. Therefore, it can give us the base line, more precisely, the theoretically data for the P(H_2) evolution with temperature in the HTHP cell, as illustrated in Fig.C.1. It includes:

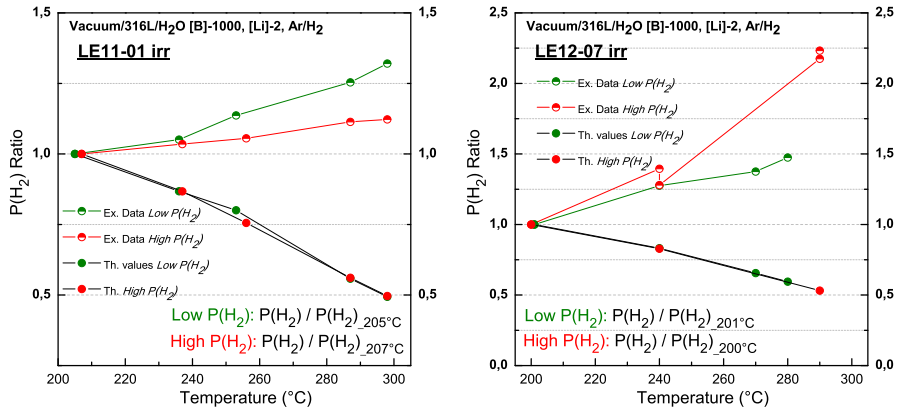

(a) Proton (b) Electron

Figure C.1: Hydrogen Pressure Ratio versus temperature: (a) LE11-01 irr, proton irradiation, $P(H_2)/P(H_2)_{205°C}$ for low $P(H_2)$ and $P(H_2)/P(H_2)_{207°C}$ for High $P(H_2)$; (b) LE12-07 irr, electron irradiation, $P(H_2)/P(H_2)_{201°C}$ for low $P(H_2)$ and $P(H_2)/P(H_2)_{200°C}$ for High $P(H_2)$.

1. *experimental data (Ex. data)*, calculated based on the experimental measurement;

2. *theoretically data (Th. data)*, calculated based on Henry's law and ideal gas law.

Therefore, further interpretation can be dragged out based on these calculations in Chapter 6.

References

[1] NIST. NIST Chemistry WebBook, Programme de Données de Référence Standard, http://webbook.nist.gov/cgi.

[2] Lide D. R. and Frederikse H. P. R. *CRC Handbook of Chemistry and Physics, 76th Edition.* CRC Press, Inc., Boca Raton, FL., 1995.

Appendix D

Techniques Details

This Appendix describes the details for each analytical technique used in this study.

D.1 Techniques for Characterisation of the Oxide films

D.1.A SEM - Scanning Electron Microscope

SEM, *Scanning Electron Microscope*, is the most commonly used electron microscope for the characterisation of surface morphology. It clearly visualises the outer layer of the oxide film, by showing their geometry and crystalline form. Along with the analysis of **EDX**, *Energy-Dispersive X-ray Spectroscopy*, an identification of chemical elements of the specimen can also be achieved. It relies on the investigation of an interaction of some source of X-ray excitation and a sample. It is normally equipped with the SEM microscope.

The SEM used in this study, is a Carl Zeiss Ultra 55 microscope, equipped with a **FEG**, *Field Emission Gun*. optimised for high resolution distortion free images of surface. It is designed to maximise imaging resolution at low beam energies. The In-Lens **SE**, *Secondary Electron*, detector situated inside the column can give a high contrast imaging of extreme surfaces. Therefore, the SEM micrographs shown below were taken with a relative low energy 2 kV, or 5 kV in order to get images with a better resolution of the outer layer.

D.1.B XPS - X-ray Photoelectron Spectroscopy

XPS, *X-ray Photoelectron Spectroscopy*, is a basic techniques for determining chemical composition of an oxide films formed on metal surface. It provides a reasonable quantification and chemically specific information for each element detected, through the chemical shift. It is a highly surface-sensitive technique. Therefore, all the informations obtained are only valid for a depth less than 10 nm. If the precipitates are small enough compared to the analysed surface, the results may conclude both layers, the inner and the outer. Otherwise, it will be the outer iron oxide mainly being analysed.

Briefly, by running the XPS analysis, we may have access to the following information:

- identification of the chemical elements on the analysed surface;
- chemical state determination of each element detected;

- relative quantification all the elements detected.

The identification and determination of chemical state for different elements can be done through their binding energy, according the binding energy database either form NIST Database [1] or the Phi Handbook [2]. However, the complexity of the spectra for Fe 2p, Cr 2p and Ni 2p, such as peak asymmetries, multiplet splitting, shake-up structure and overlapping binding energy, cause a large contribution for the determination of their chemical states [3]. Therefore, combining the spectra of the three different elements may help us to interpret the composition of the oxide in one way. In addition, studying the spectrum of O 1s may also provide a clue about the oxide type.

The quantification results are base on the area of the peaks. The different peak assignments is for the determination of the chemical states. They can barely influence each other. Thus, we may treat the qualification and quantification interpretations separately, in order to get a better understanding on the oxide film.

The XPS analyses were carried out with a Thermofisher ESCALAB 250xi spectrometer using a monochromatic Al Kα source (15mA, 14kV) X-ray source. The instrument work function was calibrated to give an Au $4f_{7/2}$ metallic gold binding energy of 84 eV. The spectrometer dispersion was adjusted to give a binding energy of 932.6 eV for metallic Cu $2p_{3/2}$.

D.1.C Raman Spectroscopy

Raman spectroscopy is used to analyse the crystal structure of the oxide film. The one used for the analysis is a Labram HR800 Raman spectroscopy (HORIBA Jobin Yvon), equipped with a Olympus microscope and a CCD detector, at the LISL laboratory, CEA Saclay. All the spectra were obtained by using a 532 nm laser.

D.1.D NRA Analysis

NRA, *Nuclear Reaction Analysis*, provides a way to estimate the oxygen atoms of the whole oxide layer, including the outer and the inner. A basic mechanism of nuclear reactions involves the formation of a compound nucleus in a highly excited state which disintegrated or decays through γ-ray emission within very short times. The nuclear reaction used for the analysis is $^{16}O(d, p)^{17}O$ with an incident energy of 900 keV, in which the cross section is relatively constant. Actually, the inner oxide layer is protective, and thus its evolution is important. Though, the existence of the precipitates, as the outer layer on the surface makes the analysis become complicated. However, it can gives a general idea on the homogeneousness of the oxide film.

All the NRA (Nuclear Reaction Analysis) analyses have been performed at the JANUUS laboratory, CEA Saclay. The analyses were performed with a 900 keV deuteron beams and the type of detector is Si-100μ. A simplified scheme is describes in Fig.D.1. The calibrations was done with two samples of Ta_2O_5 with an oxide thickness of 168 nm and 611 nm. The spot of the deuteron beam is nearly 1 mm^2.

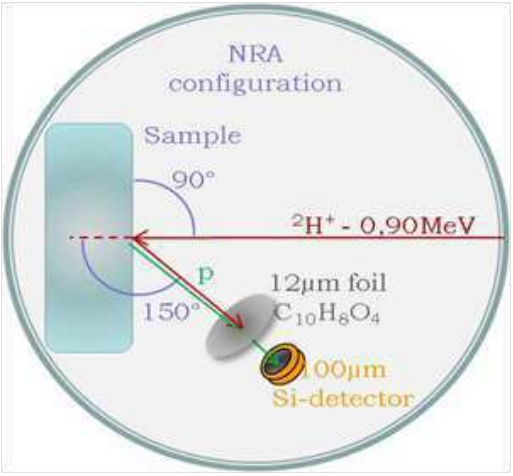

Figure D.1: Scheme of NRA analysis indicated with the beam conditions.

D.1.E TEM Analysis

TEM, *Transmission Electron Microscopy*, is a powerful technique for studying the whole oxide film, which gives information on the morphology, the composition, the crystal structure of the oxide film and even the defects in the oxide. However, it is a localised analysis for an area of about $10\mu m^2$.

The TEM investigation have been carried out on a Tecnai F20-ST field emission gun microscope, equipped with an Energy Dispersive X-ray (EDX) device, Gatan Imaging Filter (GIF) with Scanning Transmission Electron Microscopy (STEM) capabilities. STEM has been combined with High-Angle annular Dark-Field (HAADF) technique to produce chemical contrast images formed using electrons diffracted at high angle (> 40 mrad) and whose intensity is proportional to the Z atomic number of elements composing the sample. The spatial resolution of the images depends on the probe size, is about 1 nm. The EDX analysis has been performed using line-scan mode to investigate local chemical composition variation over oxide layer. Selected area electron diffraction (SAD or SAED) is used for studying the crystallographic details of the oxide layer. The High-Resolution Transmission Electron Microscopy (HRTEM) images are obtained on CCD camera and analysed using Fast Fourier Transform (FFT) techniques to investigate crystallographic details of specific location of oxide layer.

The specimen was prepared for cross-sectional characterisation. The analysis were performed in Mines Paris (Centre des Matériaux P.M. Fort). The preparation method is close to the one described elsewhere [4]. Worth noting that the TEM is a projection of the specimen volume, and involves the superposition of micro structural characteristics in the project image. However, the analysed area are thin enough to neglect this effect.

D.1.F GD-OES Analysis

GD-OES, *Glow Discharge Optical Emission Spectrometry*, is an analytical technique used for isotope ratio measurements and trace elements determination in solid samples. It provides a method to analyse elements in depth profiling of oxide films.

The GD-OES used for the analysis, is a GD-Profiler HR^{TM} (HORIBA Jobin Yvon), at the laboratory LISL, CEA Saclay. The surface of the analysis spot is about 4 mm^2 and the depth profiling

trace can go to tens of μm deep. The accuracy for elemental analysis is around 5%.

D.1.G CS-AFM Analysis

CS-AFM, *Current Sensing Atomic Force Microscopy*, can be used to study the topography and the local electronic properties of the oxide film. The analysis was carried out at the laboratory SPCSI, CEA Saclay. The current measurement range is from 1 pA to 10 mA and the resistance measurement range is from 10^3 GΩ to 10^{12} GΩ.

D.2 Techniques for Solution Analysis

D.2.A ICP-AES Analysis

ICP-AES, *Inductively Coupled Plasma Atomic Emission Spectroscopy*, is an analytical technique used for the detection of trace metals. In our case, it is for analysing the release of cations in the PWR water after irradiation.

The ICP-AES used for the analysis, is a Perkin-Elmer Optima 2000 DV, at the laboratory LISL, CEA Saclay. It uses a specific calibration method SPEX QC 21 Lot N° 41-26AS for the analysis. The incertitude of the measurement is about $\pm$3% relatively.

D.2.B pH meter

The H_3O^+ is calculated based on the pH value measured by Metrohm® 744 pH meter.

D.2.C UV Spectrophotometry

UV spectrophotometry, *Ultraviolet-Visible spetrophotometry*, is routinely used in analytical chemistry for quantitative determination of different analyses. In the study, H_2O_2 is analysed through the Ghormley method by using a UV spectrophotometry. The one used for the analysis, is a Agilent/ Varian Cary 50 UV-Vis spectrophotometer, at the laboratory LECNA, CEA Saclay.

D.2.D Ion Chromatography

Ion Chromatography, is used for water chemistry analysis. It is able to measure concentration of major anions as well as major cations in the ppb range. It is used to detect the concentration of anions in the PWR water after irradiation.

References

[1] NIST. NIST X-ray Photoelectron Spectroscopy Database, http://srdata.nist.gov/xps.

[2] Sobol P. E. Bomben K. D. Moulder J. F., Stickle W. F. *Handbook of X-ray Photoelectron Spectroscopy*. Perkin-Elmer Corp, Eden Prairie, MN, 1992.

[3] Biesinger M. C., Payne B.P., Grosvenor A. P., Lau L. W. M., Gerson A. R., Smart R. St. C. Resolving surface chemical states in XPS analysis of first row transition metals, oxides and hydroxides: Cr, Mn, Fe, Co and Ni. *Applied Surface Science*, 257:2717–2730, 2011.

[4] Sennour M., Marchetti L., Martin F., Perrin S., Molins R. Pijolat M. A detailed TEM and SEM study of Ni-base alloys oxide scales formed in primary conditions of pressurised water reactor. *Journal of Nuclear Materials*, 402:147–156, 2010.

Appendix E

Impedance Measurements

This appendix gives preliminary results of impedance measurement of 316L stainless steel in PWR water under proton irradiation. The interpretation is still ongoing, not completed yet.

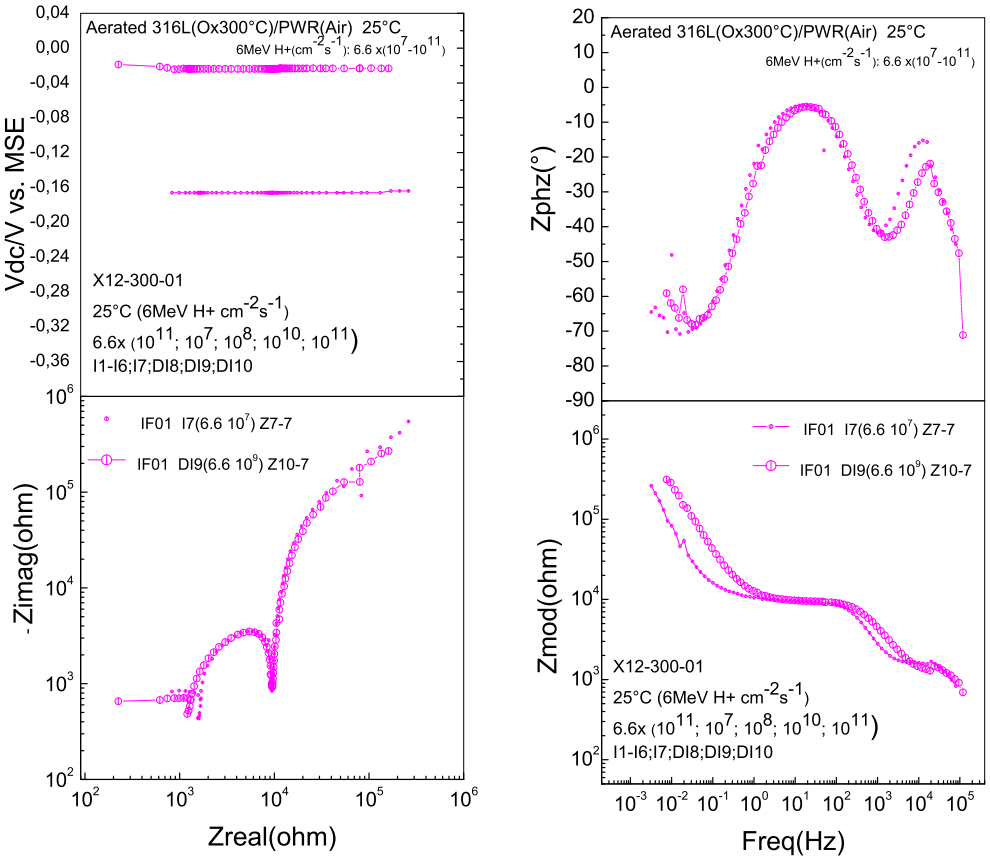

(a) (b)

Figure E.1: Impedance measurement of X12-300-01 in an aerated environment under 6 MeV proton flux: (a) free exchange potential versus MSE (*on the top*) and Z_{imag} in function of Z_{real} in log scale plot (*at the bottom*); (b) bode plot for the impedance phase (*on the top*) and module (*at the bottom*).

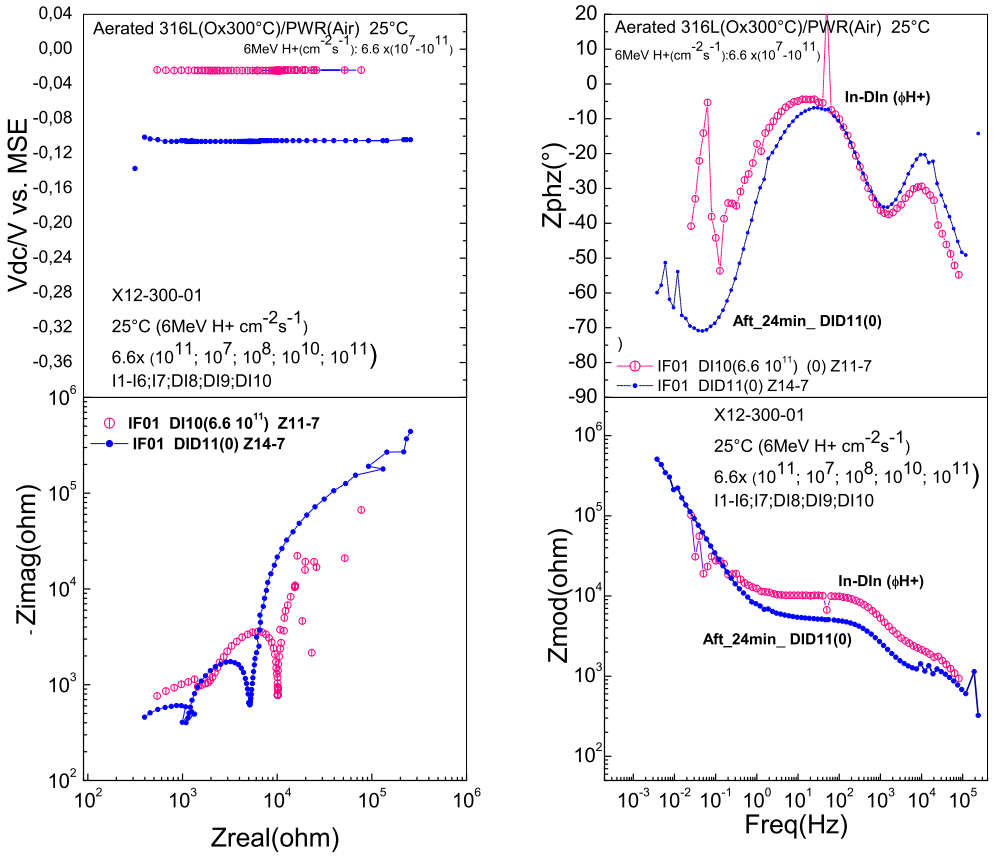

(a) (b)

Figure E.2: Impedance measurement of X12-300-01 in an aerated environment under and 24 min after 6 MeV proton flux: (a) free exchange potential versus MSE (*on the top*) and Z_{imag} in function of Z_{real} in log scale plot (*at the bottom*); (b) bode plot for the impedance phase (*on the top*) and module (*at the bottom*).

Appendix F

Solution Analysis Results

This appendix provides the original data of the solution analysis results.

Solution N°	Fe	Cr (μg/L)	Ni	pH
SX10-01	6±1	< 1	< 2	
SX10-02	5±1	< 1	< 2	
SX10-03	215±1	25±1	18±1	
SX10-04	< 1	6±1	< 2	
SX10-06 n°1	< 3	< 3	< 3	6.41
SX10-06 n°2	170	32	8±1	4.96
SX10-07	< 1	< 0.3	< 2	6.34
SX10-08	< 1	< 0.3	< 2	6.25
SX10-09	< 1	< 0.3	< 2	6.45

Table F.1: Analysis of irradiated PWR waters: X10-01 (1 solution), X10-02 (1 solution), X10-03 (1 solution), X10-04 (1 solution), X10-06 (2 solutions), X10-07 (1 solution), X10-08 (1 solution), X10-09 (1 solution). - : analysis impossible (lack of solution); **S:** solution (PWR water); n°: is the order for several solutions come form the same metal (316L) interface.

Solution N°	Fe	Cr (μg/L)	Ni	$[H_2O_2]$ (mol/L)	pH
SX10-05 n°1	43	28	15±1	3.86×10^{-5}	6.56
SX10-05 n°2	25	16	< 2	3.40×10^{-5}	7.62
SX10-05 n°3	25	13	< 2		5.85
SX10-05 n°4	65	20	< 2	2.42×10^{-5}	5.5
SX10-05 n°5	75	20	< 2		4.84
SX10-05 n°6	< 1	< 0.3	< 2		4.78

Table F.2: Analysis of irradiated PWR waters: X10-05 (6 solutions), **S:** solution (PWR water); n°: is the order for several solutions come form the same metal (316L) interface.

Solution N°	Fe	Cr (μg/L)	Ni	$[H_2O_2]$ (mol/L)	pH
SX10-10 n°1	2	0.3	< 2	3.14×10^{-5}	6.3
SX10-10 n°2	15	6.4	< 2	1.1×10^{-4}	6.15
SX10-10 n°3	48	13	< 2	8.67×10^{-5}	5.88
SX10-10 n°4	45	13	< 2	1.99×10^{-5}	5.65
SX10-10 n°5	38	14	< 2		5.34
SX10-10 n°6	30	16	< 2		5.4
SX10-10 n°7	58	20	< 2		5.29
SX10-10 n°8	86	25	< 2		5.03
SX10-10 n°9	375	87	35		3.42

Table F.3: Analysis of irradiated PWR waters: X10-10 (9 solutions), **S:** solution (PWR water); n°: is the order for several solutions come form the same metal (316L) interface.

Solution N°	Fe	Cr (μg/L)	Ni	pH
SX10-11 n°1	11	< 0.3	< 2	6.55
SX10-11 n°2	180	0.5	13	4.35
SX10-11 n°3	103	22	10 ± 1	5.15

Table F.4: Analysis of irradiated PWR waters: X10-11 (3 solutions), **S:** solution (PWR water); n°: is the order for several solutions come form the same metal (316L) interface.

Solution N°	Fe	Cr (μg/L)	Ni	$[H_2O_2]$ (mol/L)	pH
SX10-12 n°1	< 1	< 0.3	< 2	2.48×10^{-5}	6.39
SX10-12 n°2	< 1	< 0.3	< 2	6.86×10^{-5}	6.16
SX10-12 n°3	2.5	< 0.3	< 2	1.51×10^{-4}	6.02
SX10-12 n°4	58	11	< 2	1.24×10^{-5}	6.06
SX10-12 n°5	150	30	5 ± 1		3.91
SX10-12 n°6	750	160	80		3.25
SX10-12 n°7	80	21	< 2		4.82
SX10-12 n°8	130	40	33		4.48

Table F.5: Analysis of irradiated PWR waters: X10-12 (8 solutions), **S:** solution (PWR water); n°: is the order for several solutions come form the same metal (316L) interface.

Solution N°	Fe	Cr (μg/L)	Ni	$[H_2O_2]$ (mol/L)	pH
SX11-01 n°1	< 1	< 1	< 2	1.30×10^{-5}	5.76
SX11-01 n°2	23	< 1	< 2	3.94×10^{-5}	5.45
SX11-01 n°3	45	< 1	< 2	4.56×10^{-6}	4.92
SX11-01 n°4	120	7	< 2	5.09×10^{-6}	3.69
SX11-01 n°5	220	30	< 2	3.73×10^{-7}	3.4

Table F.6: Analysis of irradiated PWR waters: X11-01 (5 solutions), **S:** solution (PWR water); n°: is the order for several solutions come form the same metal (316L) interface.

Solution N°	Fe	Cr	Ni	Zn	pH
		(μg/L)			
SX11-05 n°1	< 1	< 0.7	< 3	46	
SX11-05 n°2	52	14	< 3	2	
SX11-05 n°3	1	14	< 3	12	
SX11-05 n°4	13	16	11	15	
SX11-05 n°5	37	25	14	13	
SX11-05 n°6	17	7.1	< 3	2	
SX11-05 n°7	160	64	39	8	

Table F.7: Analysis of irradiated PWR waters: X11-05 (7 solutions), **S:** solution (PWR water); n°: is the order for several solutions come form the same metal (316L) interface.

Solution N°	Fe	Cr	Ni	Zn	$[H_2O_2]$	pH
		(μg/L)			(mol/L)	
SX11-10 n°1	< 2	< 1.4	15	160		6.24
SX11-10 n°2	22	< 1.4	17	76	2.14×10^{-4}	5.9
SX11-10 n°3	16	5	17	32	1.45×10^{-4}	5.8
SX11-10 n°4	61	11	20	37	2.20×10^{-4}	4.54
SX11-10 n°5	179	37	41	22	3.39×10^{-4}	3.75

Table F.8: Analysis of irradiated PWR waters: X11-10 (5 solutions), **S:** solution (PWR water); n°: is the order for several solutions come form the same metal (316L) interface.

Solution N°	Fe	Cr	Ni	Zn	$[H_2O_2]$	pH
		(μg/L)			(mol/L)	
SX11-11 n°1	7	< 1.4	18	163	1.81×10^{-4}	6.28
SX11-11 n°2	15	3	21	60	2.82×10^{-4}	6
SX11-11 n°3	29	8	80	27	3.18×10^{-4}	5.65
SX11-11 n°4	43	12	36	22	2.65×10^{-4}	5.5
SX11-11 n°5	100	18	63	15	3.16×10^{-4}	4.25

Table F.9: Analysis of irradiated PWR waters: X11-11 (5 solutions), **S:** solution (PWR water); n°: is the order for several solutions come form the same metal (316L) interface.

Solution N°	Fe	Cr	Ni	Zn	$[H_2O_2]$	pH
		(μg/L)			(mol/L)	
SX11-12 n°1	22	5.7	33	160		6.24
SX11-12 n°2	80	20	31	33	2.47×10^{-4}	5.76
SX11-12 n°3	275	53	48	17	3.13×10^{-4}	3.54
SX11-12 n°4	123	35	103	12	6.22×10^{-5}	3.9

Table F.10: Analysis of irradiated PWR waters: X11-12 (4 solutions), **S:** solution (PWR water); n°: is the order for several solutions come form the same metal (316L) interface.

Solution N°	Fe	Cr	Ni	Zn	$[H_2O_2]$	pH
		(μg/L)			(mol/L)	
SX12-300-01 n°1	11	4	8	98		5.98
SX12-300-01 n°2	33	5	35	32		5.33
SX12-300-01 n°3	35	4	8	21	1.20×10^{-4}	4.16
SX12-300-01 n°4	48	4	12	13	2.14×10^{-4}	3.85
SX12-300-01 n°5	108	9	13	21	4.92×10^{-5}	3.47

Table F.11: Analysis of irradiated PWR waters: X12-300-01 (5 solutions), **S:** solution (PWR water); n°: is the order for several solutions come form the same metal (316L) interface.

Solution N°	Fe	Cr	Ni	Zn	$[H_2O_2]$	pH
		(μg/L)			(mol/L)	
SX12-300-05 n°1	13	10	5	265		6.29
SX12-300-05 n°2	567	525	520	2	9.29×10^{-6}	3.45
SX12-300-05 n°3	40	4	2	15	7.78×10^{-5}	3.32
SX12-300-05 n°4	2	4	2	2	7.99×10^{-5}	3.25
SX12-300-05 n°5	10	4	2	2	4.29×10^{-4}	3.14

Table F.12: Analysis of irradiated demineralised waters: X12-300-05 (5 solutions), **S:** solution (PWR water); n°: is the order for several solutions come form the same metal (316L) interface.

Solution N°	Fe	Cr	Ni	Zn	$[H_2O_2]$	pH
		(μg/L)			(mol/L)	
SX12-300-06 n°1	2	4	2	660	6.58×10^{-5}	5.95
SX12-300-06 n°2	2	4	20	1830		4.18
SX12-300-06 n°3	150	20	50	1860		3.51
SX12-300-06 n°4	2	9	20	600		3.43
SX12-300-06 n°5	290	65	70	330		3.22

Table F.13: Analysis of irradiated PWR waters: X12-300-06 (5 solutions), **S:** solution (PWR water); n°: is the order for several solutions come form the same metal (316L) interface.

Solution N°	Fe	Cr	Ni	Zn	$[H_2O_2]$	pH
		(μg/L)			(mol/L)	
SX12-300-08 n°1	2	4	2	189		5.7
SX12-300-08 n°2	2	4	10	20	2.00×10^{-4}	3.44
SX12-300-08 n°3	15	23	34	124	7.31×10^{-7}	3.47
SX12-300-08 n°4	111	42	50	50	4.03×10^{-4}	3.31
SX12-300-08 n°5	2	4	10	35	3.81×10^{-4}	3.31

Table F.14: Analysis of irradiated PWR waters: X12-300-08 (5 solutions), **S:** solution (PWR water); n°: is the order for several solutions come form the same metal (316L) interface.

Solution N°	Fe	Cr	Ni	Zn	pH
	(μg/L)				
SX12-01 n°1	< 2	< 4	< 2	70	6.14
SX12-01 n°2	< 2	< 4	< 2	< 2	6.01
SX12-01 n°3	< 2	< 4	< 2	< 2	5.98
SX12-01 n°4	< 2	< 4	< 2	< 2	5.97
SX12-01 n°5	< 2	< 4	< 2	< 2	5.92
SX12-300-09 n°1	< 2	< 4	< 2	260	6.03
SX12-300-09 n°2	< 2	< 4	< 2	< 2	5.99
SX12-300-09 n°3	< 2	< 4	< 2	< 2	5.97
SX12-300-09 n°4	< 2	< 4	< 2	< 2	5.94
SX12-300-09 n°5	< 2	< 4	< 2	< 2	5.91

Table F.15: *Blank test*: analysis of PWR waters without irradiation (experiments with Teflon® cell): X12-01 (5 solutions), X12-300-09 (5 solutions), **S:** solution (PWR water); n°: is the order for several solutions come form the same metal (316L) interface.

Solution N°	Fe	Cr	Ni	Zn
	(μg/L)			
S - Ox25°C n°1	< 2	< 4	< 2	< 2
S - Ox25°C n°2	< 2	< 4	< 2	< 2
S - Ox25°C n°3	< 2	< 4	< 2	< 2
S - Ox25°C n°4	< 2	< 4	< 2	< 2
S - Ox25°C n°5	< 2	< 4	< 2	< 2
S - Ox300°C n°1	< 2	< 4	< 2	< 2
S - Ox300°C n°2	< 2	< 4	< 2	< 2
S - Ox300°C n°3	< 2	< 4	< 2	< 2
S - Ox300°C n°4	< 2	< 4	< 2	< 2
S - Ox300°C n°5	< 2	< 4	< 2	< 2

Table F.16: *Blank test*: analysis of PWR waters without irradiation (experiments in beaker): Ox25°C(5 solutions), Ox300°C (5 solutions), **S:** solution (PWR water); n°: is the order for several solutions come form the same metal (316L) interface.

Appendix G

List of Samples

There are two tables listed below for overviewing all the samples used in the study.

Specimens	Irradiation	Pre-heating process (2h)	HTHP treatment	Fluence
LE11-02 ref	*no*	*yes*	*yes*	*no*
LE11-03 ref	*no*	*yes*	*yes*	*no*
LE12-04 ref	*no*	*yes*	*yes*	*no*
LE11-01 irr	proton	*yes*	*yes*	low
LE11-04 irr	electron	*yes*	*yes*	low
LE12-05 irr	electron	*yes*	*yes*	high - medium
LE12-07 irr	electron	*yes*	*yes*	high

Table G.1: List of the 316L stainless steel samples used for the HTHP experiments in the study.

Specimens	Preparation procedure	Irradiation	Experiments
X10-01	$25°C$	proton	electrochemistry
X10-02	$25°C$	proton	electrochemistry
X10-03	$25°C$	proton	electrochemistry
X10-04	$25°C$	proton	electrochemistry
X10-05	$25°C$	proton	solution analysis
X10-06	$25°C$	proton	electrochemistry & solution analysis
X10-07	$25°C$	proton	electrochemistry
X10-08	$25°C$	proton	electrochemistry
X10-09	$25°C$	proton	electrochemistry
X10-10	$25°C$	proton	electrochemistry & solution analysis
X10-11	$25°C$	proton	solution analysis
X10-12	$25°C$	proton	solution analysis
X11-01	$25°C$	proton	solution analysis
X11-05	$25°C$	proton	solution analysis
X11-10	$25°C$	proton	solution analysis
X11-11	$25°C$	proton	solution analysis
X11-12	$25°C$	proton	solution analysis
X12-300-01	$300°C$	proton	electrochemistry & solution analysis
X12-300-04	$300°C$	proton	electrochemistry & solution analysis
X12-300-05	$300°C$	proton	solution analysis
X12-300-06	$300°C$	proton	solution analysis
X12-300-08	$300°C$	proton	solution analysis
X12-300-09	$300°C$	proton	solution analysis

Table G.2: List of the 316L stainless steel samples used for the Teflon® cell in the study.

List of Figures

List of Tables

RÉSUMÉ

Cette thèse est dédiée à l'étude du comportement des aciers inoxydables sous irradiation exposés en condition primaire des réacteurs à eau pressurisée (REP). Le potentiel électrochimique de l'acier inoxydable austénitique 316L et les paramètres environnementaux comme la teneur en hydrogène, ont été mesurés de façon continue à haute température (HT) et haute pression (HT) grâce à un dispositif expérimental unique, la cellule HTHP.

Deux sources d'irradiation ont été utilisées: les protons et les électrons. Le comportement électrochimique du 316L s'est avéré similaire dans les deux cas: (i) une augmentation du potentiel sous irradiation de l'ordre de la dizaine de millivolts ("réponse oxydative"); (ii) l'augmentation de la teneur en hydrogène diminue cette augmentation du potentiel sous irradiation; (iii) une synergie est observée entre le vieillissement à 300°C et la fluence qui conduit également à limiter la réponse oxydative sous irradiation.

Les observations du film passif d'oxydes mettent en évidence la présence de nickel métallique dans l'ensemble des oxydes (interne et externe) en présence d'hydrogène, sans irradiation. Après les irradiations les plus fortes, des cavités (piqûres) sont observées en surface du 316L. Ces défauts sont attribués à l'effet de la radiolyse de l'eau et de l'irradiation de la couche passive. La radiolyse influence également l'évolution de la chimie du milieu primaire qui devient plus acide et plus oxydante. Il en résulte une augmentation du relâchement des cations métalliques et la présence d'hématite (α-Fe_2O_3) sur le film d'oxyde externe de l'acier inoxydable lorsque les cavités (piqûres) sont formées.

Mots clefs: acier inoxydable 316L, condition primaire REP, radiolyse d'eau, corrosion, comportement electrochimique

ABSTRACT

The dissertation focuses on the behaviour of stainless steel under irradiation and exposed to primary PWR conditions. The electrochemical potential of austenitic 316L stainless steel and the environmental parameters (hydrogen pressure, temperature, etc.,) have been measured continuously at high temperature (HT) and high pressure (HP) under irradiation, using a unique experimental HTHP working cell.

Two sources of irradiation, proton and electron beams, have been employed in the study. A high similarity of electrochemical behaviour under both types of irradiations has been observed: (i) an oxidative potential response under irradiation (few tens of millivolts); (ii) an increase in the hydrogen pressure reduces the oxidative potential response; (iii) a synergetic effect of thermal ageing and fluence leading to a decrease of the oxidative response under irradiation.

The observations of the oxide film showed that without irradiation, metallic nickel in the inner and outer oxide films has been observed under a high hydrogen pressure. Under irradiation, μm scale cavities (pits) have been observed in the strongly electron irradiated oxide film formed on 316L stainless steel. These defects are induced by the effect of irradiation of the passive film and water radiolysis. It is also shown that water radiolysis influences the PWR water chemistry by making it become a stronger oxidant at the oxide/solution interface. As a result, the release of metallic cations is increased and α-Fe_2O_3 hematite has been observed on the irradiated outer oxide film where cavities were formed.

Keywords: stainless steel 316L, primary PWR conditions, water radiolysis, corrosion, electrochemical behaviour